UNIVERSITY OF CALIFORNIA

Santa Barbara

The Synthesis and Development of Photo-Actuating Materials using Organic Photochromes

A dissertation submitted in partial satisfaction of the

requirements for the degree Doctor of Philosophy

in Chemistry

by

Miranda May Sroda

Committee in charge:

Professor Javier Read de Alaniz, Chair

Professor Megan T. Valentine

Dr. Louis Perez

Professor Christopher M. Bates

Professor Armen Zakarian

December 2021

The dissertation of Miranda May Sroda is approved.

_____

Megan T. Valentine

_____

Louis Perez

_____

Christopher M. Bates

_____

Armen Zakarian

_____

Javier Read de Alaniz, Committee Chair

December 2021

The Synthesis and Development of Photo-Actuating Materials using Organic Photochromes

by

Miranda May Sroda

ACKNOWLEDGEMENTS

I am thankful for my wonderful support system including family, friends, and mentors that have believed, inspired, and challenged me to reach this accomplishment.

I would like to thank my brilliant advisor, Professor Javier Read de Alaniz. Javier's excitement, optimism, and curiosity towards science are truly contagious. I started in his lab as an undergraduate summer intern and quickly knew this was the culture, mentorship, and chemistry that would facilitate growing into the scientist I am today. Throughout my Ph.D., I have learned from him about chemistry and life, specifically how to clear every hurdle with positivity and patience. I thank him for always supporting me; he helped me to build the self-confidence I needed to achieve this goal.

I would also like to thank my colleagues at Apeel Sciences, especially Dr. Louis Perez. Lou's training would become the foundation in which I developed the skills, discipline, and confidence as a scientist to pursue a doctorate degree. Throughout my graduate studies, he has continued to be available offering guidance as I navigated graduate school. I appreciate Lou teaching me how to advocate for myself.

Through collaborative projects, I have had the opportunity to conduct research with several outstanding scientists at UCSB, as well as other universities. I worked closely with Professor Megan Valentine and Dr. Jaejun Lee, which was truly a turning point in my research. The partnership allowed us to merge ideas of organic chemistry, polymer synthesis, and mechanical engineering to advance the field of DASA-based materials.

I would like to thank the Read de Alaniz group, past and present, for cultivating a culture of support, positivity, and great jams on the roller coaster of graduate school. I am thankful to Jamie for his patience and dedication to mentoring me throughout undergraduate

and graduate school. My coffee breaks with Helena were the highlight of the day when science was not going well. The research I was able to accomplish with Fritz has changed the way we think about DASAs today. Thank you to Serena for always being there to discuss science as well as life.

Tanya, Sandy, and Jessica, thank you all for showing up for me constantly!

Justin, thank you for taking on this journey with me from the beginning and being by my side ever since. You are my best friend and I love doing life with you. You have had a front-row seat to the ups and downs and moved mountains to keep a smile on my face.

Finally, thank you to my family who have been always cheering me on from the sidelines. Thank you to my extended family for encouraging me and celebrating me every time I came home to visit. Thank you to my grandparents, Grandma and Grandpa Gauthier, for their eternal wisdom and unwavering support. A special acknowledgment to Grandma and Grandpa Sroda for sharing their devotion to teaching and science. I want to thank my sisters, Mikayla and Miriah, and parents for never making me feel far away and for their many trips to Santa Barbara. Thank you to my sisters for always providing moral support during some of the most challenging times, continuously begging me to come home for every holiday and bringing my wonderful nieces and nephews into this world. I want to thank my Dad for helping me with my AP Chem homework all those years ago. I know all of this would not be possible without the relentless love and support of my Mother, whose endless sacrifices have allowed me to chase every opportunity to get to this moment. I love you all!

Thank you all for your support, I would not have reached this milestone without you.

VITA OF MIRANDA MAY SRODA
December 2021

EDUCATION

Bachelor of Science in Biochemistry and Cell Biology, University of California, San Diego, March 2017
Doctor of Philosophy in Chemistry, University of California, Santa Barbara, December 2021 (expected)

PROFESSIONAL EMPLOYMENT

Graduate Student Researcher, University of California, Santa Barbara, CA.
July 2017 – December 2021

Chemistry Teaching Assistant, University of California, Santa Barbara, CA.
September 2017 – June 2018

Undergraduate Researcher, The Scripps Research Institute, La Jolla, CA.
September 2016 – March 2017

Undergraduate Researcher, University of California, Santa Barbara, CA.
June 2016 – September 2016

Formulation Engineer Intern, Apeel Sciences, Santa Barbara, CA.
June 2014 – September 2014
June 2015 – September 2015

PUBLICATIONS

Sroda, M. M.; Lee, J; Read de Alaniz, J.; et al. "The role of polymer matrix and photochrome incorporation on the photothermal actuation of DASA-based polymers" **2021**, under review.

Sroda, M. M.; Lee, J; Kwon, Y.; El-Arid, S.; Valentine, M.; Read de Alaniz, J.; et al. "Tunable photothermal actuation enabled by photoswitching of DASAs" *ACS Appl. Mater. Interfaces* **2020**, *12*, 48, 54075-54082.

Sroda, M. M.; Stricker, F.; Peterson, J.; Bernal, A.; Read de Alaniz, J. "DASAs: Exploring the effects of ionic character" *Chem. Eur. J.* **2020**, *27*, 1-9.

Seshadri, S.; Bailey, S. J.; Zhao, L.; Fisher, J.; **Sroda, M. M.**; Chiu, M.; et al. "Influence of polarity change and photophysical effects of photosurfactant-driven wetting" *Langmuir* **2021**, *37*, 33, 9939-9951.

Clerc, M.; Stricker, F.; Ulrich, S.; **Sroda, M. M.**; Bruns, N.; Boesel, L., Read de Alaniz, J. "Promoting the furan ring-opening reaction to access new DASAs with hexafluoroisopropanol" *Angew. Chem.* **2021**, *133*, 2-11.

Seshadri, S.; Gockowski, L. F.; Lee, J.; **Sroda, M. M.**; Read de Alaniz, J, et al. "Self-regulating photochemical Rayleigh-Bénard convection using a highly-absorbing organic photoswitch" *Nat. Commun.* **2020**, *11*, 2599.

Lui, B.; Tierce, N.; Tong, F. **Sroda, M. M.**; Read de Alaniz, J.; et al. "Unusual concentration dependence of the photoisomerization reaction in DASAs" *Photochem. Photobiology. Sci.*, **2019**, *18*, 1587-1595.

Shaum, J. B.; Fisher, D. J.; **Sroda, M. M.**; Limon, L.; Read de Alaniz, J. "Direct introduction of nitrogen and oxygen functionality with spatial control" *Chem. Sci.*, **2018**, *9*, 8748-8752.

Gurak, J. A., Jr.; Tran, V. T.; **Sroda, M. M.**; Engle, K. M. "N-Alkylation of 2-Pyridone Derivatives via Palladium (II)-Catalyzed Directed Alkene Hydroamination" *Tetrahedron* **2017**, *73*, 3636-3642.

AWARDS

Dow BEST Symposium, The Dow Chemical Company, 2021
Graduate Division Dissertation Fellowship, UC Santa Barbara 2021
Graduate Opportunity Research Fellowship, UC Santa Barbara 2019-2020
Graduate Opportunity Research Fellowship, UC Santa Barbara 2020-2021
DeWolfe Distinguished Teaching Fellow Award, UC Santa Barbara 2019-2020
Outstanding Service to the Department, UC Santa Barbara 2019-2020
Department of Chemistry Early Start Summer Research Fellowship, UC Santa Barbara 2017
Future Leaders in Advanced Materials Summer Research Fellowship, UC Santa Barbara 2016

ABSTRACT

The Synthesis and Development of Photo-Actuating Materials using Organic Photochromes

by

Miranda May Sroda

The question that motivates my PhD research is how to convert light directly into actuation using organic photoswitches. To accomplish this goal, we must first move beyond traditional chromophores to find photoswitches whose optoelectronic properties are optimized for a given scenario. Among these, donor–acceptor Stenhouse adducts (DASAs), are especially promising due to their negative photochromism, tunable absorption profile, and large volume change. To incorporate DASAs into photo-actuating materials a better understanding of the photophysical properties is crucial, as well as understanding the concentration dependence. In this effort, we explored the concentration dependence and effect of ionic character on DASAs. The effects of solution-state dielectric and intermolecular interactions on the degree of charge separation of the open form provides a route to understanding the switching properties and concentration dependence of DASAs. Second, developing a high efficiency photoswitch is not sufficient to make a viable photo-actuating material. Once such a molecule is incorporated into a solid matrix, numerous factors can affect its ability to react, including polymer matrix and photochrome density. We need robust, scalable, and efficient methods to access a range of DASA-based materials and actuator

designs to evaluate actuation performance. We demonstrate a synthetic platform to chemically conjugate DASA to a load-bearing poly(hexyl methacrylate) (PHMA) matrix via Diels−Alder click chemistry that enables access to DASA-based materials on scale. By leveraging the ease of fabrication of a bilayer design, we developed a tunable, visible light-responsive bilayer actuator driven by the photothermal properties of DASAs. Further, we investigate the influence of the host matrix on the photothermally-driven actuation performance of DASA-based polymers. We designed polymeric materials with varying photochrome incorporation and investigated the relationships between material composition and the resulting physical, mechanical, and photoswitching properties. Finally, we report and compare the light-induced property changes in the glass transition temperature and elastic modulus between the materials comprising of the open or closed form of DASAs. This work establishes the foundational relationships between mechanical and photoswitching properties and is critical to advancing the use of DASA-based materials.

Table of Contents

Table of Figures

Abbreviations

a.u.	absorbance unit
AF	activated furan
$CDCl_3$	deuterated chloroform
DABCO	1,4-Diazabicyclo[2.2.2]octane
DASA	donor-acceptor Stenhouse adduct
DCM	dichloromethane
DEA	diethylamine
DI	deionized (water)
DMAP	dimethylaminopyridine
DMSO	dimethyl sulfoxide
DSC	differential scanning calorimetry
Đ	dispersity
EDC	1-ethyl-3-(3-dimethylaminopropyl) carbodiimide Et_3SiH triethylsilane
EtOAc	ethyl acetate
Equiv.	equivalence
FT-IR	Fourier Transform Infrared
g	gram(s)
h	hour(s)
HCl	hydrochloric acid
K_2CO_3	potassium carbonate
M	molar
MeCN	acetonitrile
mg	milligram(s)
MHz	megahertz
min	minute(s)
mL	milliliter(s)
mM	millimolar
mol	mole
NaOH	sodium hydroxide
NB-AF	oxa-norbornene furan monomer
nm	nanometer(s)
NMR	nuclear magnetic resonance
o	*ortho*
P	*para*
PS	polystyrene
RAFT	reversible addition fragmentation chain transfer RI refractive index
ROMP	ring-opening metathesis polymerization
RPM	revolutions per minute
SEC	size exclusion chromatography
T_g	glass transition temperature
THF	tetrahydrofuran

Abbreviations (cont.)

TLC	thin layer chromatography
TMS	tetramethylsilane
UV-NIR	ultraviolet-near IR
UV-vis	ultraviolet-visible
ε	molar absorptivity
μg	microgram(s)
μL	microliter(s)
μM	micromolar
μm	micrometer(s)

Chapter 1. Introduction

Nature has provided us with remarkable light-driven processes including human vision, solar energy, and photosynthesis. The range of these applications highlight how nature uses light as both an energy source and signal for high spatiotemporal resolution control. Other advantageous properties of light include the ability to readily tune intensity, spot size and wavelength, on/off control and remote control. In order to develop light-responsive materials, organic photochromes have gained considerable attention.[1]

1.1. Commonly used photochromes

Organic photochromes, also known as photoswitches, date back to Fritzsche in 1867.[2] Photochromism is defined as a "reversible transformation of a chemical species induced in one or both directions by absorption of electromagnetic radiation between two forms, A and B, having different absorption spectra".[3] The thermodynamically stable form A is transformed by irradiation into form B, as shown in Figure 1.1.[3] Types of photoswitches are often defined by their recovery mechanism; T-type revert thermally to their original form, whereas P-type reversibility require a second photon, usually at a different wavelength, to revert to their original form.[4,5] One can also choose between positive photochromes (whose absorption remains unchanged or increases at the wavelength used for excitation upon isomerization) and negative photochromes (whose absorption diminishes at the wavelength used for excitation upon isomerization). Additionally, there are many different chemical reactions involved in the light-induced transformation, including *E/Z* isomerizations, electrocyclizations, and cycloadditions.[6] Example of commonly used photoswitches include azobenzenes,[7] spiropyrans[6] and diarylethenes,[8,9] shown in Figure 1.2.

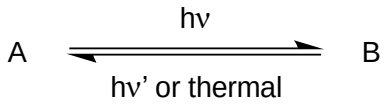

Figure 1.1 General scheme of photochromism.

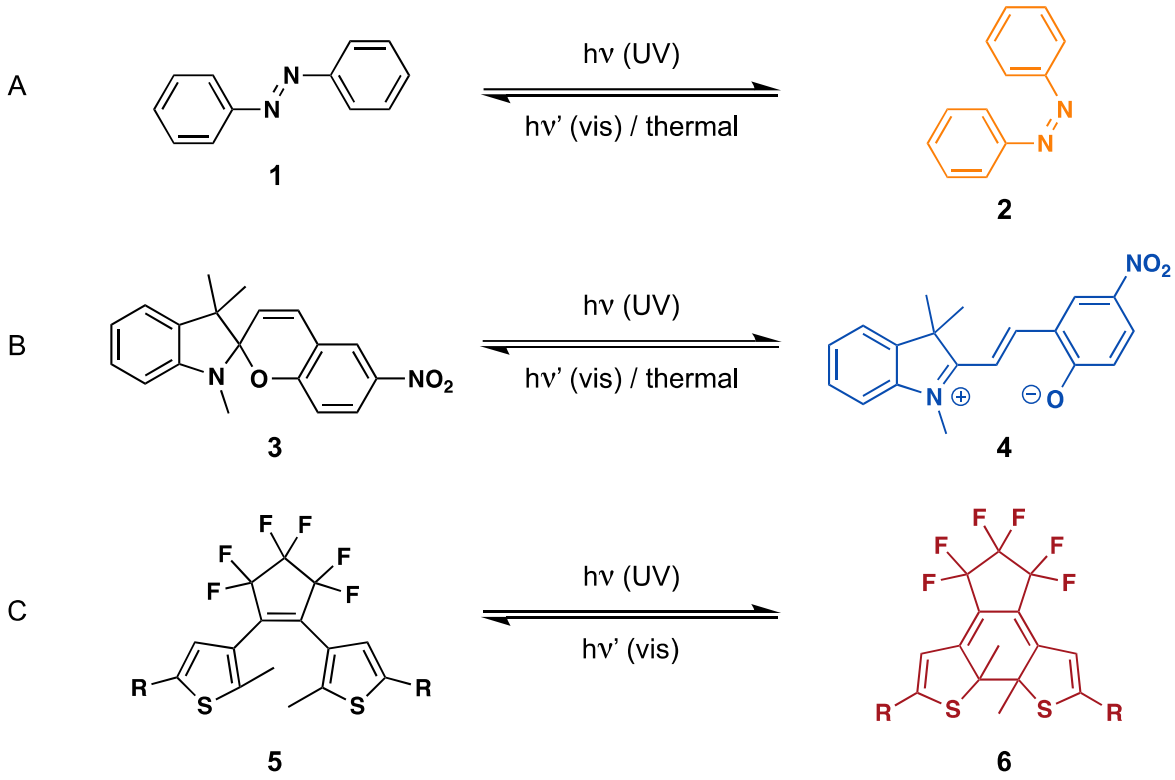

Figure 1.2 Example of traditional photoswitches. A: azobenzene, B: spiropyran, C: diarylethene.

The most widely used photoswitch, with over 100,000 scientific publications, is azobenzene (Figure 1.2a).[7] Azobenzenes often start in a *trans* isomer and upon irradiation with UV-light undergo an *E/Z* isomerization to a meta-stable *cis* isomer. These can be either P-type of T-type, meaning reverse isomerization back to the *trans* isomer occurs either thermally or can be driven back to the original form with a second wavelength of light. Azobenzenes are the workhorse molecule for photomechanical materials owing to being

chemically robust, large volume change between isomers and relatively simple and well-understood photochemistry.[10–12] However, they are not without inherent limitations, including the use of UV light which offers limited penetration and can damage material, as well as overlapping *cis* and *trans* absorption profiles can limit selectivity and photoconversion. To address part of these challenges, there has been considerable effort to synthesize visible light responsive azobenzenes by Aprahamian, Hecht, Burdette and others.[13–15] Despite progress, many of these new derivatives also suffered from overlapping *cis* and *trans* absorption profiles, low molar extinction coefficients (ε = 2000–3000 M^{-1} cm^{-1}), hydrolysis in water, and unfavorable switching kinetics.[13–15]

The second most studied photoswitch with over 15,000 publications is spiropyran, shown in Figure 1.2b.[6] Spiropyrans undergo an electrocyclization upon irradiation with UV light, starting from a colorless spiro form leading to ring opening via carbon-oxygen bond cleavage, followed by *Z/E* isomerization to give the blue colored merocyanine structure. Similar to azobenzenes, these can be either P-type of T-type. The electrocyclization also induces a large polarity change, which was leveraged by Schenning and coworkers to develop light-responsive hydrogels for microfluidic applications.[16] These switches are also limited by the use of UV light, as well as low fatigue resistance and aggregation of the open form.[6]

Another prominent class of photoswitches is diarylethenes, with over 10,000 publications, shown in Figure 1.2c.[8,9] Diarylethenes are P-type photoswitches that undergo a 6π electrocyclization, changing from colorless to red.[8] Both isomers are remarkably stable with half-lives for the metastable isomer of more than 470,000 years. In addition, physical properties change upon isomerization include fluorescence, electrical conductivity and

magnetism.[9] While diarylethenes have a smaller volume change compared to spiropyran and azobenzene, they undergo reversible isomerization in single crystals which has been leveraged for photomechanical actuation by Bardeen and coworkers.[17]

While commonly used switches have been used for a variety of different applications including optoelectronic devies,[8] self-healing,[18] erasable writing,[19] they have inherent limitations. They all require the use of UV light, which offers limited penetration depth and damage to material, and many have a highly absorbing photoproduct which can also limit light penetration and result in absorption profile overlap. Thus, we need to develop new chromophores that overcome these limitations. This thesis will explore a recently discovered photoswitch which has the promising property of negative photochromism, as well as other advantageous properties.

1.2. Donor-acceptor Stenhouse adducts (DASAs)

Donor–acceptor Stenhouse adducts (DASAs) were first reported by Read de Alaniz and coworkers in 2014 and were termed after the pioneering work of John Stenhouse (described in more detail below).[20–22] DASA consist of an amine donor and carbon acid acceptor connected by a triene bridge in a push-pull system, as shown in Figure 1.3. DASAs have garnered a significant amount of attention due to their negative photochromism, visible light activation, and large volume change.

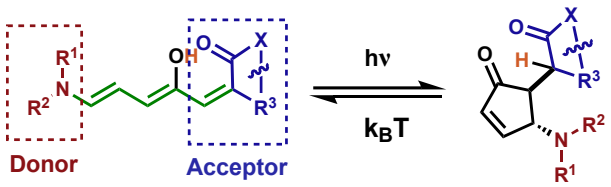

7 8

Figure 1.3 General reaction scheme of DASA.

A number of pioneering studies led by Stenhouse,[20,23] Schiff,[24] Honda,[25] Lewis and Mulquiney,[21] and Safar[26] were crucial to the development of DASAs.[22,27] In 1850, Stenhouse reported the formation of a highly colored salt after reacting two equivalents of primary or secondary amine and one equivalent of protic acid to furfural.[20] The structure was later determined by Schiff as a five-carbon cyanine dye with an -OH group.[24] However, it was not until 1982 that Honda revealed Stenhouse salts exhibited negative photochromism.[25]

Unrelated to their photochromic properties, the structure of the colorless isomer of Stenhouse adducts was established as a cyclopentenone by Lewis and Mulquiney.[21] The synthesis of Stenhouse salt proceeds through an imine/iminium activation between furfural and anilines, as shown in Figure 1.4 (path a). To further explore the synthetic utility of the ring-opening reaction of furfural derivatives, Safar demonstrated that condensation of Meldrum's acid onto furfural creates an activated furan adduct that undergoes a ring opening reaction with aliphatic amines to form a mixture of the highly colored triene and colorless cyclopentanone (Figure 1.4, path b).[26] In 2010, Read de Alaniz demonstrated that treatment of furfural alcohol with dysprosium triflate ($Dy(OTf)_3$ also mediated a ring opening reaction with anilines, resulting in aminocyclopentenones (Figure 1.4, path c).[28–31] Collectively, these reports ultimately led to Read de Alaniz and coworkers to discover and develop Donor-Acceptor Stenhouse Adducts as a new class of visible light photochromes 2014.[22,27]

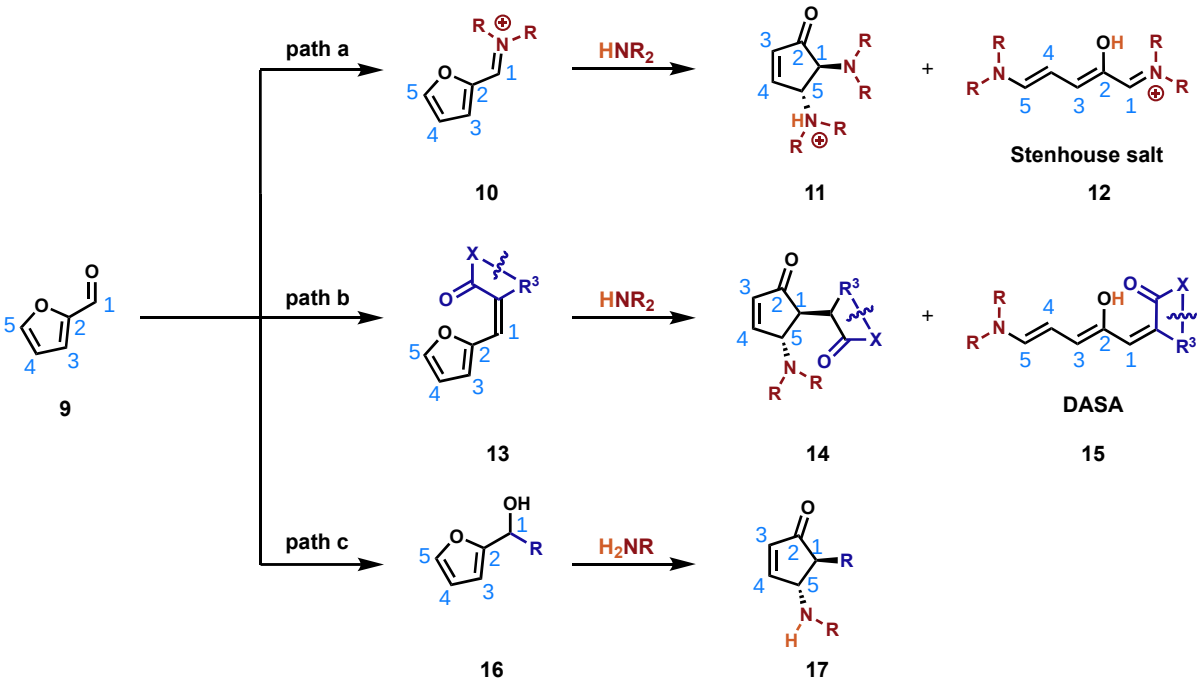

Figure 1.4 Synthesis of Stenhouse salts, DASAs and aminocyclopentenones.

Unlike commonly used photoswitches, DASAs exhibit negative photochromism and visible light activation.[22,27,32,33] They are prepared by a simple two-step synthesis from the commodity chemical furfural. The acceptor moiety is prepared by a knoevenagel condensation reaction of furfural with a carbon acid to yield the furan adduct. The first carbon acids explored were Meldrum's acid and barbituric acid. Treatment of these "activated" adducts with secondary aliphatic amine resulted in a highly colored DASA.[34,35] Upon irradiation, DASAs are converted from a highly light-absorbing colored "open" form into a colorless and transparent "closed" form, as shown in Figure 1.5, with overall switching kinetics highly dependent on the DASA architecture and surrounding environment. These are better described as photothermalstationary states because the 4π electrocyclization that results in the closed form is thermally driven.[36]

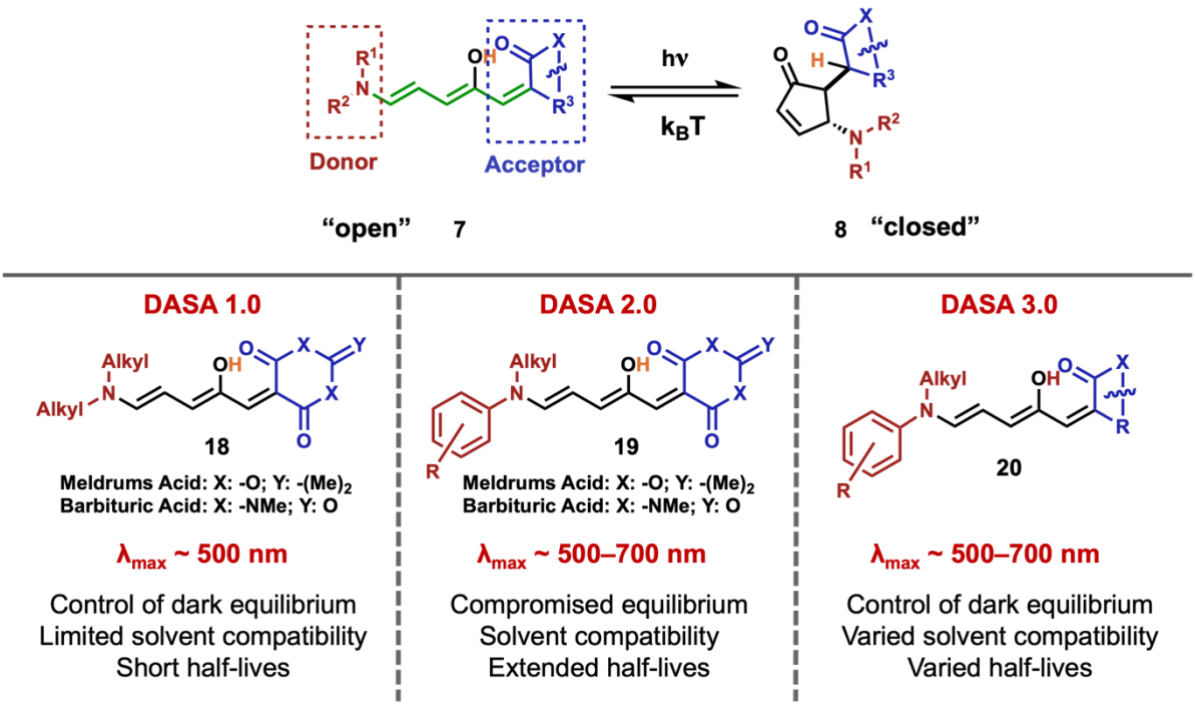

Figure 1.5 Synthetic efforts have resulted in three generations of DASAs that vary in their photoswitching properties, including control of thermodynamic equilibrium, solvent compatibility, and switching kinetics. The closed form is only depicted with the acceptor group in the enol form, however, as reported in the literature, it can reside in a zwitterionic, enol, or keto form, depending on the architecture and conditions.[22,32,37] Figure adapted with permission from *Chem. Eur. J.* **2021**, 27, 1 – 9. Copyright (2020) Wiley-VCH GmbH.

Synthetic efforts have resulted in three architecturally distinct DASA derivatives that vary in nature of the donor and acceptor groups used to connect the triene backbone. These derivatives also possess different photoswitching properties, such as thermodynamic equilibrium (dark equilibrium between the open and closed forms), wavelength tuneability (500–700 nm), switching rates, and solvent dependence as shown in Figure 1.6.[22,27,32,33] The first generation of DASAs, published in 2014, consist of strongly electron-donating dialkylamine donors and Meldrum's or barbituric acid acceptors.[22,27] These derivatives

generally show excellent equilibrium control and fatigue resistance, but are often limited in wavelength tuneability and solvent compatibility, defined herein as the ability to switch reversibly upon irradiation in a range of solvents. This generation was further investigated by Beves and coworkers and demonstrated amines such as dimethylamine are able to switch in a wider range of solvents.[38] In 2016, the second generation of DASAs were created by employing weakly donating cyclic and acyclic arylamines.[32,37] These substrates show improved wavelength tuneability (500–700 nm) and enhanced switching properties, including low PTSS, higher solvent compatibility, and solid-state switching, but compromised thermodynamic equilibria in the dark (~50–7% open form in the absence of light) and extended half-lives of the closed form. The third generation of DASAs, developed in 2018, introduce strongly electron-withdrawing carbon acids as acceptors. Generally, these derivatives have enhanced switching properties, such as increased solvent compatibility and tunable half-lives of the closed form, while maintaining high equilibrium control.[33]

The synthetic effort toward DASAs has been tightly coupled with extensive mechanistic studies by Feringa, Beves, Martinez, Marazzi and others.[35,37–43] It was demonstrated that the actinic *Z/E* isomerization step is independent of solvent and concentration, and occurs on a femto- to nanosecond timescale.[40,44] This is followed by C3-C4 bond rotation and thermal 4π electrocyclization, leading to ring-closed cyclopentenone with a *trans* relationship between the C1 and C5 groups, which occurs on a nano- to millisecond timescale (Figure 1.6). In contrast to the actinic step, the thermal part of the mechanism is highly solvent-dependent.[40]

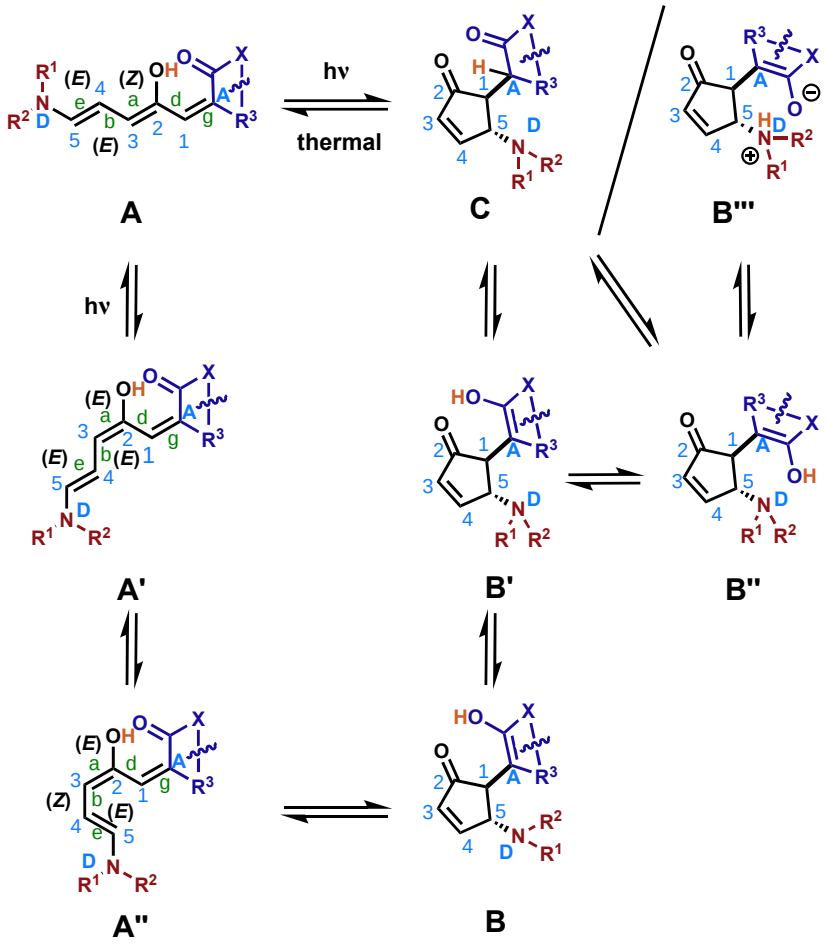

Figure 1.6 Current proposed productive mechanism for photoswitching by Feringa et al.[43]

Since their discovery, DASAs have been exploited in a number of applications including targeted drug release,[27,45,46] orthogonal photoswitching,[47] and chemical and thermal sensing.[48–51] Further use of DASA in more widespread applications has been hampered by limited understanding of solvent compatibility, concentration dependence and thermal recovery. Additionally, there is not a reliable, modular, and scalable method to access DASA-based materials. This thesis aims to contribute to improving that understanding and accessibility, by exploring the concentration dependence (Chapter 2), switching properties in polymer matrix (Chapters 3 and 4) and application in photo-thermal driven actuation (Chapters 3 and 4).

1.2.1. Concentration dependence of DASA

The concentration dependence of DASA 2-methyl indoline and CF_3 pyrazalone bearing third generation architecture was studied by Bardeen, Read de Alaniz and coworkers.[52] Through these studies, we demonstrate that DASA switches efficiently at micromolar concentrations in both liquid solution and in polymers, however, the photoswitching is dramatically inhibited at higher concentrations. Both the initial rate of absorbance decay and the asymptotic PTSS value change with increasing concentration, as shown in Figure 1.7a. There was also a significant increase in the back reaction rate with increasing concentration, as shown in Figure 1.7b. Overall, the forward photo-isomerization and the thermal backward reaction can change by factors of 20 or more depending on DASA concentration. There was no sign of aggregation or electronic coupling, as indicated by the absence of broadening of shifting in the absorption spectra of DASA at various concentrations. Using femtosecond transient absorption experiments, they found the light-driven *cis* → *trans* step of the isomerization was not affected by concentration, suggesting the concentration inhibition occurs in the following thermal pathway. Chapter 2 describes our efforts to help better understand this unusual concentration dependence.

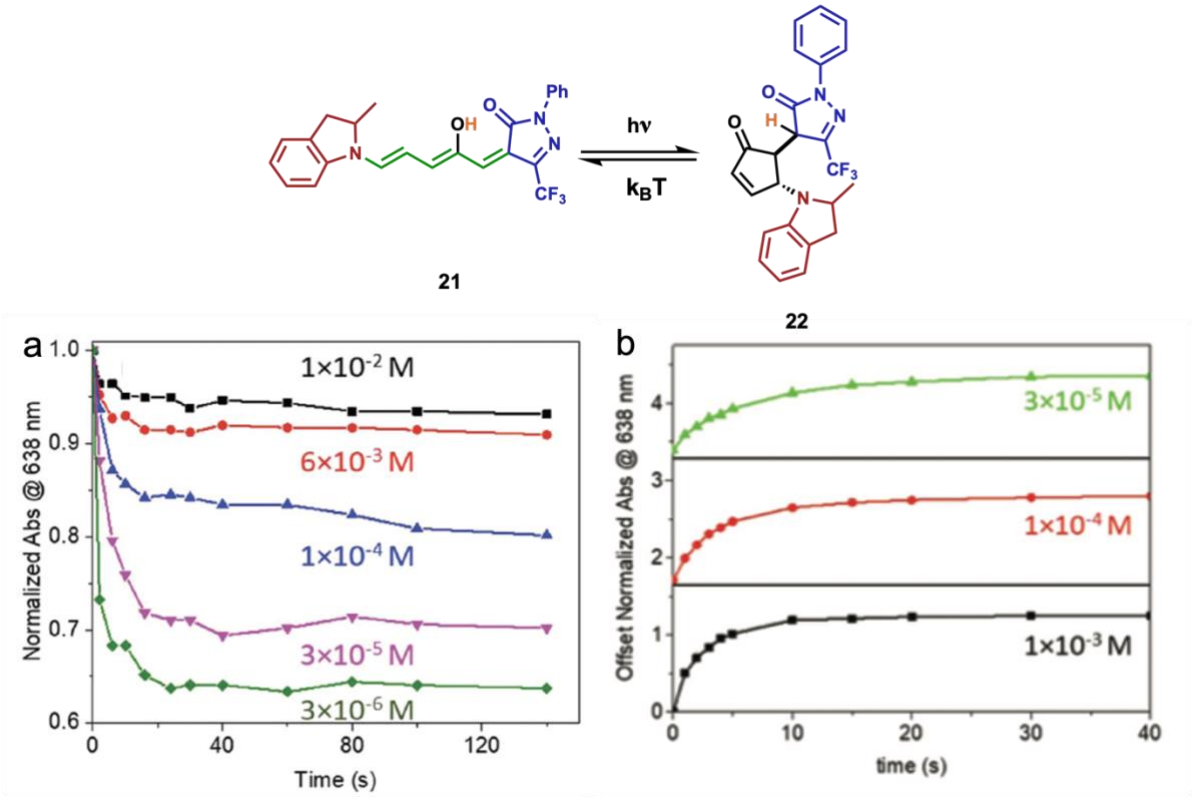

Figure 1.7 a) The decay of absorption monitored at 638 nm versus time for different DASA concentrations in chloroform. b) Absorption recovery curves for different DASA concentrations in toluene, monitored at 638 nm, reflecting the decrease in k_{back}. This figure was adapted with permission from *Photochem. Photobiol. Sci.* **2019**, *18* (6), 1587–1595.[52] Copyright (2019) Royal Society of Chemistry.

1.2.2. Synthesis of DASA-based materials

Due to the reactivity of the open and closed forms to radical and nucleophilic addition, common methods to prepare DASA-based materials has been limited. To overcome these challenges and provide access to photoresponsive materials bearing DASA photoswitches, a number of strategies have been developed.[27,51,53–57] The strategies can be broken down into three general categories (1) post-functionalization using "click" chemistry; (2) attachment of the donor group to the polymer backbone, followed by DASA

formation; (3) attachment of the acceptor group to the polymer backbone, followed by DASA formation. In the first approach, Read de Alaniz and coworkers utilized a post-functionalization "click" chemistry to synthesize a DASA-functionalized amphiphilic polymer as shown in Figure 1.8a.[27] They first synthesized a DASA bearing a terminal azide, which was further reacted to alkyne terminated monomethyl poly(ethylene glycol) via "click" chemistry to form the desired DASA end-functionalized polymer. The second approach led to the first DASA pendant-functionalized polymers by conjugation of the donor to a polymer.[55] Wang and coworkers synthesized styrene-vinylbenzyl chloride copolymer using free radical polymerization. This is followed by nucleophilic substitution reaction between chloro-methyl unit and *n*-butylamine to form an amino-functionalized PS-*co*-PCMS. The secondary alkyl amine reactions with Meldrum's furan adduct to form first generation DASA pendant polymer. Read de Alaniz used pentafluorophenylester chemistry to incorporate aromatic amines into acrylate and methacrylate copolymers, which could further be reacted with furan adducts to synthesize second generation DASA pendant polymers, as shown in Figure 1.8b.[53] This method was further improved upon with the addition of 1,1,1,3,3,3-hexafluoro-2-propanol (HFIP), reducing the reaction time from days to hours.[54] Beves and coworkers synthesized DASA-based homopolymers and compared the photoswitching of acrylate and methacrylate polymers, as well as block copolymer.[57] In a third approach, Read de Alaniz and coworkers reported synthesizing DASA pendant-functionalized polymers using conjugation of the acceptor to the polymer, as shown in Figure 1.8c.[51] They used ring-opening metathesis polymerization (ROMP) of an activated furan monomer that is followed by DASA formation.

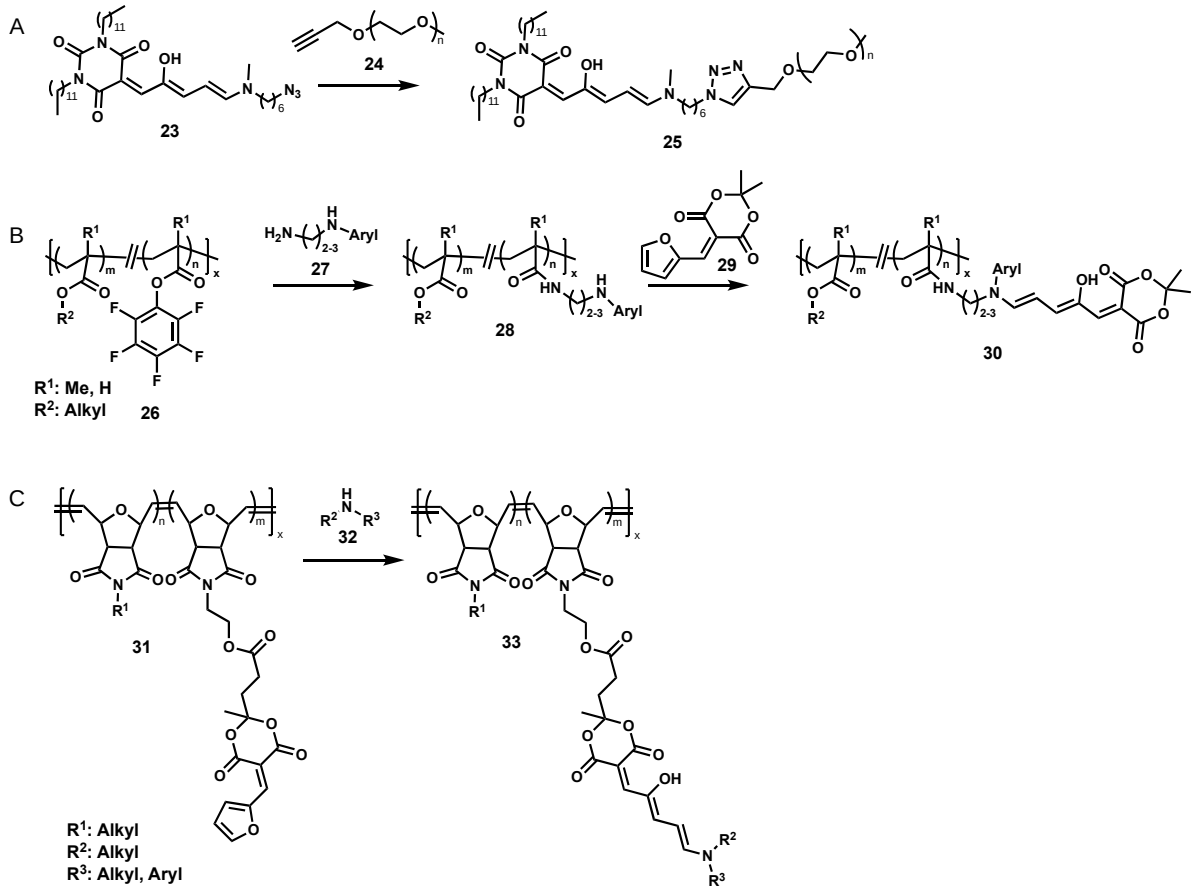

Figure 1.8 Synthetic approaches for DASA-functionalized polymers. a) post-functionalization using "click" chemistry; b) attachment of the donor group to the polymer backbone, followed by DASA formation; c) attachment of the acceptor group to the polymer backbone, followed by DASA formation.[27,51,58]

While these approaches have led to the development of DASA-based materials which have been leveraged in a variety of different applications including chemical and thermal sensing,[51,56] photopatterning,[53] and nanoreactors,[58] they introduce a number of limitations. The pendant-functionalization strategies rely on DASA formation in the final step resulting in long reaction times, incomplete functionalization, and multiple post-polymerization steps. This also limits the modular nature of the approach, for example,

different synthetic approaches are needed for incorporating different generations of DASAs or potentially a different class of photoswitch, such as an azobenzene. We need modular, scalable, and efficient methods to access a range of DASA-based materials. To do this, we will explore a pendant-functionalization strategy using a "click" chemistry approach in Chapter 3 and Chapter 4.

1.3. Photo-actuation

Extensive use of light to achieve controlled actuation has been reported using photoresponsive agents, including photoswitches,[59–61] organic dyes,[62–64] carbon-based materials,[65,66] and gold nanoparticles.[67,68] The two mechanisms of photo-actuation include: photomechanical and photothermal. Photochemical reactions can lead to photomechanical actuation based on the organization of molecules, resulting in macroscopic deformation based on molecular-scale shape changes.[10,69] The concept of using many molecular-scale photochemical shape changes to generate a larger deformation is illustrated in Figure 1.9. In order to induce molecular organization a photoswitch is aligned into a liquid crystal network, resulting in intrinsic anisotropy.[70] This approach is typically limited to the use of azobenzene, owing to the required alignment chemistries such as thiol-Michael additions[71] and radical polymerizations.[69] In contrast, photothermal shape changes are driven by the conversion of absorbed optical energy into thermal energy, which by different mechanisms, can generate deformation.[72] The temperature locally increases due to photothermal excitation of the photoresponsive agent[70] and macroscopic motion is governed by the combination of material and geometrical parameters, such as mismatches in expansion coefficients, elastic modulus ratios and relative thickness ratios.[73] An elegant cooperative use of photochemical patterning and photothermal actuation in a liquid crystalline network

(LCN) was developed by Priimagi and coworkers.[74] This strategy relies on molecular alignment of the azobenzene-based LCN: *E*/*Z* photoisomerization programs strain while red light irradiation of an anthraquinone dye triggers photothermal actuation. The absorption properties of the azobenzene photoswitch require use of narrow bandwidth (< 100 nm) high-energy UV-light to embed programming logic via photoisomerization.[75] The challenge remains to design materials that leverage the cooperative use of photochemical and photothermal properties to tune actuation that operates with less harmful, abundant, and economically beneficial broadband light sources (i.e., halogen lamps, white LEDs, sunlight). In addition, negative photochromism has not been explored for photo-actuating application. Upon irradiation, material results in decoloration lowering the material's optical density, resulting in increased light penetration through the entire material.[6] Achieving this would require moving away from traditional azobenzene-based stimuli responsive materials. To do this, we will explore photothermal actuation of DASA-based polymers in Chapter 3 and Chapter 4.

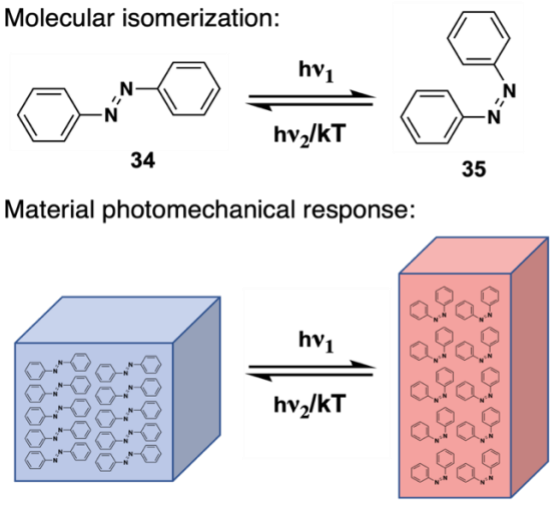

Figure 1.9 Schematic illustration of organized molecular switches that drive macroscopic mechanical motion.

1.4. References

(1) Goulet-Hanssens, A.; Eisenreich, F.; Hecht, S. Enlightening Materials with Photoswitches. *Adv. Mater.* **2020**, *32* (20).

(2) Fritzsche, J. Note Sur Les Carbures d'hydrogene Solides, Tires Du Goudron de Houille. *C.R. Acad. Sci.* **1867**, *69* (1035), 78.

(3) Bouas-Laurent, H.; Dürr, H. Organic Photochromism. *Pure Appl. Chem.* **2001**, *73* (4), 639–665.

(4) Durr, H.; Bouas-Laurent, H. *Photochromism: Molecules and Systems*; Elsevier: New York, 1990.

(5) Irie, M.; Yokoyama, M.; Seki, T. *New Frontiers in Photochromism*, 1st ed.; Springer Japan, 2013.

(6) Boelke, J.; Hecht, S. Designing Molecular Photoswitches for Soft Materials Applications. *Adv. Opt. Mater.* **2019**, *1900404*.

(7) Bandara, H. M. D.; Burdette, S. C. Photoisomerization in Different Classes of Azobenzene. *Chem. Soc. Rev.* **2012**, *41* (5), 1809–1825.

(8) Irie, M. Photochromism of Diarylethene Molecules and Crystals. *Proc. Japan Acad. Ser. B Phys. Biol. Sci.* **2010**, *86* (5), 472–483.

(9) Matsuda, K.; Irie, M. Diarylethene as a Photoswitching Unit. *J. Photochem. Photobiol. C Photochem. Rev.* **2004**, *5* (2), 169–182.

(10) Barrett, C. J.; Mamiya, J.; Yager, K. G.; Ikeda, T. Photomechanical Effects in Azobenzene-Containing Soft Materials. *Soft Matter* **2007**, *3* (1249).

(11) Finkelmann, H.; Nishikawa, E.; Pereira, G. G.; Warner, M. A New Opto- Mechanical Effect in Solids. *Phys. Rev. Lett.* **2001**, *87* (015501/1).

(12) Ikeda, T.; Mamiya, J.; Yu, Y. Photomechanics of Liquid-Crystalline Elastomers and Other Polymers. *Angew. Chemie Int. Ed.* **2007**, *46* (506).

(13) Yang, Y.; Hughes, R. P.; Aprahamian, I. Visible Light Switching of a BF 2-Coordinated Azo Compound. *J. Am. Chem. Soc.* **2012**, *134* (37), 15221–15224.

(14) Yang, Y.; Hughes, R. P.; Aprahamian, I. Near-Infrared Light Activated Azo-BF 2 Switches. *J. Am. Chem. Soc.* **2014**, *136*, 4–7.

(15) Bléger, D.; Schwarz, J.; Brouwer, A. M.; Hecht, S. O -Fluoroazobenzenes as Readily Synthesized Photoswitches Offering Nearly Quantitative Two-Way Isomerization with Visible Light. *J. Am. Chem. Soc.* **2012**, *134* (51), 20597–20600.

(16) Ter Schiphorst, J.; Coleman, S.; Stumpel, J. E.; Ben Azouz, A.; Diamond, D.; Schenning, A. P. H. J. Molecular Design of Light-Responsive Hydrogels, for in Situ Generation of Fast and Reversible Valves for Microfluidic Applications. *Chem. Mater.* **2015**, *27* (17), 5925–5931.

(17) Tong, F.; Kitagawa, D.; Dong, X.; Kobatake, S.; Bardeen, C. J. Photomechanical Motion of Diarylethene Molecular Crystal Nanowires. *Nanoscale* **2018**, *10* (7), 3393–3398.

(18) Kathan, M.; Kovaˇríc̆ek, P.; Jurissek, C.; Senf, A.; Dallmann, A.; Thünemann, A. F.; Hecht, S. Control of Imine Exchange Kinetics with Photoswitches to Modulate Self-Healing in Polysiloxane Networks by Light Illumination. *Angew. Chemie Int. Ed.* **2016**, *55* (13882).

(19) Bao, B.; Fan, J.; Xu, R.; Wang, W.; Yu, D. Rewritable Spiropyran/Polyacrylonitrile Hybrid Nanofiber Membrane Prepared by Electrospinning. *Nano* **2020**, *15* (1), 1–13.

(20) Stenhouse, J. Ueber Die Oele, Die Bei Der Einwirkung Der Schwefelsäure Auf

Verschiedene Vegetabilien Entstehen. *Justus Liebigs Ann. Chem.* **1850**, *74* (3), 278–297.

(21) Lewis, K. G.; Mulquiney, C. E. Aspects of the Formation and Use of Stenhouse Salts and Related Compounds. *Tetrahedron* **1977**, *33* (5), 463–475.

(22) Helmy, S.; Oh, S.; Leibfarth, F. A.; Hawker, C. J.; Read de Alaniz, J. Design and Synthesis of Donor-Acceptor Stenhouse Adducts: A Visible Light Photoswitch Derived from Furfural. *J. Org. Chem.* **2014**, *79* (23), 11316–11329.

(23) Stenhouse, J. No Title. *J. Ann. Chem. Pharm.* **1870**, *156* (197).

(24) Schiff, H. Ueber Farbstoff Basen. *Justus Liebigs Ann. Chem.* **1887**, *239* (349).

(25) Honda, K.; Komizu, H.; Kawasaki, M. Reverse Photocharomism of Stenhouse Salts. *J. Am. Chem. Soc. Chem. Commun.* **1982**, *253* (4).

(26) Šafář, P.; Považanec, F.; Prónayová, N.; Baran, P.; Kickelbick, G.; Kožíšek, J.; Breza, M. Dichotomy in the Ring Opening Reaction of 5-[(2-Furyl)Methylidene]-2,2-Dimethyl-1,3-Dioxane-4,6-Dione with Cyclic Secondary Amines. *Collect. Czechoslov. Chem. Commun.* **2000**, *65* (12), 1911–1938.

(27) Helmy, S.; Leibfarth, F. A.; Oh, S.; Poelma, J. E.; Hawker, C. J.; Read de Alaniz, J. Photoswitching Using Visible Light: A New Class of Organic Photochromic Molecules. *J. Am. Chem. Soc.* **2014**, *136* (23), 8169–8172.

(28) Veits, G. K.; Wenz, D. R.; Read de Alaniz, J. Versatile Method for the Synthesis of 4-Aminocyclopentenones: Dysprosium(III) Triflate Catalyzed Aza-Piancatelli Rearrangement. *Angew. Chemie Int. Ed.* **2010**, *49* (49), 9484–9487.

(29) Wenz, D. R.; Read de Alaniz, J. Aza-Piancatelli Rearrangement Initiated by Ring Opening of Donor-Acceptor Cyclopropanes. *Org. Lett.* **2013**, *15* (13), 3250–3253.

(30) Palmer, L. I.; Read de Alaniz, J. Direct and Highly Diastereoselective Synthesis of Azaspirocycles by a Dysprosium(III) Triflate Catalyzed Aza-Piancatelli Rearrangement. *Angew. Chemie Int. Ed.* **2011**, *50* (31), 7167–7170.

(31) Veits, G. K.; Wenz, D. R.; Palmer, L. I.; St. Amant, A. H.; Hein, J. E.; Read de Alaniz, J. Cascade Rearrangement of Furylcarbinols with Hydroxylamines: Practical Access to Densely Functionalized Cyclopentane Derivatives. *Org. Biomol. Chem.* **2015**, *13* (31), 8465–8469.

(32) Hemmer, J. R.; Poelma, S. O.; Treat, N.; Page, Z. A.; Dolinski, N. D.; Diaz, Y. J.; Tomlinson, W.; Clark, K. D.; Hooper, J. P.; Hawker, C.; Read de Alaniz, J. Tunable Visible and Near Infrared Photoswitches. *J. Am. Chem. Soc.* **2016**, *138* (42), 13960–13966.

(33) Hemmer, J. R.; Page, Z. A.; Clark, K. D.; Stricker, F.; Dolinski, N. D.; Hawker, C. J.; Read de Alaniz, J. Controlling Dark Equilibria and Enhancing Donor-Acceptor Stenhouse Adduct Photoswitching Properties through Carbon Acid Design. *J. Am. Chem. Soc.* **2018**, *140* (33), 10425–10429.

(34) Nieto Faza, O.; Silva López, C.; Álvarez, R.; De Lera, Á. R. Theoretical Study of the Electrocyclic Ring Closure of Hydroxypentadienyl Cations. *Chem. - A Eur. J.* **2004**, *10* (17), 4324–4333.

(35) Lerch, M. M.; Szymański, W.; Feringa, B. L. The (Photo)Chemistry of Stenhouse Photoswitches: Guiding Principles and System Design. *Chem. Soc. Rev.* **2018**, *47* (6), 1910–1937.

(36) Stranius, K.; Börjesson, K. Determining the Photoisomerization Quantum Yield of Photoswitchable Molecules in Solution and in the Solid State. *Sci. Rep.* **2017**, *7*

(September 2016), 1–9.

(37) Mallo, N.; Brown, P. T.; Iranmanesh, H.; MacDonald, T. S. C.; Teusner, M. J.; Harper, J. B.; Ball, G. E.; Beves, J. E. Photochromic Switching Behaviour of Donor-Acceptor Stenhouse Adducts in Organic Solvents. *Chem. Commun.* **2016**, *52* (93), 13576–13579.

(38) Mallo, N.; Foley, E. D.; Iranmanesh, H.; Kennedy, A. D. W.; Luis, E. T.; Ho, J.; Harper, J. B.; Beves, J. E. Structure-Function Relationships of Donor-Acceptor Stenhouse Adduct Photochromic Switches. *Chem. Sci.* **2018**, *9* (43), 8242–8252.

(39) Lerch, M. M.; Wezenberg, S. J.; Szymanski, W.; Feringa, B. L. Unraveling the Photoswitching Mechanism in Donor-Acceptor Stenhouse Adducts. *J. Am. Chem. Soc.* **2016**, *138* (20), 6344–6347.

(40) Lerch, M. M.; Di Donato, M.; Laurent, A. D.; Medved', M.; Iagatti, A.; Bussotti, L.; Lapini, A.; Buma, W. J.; Foggi, P.; Szymański, W.; Feringa, B. L. Solvent Effects on the Actinic Step of Donor–Acceptor Stenhouse Adduct Photoswitching. *Angew. Chemie Int. Ed.* **2018**, *57* (27), 8063–8068.

(41) Sanchez, D. M.; Raucci, U.; Ferreras, K. N.; Martínez, T. J. Putting Photomechanical Switches to Work: An Ab Initio Multiple Spawning Study of Donor-Acceptor Stenhouse Adducts. *J. Phys. Chem. Lett.* **2020**, *11* (18), 7901–7907.

(42) García-Iriepa, C.; Marazzi, M.; Sampedro, D. From Light Absorption to Cyclization: Structure and Solvent Effects in Donor-Acceptor Stenhouse Adducts. *ChemPhotoChem* **2019**, *3* (9), 866–873.

(43) Zulfikri, H.; Koenis, M. A. J. J.; Lerch, M. M.; Di Donato, M.; Szymański, W.; Filippi, C.; Feringa, B. L.; Buma, W. J.; Di, M.; Szyma, W.; Filippi, C.; Feringa, B.

L.; Buma, W. J. Taming the Complexity of Donor-Acceptor Stenhouse Adducts: Infrared Motion Pictures of the Complete Switching Pathway. *J. Am. Chem. Soc.* **2019**, *141* (18), 7376–7384.

(44) Lui, B. F.; Tierce, N. T.; Tong, F.; Sroda, M. M.; Lu, H.; Read de Alaniz, J.; Bardeen, C. J. Unusual Concentration Dependence Ofthe Photoisomerization Reaction in Donor-Acceptor Stenhouse Adducts. *Photochem. Photobiol. Sci.* **2019**, *18* (6), 1587–1595.

(45) Burnett, G. L.; Soh, H. T.; Hawker, J.; Read de Alaniz, J. Controlled Drug Release to Cancer Cells from Modular One-Photon Visible Light-Responsive Micellar System. *ChemComm* **2016**, *52*, 10525–10528.

(46) Yap, J. E.; Zhang, L.; Lovegrove, J. T.; Beves, J. E.; Stenzel, M. H. Visible Light-Responsive Drug Delivery Nanoparticle via Donor–Acceptor Stenhouse Adducts (DASA). *Macromol. Rapid Commun.* **2020**, *2000236*, 1–8.

(47) Lerch, M. M.; Hansen, M. J.; Velema, W. A.; Szymanski, W.; Feringa, B. L. Orthogonal Photoswitching in Multifunctional Molecular System. *Nat. Commun.* **2016**, *7* (12054), 1–10.

(48) Diaz, Y. J.; Page, Z. A.; Knight, A. S.; Treat, N. J.; Hemmer, J. R.; Hawker, C. J.; Read de Alaniz, J.; Hemmer, R.; Hawker, C. J.; Read de Alaniz, J. A Versatile and Highly Selective Colorimetric Sensor for the Detection of Amines. *Chem. - A Eur. J.* **2017**, *23* (15), 3562–3566.

(49) Balamurugan, A.; Lee, H. Il. A Visible Light Responsive On-Off Polymeric Photoswitch for the Colorimetric Detection of Nerve Agent Mimics in Solution and in the Vapor Phase. *Macromolecules* **2016**, *49* (7), 2568–2574.

(50) Ulrich, S.; Moura, S. O.; Diaz, Y.; Clerc, M.; Géraldine, A.; Read de Alaniz, J.; Martins, A.; Neves, N. M.; Rottmar, M.; Rossi, R. M.; Fortunato, G.; Boesel, L. F. Chemical Electrospun Colourimetric Sensors for Detecting Volatile Amines. *Sensors Actuators B. Chem.* **2020**, *322*, 128570.

(51) Chen, Q.; Diaz, Y. J.; Hawker, M. C.; Martinez, M. R.; Page, Z. A.; Zhang, S. X.; Hawker, C. J.; Read de Alaniz, J. Stable Activated Furan and Donor–Acceptor Stenhouse Adduct Polymer Conjugates as Chemical and Thermal Sensors. *Macromolecules* **2019**, *52*, 4370–4375.

(52) Lui, B. F.; Tierce, N. T.; Tong, F.; Sroda, M. M.; Lu, H.; Read de Alaniz, J.; Bardeen, C. J. Unusual Concentration Dependence of the Photoisomerization Reaction in Donor-Acceptor Stenhouse Adducts. *Photochem. Photobiol. Sci.* **2019**, *18* (6), 1587–1595.

(53) Ulrich, S.; Hemmer, J. R.; Page, Z. A.; Dolinski, N. D.; Rifaie-graham, O.; Bruns, N.; Hawker, C. J.; Boesel, L. F.; Read de Alaniz, J. Visible Light-Responsive DASA-Polymer Conjugates. *ACS Macro Lett.* **2017**, *6*, 738–742.

(54) Clerc, M.; Stricker, F.; Ulrich, S.; Sroda, M. M.; Bruns, N.; Boesel, L. F.; Read de Alaniz, J. Promoting the Furan Ring-Opening Reaction to Access New Donor–Acceptor Stenhouse Adducts with Hexafluoroisopropanol. *Angew. Chemie Int. Ed. Ed.* **2021**, *60*, 10219–10227.

(55) Sinawang, G.; Wu, B.; Wang, J.; Li, S.; He, Y. Polystyrene Based Visible Light Responsive Polymer with Donor – Acceptor Stenhouse Adduct Pendants. *Macromol. Chem. Phys.* **2016**, *217*, 2409–2414.

(56) Zhong, D.; Cao, Z.; Wu, B.; Zhang, Q.; Wang, G. Polymer Dots of DASA-

Functionalized Polyethyleneimine: Synthesis, Visible Light/PH Responsiveness, and Their Applications as Chemosensors. *Sensors Actuators, B Chem.* **2018**, *254* (July 2017), 385–392.

(57) Yap, E.; Mallo, N.; Stenzel, M. H.; Thomas, D. S.; Beves, J. E. Comparing Photoswitching of Acrylate or Methacrylate Polymers Conjugated with Donor–Acceptor Stenhouse Adducts. *Polym. Chem.* **2019**, *10*, 6515–6522.

(58) Rifaie-Graham, O.; Ulrich, S.; Galensowske, N. F. B.; Balog, S.; Chami, M.; Rentsch, D.; Hemmer, J. R.; Read De Alaniz, J.; Boesel, L. F.; Bruns, N. Wavelength-Selective Light-Responsive DASA-Functionalized Polymersome Nanoreactors. *J. Am. Chem. Soc.* **2018**, *140* (25), 8027–8036.

(59) Ryabchun, A.; Li, Q.; Lancia, F.; Aprahamian, I.; Katsonis, N. Shape-Persistent Actuators from Hydrazone Photoswitches. *J. Am. Chem. Soc.* **2019**, *141* (3), 1196–1200.

(60) Aßhoff, S. J.; Lancia, F.; Iamsaard, S.; Matt, B.; Kudernac, T.; Fletcher, S. P.; Katsonis, N. High-Power Actuation from Molecular Photoswitches in Enantiomerically Paired Soft Springs. *Angew. Chemie - Int. Ed.* **2017**, *56* (12), 3261–3265.

(61) Boelke, J.; Hecht, S. Designing Molecular Photoswitches for Soft Materials Applications. **2019**, *1900404*, 1–14.

(62) Livshits, M. Y.; Razgoniaev, A. O.; Arbulu, R. C.; Shin, J.; McCullough, B. J.; Qin, Y.; Ostrowski, A. D.; Rack, J. J. Generating Photonastic Work from Irradiated Dyes in Electrospun Nanofibrous Polymer Mats. *ACS Appl. Mater. Interfaces* **2018**, *10* (43), 37470–37477.

(63) Liu, L.; Liu, M.-H.; Deng, L.-L.; Lin, B.-P.; Yang, H. Near-Infrared Chromophore Functionalized Soft Actuator with Ultrafast Photoresponsive Speed and Superior Mechanical Property. *J. Am. Chem. Soc.* **2017**, *139*, 11333–11336.

(64) Zuo, B.; Wang, M.; Lin, B. P.; Yang, H. Visible and Infrared Three-Wavelength Modulated Multi-Directional Actuators. *Nat. Commun.* **2019**, *10(1)* (4539), 1–11.

(65) Jiang, W.; Niu, D.; Liu, H.; Wang, C.; Zhao, T.; Yin, L.; Shi, Y.; Chen, B.; Ding, Y.; Lu, B. Photoresponsive Soft-Robotic Platform: Biomimetic Fabrication and Remote Actuation. *Adv. Funct. Mater.* **2014**, *24* (48), 7598–7604.

(66) Ma, H.; Hou, J.; Wang, X.; Zhang, J.; Yuan, Z.; Xiao, L.; Wei, Y.; Fan, S.; Jiang, K.; Liu, K. Flexible, All-Inorganic Actuators Based on Vanadium Dioxide and Carbon Nanotube Bimorphs. *Nano Lett.* **2017**, *17* (1), 421–428.

(67) Lu, X.; Zhang, H.; Fei, G.; Yu, B.; Tong, X.; Xia, H.; Zhao, Y. Liquid-Crystalline Dynamic Networks Doped with Gold Nanorods Showing Enhanced Photocontrol of Actuation. *Adv. Mater.* **2018**, *30* (14), 1–8.

(68) Kuenstler, A. S.; Kim, H.; Hayward, R. C. Liquid Crystal Elastomer Waveguide Actuators. *Adv. Mater.* **2019**, *31* (24), 25.

(69) White, T. J. Photomechanical Effects in Liquid Crystalline Polymer Networks and Elastomers. *J. Polym. Sci. Part B Polym. Phys.* **2018**, *56* (9), 695–705.

(70) Gelebart, A. H.; Vantomme, G.; Meijer, E. W.; Broer, D. J. Mastering the Photothermal Effect in Liquid Crystal Networks: A General Approach for Self-Sustained Mechanical Oscillators. *Adv. Mater.* **2017**, *29* (18).

(71) Yakacki, C. M.; Saed, M.; Nair, D. P.; Gong, T.; Reed, S. M.; Bowman, C. N. Tailorable and Programmable Liquid-Crystalline Elastomers Using a Two-Stage

Thiol−Acrylate Reaction. *RSC Adv.* **2015**, *5*, 18997–19001.

(72) Wang, T.; Torres, D.; Fernandez, F. E.; Wang, C.; Sepulveda, N. Maximizing the Performance of Photothermal Actuators by Combining Smart Materials with Supplementary Advantages. *Sci. Adv.* **2017**, *3* (4).

(73) Verpaalen, R. C. P.; Engels, T.; Schenning, A. P. H. J.; Debije, M. G. Stimuli-Responsive Shape Changing Commodity Polymer Composites and Bilayers. *ACS Appl. Mater. Interfaces* **2020**, *12* (35), 38829–38844.

(74) Lahikainen, M.; Zeng, H.; Priimagi, A. Reconfigurable Photoactuator through Synergistic Use of Photochemical and Photothermal Effects. *Nat. Commun.* **2018**, *9* (1), 1–8.

(75) Vapaavuori, J.; Bazuin, C. G.; Priimagi, A. Supramolecular Design Principles for Efficient Photoresponsive Polymer−Azobenzene Complexes. *J. Mater. Chem. C* **2018**, *6*, 2168–2188.

Chapter 2. Investigating the effect of ionic character of DASAs

2.1. Abstract

The effects of solution-state dielectric and intermolecular interactions on the degree of charge separation provide a route to understanding the switching properties and concentration dependence of donor–acceptor Stenhouse adducts (DASAs). Through solvatochromic analysis of the open-form DASA in conjunction with X-ray diffraction and computational theory, we have analyzed the ionic character of a series of DASAs. First- and third-generation architectures lead to a higher zwitterionic resonance contribution of the open form and a zwitterionic closed form, whereas the second-generation architecture possesses a less charge-separated open form and neutral closed form. This can be correlated with equilibrium control and photoswitching solvent compatibility. As a result of the high contribution of the zwitterionic resonance forms of first- and third-generation DASAs, we were able to control their switching kinetics by means of ion concentration, whereas second-generation DASAs were less affected. Importantly, these results show how the previously reported concentration dependence of DASAs is not universal, and that DASAs with a more hybrid structure in the open form can achieve photoswitching at high concentrations. This chapter was adapted with permission from *Chem. A Eur. J.* **2021**, *27* (12), 4183–4190.[1]

doi.org/10.1002/chem.202005110

2.2. Introduction

Simply stated, improved photomechanical materials require improved photochromic molecules and better understanding of their switching properties. The field must move beyond commonly used photoswitches to find photoswitches whose chemical structures and optoelectronic properties are optimized for a given scenario. Within the context of photoswitches, DASAs are a relative new class of material whose widespread applications have been hampered by limited understanding of solvent compatibility and, most importantly, concentration dependence. The concentration dependence, first reported by Bardeen, Read de Alaniz and coworkers in 2019, shows decreasing half-lives of the closed isomers at increased concentration, while also lowering overall quantum yields.[2] This severely hinders applications requiring high concentrations (e.g. 1-10M) of DASA molecules. This chapter aims to improve our understand of the photophysical properties governing DASA photoswitching and overcome the concentration dependence.

In this study we investigated the medium effects on the charge separation of DASAs through a series of X-ray diffraction (XRD) analyses, solution-state studies, and time-dependent pump-probe UV/Vis spectroscopic analyses. This work builds on four important independent preliminary studies by Beves,[3,4] Jacquemin,[5] Feringa,[6] and Wagner[7] that showed the zwitterionic character of the open form of DASAs. Using XRD data, Beves and co-workers reported open linear zwitterionic forms for first- and second-generation DASAs, concluding that the polyene systems in second-generation DASA are significantly delocalized.[3,4] In a separate theoretical investigation, Jacquemin and co-workers reported that the first-generation DASAs in both the open and closed forms have significant negative Mulliken charge (-0.54*e* and -0.56*e*, respectively), which suggests both have zwitterionic

nature.[5] Furthermore, they performed calculations on the open and closed DASA isomers, which revealed similar and large ground-state dipole moments exceeding 15 D. Feringa and co-workers used solvatochromic analysis to investigate the role of the hydroxy group on the photoisomerization pathway.[6] In addition, Wagner and co-workers recently reported the effect of this zwitterionic character on DASA fluorescence emission and its effects on first-generation DASAs in protic solvents.[7] Despite these initial reports, no effort has been made to understand the implications of the ionic character of the open form of DASA on solvent compatibility and concentration effects. By using solvatochromic shift analyses, XRD and charged ionic liquids as dopant, we demonstrate here how the ionic character of DASA influences their solvent compatibility and concentration effects.

2.3. Analysis of the ionic character of DASAs

For this study, we selected DASA derivatives with a range of photoswitching properties, including thermodynamic equilibrium between the open and closed forms in the absence of light irradiation, solvent compatibility, photothermalstationary state, and half-life (the properties are summarized in Table 2.1 and structures are shown in Figure 2.1A, 2.3A, 2.15). For these studies, we choose **DASA 1-MM** consisting of a dimethylamine donor and a Meldrum's acid derived acceptor. This derivative belongs to our first generation derivative and has high thermodynamic equilibrium control in chloroform, with 94% in the open form in the dark. This compound also exhibits a short half-life in chloroform (172 s), leading to a PTSS of 76%. For comparison, we choose **DASA 2-IM** bearing an indoline-based donor with a Meldrum's acid acceptor (referred to herein as second generation). Compared to **DASA 1-MM**, it suffers from compromised thermodynamic equilibrium, with only 50% residing in the open form in the dark and an extended half-life of the closed form of 3,240 s

in chloroform. However, it also shows reversible switching in more polar solvents such as acetonitrile.[8] To represent a DASA derivative derived from our "third" generation, we selected **DASA 3-IP** bearing an indoline-based donor and CF_3-pyrazalone-based acceptor. This derivative shows excellent thermodynamic equilibrium control, with >95% in the open form in the dark and a short-lived closed form with a half-life of 5 s in chloroform. In contrast to **DASA 2-IM** and many second-generation DASAs, this compound does not exhibit switching in acetonitrile.[8] The first- and third-generation derivatives show very similar behavior, with high thermodynamic equilibria and short half-lives, while being limited to apolar solvents such as chloroform. To round out this study, DASA derivative **DASA 4-II** was chosen; this substrate shows linear photodegradation upon irradiation and no recovery.[8]

Table 2.1 Photoswitching properties of DASAs studied. Structures are shown in Figure 2.1A and Figure 2.3A.

DASA Compound	Solvent	λ_{max} (nm)	therm. equi. (% open form in the dark)	PTS (% closed under irradiation)	Half-life, $t_{1/2}$ (s)
DASA 1-EM[8,9]	Chloroform	540	100%	12%	11 s
	Toluene	545	100%	94%	100 s
DASA 1-MM	Chloroform	541	94%[a]	76%	172 s
DASA 2-IM[8]	Chloroform	590	50%	100%	3,240 s
DASA 3-IP[8]	Chloroform	650	99%	94%	5 s
	Toluene	655	100%	100%	40 s
DASA 4-II[7]	Chloroform	640	42%	-	-
	Toluene	636	N/A	-	-

[a]determined through UV-Vis.

2.3.1. Solid-state analysis of the ionic character of DASAs

X-ray structural analysis of the open form of DASAs provided valuable insight into the ground-state ionic character in the solid-state.[4,10] Bond length alternations (BLA) patterns were used to analyze the ionic character, with a negative BLA value indicating zwitterionic character. To compare the crystal structures of DASA derivatives, we grew single crystals of **DASA 2-IM-H, 3-IP-H**, and **4-II-H** and used previously reported XRD data, including **DASA 1-EM** (Figure 2.1).[3,4,11] The previously reported **DASA 1-EM**[11] was used due to increased crystallinity provided by the diethylamine donor in comparison with **DASA 1-MM**. In addition, DASA derivatives bearing non-methylated indoline donors (**DASA 2-IM-H** and **DASA 3-IP-H,** indicated by "-H" in the compound label) were used as model compounds for **DASA 2-IM** and **DASA 3-IP**, respectively.

As expected, for **DASA 1-EM**, bearing a strongly donating alkyl donor, the bond length alternations ($BLA_{\textbf{DASA 1-EM}}$ = -0.056 Å) shows a more zwitterionic form than **DASA 2-IM-H** and **DASA 3-IP-H** with weakly donating indoline-based donors, which have similar, hybrid/zwitterionic ground-states ($BLA_{\textbf{DASA 2-IM}}$ = -0.013 Å and $BLA_{\textbf{DASA 3-IP}}$ = -0.018 Å).

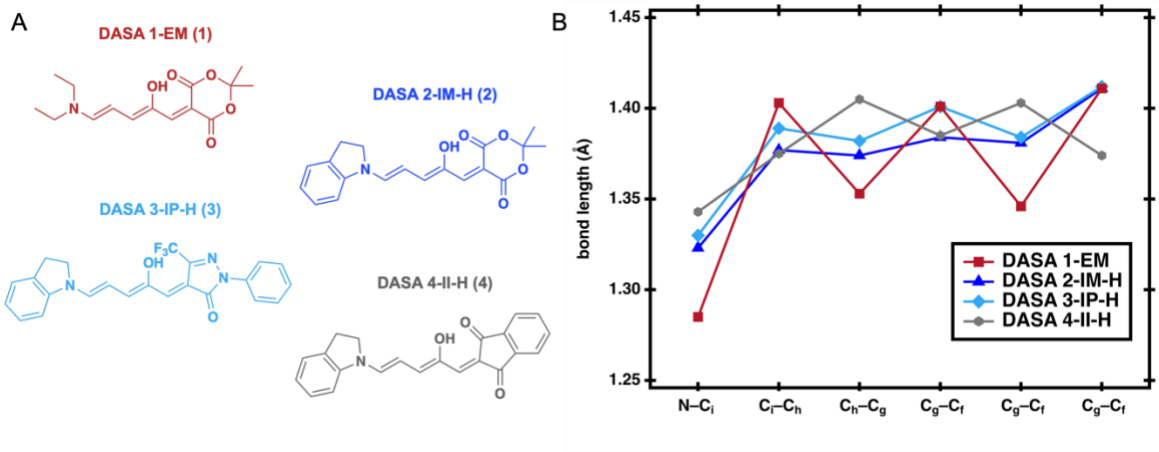

Figure 2.1 A. Photoswitches used for the XRD study. B. Bond length alternation (BLA) patterns for the triene moieties of the open forms of the DASAs derived from single-crystal XRD. For the BLA calculations, only the C–C bonds were considered. DASAs with diethylamine and non-methylated indoline donors were used as model compounds due to their increased crystallinity compared with their counterparts with dimethylamine and 2-methylindoline donors. Figure reprinted with permission from *Chem. A Eur. J.* **2021**, *27* (12), 4183–4190. Copyright (2021) John Wiley and Sons.

Herein, we define a hybrid as having a more delocalized conjugated triene system. Interestingly, **DASA 4-II-H**, with shows irreversible photoswitching, reveals opposite alternating bond slopes ($BLA_{\textbf{DASA 4-II-H}}$ = 0.026 Å) and resides in a more neutral ground state, as shown in Figure 2.1B. This is in agreement with XRD data reported previously that revealed non-photochromic spiro-oxazines predominantly reside in a neutral "quinoidal" structure.[12] To further extend this study, we compared the BLA values of 13 previously published open-form crystals,[3,4,11] in addition to those of the three crystals grown in this study, shown in Figure 2.2 and Table 2.2. In most cases, the XRD data supported that photoswitching DASA molecules evaluated by using this approach have some zwitterionic

character in the solid-state, as exemplified by negative BLA values ranging from -0.013 to -0.056 Å (Table 2.2). Conversely, **DASA 4-II-H**, has the most positive BLA of 0.026 Å, and shows linear photodegradation and irreversible switching. These results suggest that a charge-separated, hybrid/zwitterionic ground-state is an important design principle for photoswitchable DASAs. Of note, the BLA values derived from the crystal structures are similar for both the second- and third- generation derivatives (-0.013 and -0.018 Å), which is not consistent with the vastly different photoswitching behavior observed for the two generations in solution. This is not surprising because XRD relies on a single crystal environment, whereas the photoswitching properties of DASAs have been shown to be highly dependent on environmental factors such as solvent and concentration.

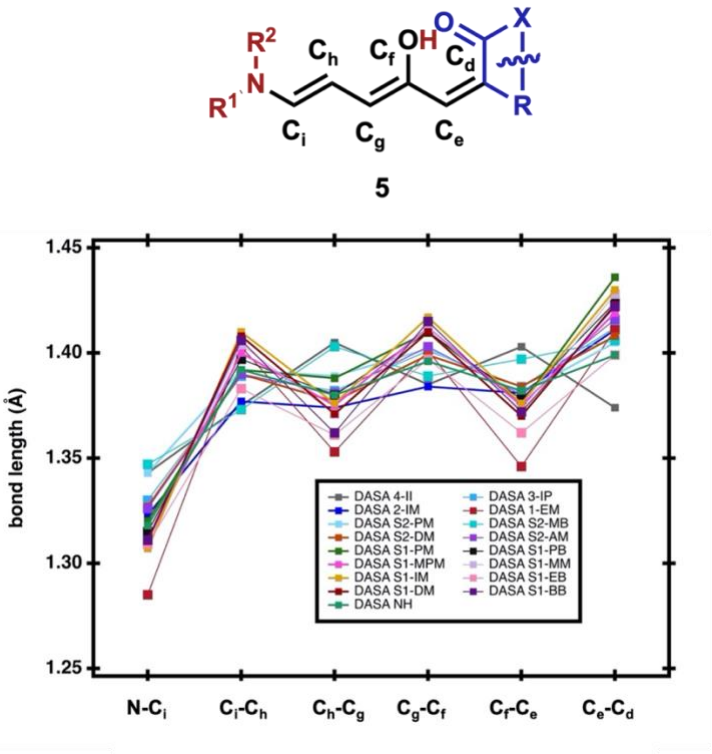

Figure 2.2 Comparison of bond lengths along the triene of 17 open form DASA crystals showing a varying degree of charge-separation.

Table 2.2 Bond lengths along the conjugated triene of seventeen linear DASA compounds as determined by single crystal X-ray structures. Bond length alterations (BLA) defined as the difference between the average bond length of the C–C single bonds and the average bond length of the C–C double bonds

	N-Ci	Ci-Ch	Ch-Cg	Cg-Cf	Cf-Ce	Ce-Cd	BLA
DASA 1-EM[11]	1.285	1.403	1.353	1.401	1.346	1.411	-0.056
DASA 2-IM-H	1.323	1.377	1.374	1.384	1.381	1.411	-0.013
DASA 3-IP-H	1.330	1.389	1.382	1.401	1.384	1.412	-0.018
DASA 4-II-H	1.343	1.375	1.405	1.385	1.403	1.374	0.026
DASA S1-IM[11]	1.307	1.410	1.376	1.417	1.376	1.430	-0.043
DASA S2-DM[3]	1.327	1.390	1.377	1.399	1.384	1.408	-0.018
DASA S2-PM[3]	1.343	1.392	1.389	1.402	1.381	1.405	-0.015
DASA S1-EB[11]	1.309	1.383	1.361	1.397	1.362	1.399	-0.032
DASA S1-DM[11]	1.311	1.408	1.371	1.410	1.370	1.423	-0.043
DASA S1-MM[11]	1.311	1.404	1.371	1.412	1.373	1.428	-0.043
DASA S1-PM[11]	1.320	1.392	1.388	1.410	1.376	1.436	-0.031
DASA S1-MPM[2]	1.311	1.400	1.375	1.412	1.375	1.419	-0.035
DASA S2-AM[3]	1.326	1.390	1.381	1.403	1.380	1.416	-0.022
DASA S1-PB[4]	1.315	1.397	1.380	1.410	1.378	1.424	-0.031
DASA S1-BB[4]	1.311	1.406	1.362	1.415	1.372	1.422	-0.047
DASA S2-MB[4]	1.347	1.373	1.403	1.389	1.397	1.406	0.011
DASA NH	1.318	1.392	1.38	1.396	1.382	1.399	-0.015

2.3.2. Solution-state analysis of the ionic character of DASAs

To gain insight into the charge separation of DASAs in solution, we analyzed the solvatochromic shifts of DASA derivatives. For this we used the Dimroth–Reichardt E_T solvent polarity scale to explore the dipolar nature of the DASAs.[12] The Dimroth–Reichardt E_T^N solvent polarity scale takes into account solvation effects arising from both nonspecific (e.g., dipole-dipole, induced dipole-induced dipole) and specific (e.g., hydrogen bonding) interactions, and the slope can provide insight into the difference in dipolar character

between the ground and the excited states. A negative solvatochromic slope (blueshifts in more polar solvents) suggests stabilization of the zwitterionic ground state with increasing solvent polarity. Conversely, a positive solvatochromic slope suggests a more dipolar excited state that is stabilized with increasing solvent polarity. The scale is based on the electronic transitions of a polarity probe dye in a range of solvents with nonpolar tetramethylsilane (TMS) ($E_T^N = 0$) and polar water ($E_T^N = 1.0$) as references. The features of the absorption bands were correlated with the Dimroth-Reichardt E_T^N solvent polarity scale of 10 solvents (Table 2.3).[13] The four photoswitches studied and their corresponding photoswitching properties (thermodynamic equilibrium, PTS, and thermal half-life) in chloroform are shown in Figure 2.3A. Figure 2.3B shows the blue-shift of the absorption band of **DASA 3-IP** with increasing solvent polarity. Figure 2.3C shows the plots of absorption maximum versus the polarity of the solvents of the four DASA derivatives. **DASA 1-MM**, **DASA 2-IM**, and **DASA 3-IP** all show negative solvatochromic shifts (blue-shifts in more polar solvents), which suggests stabilization of the zwitterionic ground state with increasing solvent polarity (with a slope ranging from -7 to -60 nm). Interestingly, **DASA 4-II-H** shows a positive solvatochromic shift with a slope of 14 nm (red-shift in more polar solvents), which suggests a more dipolar excited state that is stabilized with increasing solvent polarity. In agreement with the XRD results, this suggests that the reversible and non-reversible DASAs have different dipolar nature.

Table 2.3 The ten solvents and corresponding E_T^N solvent polarity value using the Dimroth—Reichardt E_T solvent polarity scale. The E_T^N scale is based on the electronic transitions of a polarity probe dye in a range of solvents which is normalized to nonpolar tetramethylsilane (TMS) ($E_T^N = 0$) and polar water ($E_T^N = 1.0$).[13]

Solvent	Tol	Et_2O	THF	EtOAc	$CHCl_3$	CH_2Cl_2	Acetone	DMSO	ACN	MeOH
E_T^N	0.099	0.117	0.207	0.228	0.259	0.309	0.355	0.444	0.460	0.762

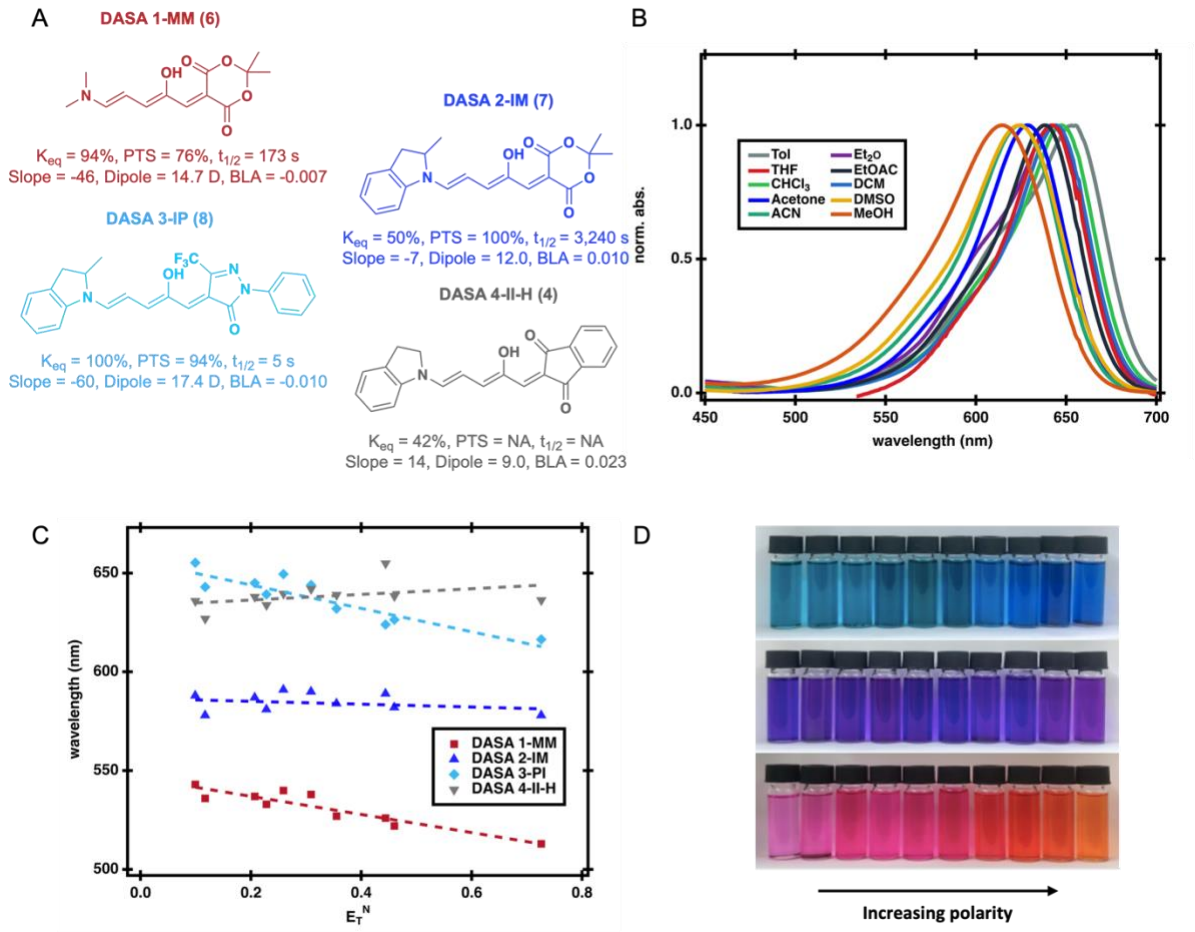

Figure 2.3 A. DASA derivatives studied together with the thermodynamic equilibria, photothermal stationary states, and thermal half-lives in chloroform for each DASA. B. UV/Vis spectra of DASA 3-IP in a range of solvents. Blue-shifts are observed with

increasing solvent polarity. C. Solvatochromic shift analysis for **DASA 1-MM**, **DASA 2-MI, DASA 3-IP** and **DASA 4-II-H** in solvents of different polarity using the Dimroth–Reichardt E_T solvent polarity scale. D. The solvatochromic trends of **DASA 3-IP** (top), **DASA 2-IM** (middle) and **DASA 1-MM** (bottom) are visible to the naked eye. The images shows that **DASA 3-IP** and **DASA 1-MM** are more sensitive to the environment than **DASA 2-IM**. Figure reprinted with permission from *Chem. A Eur. J.* **2021**, *27* (12), 4183–4190. Copyright 2021 John Wiley and Sons.

To gain a better understanding of the varying contributions of the zwitterionic resonance form, we compared the negative slopes of the reversible switching DASAs. The slopes of **DASA 1-MM** and **DASA 3-IP** are comparable, with slopes of -46 and -60 nm. This is in contrast with the XRD data, which suggests **DASA 3-IP** has less zwitterionic character than **DASA 1-MM**. **DASA 2-IM**, however, has a significantly lower negative shift, with a slope of -7 nm, which supports the hybrid character shown by the XRD data. The more pronounced negative solvatochromism of **DASA 1-MM** and **DASA 3-IP** suggests that these derivatives have more zwitterionic character than **DASA 2-IM**, which correlates with the respective electronic character of the donor and acceptor. The solvatochromic trends area visible by eye. Figure 2.3D shows that **DASA 3-IP** and **DASA 1-MM** are more sensitive to the environment than **DASA 2-IM**. **DASA 1-MM** has a strongly donating alkylamine donor and a weakly withdrawing Meldrum's acid based acceptor, whereas **DASA 3- IP** contains a weaker arylamine donor and a strongly electron-withdrawing CF3-pyrazolone acceptor. **DASA 2-IM** consists of both a weak donor and a weak acceptor, resulting in overall weaker charge separation or a hybrid structure. The highly charge-separated DASAs (**DASA 1-MM** and **DASA 3-IP**) show similar switching properties,

including a high percent of open form in the dark (94 and >95% in chloroform), fast thermal reversion ($t_{1/2}$ = 173 s and 5 s), and limited solvent capability. In contrast, **DASA 2-IM** is less sensitive to the environment and experimentally switches in a wider range of solvents but has a compromised equilibrium. Beves and co-workers reported absorption profiles for a series of second-generation DASAs bearing aniline-based donors in various solvents. In agreement with our observed trend, these solvatochromic slopes can be correlated with the relative dark equilibrium (Figure 2.4).[3] The solvatochromic shifts reveal the dipolar nature of DASAs and provide a simple experimental method to help understand the switching properties of different DASA derivatives while also providing a more accurate representation of the push-pull system than the XRD data. Feringa[9] and Marazzi[14] and their co-workers have both independently shown in theoretical studies that an increasing zwitterionic resonance contribution lowers the energy barrier of the thermal reversion between A and A' (Figure 1.7), which is consistent with our results. This inhibits switching in more polar solvents, as thermal reversion outcompetes electrocyclization.

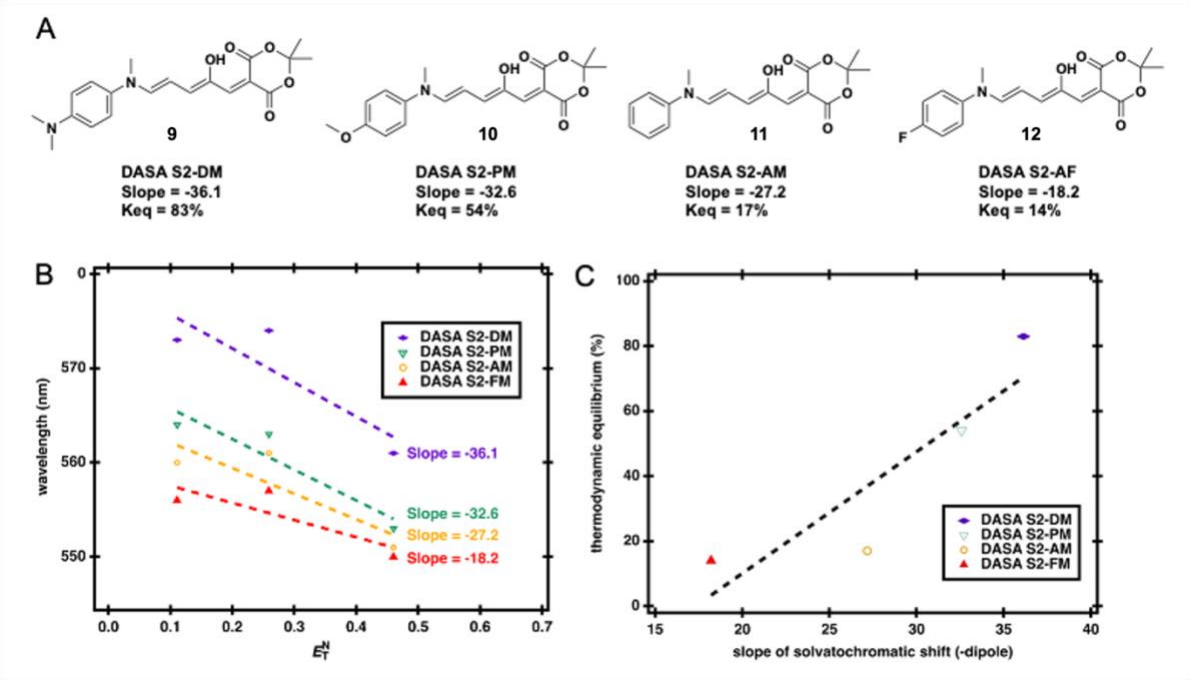

Figure 2.4 A. Aniline-based donor studied by Beves et al.[3] B. Reported absorption maximum vs the polarity value of the solvents for the studied DASAs all show negative solvatochromic slopes. C. Negative solvatochromic slopes correlated with the reported relative dark equilibrium in chloroform.

To extend this study to polymers, we analyzed absorbance shifts within polymer blends that have been shown to facilitate photoswitching.[15–18] We blended the DASAs into polymer matrices varying in polarity. For the polarity values of the polymer study, we extracted and predicted polarity value based on the well-defined value of the solvent small molecules. For example, E_T^N ~ mu of polyacrylonitrile was estimated to have similar polarity as acetonitrile, polystyrene to toluene and poly (methyl methacrylate) to ethyl acetate. Although this assumption does not consider factors such as intermolecular interactions specific to the polymer blends. Thin film DASA blends were prepared by spin coating on an ozone treated microscope glass slide. First, an 89 mg/mL polymer solution in DCM or DMF

was prepared in a vial and sonicated at room temperature for 1 hr. Separately the corresponding DASA solution (an approximately 7 mg/mL was prepared in DCM or DMF and 0.15 mL was added to the polymer solution resulting in a 90 mg/mL solution.) After spin-coating, the slides were put in a vacuum oven at 60 °C for 2 hours and the maximum absorbance was measured using UV–Vis spectroscopy. We observed the same negative solvatochromic trends for the polymer blends as we did for the solution solvatochromatic study (Figure 2.3C and Figure 2.5). Taken together, these results show that DASA photoswitching molecules have a high degree of charge-separation in the ground state in both solution and solid macromolecular environments.

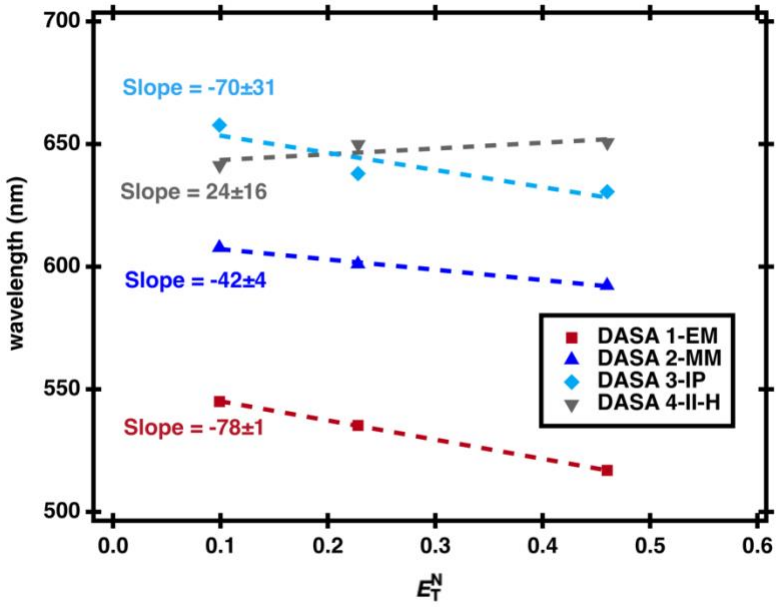

Figure 2.5 The maximum absorbance of DASA 1-EM, 2-MM, 3-IP, and 4-II-H in polymer blends (PS, PMMA, PAN) correlated with mu polymer polarity with error.

With a better understanding of the contribution of the zwitterionic resonance open form, we were also interested in evaluating the ionic character of the closed form. Previous studies have shown the closed form of first-generation DASAs with alkyl donors to be

zwitterionic, whereas second-generation DASAs have been shown to form neutral (keto or enol) closed-form isomers by 2D NMR analysis.[3,4] There have been no reports on the closed-form isomers of third-generation derivatives. In accordance with the previous reports, 2D NMR analysis shows a zwitterionic closed form for **DASA 1-MM** (Scheme 2.1-2.2) and a neutral (keto) closed form for **DASA 2-IM** (Scheme 2.3-2.4). Interestingly, despite the weakly donating indoline-based donor, 2D NMR analysis reveals a zwitterionic closed form for **DASA 3-IP,** similarly to first-generation DASAs (Scheme 2.5-2.6).

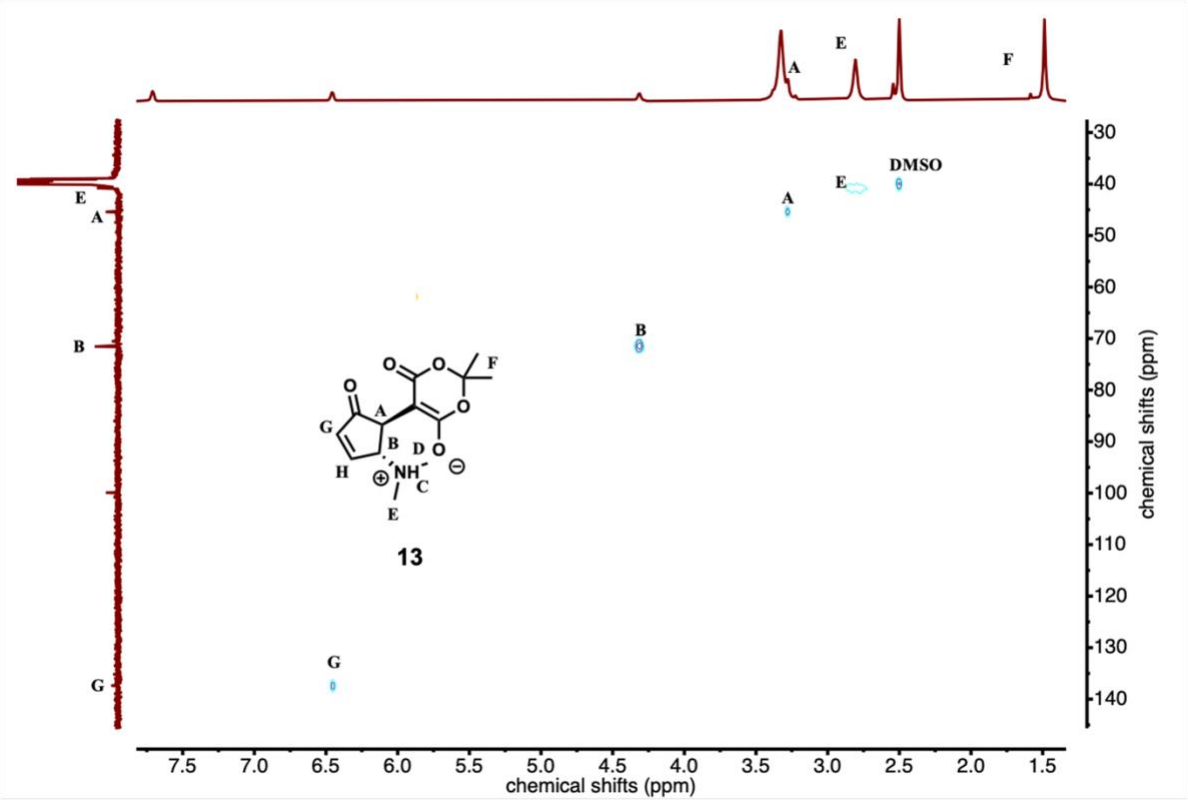

Scheme 2.1 HSQC-NMR (600 MHz, DMSO-d_6) of **DASA 1-MM**. Only the zwitterionic closed form can be observed. Only three C-H interactions in the region between 5.5 and 2.5 ppm can be observed.

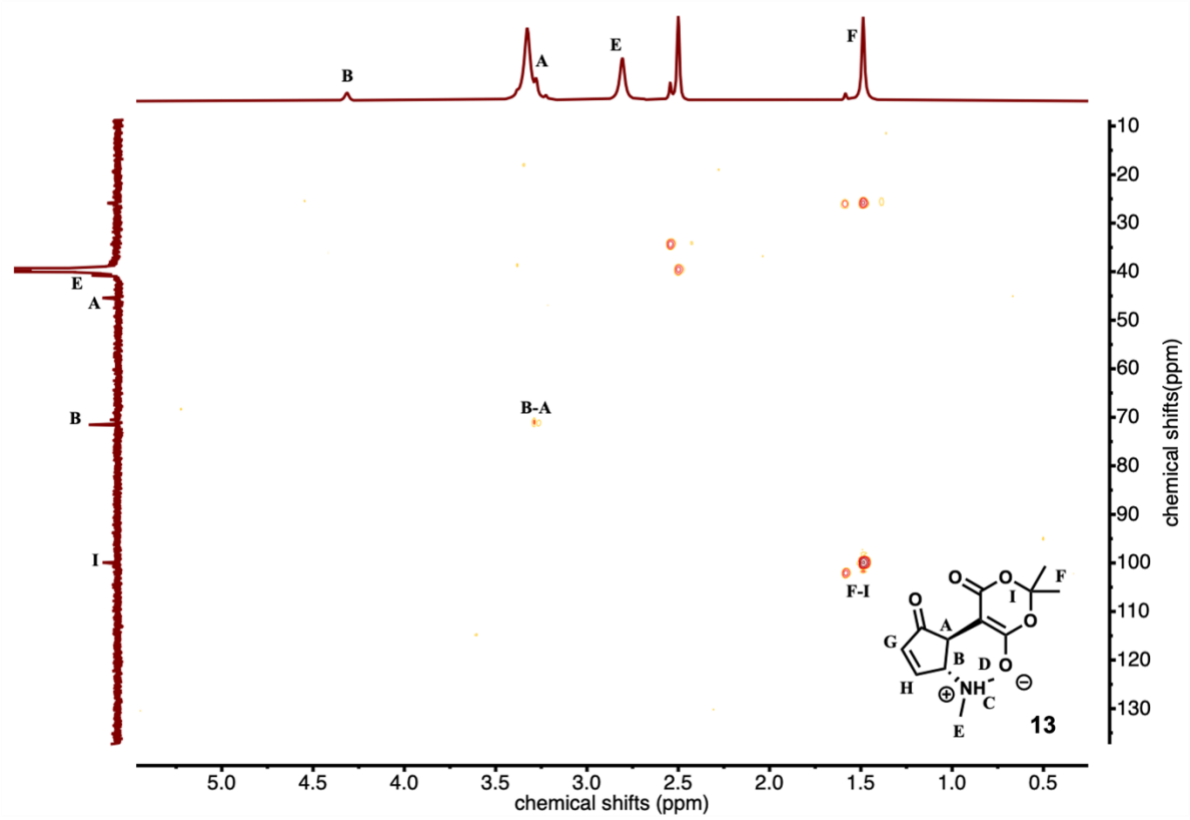

Scheme 2.2 HMBC-NMR (600 MHz, DMSO-d_6) of **DASA 1-MM**. Only the zwitterionic closed form can be observed.

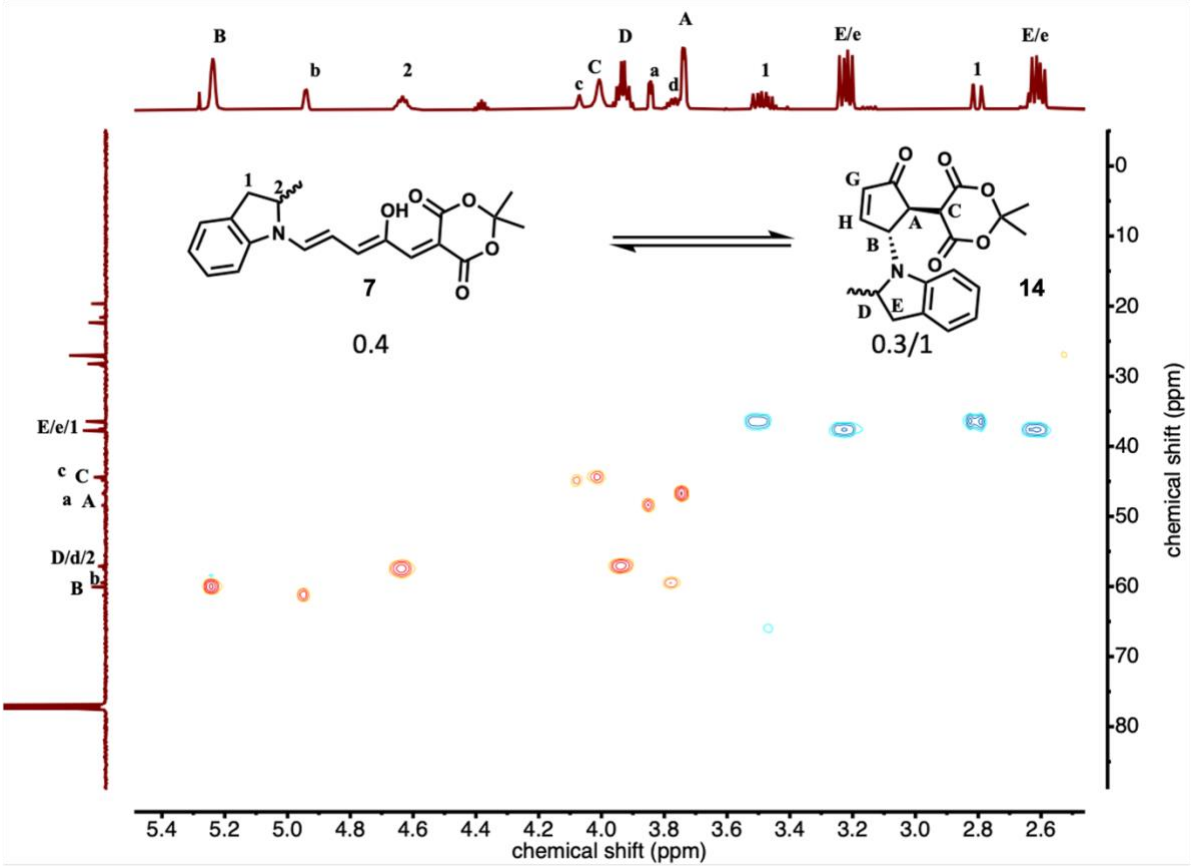

Scheme 2.3 HSQC-NMR (600 MHz, chloroform-*d*) of **DASA 2-IM**. The different isomers are marked. For the keto isomer integrating with 0.3 lower case letters were used. Importantly all signals are bound to a carbon.

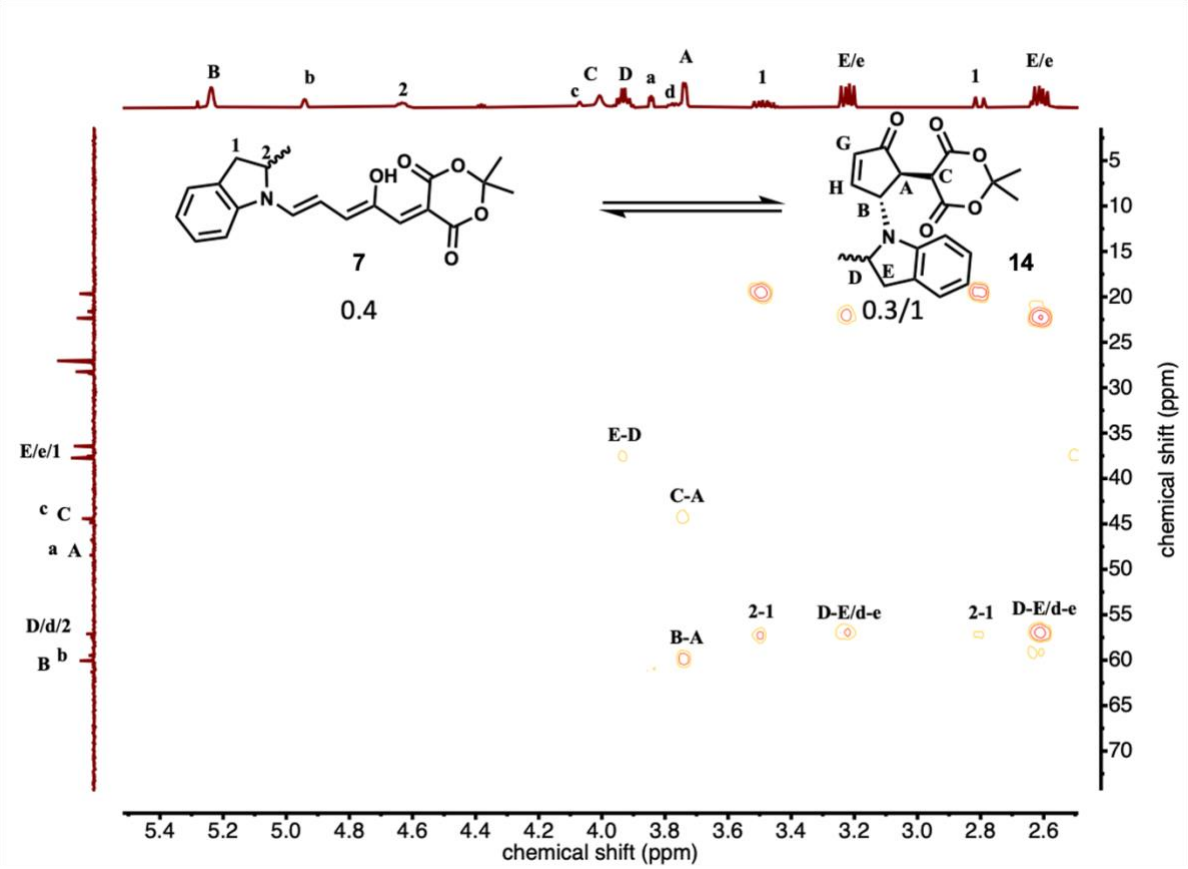

Scheme 2.4 HMBC-NMR (600 MHz, chloroform-*d*) of **DASA 2-IM**. The different isomers are marked. For the keto isomer integrating with 0.3 lower case letters were used. Importantly all signals are Signal A interacts with both the carbons of C and B.

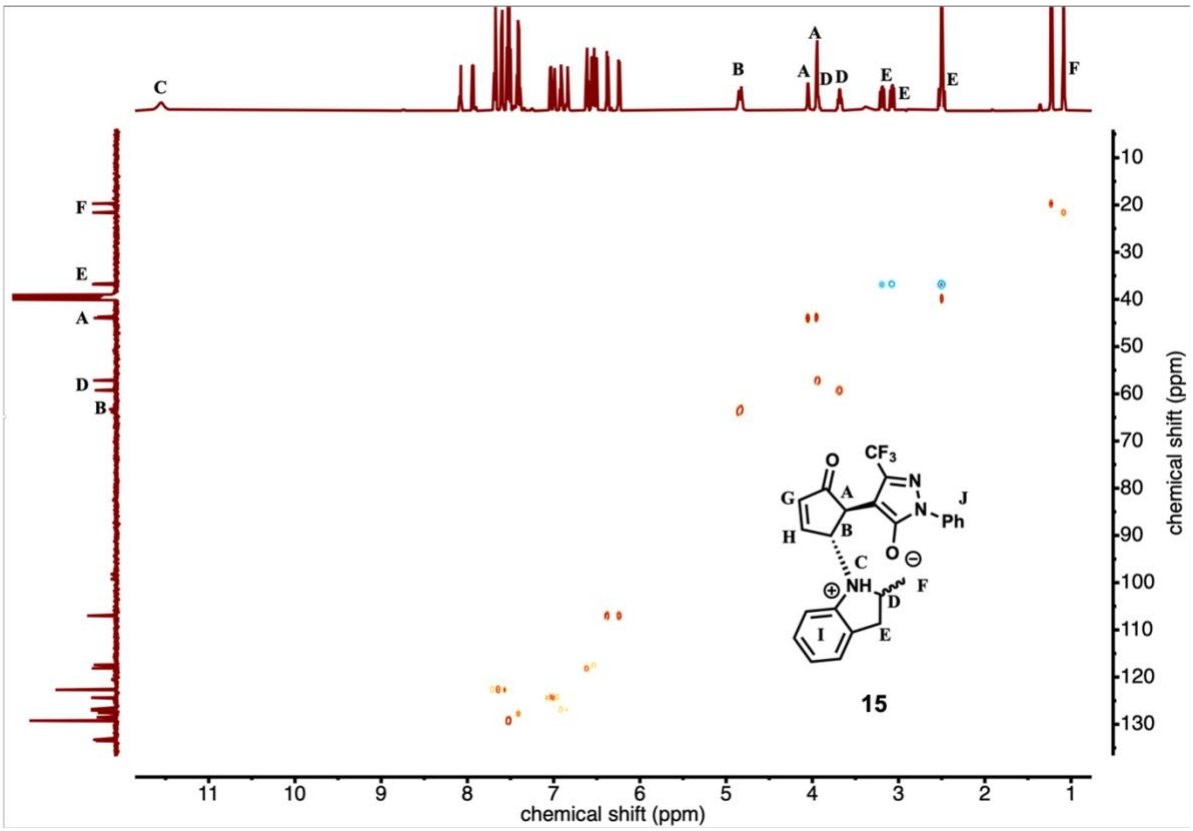

Scheme 2.5 HSQC-NMR (600 MHz, DMSO-d_6) of **DASA 3-IP**. Two zwitterionic closed isomers can be observed. No C-H interaction for the N-H proton at 11.5 ppm (C) can be observed.

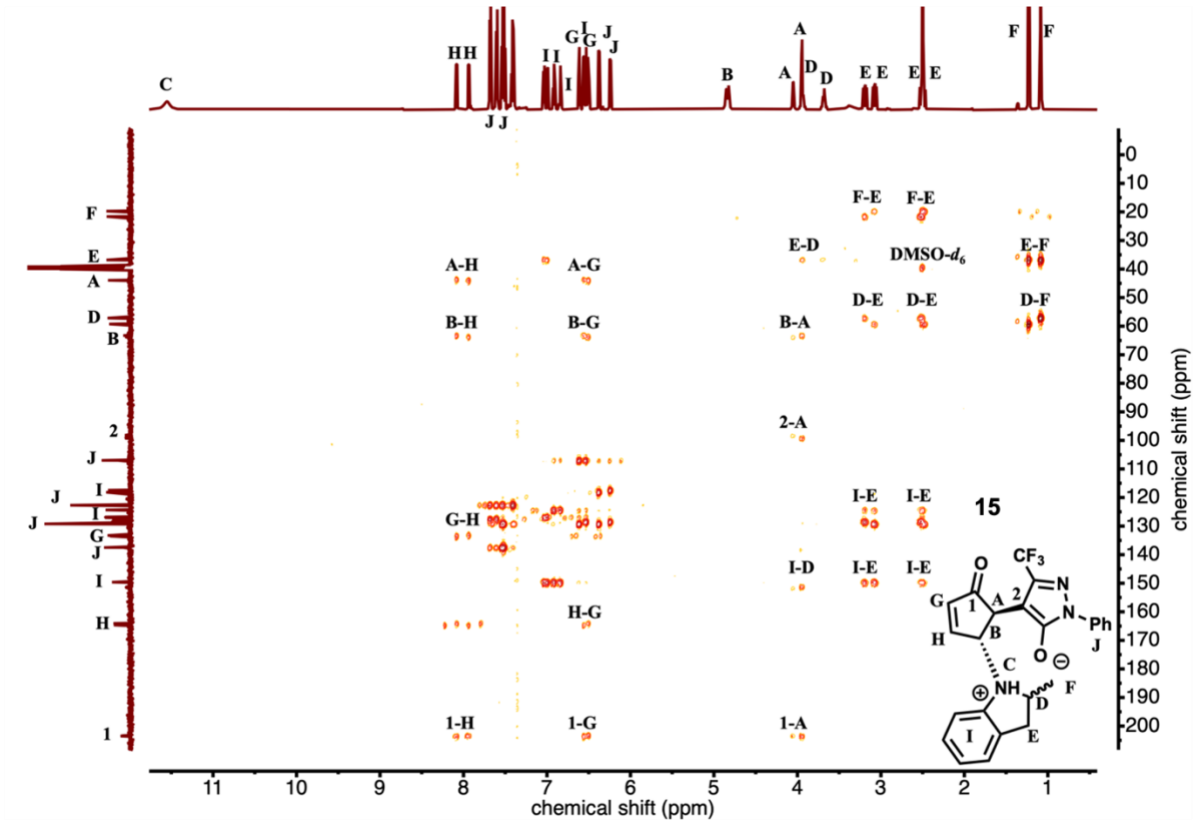

Scheme 2.6 HMBC-NMR (600 MHz, DMSO-d_6) of **DASA 3-IP**. Two zwitterionic closed isomers can be observed.

2.3.3. Computational calculations of the ionic character of DASAs

Our results from the solvatochromic analysis are supported by theoretical calculations performed at the M06-2X/6-31+G(d,p) level of theory in toluene, chloroform, and acetonitrile with the SMD solvent model using the Gaussian16 software.[19–22] The calculated dipole moments and BLAs in chloroform were compared with the experimental results summarized in Table 2.4. Importantly, the calculations show the same trends as provided by the solvatochromatic slopes (derived by linear trend extraction from Figure 2.3C). Where **DASA 1-MM** and **DASA 3-IP** have the highest calculated dipole and most negative BLA values, in agreement with the more negative solvatochromic slopes.

Consistent with the experimental results, **DASA 4-II** has a smallest dipole and the most positive BLA. Interestingly, the variation in solvent polarity with the HOMO-LUMO energy gap shows that the gap in **DASA 2-IM** is relatively unchanged as a function of solvent, whereas the gap for **DASA 3-IP** increases with increasing solvent polarity, in agreement with the blue-shift observed in the solvatochromic study (Figure 2.6). The calculations also revealed the change in the length of the hydrogen bond between the –OH and carbonyl of the acceptor as a function of solvent (Figure 2.7). The hydrogen bond in **DASA 3-IP** is strengthened in more polar solvents compared with in **DASA 2-IM**. It is possible that this hydrogen bond plays a key role in stabilizing the open form in the absence of light, resulting in equilibrium control.

Table 2.4 Experimental data compared to computational calculations.

DASA	Slope[a] [nm]	BLA[b] [Å]	Dipole[c] [D]	BLA[c] [Å]
DASA 3-IP	-60	-0.018	17.4	-0.010
DASA 1-MM	-46	-0.056	14.7	-0.007
DASA 2-IM	-7	-0.013	12.0	0.010
DASA 4-II	14	0.026	9.0	0.023

[a] Solvatochromic slopes derived by linear trend extraction of Figure 2.3C. [b] Bond length alternation values are extracted from the XRD data of the model compounds **DASA 1-EM**, **DASA 2-IM-H**, **DASA 3-IP-H**, and **DASA 4-II-H** shown in Figure 2.1. [c] Dipole and BLA values calculated at the M06-2X/6-31+G(d,p) level of theory in chloroform using the SMD solvent model.

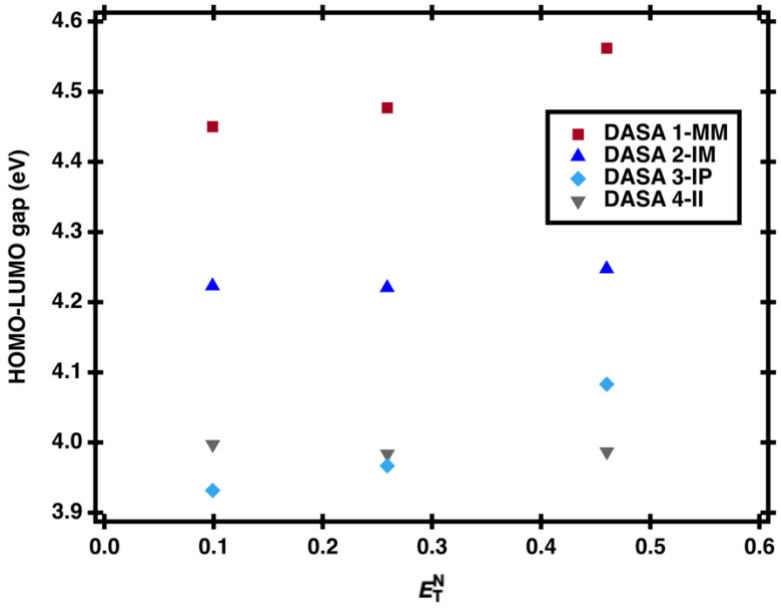

Figure 2.6 Comparison of solvent polarity vs HOMO-LUMO energy levels of **DASA 1-MM**, **DASA 2-IM**, **DASA 3-IP**, and **DASA 4-II**. The HOMO-LUMO gaps of DASA 2-IM and DASA 4-II are relatively unchanged as a function of solvent polarity, while the gap of DASA 1-MM and DASA 3-IP increases with increasing solvent polarity, in agreement with the observed blue shift in Figure 2.6B.

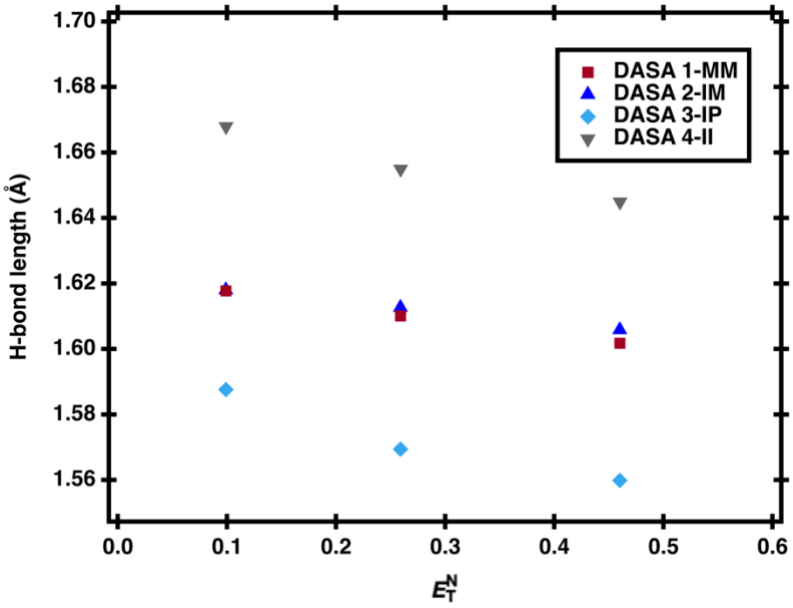

Figure 2.7 Comparison of solvent polarity vs the hydrogen bond length between the –OH and the carbonyl of the acceptor of **DASA 1-MM**, **DASA 2-IM**, **DASA 3-IP**, and **DASA 4-II**. The hydrogen bond in **DASA 3-IP** is strengthened in more polar solvents compared to **DASA 2-IM**.

2.4. Influence of ionic character of DASA on photoswitching

To study the importance of the ionic character of the DASA derivatives for their switching kinetics, we next sought to demonstrate the ability to tune the switching kinetics by using ion concentration as an external trigger. For this, we used the ionic liquid 1-butyl-3-methylimidazolium hexafluorophosphate (**IL** for ionic liquid) as an ion pair soluble in organic solvents. We added 1 and 10 mM **IL** to each derivative and monitored the rates of the forward photoswitching and thermal back reaction (k_B) by using time-dependent pump-probe UV/Vis spectroscopy. The recovery data obtained from time-dependent UV/Vis spectroscopy was fit to an isomer equilibrium model assuming first order rates of opening and closing. The model used was of the form:

$$\frac{d[\text{Open}]}{dt} = -k_{\text{F}}[\text{Open}]_t + k_{\text{B}}([\text{Open}]_0 - [\text{Open}]_t)$$

For recovery:

$$[\text{Open}]_t = 1 - \frac{k_{\text{F}} + k_{\text{B}}e^{-(k_{\text{B}}+k_{\text{F}})t}}{k_{\text{B}} + k_{\text{F}}}[\text{Open}]_0$$

where k_{F}, k_{B}, and $[\text{Open}]_0$ represent the rate of closing in the dark, the rate of opening in the dark, and the initial concentration. Samples were left to equilibrate overnight, and thermodynamic equilibrium was considered for initial concentration. Samples were irradiated for 100 s before recovery. During the recovery 100 measurements were taken at varying time intervals (14 s for **DASA 1-MM**, 125 s for **DASA 2-IM**, 2 s for **DASA 3-IP**). Upon addition of **IL** to **DASA 1-MM**, we observed a significant decrease in the rate of the forward reaction under light irradiation with 10 mM **IL**, almost completing inhibiting photoswitching (Figure 2.8). Due to low solubility of the closed form at higher concentration, we were unable to obtain a thermodynamic equilibrium and therefore the switching kinetics. For **DASA 2-IM**, bearing the most neutral open and closed form, a slight decrease in the forward reaction kinetics was observed with only a small effect on the recovery to the open form (k_{B} increases from 0.006 to 0.008 min^{-1} upon the addition of 10 mM **IL**, a 1.4-fold rate increase; Figure 2.9). Although less dramatic than for **DASA 1-MM**, the addition of **IL** to a solution of **DASA 3-IP** also resulted in a change in PTSS from 89% to 55% under light irradiation. After the irradiation of **DASA 3-IP** was stopped, we can observe a 2.3-fold increase in the rate of recovery from 7.9 min^{-1} to 17.8 min^{-1} upon the addition of 10 mM **IL**. Taken together, these results highlight that the change in PTSS results from a combination of a decrease in the forward reaction rate and increased recovery (Figure 2.10).

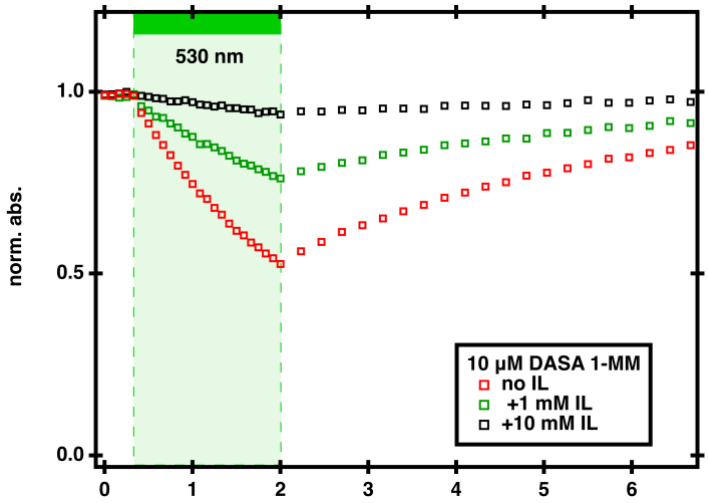

Figure 2.8 Time-dependent UV/Vis analysis of **DASA 1-MM** monitored at 540 nm, (λ_{max}), irradiated with a 530 nm LED with no **IL**, 1mM **IL** and 10mM **IL**. Figure adapted with permission from Chem. Eur. J. 2021, 27, 1 – 9 (1). Copyright 2021 John Wiley and Sons.

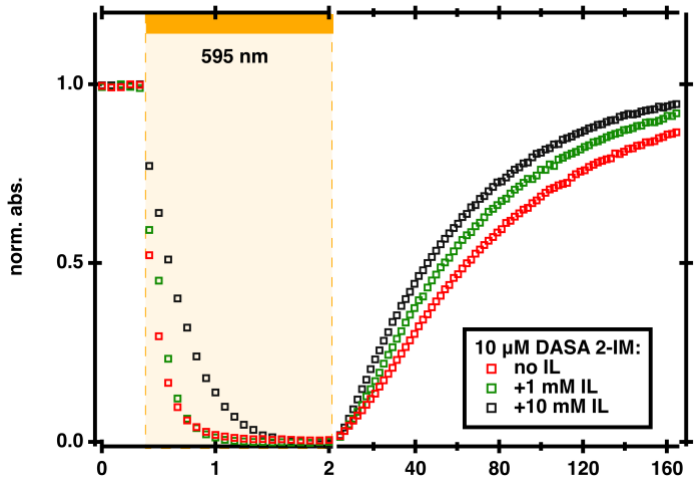

Figure 2.9 Time-dependent UV/Vis analysis of **DASA 2-IM** monitored at 591 nm, (λ_{max}), irradiated with a 595 nm LED with no **IL**, 1mM **IL** and 10mM **IL**. Figure adapted with permission from Chem. Eur. J. 2021, 27, 1 – 9 (1). Copyright 2021 John Wiley and Sons.

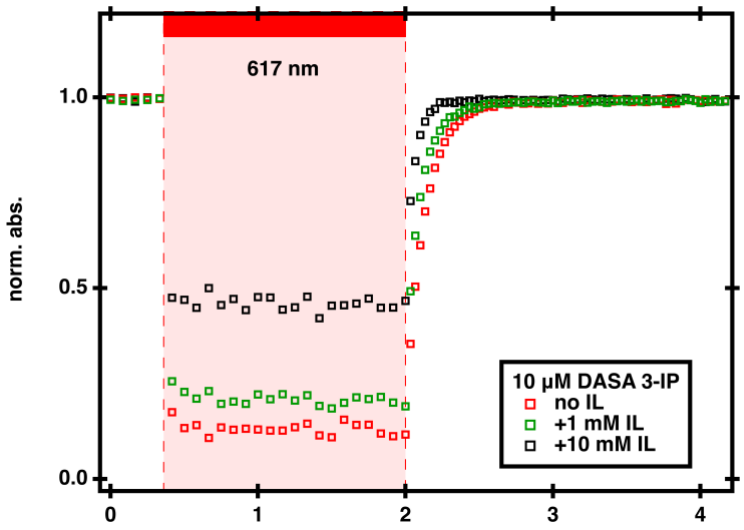

Figure 2.10 Time-dependent UV/Vis of **DASA 3-IP** monitored at 647 nm, (λ_{max}), irradiated with a 617 nm LED with no **IL**, 1mM **IL** and 10mM **IL**. Figure adapted with permission from Chem. Eur. J. 2021, 27, 1 – 9 (1). Copyright 2021 John Wiley and Sons.

2.5. Influence of ionic character mimics observed concentration effects

The switching properties of DASA derivatives with highly charge-separated open and closed forms, such as **DASA 1-MM** and **DASA 3-IP**, can be tuned by modifying the ionic character of the solution. In contrast, the addition of IL to DASA derivatives with hybrid open and neutral closed forms, such as **DASA 2-IM**, has only a small effect on switching kinetics. These results mirror the previously reported concentration dependence of **DASA 3-IP** on photoswitching, suggesting that the higher contribution of the zwitterionic resonance form of **DASA 3-IP** might be responsible for the reduced photoswitching observed at high concentrations. To test this hypothesis, we compared the effect of concentration on the less charge-separated **DASA 2-IM** and the more charge-separated **DASA 3-IP** by using time-dependent pump-probe UV/Vis spectroscopy with a demountable liquid cell with variable pathlengths. A demountable liquid cell (DLC-M13) with variable

pathlengths, UV-grade fused silica windows (WAD-U22) and an optical table sample slide holder (HSS-OTE) were purchased from Harrick Scientific Products Inc. The pathlength through the DLC can be varied from 6 μm to 1 mm by selecting the appropriate PTFE spacers. The hybrid **DASA 2-IM** shows a negligible change in PTSS at concentrations from 125 μM to 10 mM (Figure 2.11A), with the rate of recovery increasing from 0.0058 min^{-1} at 125 μM to 0.0067 min^{-1} at 10 mM. In contrast, the effect of concentration on **DASA 3-IP** was more dramatic. In this case we observed a change in PTSS from 91% to 64% and a 1.6-fold increase in recovery (10 min^{-1} at 125 μM to 16 min^{-1} at 10 mM) as the concentration increased (Figure 2.11B), which is consistent with previously reported results.[2] Similar experiments with **DASA 1-MM** were unsuccessful due to limited solubility of the closed isomer at concentration above 100 μM. These results reveal the previously reported concentration dependence is not universal for all DASA derivatives, for example, **DASA 2-IM**, which has a PTSS of 100% at 10 mM. Importantly, these results provide a path towards designing DASA derivatives able to operate at high concentrations by lowering the ground state charge separation in the open form and enabling the formation of a neutral closed isomer.

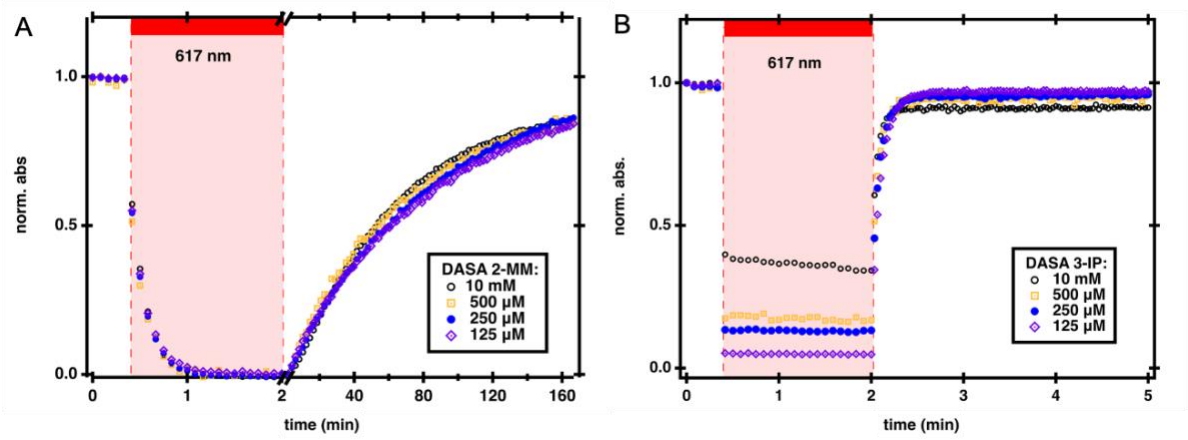

Figure 2.11 Influence of increasing concentration of DASA derivatives on their switching kinetics, determined by using time-dependent pump-probe UV/Vis spectroscopy equipped with a flow cell with variable pathlengths. The concentrations measured were from 125 µM to 10 mM and the samples were irradiated with a 617 nm LED. The irradiation started at t=0.3 min and ceased at t=2.0 min; the subsequent thermal recovery in the dark was measured. A. Time-dependent UV/Vis of **DASA 2-IM** monitored at 591 nm, (λ_{max}). B. Time-dependent UV/Vis of **DASA 3-IP** monitored at 647 nm, (λ_{max}). Figure reprinted with permission from *Chem. A Eur. J.* **2021**, *27* (12), 4183–4190. Copyright 2021 John Wiley and Sons.

2.6. Using additives to overcome the concentration dependence

Guided by the studies describe above, we sought to demonstrate the ability to tune the switching kinetics by using as an external additive, ionic liquid. Specifically, we wanted to investigate if the addition of additives could be used to decrease the rate of the back reaction. Interestingly, we found using small amount of ethanol, ether and water had a dramatic effect of the back reaction rate. For example, 0.75 vol% ethanol effects the back reaction rate by an order of magnitude as shown in Figure 2.12. This introduced another

method for overcoming the concentration dependence by decreasing thermal recovery. By utilizing additives, we demonstrated switching of more charge-separated DASAs such as **DASA 3-IP** at concentrations not previously possible, as shown in Figure 2.13. Finally, this study has a broader impact to the DASA community because it highlights how sensitive some DASAs are to the environment. It is important to note that companies sell chloroform which is stabilized by 0.75% ethanol. Thus, there have been inconsistencies within the literature, specially the experimental and theoretical work, whether thermal recovery in faster in aprotic polar or nonpolar environments. Whereas theoretical studies support thermal reversion should be faster in polar solvents such as chloroform compared to toluene,[9] experimental studies shows the opposite.[2,23] We believe this discrepancy and some of the inconsistencies in the literature can be explained by the use of chloroform that is stabilized by ethanol, resulting in a dramatic decrease in the back reaction rate. To test this hypothesis, we measured the switching kinetics with multiple different types of chloroform including unstabilized (HPLC grade), deuterated, amylene stabilized, and ethanol stabilized. We found in the case of the ethanol stabilized chloroform there was a significant change in kinetics as shown in Figure 2.14, which accounts for the experimental observations. Thus, to compare photoswitching kinetics of DASAs throughout the literature it is crucial to use dry solvents and materials, as well as make sure solvent stabilizers are not playing a role. Further studies to understand the role of additives on the energy landscape are currently in process.

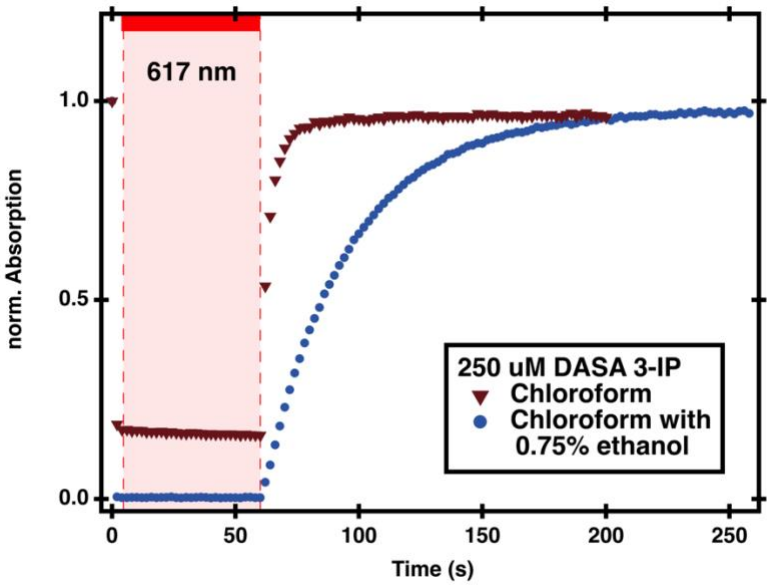

Figure 2.12 Time-dependent UV/Vis of **DASA 3-IP** monitored at 647 nm, (λ_{max}), irradiated with a 617 nm LED at 250 μM with no ethanol and 0.75% ethanol.

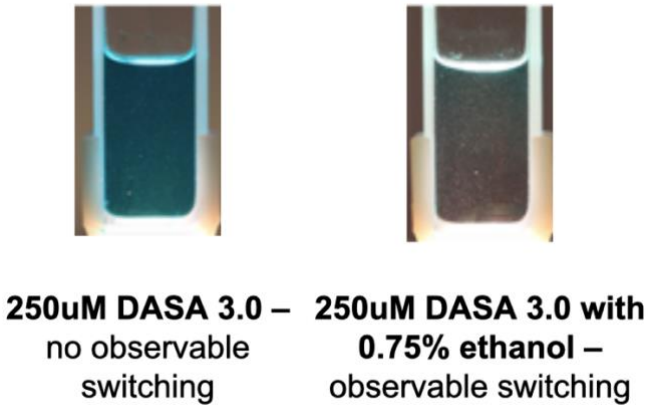

Figure 2.13 Images of **DASA 3-IP** at 250 μM in chloroform. The left shows a solution with no additives resulting in no observable switching upon irradiation with white light. The right shows a solution with 0.75% ethanol resulting in observable switching to a colorless solution upon irradiation with white light.

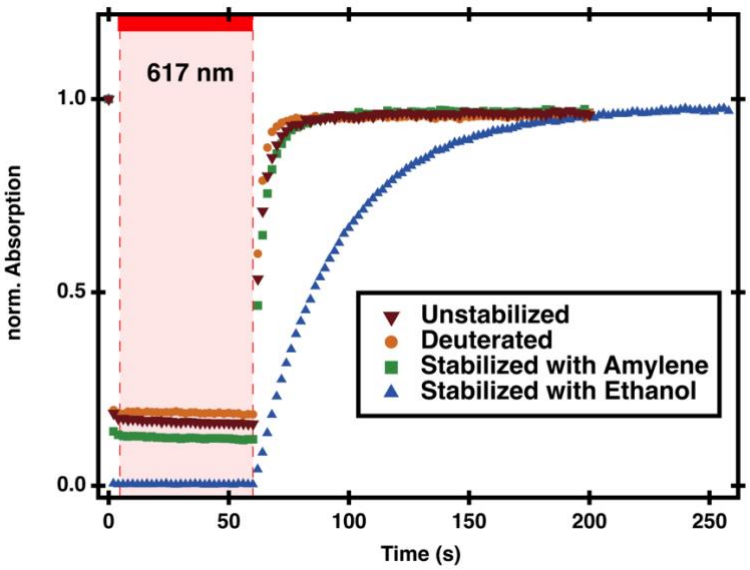

Figure 2.14 Time-dependent UV/Vis of **DASA 3-IP** monitored at 647 nm, (λ_{max}), irradiated with a 617 nm LED at 250 μM with different types of chloroform.

2.7. Conclusion

The effects of solution-state dielectric and intermolecular interactions on the degree of charge separation provides a route to understand the switching properties and concentration dependence of DASAs in solution. Through easy-to-perform solvatochromic analysis, absorption data can be used to correlate switching behavior and charge separation in conjunction with XRD, computational theory, and time-dependent pump-probe UV/Vis spectroscopy. We have shown that DASAs with the first- and third-generation architectures have higher zwitterionic resonance contributions of the open form and zwitterionic closed forms in solution, whereas the second-generation structure exhibits a hybrid open form and neutral closed isomer. Furthermore, the **DASA 4-II-H** exhibits a different dipolar nature, which could be a potential reason for its irreversible switching behavior. Importantly, we have highlighted the influence of ionic character of the DASAs on their photoswitching properties through the addition of ionic liquids. The more hybrid **DASA 2-IM** showed only

limited change in switching behavior upon addition of the ionic liquid, whereas **DASA 1-MM** and **DASA 3-IP** with more zwitterionic open and closed forms showed a more dramatic effect. Additionally, we have shown that the previously reported concentration dependence of **DASA 3-IP** relies on the ionic character of the respective open and closed forms, with the more hybrid **DASA 2-IM** being less affected. These results highlight the importance of the charge separation of the DASAs on their switching kinetics and the ability to influence certain DASA derivatives through external stimuli. We introduce two methods for overcoming the concentration dependence of DASA: 1) to achieve photoswitching of DASAs at high concentration, a more hybrid DASA architecture should be used; and 2) the ability to use external triggers to decrease the back reaction rate of more charge-separated DASAs. Furthermore, these results enable photoswitching at concentrations not previously possible, thereby overcoming a major challenge for applications needing high concentrations of DASA photoswitches as organic photomechanical materials.

2.8. References

(1) Sroda, M. M.; Stricker, F.; Peterson, J. A.; Bernal, A.; Read de Alaniz, J. Donor–Acceptor Stenhouse Adducts: Exploring the Effects of Ionic Character. *Chem. A Eur. J.* **2021**, *27* (12), 4183–4190.

(2) Lui, B. F.; Tierce, N. T.; Tong, F.; Sroda, M. M.; Lu, H.; Read de Alaniz, J.; Bardeen, C. J. Unusual Concentration Dependence Ofthe Photoisomerization Reaction in Donor-Acceptor Stenhouse Adducts. *Photochem. Photobiol. Sci.* **2019**, *18* (6), 1587–1595.

(3) Mallo, N.; Brown, P. T.; Iranmanesh, H.; MacDonald, T. S. C.; Teusner, M. J.; Harper, J. B.; Ball, G. E.; Beves, J. E. Photochromic Switching Behaviour of Donor-Acceptor Stenhouse Adducts in Organic Solvents. *Chem. Commun.* **2016**, *52* (93), 13576–13579.

(4) Mallo, N.; Foley, E. D.; Iranmanesh, H.; Kennedy, A. D. W.; Luis, E. T.; Ho, J.; Harper, J. B.; Beves, J. E. Structure-Function Relationships of Donor-Acceptor Stenhouse Adduct Photochromic Switches. *Chem. Sci.* **2018**, *9* (43), 8242–8252.

(5) Laurent, A. D.; Medved, M.; Jacquemin, D. Using Time-Dependent Density Functional Theory to Probe the Nature of Donor–Acceptor Stenhouse Adduct Photochromes. *ChemPhysChem* **2016**, *17*, 1846–1851.

(6) Lerch, M. M.; Medved, M.; Lapini, A.; Laurent, A. D.; Iagatti, A.; Bussotti, L.; Szymański, W.; Buma, W. J.; Foggi, P.; Di Donato, M.; Feringa, B. L. Tailoring Photoisomerization Pathways in Donor-Acceptor Stenhouse Adducts: The Role of the Hydroxy Group. *J. Phys. Chem. A* **2018**, *122* (4), 955–964.

(7) Payne, L.; Josephson, J. D.; Murphy, R. S.; Wagner, B. D. Photophysical Properties of Donor-Acceptor Stenhouse Adducts and Their Inclusion Complexes with Cyclodextrins and Cucurbit[7]Uril. *Molecules* **2020**, *25* (21), 4928.

(8) Hemmer, J. R.; Page, Z. A.; Clark, K. D.; Stricker, F.; Dolinski, N. D.; Hawker, C. J.; Read de Alaniz, J. Controlling Dark Equilibria and Enhancing Donor-Acceptor Stenhouse Adduct Photoswitching Properties through Carbon Acid Design. *J. Am. Chem. Soc.* **2018**, *140* (33), 10425–10429.

(9) Zulfikri, H.; Koenis, M. A. J. J.; Lerch, M. M.; Di Donato, M.; Szymański, W.; Filippi, C.; Feringa, B. L.; Buma, W. J.; Di, M.; Szyma, W.; Filippi, C.; Feringa, B. L.; Buma, W. J. Taming the Complexity of Donor-Acceptor Stenhouse Adducts: Infrared Motion Pictures of the Complete Switching Pathway. *J. Am. Chem. Soc.* **2019**, *141* (18), 7376–7384.

(10) Hemmer, J. R.; Poelma, S. O.; Treat, N.; Page, Z. A.; Dolinski, N. D.; Diaz, Y. J.; Tomlinson, W.; Clark, K. D.; Hooper, J. P.; Hawker, C.; Read de Alaniz, J. Tunable Visible and Near Infrared Photoswitches. *J. Am. Chem. Soc.* **2016**, *138* (42), 13960–13966.

(11) Helmy, S.; Oh, S.; Leibfarth, F. A.; Hawker, C. J.; Read de Alaniz, J. Design and Synthesis of Donor-Acceptor Stenhouse Adducts: A Visible Light Photoswitch Derived from Furfural. *J. Org. Chem.* **2014**, *79* (23), 11316–11329.

(12) Patel, D. G.; Paquette, M. M.; Kopelman, R. A.; Kaminsky, W.; Ferguson, M. J.; Frank, N. L. A Solution- and Solid-State Investigation of Medium Effects on Charge Separation in Metastable Photomerocyanines. *J. Am. Chem. Soc.* **2010**, *132* (36), 12568–12586.

(13) Reichardt, C. Solvatochromic Dyes as Solvent Polarity Indicators. *Chem. Rev.* **1994**, *94* (8), 2319–2358.

(14) García-Iriepa, C.; Marazzi, M.; Sampedro, D. From Light Absorption to Cyclization: Structure and Solvent Effects in Donor-Acceptor Stenhouse Adducts. *ChemPhotoChem* **2019**, *3* (9), 866–873.

(15) Sinawang, G.; Wu, B.; Wang, J.; Li, S.; He, Y. Polystyrene Based Visible Light Responsive Polymer with Donor – Acceptor Stenhouse Adduct Pendants. *Macromol. Chem. Phys.* **2016**, *217*, 2409–2414.

(16) Ulrich, S.; Hemmer, J. R.; Page, Z. A.; Dolinski, N. D.; Rifaie-graham, O.; Bruns, N.; Hawker, C. J.; Boesel, L. F.; Read de Alaniz, J. Visible Light-Responsive DASA-Polymer Conjugates. *ACS Macro Lett.* **2017**, *6*, 738–742.

(17) Chen, Q.; Diaz, Y. J.; Hawker, M. C.; Martinez, M. R.; Page, Z. A.; Zhang, S. X.; Hawker, C. J.; Read de Alaniz, J. Stable Activated Furan and Donor–Acceptor Stenhouse Adduct Polymer Conjugates as Chemical and Thermal Sensors. *Macromolecules* **2019**, *52*, 4370–4375.

(18) Yap, E.; Mallo, N.; Stenzel, M. H.; Thomas, D. S.; Beves, J. E. Comparing Photoswitching of Acrylate or Methacrylate Polymers Conjugated with Donor–Acceptor Stenhouse Adducts. *Polym. Chem.* **2019**, *10*, 6515–6522.

(19) Zhao, Y.; Truhlar, D. G. The M06 Suite of Density Functionals for Main Group Thermochemistry, Thermochemical Kinetics, Noncovalent Interactions, Excited States, and Transition Elements: Two New Functionals and Systematic Testing of Four M06-Class Functionals and 12 Other Function. *Theor. Chem. Acc.* **2008**, *120* (1–3), 215–241.

(20) Zhao, Y.; Truhlar, D. G. Density Functionals with Broad Applicability in Chemistry. *Acc. Chem. Res.* **2008**, *41* (2), 157–167.

(21) Marenich, A. V.; Cramer, C. J.; Truhlar, D. G. Universal Solvation Model Based on

Solute Electron Density and on a Continuum Model of the Solvent Defined by the Bulk Dielectric Constant and Atomic Surface Tensions. *J. Phys. Chem. B* **2009**, *113* (18), 6378–6396.

(22) Frisch, M. J.; Trucks, G. W.; Schlegel, H. B.; Scuseria, G. E.; Robb, M. a.; Cheeseman, J. R.; Scalmani, G.; Barone, V.; Petersson, G. a.; Nakatsuji, H.; Li, X.; Caricato, M.; Marenich, a. V.; Bloino, J.; Janesko, B. G.; Gomperts, R.; Mennucci, B.; Hratchian, H. P.; Ortiz, J. V.; Izmaylov, a. F.; Sonnenberg, J. L.; Williams; Ding, F.; Lipparini, F.; Egidi, F.; Goings, J.; Peng, B.; Petrone, A.; Henderson, T.; Ranasinghe, D.; Zakrzewski, V. G.; Gao, J.; Rega, N.; Zheng, G.; Liang, W.; Hada, M.; Ehara, M.; Toyota, K.; Fukuda, R.; Hasegawa, J.; Ishida, M.; Nakajima, T.; Honda, Y.; Kitao, O.; Nakai, H.; Vreven, T.; Throssell, K.; Montgomery Jr., J. a.; Peralta, J. E.; Ogliaro, F.; Bearpark, M. J.; Heyd, J. J.; Brothers, E. N.; Kudin, K. N.; Staroverov, V. N.; Keith, T. a.; Kobayashi, R.; Normand, J.; Raghavachari, K.; Rendell, a. P.; Burant, J. C.; Iyengar, S. S.; Tomasi, J.; Cossi, M.; Millam, J. M.; Klene, M.; Adamo, C.; Cammi, R.; Ochterski, J. W.; Martin, R. L.; Morokuma, K.; Farkas, O.; Foresman, J. B.; Fox, D. J. G16_C01. 2016, p Gaussian 16, Revision C.01, Gaussian, Inc., Wallin.

(23) Seshadri, S.; Gockowski, L. F.; Lee, J.; Sroda, M.; Helgeson, M. E.; Read de Alaniz, J.; Valentine, M. T. Self-Regulating Photochemical Rayleigh-Bénard Convection Using a Highly-Absorbing Organic Photoswitch. *Nat. Commun.* **2020**, *11* (1), 1–8.

2.9. Experimental section

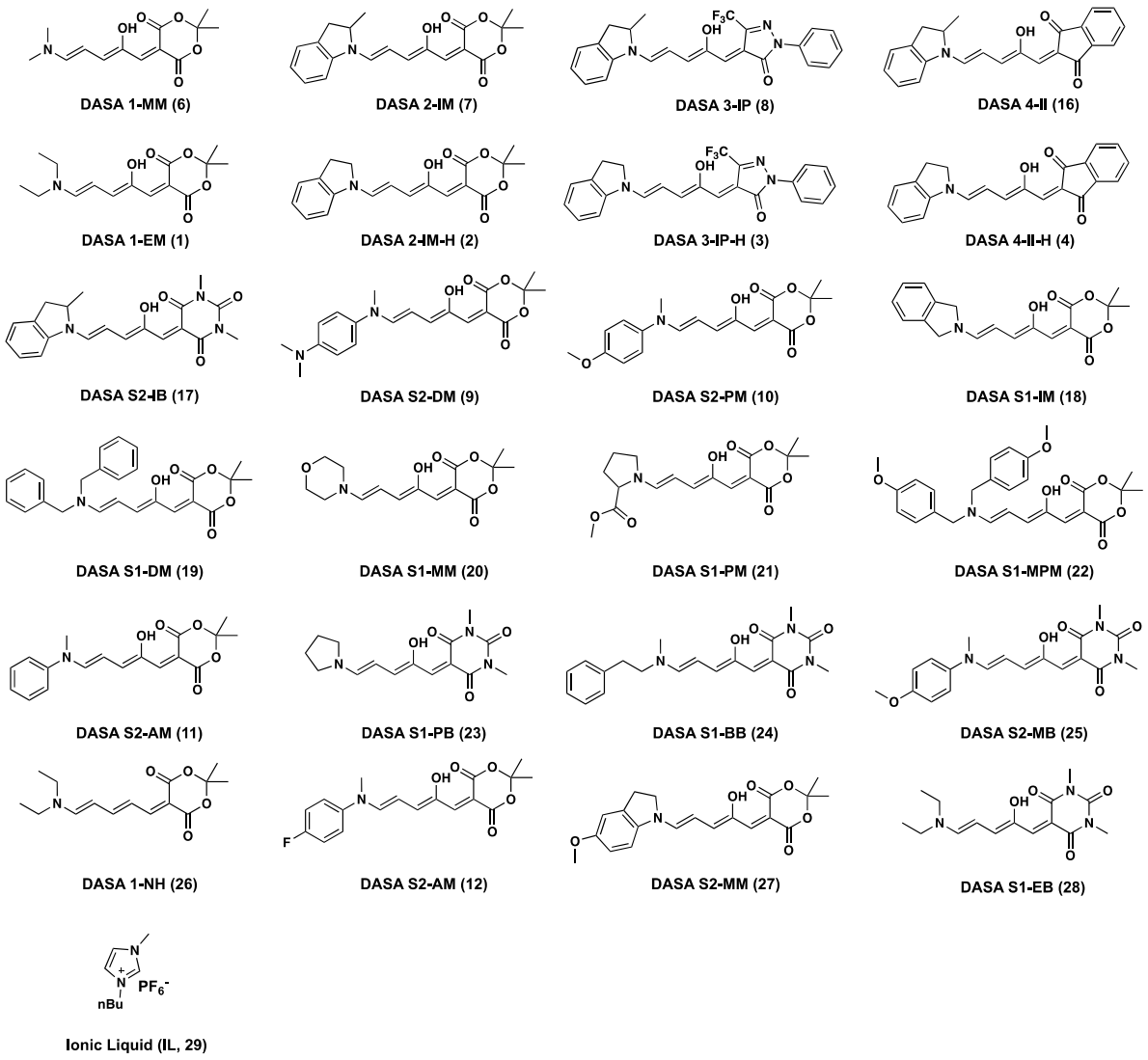

Figure 2.15 All open form compounds referenced in either the paper or supporting information.

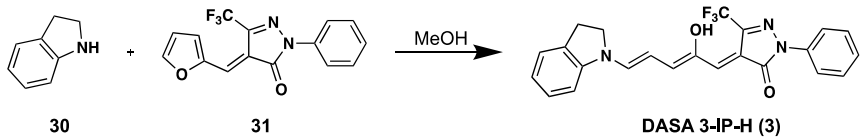

Scheme 2.7 (Z)-4-((2Z,4E)-2-hydroxy-5-(indolin-1-yl)penta-2,4-dien-1-ylidene)-2-phenyl-5-(trifluoromethyl)-2,4-dihydro-3H-pyrazol-3-one (**DASA 3-IP-H (3)**):

The furan adduct 2 (500 mg, 1.63 mmol, 1.0 equiv) was stirred in minimal methanol (approximately 5 mL) then indoline 1 (0.28 mL, 292 mg, 2.45 mmol, 1.5 equiv) was added. The reaction was stirred for 4 h and monitored by TLC for consumption of 2. The reaction mixture was then filtered to yield the product as a green powder and washed with ether to afford the product DASA 3-IP-H (458 mg, 1.08 mmol, 66%). Crystals of (DASA 3-IP-H) were grown by dissolving 10 mg in 1.5 mL of THF. The solution was stirred, sonicated and filtered. 2.5 mL of ether was layered on top as an anti-solvent. The vial was then capped and allowed to sit in the dark for three days for the crystals to grow. CCDC Deposition number: 2039176.

DASA 3-IP-H (3): ^{1}H NMR (500 MHz, chloroform-*d*) δ/ppm: 7.95 (d, *J* = 8.1 Hz, 2H), 7.77 (d, *J* = 11.0 Hz, 1H), 7.52 – 7.36 (m, 2H), 7.17 (t, *J* = 7.5 Hz, 1H), 7.11 (d, *J* = 8.2 Hz, 1H), 6.75 (d, *J* = 12.1 Hz, 1H), 6.66 (s, 1H), 6.34 (t, *J* = 12.3 Hz, 1H), 4.20 (t, *J* = 8.0 Hz, 2H), 3.37 (t, *J* = 8.0 Hz, 2H). IR (thin film) 2920, 2112, 1604, 1556, 1487, 1474, 1354, 1304, 1275, 1253, 1236, 1222, 1205, 1166, 1148, 1094, 1000, 980, 944, 905, 878, 831, 785, 755, 710, 686, 618, 558 cm^{-1}. HRMS (ESI), calculated for $C_{23}H_{18}F_3N_3NaO_2^+$ ($M+Na^+$): 448.1249, observed 448.1257.

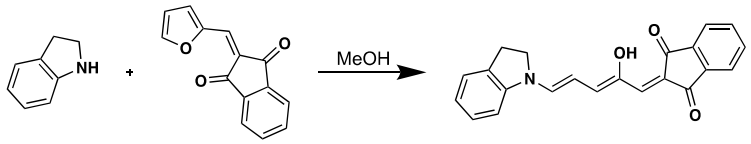

30 32 DASA 4-II-H (4)

Scheme 2.8 2-((2*Z*,4*E*)-2-hydroxy-5-(indolin-1-yl)penta-2,4-dien-1-ylidene)-1*H*-indene-1,3(2*H*)-dione (**DASA 4-II-H(4)**):

The furan adduct 3[11] (200 mg, 0.89 mmol, 1.0 equiv) was stirred in minimal methanol (approximately 4 mL) then indoline 1 (0.12 mL, 127 mg, 1.07 mmol, 1.2 equiv) was added. The reaction was stirred overnight and monitored by TLC for consumption of 3. The reaction mixture was then filtered to yield the product as a blue powder and washed with ether to afford the product DASA 4-II-H (188 mg, 0.55 mmol, 62%). Crystals of (DASA 4-II-H) were grown by dissolving 10 mg in 1mL of THF. The solution was stirred, sonicated, and filtered. A mL of ether was added on top as the anti-solvent. The vial was then capped and allowed to sit in the dark for three days. CCDC Deposition number: 2039175.

DASA 4-II-H(4): ^{1}H NMR (600 MHz, chloroform-*d*) δ/ppm: 11.31 (s, 1H), 7.78 (ddd, *J* = 10.7, 6.2, 2.1 Hz, 2H), 7.64 (tt, *J* = 7.3, 5.9 Hz, 2H), 7.58 (s, 1H), 7.23 (d, *J* = 7.2 Hz, 1H), 7.02 (dd, *J* = 8.6, 5.6 Hz, 2H), 6.97 (s, 1H), 6.54 (d, *J* = 11.9 Hz, 1H), 6.10 (s, 1H), 4.07 (t, *J* = 8.2 Hz, 2H), 3.29 (t, *J* = 8.2 Hz, 2H). IR (thin film) 2324, 2062, 1982, 1687, 1615, 1585, 1528, 1487, 1451, 1434, 1328, 1291, 1229, 1202, 1181, 1137, 1112, 932, 875, 846, 812, 798, 750, 728 cm^{-1}. HRMS (ESI), calculated for $C_{22}H_{17}NNaO_3^+$ ($M+Na^+$): 366.1106, observed 366.1106.

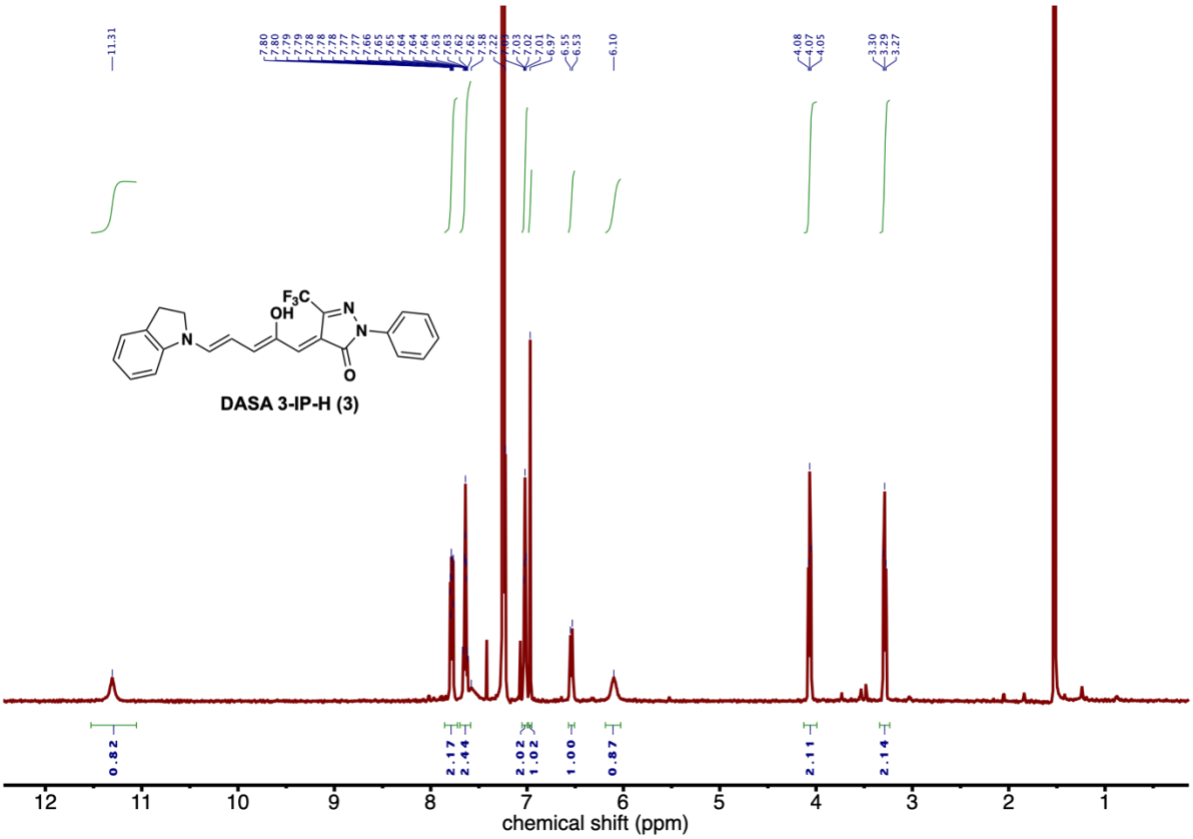

Scheme 2.9 ^{1}H NMR (500 MHz, chloroform-*d*) of **DASA 3-IP-H (3)**.

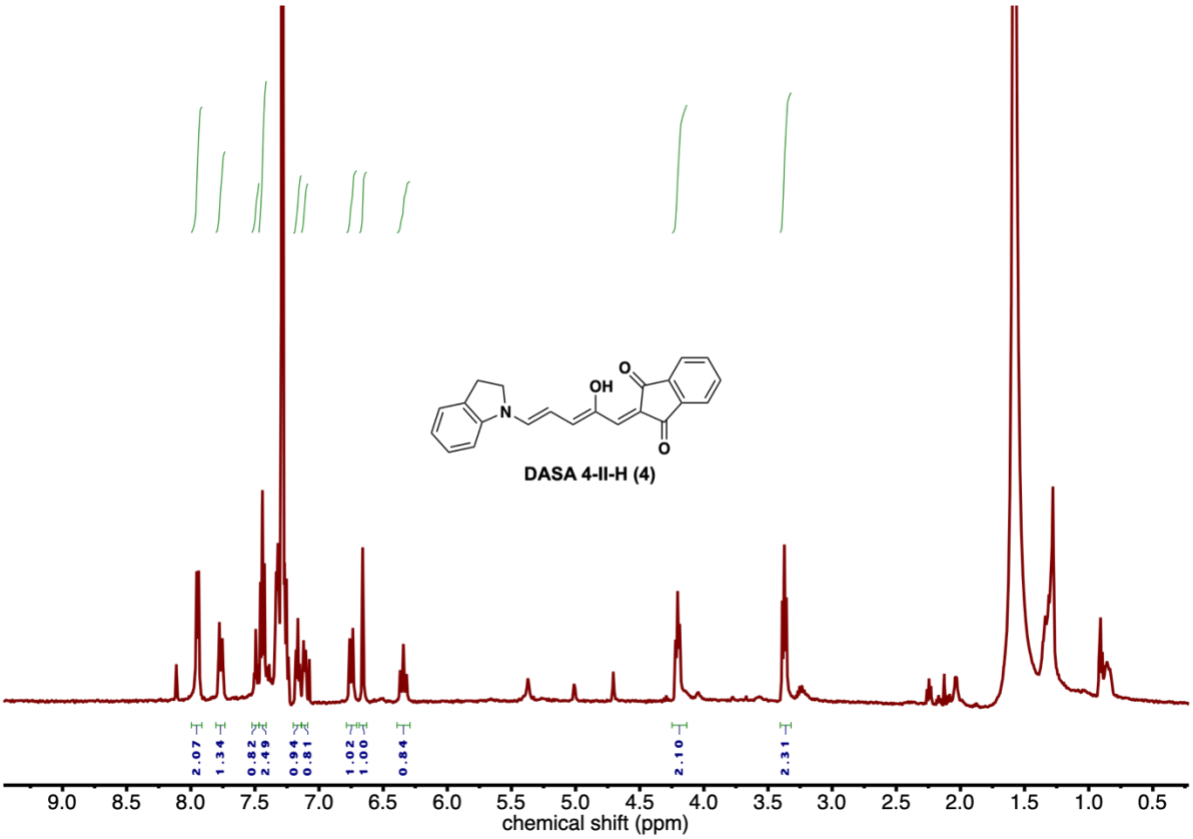

Scheme 2.10 ^{1}H NMR (600 MHz, chloroform-*d*) of **DASA 4-IP-H (4)**.

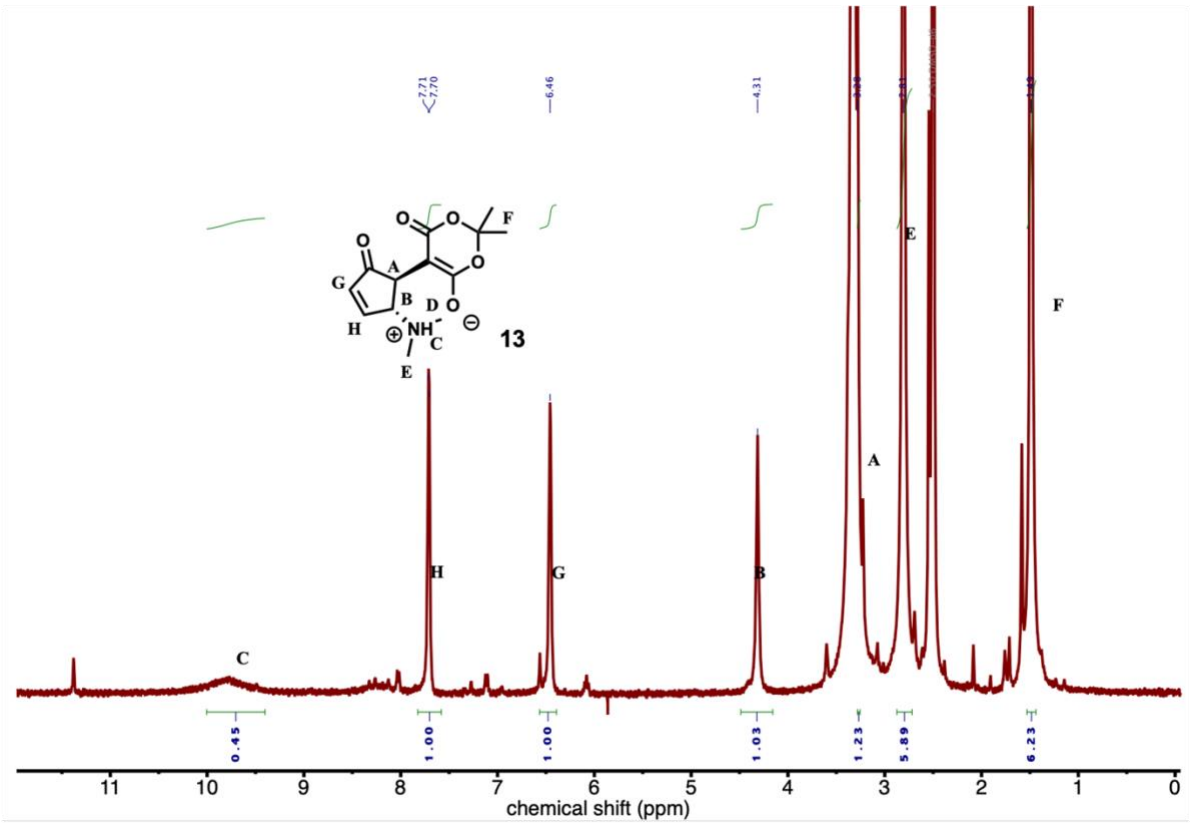

Scheme 2.11 ^{1}H-NMR (600 MHz, DMSO-d_6) of **DASA 1-MM (13)**. Only the zwitterionic closed form can be observed.

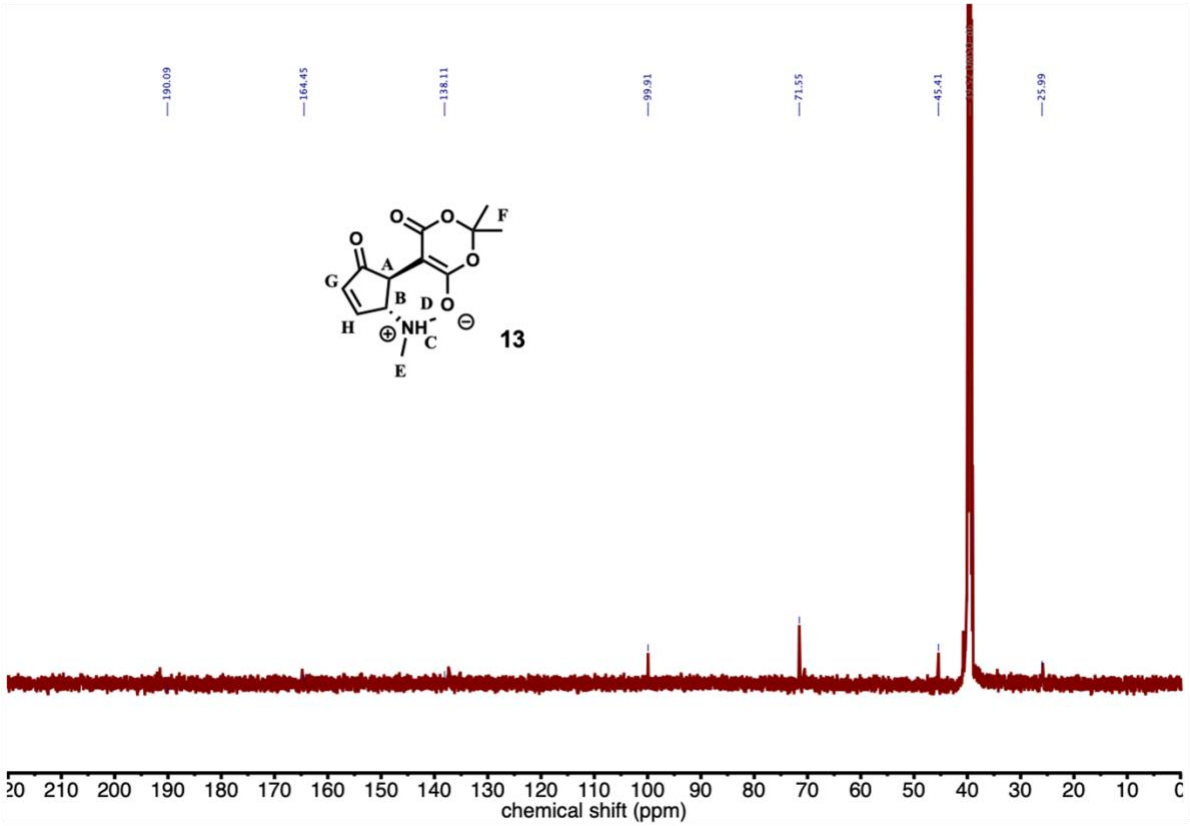

Scheme 2.12 ^{13}C-NMR (125 MHz, DMSO-d_6) of **DASA 1-MM (13)**. Limited solubility of the closed isomer results in minimal signal.

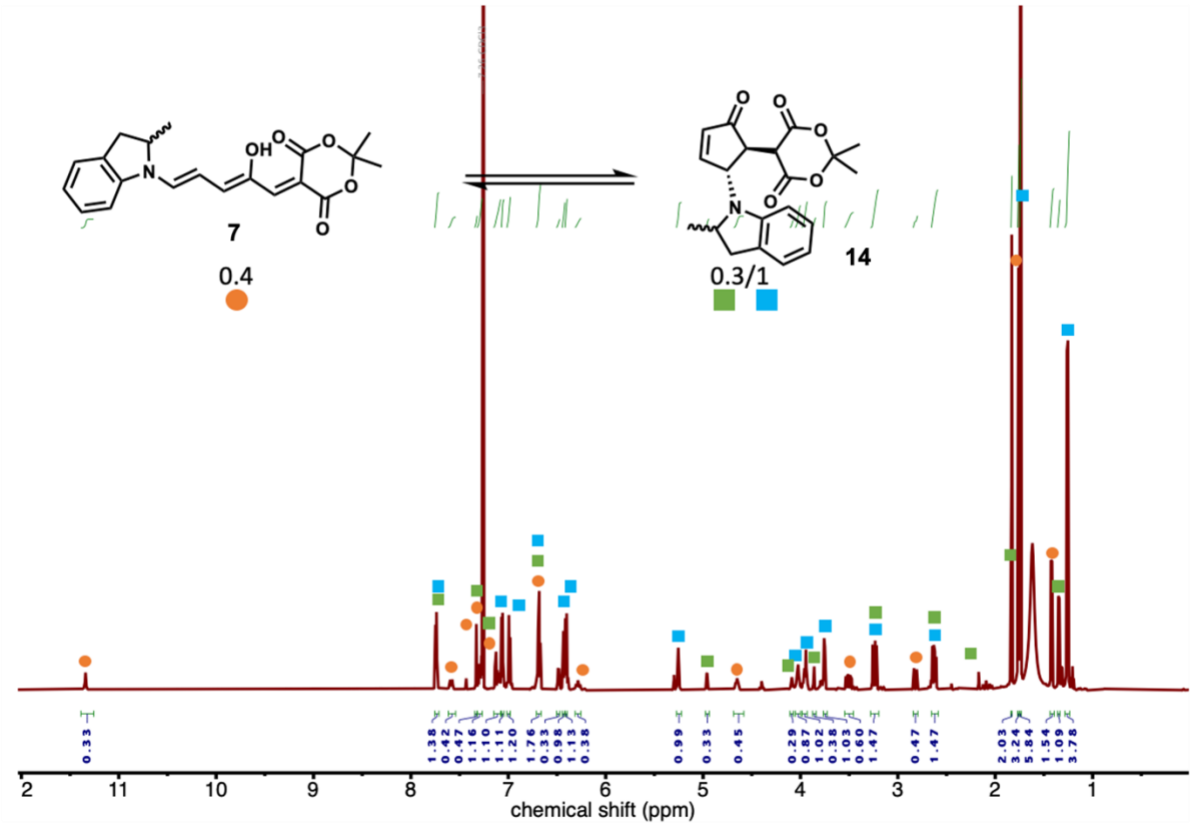

Scheme 2.13 ^{1}H-NMR (600 MHz, chloroform-*d*) of **DASA 2-IM (7)**. The different isomers are marked.

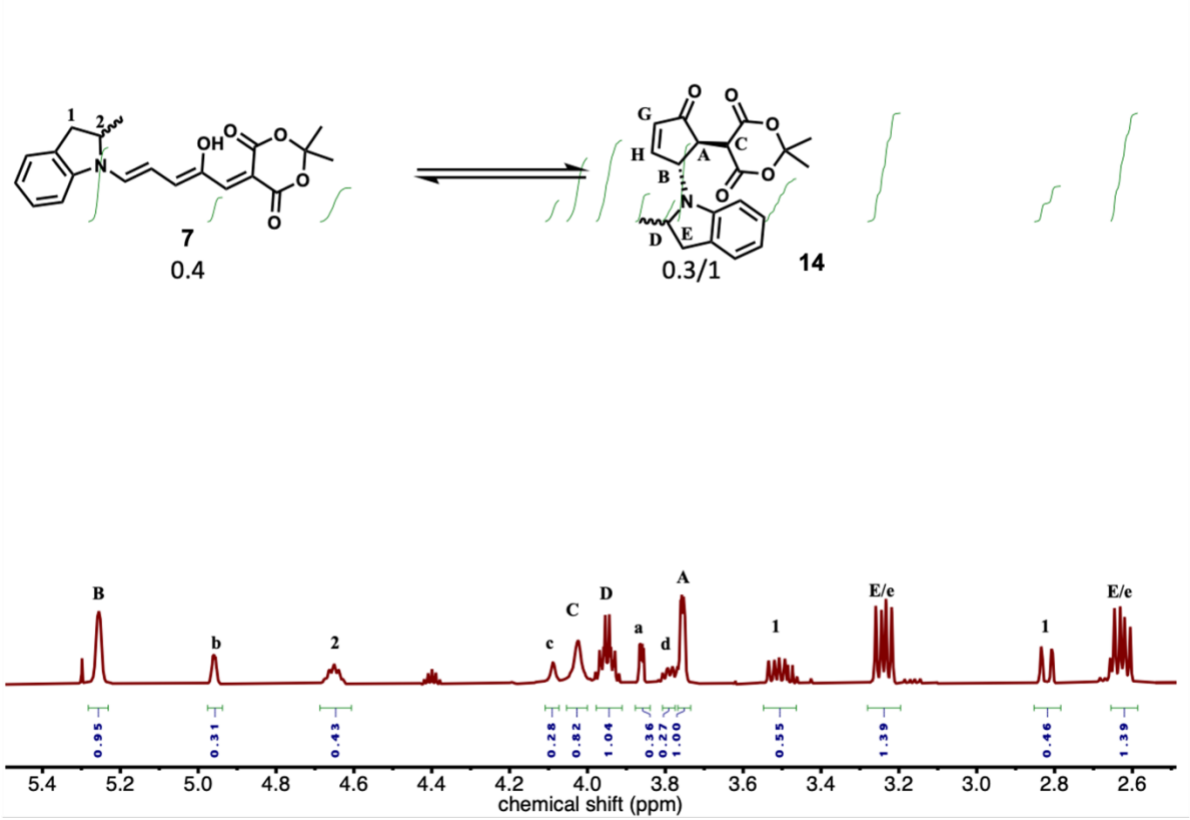

Scheme 2.14 ^{1}H-NMR (600 MHz, chloroform-*d*) of **DASA 2-IM (7)** between 5.5 and 2.5 ppm. The different isomers are marked. For the keto isomer integrating with 0.3 lower case letters were used.

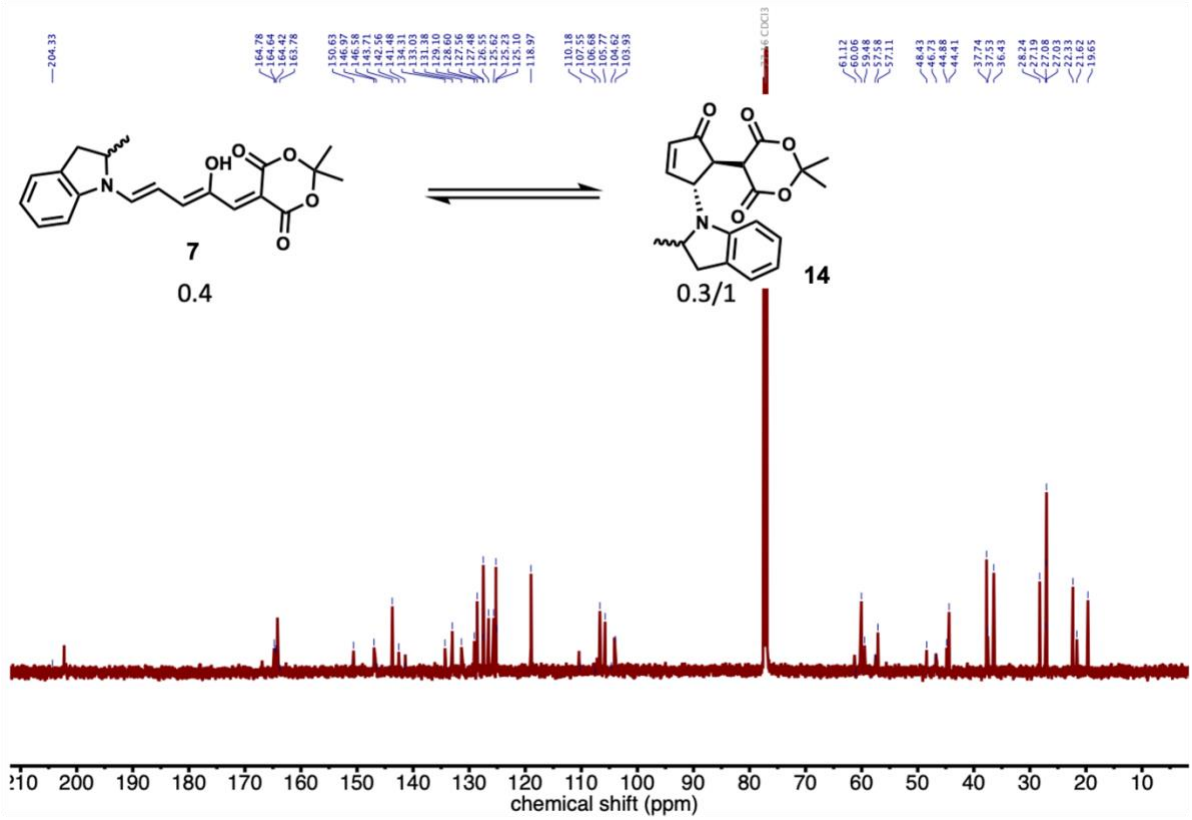

Scheme 2.15 ^{13}C-NMR (125 MHz, chloroform-*d*) of **DASA 2-IM (7)**.

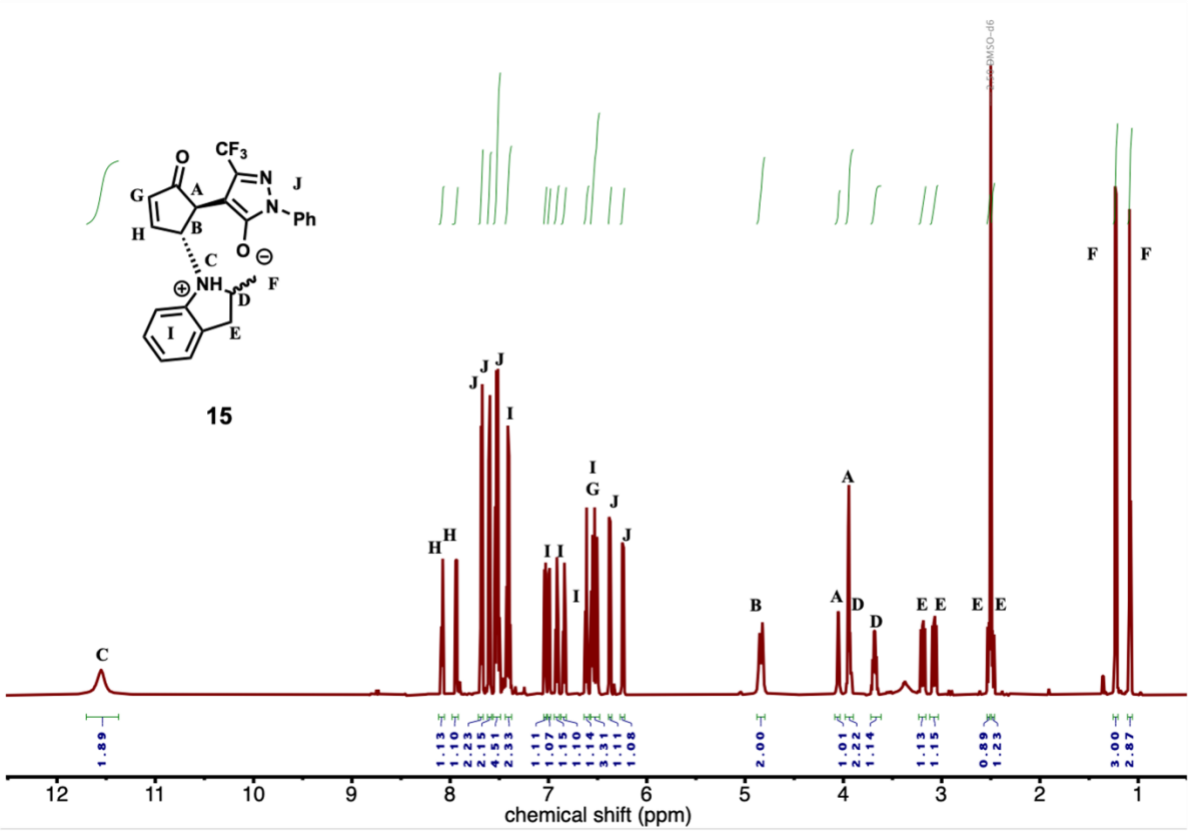

Scheme 2.16 ^{1}H-NMR (600 MHz, DMSO-d_6) of **DASA 3-IP (15)**. Two zwitterionic closed isomers can be observed.

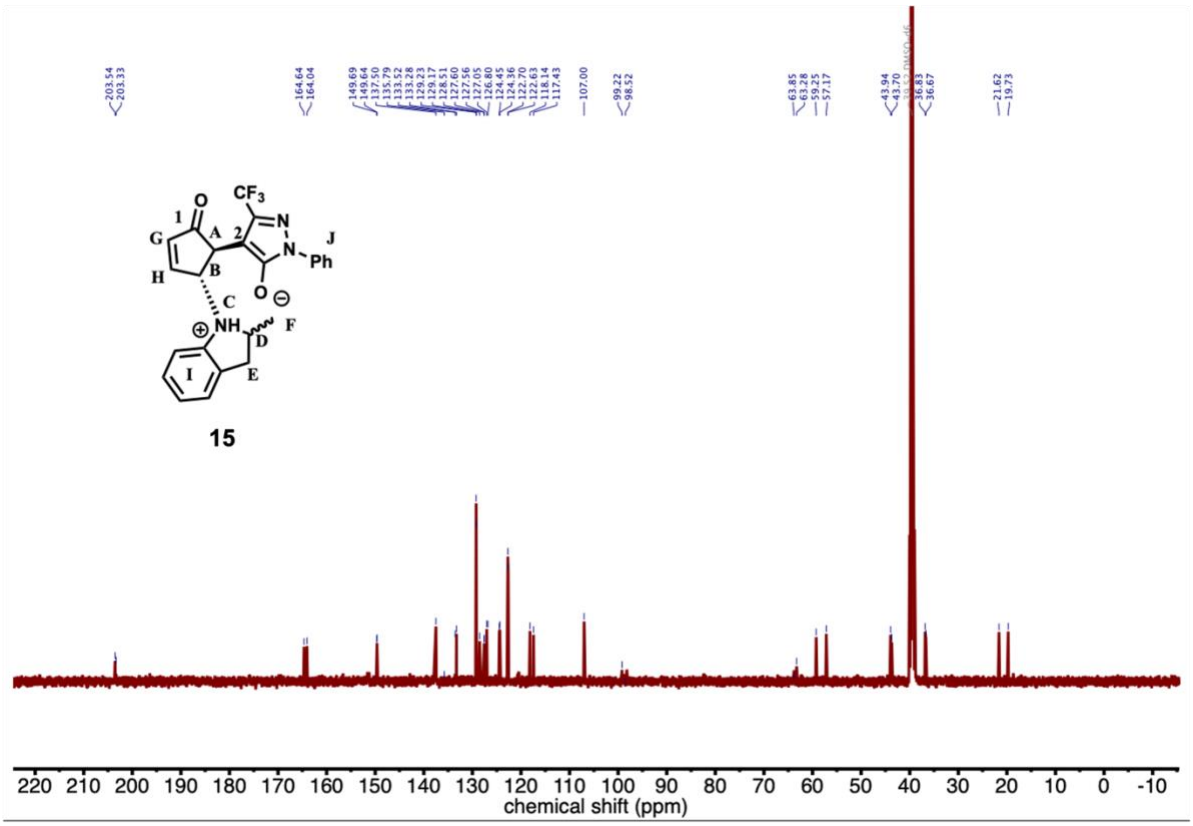

Scheme 2.17 ^{13}C-NMR (126 MHz, DMSO-d_6) of **DASA 3-IP (15)**. Two zwitterionic closed isomers can be observed.

Chapter 3. Tunable photothermal actuation enabled by photoswitching of DASAs

3.1. Abstract

We report a visible light-responsive bilayer actuator driven by the photothermal properties of a unique molecular photoswitch: donor–acceptor Stenhouse adduct (DASA). We demonstrate a synthetic platform to chemically conjugate DASA to a load-bearing poly(hexyl methacrylate) (PHMA) matrix via Diels–Alder click chemistry that enables access to stimuli-responsive materials on scale. By taking advantage of the negative photochromism and switching kinetics of DASA, we can tune the thermal expansion and actuation performance of DASA–PHMA under constant light intensity. This extends the capabilities of currently available responsive soft actuators for which mechanical response is determined exclusively by light intensity and enables the use of abundant broadband light sources to trigger tunable responses. We demonstrate actuation performance using a visible light-powered cantilever capable of lifting weight against gravity as well as a simple crawler. These results add a new strategy to the toolbox of tunable photothermal actuation by using the molecular photoswitch DASA. This Chapter was adapted with permission from *ACS Appl. Mater. Interfaces* **2020**, *12*, 54075–54082.[1] Copyright 2020 American Chemical Society.

3.2. Introduction

Developing a high efficiency photoswitch is not sufficient to make a viable photomechanical material. Once such a molecule is incorporated into a solid matrix, numerous factors can affect its ability to react, including polymer matrix and photochrome density. We need reliable, modular, and efficient methods to access photoresponsive materials. DASA-based materials hold tremendous promise in this area, however actuator designs to explore these novel switches remains unexplored.

In this chapter, we aim to develop a load-bearing material that can respond to broadband visible light and empower tunable actuation. We enable tunability by exploiting a previously unexplored strategy that introduces cooperative photothermal actuation and photochemical control using negatively photochromic materials. To achieve this, we leverage the intrinsic photochemical properties of donor–acceptor Stenhouse adducts (DASAs).[2-4] DASAs have a high molar absorptivity (>100,000 $M^{-1}cm^{-1}$) and adjustable absorption profiles in the visible to near-IR window.[2] We hypothesize that upon irradiation with visible light, the rapid photothermal energy conversion of DASAs can be harnessed to drive mechanical actuation, while the conversion from a highly absorbing colored form to a colorless and transparent form can switch off the photothermal sensitizer to enable photochemical control (Figure 3.1). The rapid photothermal heating enables the use of simple design principles including an amorphous structure and bilayer configuration, avoiding the complex processing step of molecular alignment of LCNs.[5] The kinetics of these transitions can be controlled by the design of the photoswitch and physicochemical conditions.[6-8] This allows photothermal actuation and photochemical control to occur on different timescales under constant external input, thereby enabling novel forms of tunability. We recently demonstrated how the controllable photothermal properties, negative

photochromism and high molar absorptivity of DASAs could be leveraged to achieve self-regulating control of fluid motion.[9] In conceptually related work, the use of switchable tungsten-(VI) oxide nanoparticles, WO_3, was used to as photothermal sensitizer for high color quality 3D printing.[10]

Herein, we report the development and use of a DASA–polymer conjugate in the solid state to enable tunable, load-bearing actuation to produce mechanical work. We demonstrate visible light-powered actuation performance with a cantilever capable of lifting a weight against gravity and a remotely powered and controlled crawler. Our results demonstrate the promise of this material design strategy for rapid and self-tunable photoinduced actuation using negatively photochromic, amorphous materials.

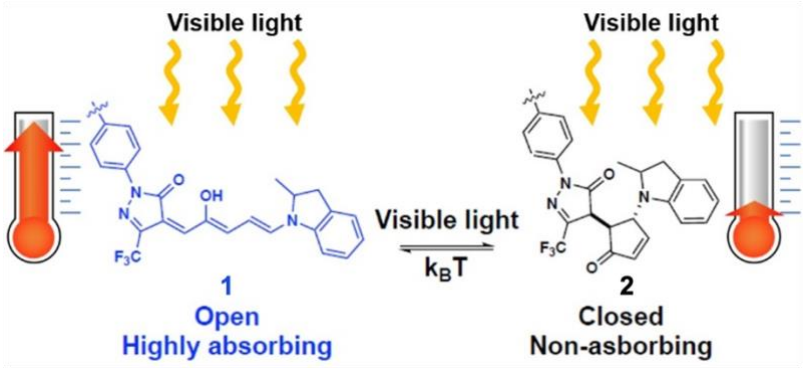

Figure 3.1 Structure and photoswitching of donor-acceptor Stenhouse adducts. The highly absorbing, colored open form empowers photothermal energy conversion, while the non-absorbing, colorless closed form generates less heat upon irradiation providing control over the magnitude of actuation. Reprinted with permission from *ACS Appl. Mater. Interfaces* **2020**, *12*, 54075–54082. Copyright 2020 American Chemical Society.

3.3. Synthesis of DASA-PHMA and bilayer fabrication

To construct the DASA–polymer conjugate and generate a negatively photochromic light-responsive bilayer actuator, we developed a new synthetic strategy using Diels–Alder click chemistry (Figure 3.2).[11] This method overcomes many limitations of the current functionalization strategies that rely on DASA formation in the final step including long reaction times, incomplete functionalization, and multiple post-polymerization steps.[7, 12-14] We chemically conjugated the DASA molecules to the polymer backbone to provide more uniform dispersion and high thermal stability as compared to physical blending.[15] In detail, copolymers containing poly(hexyl methacrylate) (PHMA) and the functional monomer, norbornadiene methacrylate (NBD-MA), were synthesized using reversible addition–fragmentation chain transfer (RAFT) polymerization to generate 10 mol% NBD–PHMA. Hexyl methacrylate was chosen as a comonomer, due to its optical transparency in the visible region[16] and mechanical properties.[17] A maleimide bearing a 3rd generation DASA-based photoswitch bearing a CF_3-pyrazolone acceptor and a 2-methyl indoline donor was prepared (Scheme 3.1a) due to its high molar absorptivity and enhanced dark equilibrium compared to prior generations[7] and "clicked" onto the polymer using tetrazine to initiate the cascading Diels–Alder reaction (Scheme 3.1b). Detailed synthetic procedures and characterization results are shown in the Experimental Section of this Chapter.

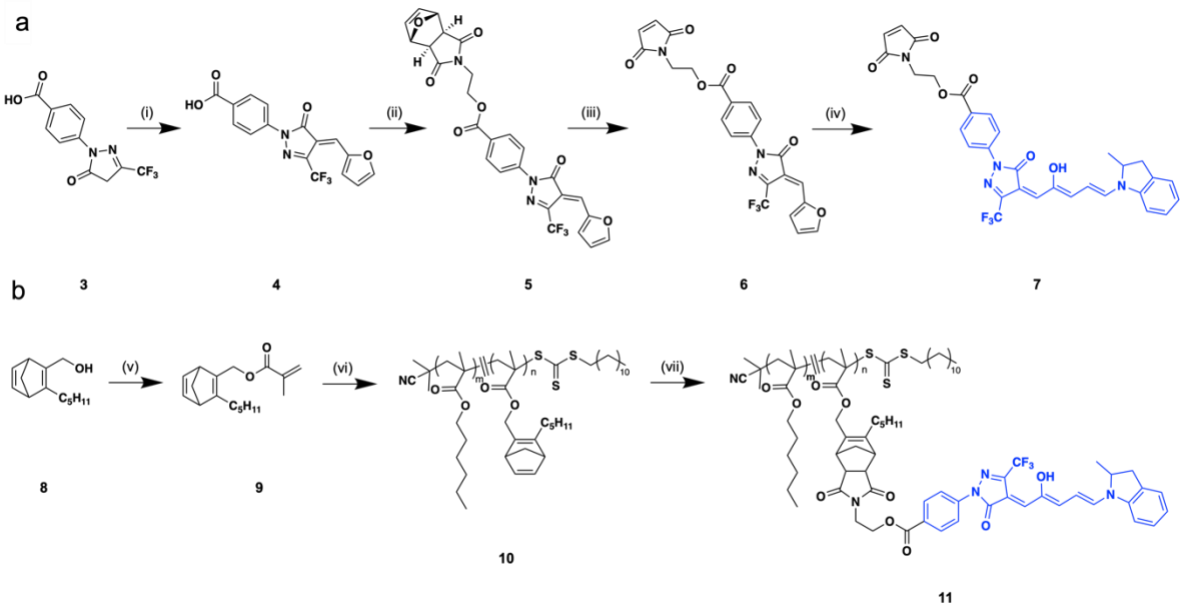

Scheme 3.1 Molecular design of a photothermally-responsive DASA polymer. Synthetic pathways for (a) DASA–maleimide and (b) DASA–PHMA by "clicking" DASA–maleimide onto NBD–PHMA using Diels–Alder chemistry. Adapted with permission from *ACS Appl. Mater. Interfaces* 2020, *12* (48), 54075–54082. Copyright 2020 American Chemical Society.

A target incorporation of 10 mol% DASA was chosen to provide sufficient photothermal heat generation to drive actuation, while enabling control of the switching kinetics to impart programmability.[18] ^{1}H NMR and UV–Vis spectroscopy were used to confirm DASA incorporation: a distinct DASA peak centered at ~ 648 nm was observed in both the DASA–maleimide and the 10 mol% DASA–PHMA samples (Figure 3.2a).

To demonstrate light-driven motion using this photo-responsive material, a 20 mm × 1.5 mm bilayer actuator was prepared by drop casting (Figure 3.2b). In contrast to the aligned LCN systems that offer the ability to program complex 3D shape changes, we initially explored the use of a DASA–PHMA polymer-based system in an amorphous bilayer in order to lift weight and generate work. Our use of amorphous fabrication

techniques avoids the complexities of molecular alignment of LCNs, while also eliminating the need for thiol-Michael additions[19] and radical polymerizations[20] that are traditionally used for LCN preparation but are not compatible with DASA functionality. The fabrication method is straightforward: a thin film of DASA–PHMA was deposited (film thickness of ~10 μm) onto a commercially obtained polyimide (PI) film (thickness of ~25 μm) that serves as the inactive layer. The thickness was confirmed by scanning electron microscopy and optical microscopy (Figure 3.2c). Differential scanning calorimetry (DSC) of the DASA−PHMA conjugate indicated an increase in T_g from the parent polymer from −10 °C to 45 °C (Figure 3.3).

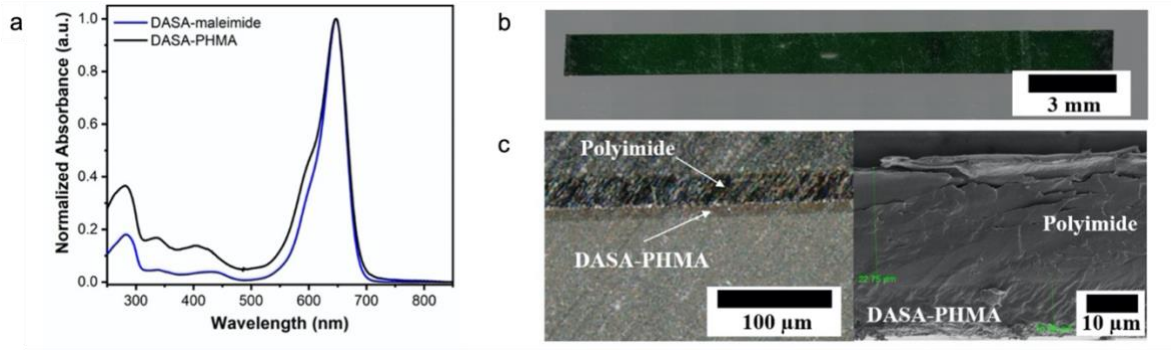

Figure 3.2 (a) DASA–maleimide and DASA–PHMA UV–Vis spectra exhibit identical absorbance max at ~ 648 nm in solution (chloroform). (b) A photographic image of bilayer specimen and (c) a cross sectional image of the bilayer (left) taken by an optical microscope, and (right) an SEM image of the cross section. Adapted with permission from *ACS Appl. Mater. Interfaces* 2020, *12* (48), 54075–54082. Copyright 2020 American Chemical Society.

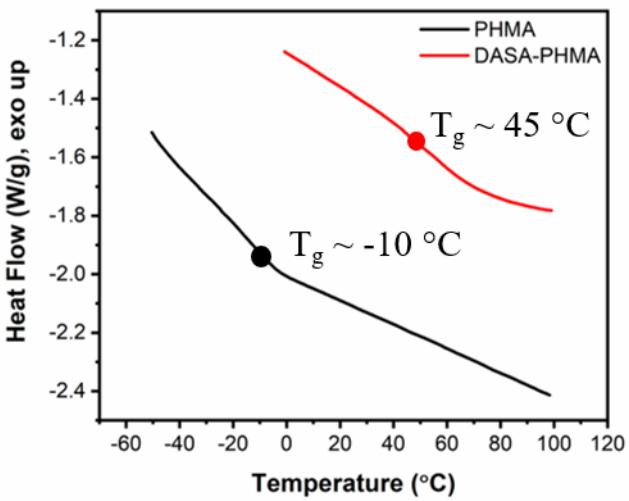

Figure 3.3 Differential scanning calorimetry (DSC) measurements of PHMA and DASA–PHMA indicate that the glass transition temperature increases from -10 °C to 45 °C due to the chemical conjugation of 10 mol% DASA to PHMA.

3.4. Photothermally driven actuation with DASA-PHMA/PI bilayer

With access to DASA–PHMA photoresponsive material, we set out to explore photothermally-driven actuation using a bilayer DASA–PHMA/PI cantilever system (Figure 3.4) that takes advantage of the differences in thermal expansion caused by DASA-dependent heat generation to induce bending.[21] A light source (halogen lamp, EKE 150 W with a fiber optic illuminator) located above the cantilever directly illuminated the DASA–PHMA layer. A small weight was placed on the tip of the cantilever to evaluate the capability of the actuator to lift against gravity, thereby performing mechanical work (Figure 3.4a). For each experiment, the deflection of the cantilever tip was continuously recorded before, during, and after irradiation. Representative snapshot images of the motion are presented in Figure 3.4b; the dotted blue line indicates the initial cantilever position, which has bowed under the added weight at the tip. Upon illumination an initial fast lifting motion

was observed with a speed of ~ 1.8 mm/s for ~ 1 second, followed by a gradual slowing as the cantilever reached its steady-state deflection (Figure 3.4c). The peak deflection was achieved within ~ 1.5 s of illumination, and once the light was turned off, the cantilever returned to its initial position on a similar timescale.

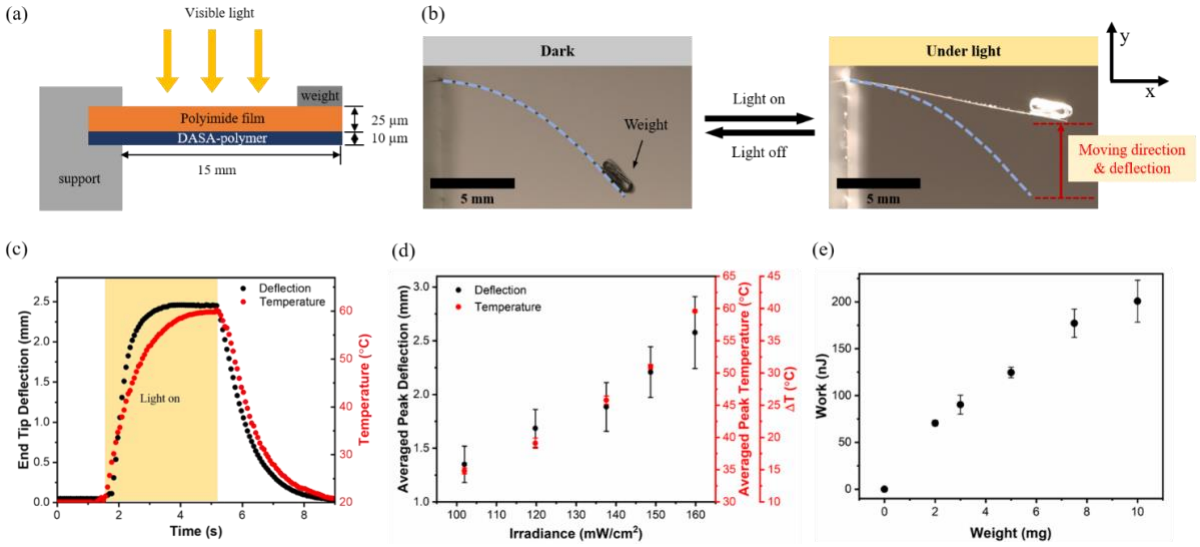

Figure 3.4 Photothermally-powered DASA–PHMA/PI bilayer cantilever: actuation performance and temperature response. (a) Schematic of the experimental configuration. (b) Snapshot images show that the cantilever lifts under light and drops when light is turned off. Weight is 5 mg. (c) Representative data traces showing tip defection (*y*-axis displacement) and temperature as a function of time (5 mg weight, 160 mW/cm^2 irradiance, halogen lamp). (d) Averaged peak deflection (with 5 mg weight), and averaged peak temperature are plotted as a function of irradiances; both values increase linearly with irradiance. (e) The photothermally-driven mechanical work calculated by $m_0 g \Delta h$, where m_0 is mass of the added weight at the tip, g is the acceleration due to gravity, and Δh is the maximal change in tip position before and after illumination plotted as a function of added weight (red arrow in

panel b). Reprinted with permission from *ACS Appl. Mater. Interfaces* **2020**, *12*, 54075–54082. Copyright 2020 American Chemical Society.

The beam dynamics appear to closely track the temperature change as measured using an IR camera (FLIR® E60), as expected for the photo-driven asymmetric thermal expansion of the bilayer. This was further confirmed through thermal mechanical analysis. The linear coefficient of thermal expansion (CTE) for DASA–PHMA was measured to be 9 times higher than that of PI (Figure 3.5) for temperatures ranging from 0 to 35 °C. As irradiance was increased, the average peak deflection and temperature increased proportionally (Figure 3.4d). As a further confirmation that the dominant mechanism of actuation is photothermal, we subjected a cantilever to a temperature ramp at a rate of 3 ºC/min using a temperature-controlled chamber and observed similar bending profiles as compared to those obtained via illumination at room temperature (Figure 3.6).

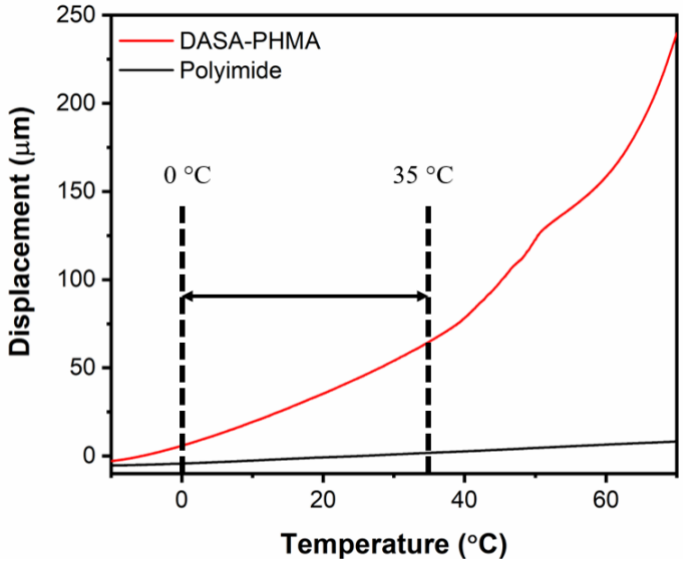

Figure 3.5 Displacements of DASA–PHMA and PI films at various temperatures. The temperature ranges from 0 to 35 °C was used to calculate the CTEs.

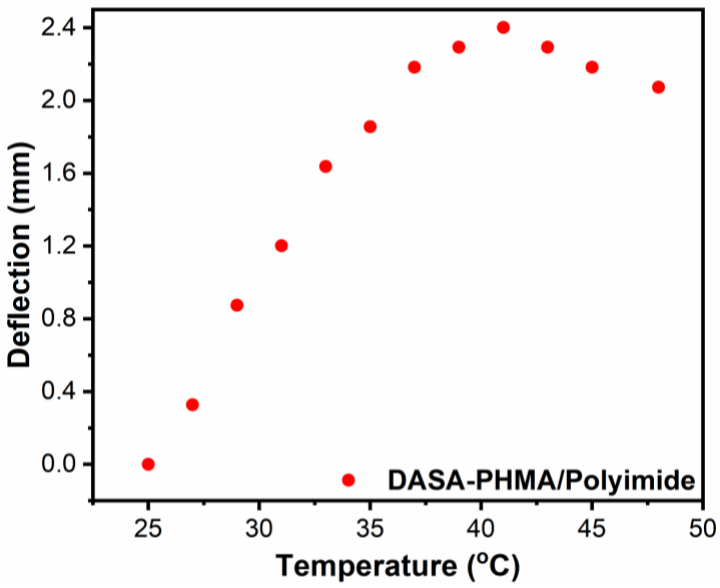

Figure 3.6 Deflections of DASA-PHMA/PI at different temperatures.

To evaluate the mechanical actuation performance of the cantilever, the mechanical work generated under illumination was measured by calculating potential energy difference between the initial position and final position under peak deflection as a function of added weight (Figure 3.4e). We found that the work increased linearly with increasing weight and that the simple actuator could lift against gravity a weight up to 13 times that of the DASA–PHMA/PI cantilever alone. Finally, the light-driven bending action is robust and repeatable, as evident through a series of 30 illumination-dark cycles using a 5 mg weight at the cantilever tip (Figure 3.7), although a slight decrease of peak deflection after several illumination-dark cycles was observed. We speculate that slow switching from the open, highly absorbing form to the closed, transparent, and less absorbing form of DASA results in the gradual performance decline. The full conversion time of the 10-μm thick DASA-PHMA specimen under 160 mW/cm^2 light illumination is ~400 s, which is significantly longer than the photothermal actuation time scale of ~ 1.5 s (Figure 3.8). As such, repeated

illuminations could decrease the absorbance, which leads to the reduction of deflection after multiple cycles. When light irradiation is ceased, the DASA–polymer conjugate undergoes slight thermal reversion extremely slowly under ambient conditions (Figure 3.8).

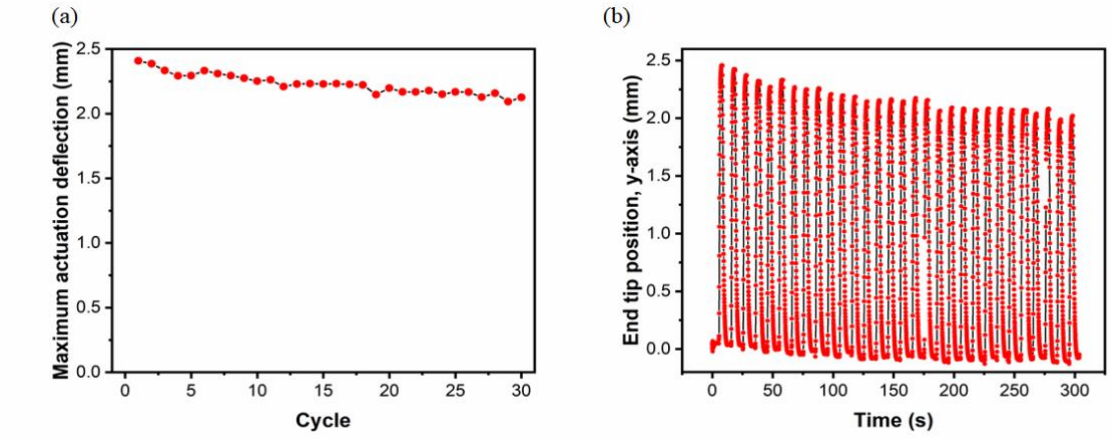

Figure 3.7 Repeatability of the actuation. (a) Maximum actuation displacements of DASA–PHMA/PI cantilever as a function of cycle number. (b) End tip position (z-axis) of the cantilever over time. 3 seconds illumination and 7 seconds no-illumination were cycled.

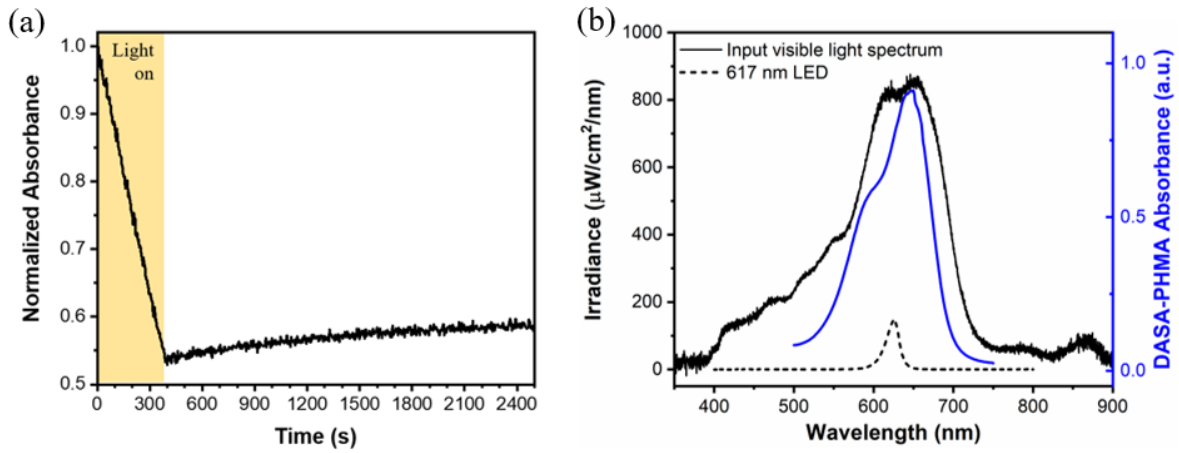

Figure 3.8 Slow switching kinetics of DASA–PHMA. (a) Normalized absorbance of DASA–PHMA at λ_{max}= 645 nm under 617 nm LED light illumination as a function of time.

(b) Irradiance spectra of 617 nm LED and visible light (black curves, left axis) compared to the DASA–PHMA absorbance spectrum (blue curve, right axis).

3.5. Remote-controlled crawler

To further demonstrate the actuation capabilities of our material, a photothermally-powered crawler was designed to exploit the bending motions of the DASA–PHMA/PI bilayer film under illumination to enable locomotion. The crawler consisted of a thin bilayer cantilever (20 mm × 1.5 mm × 35 μm, where the bilayer film consists of a 25 μm PI layer, and 10 μm DASA–PHMA layer, identical to that described above) attached to a pair of asymmetric legs made of a polystyrene film (5 mm × 1 mm × 200 μm). The crawler is cyclically illuminated by 160 mW/cm^2 light intensity using the halogen lamp, and its motion is recorded as a function of time. When the bilayer is oriented with the DASA–PHMA layer on the top, crawling motions with convex bending were observed (Figure 3.9a). During each cycle of illumination, the cantilever bends, causing the rear legs to retract. When the light is turned off, the cantilever returns to its original shape, but the rear legs have anchored at their new position, causing the forelegs to extend, and shifting the crawler center of mass to the left. If we construct a robot using an inverted specimen structure with the DASA–PHMA layer on the top, we observe an inversion in the bending curvature but similar crawling performance (Figure 3.9). In this case, the forelegs stretch first and anchor, and the rear legs follow once the light has ceased. Moreover, the cyclic directional motion of the crawler under periodic illumination is robust regardless of illumination spot position due to the photothermal nature of the actuation. Thus, the negatively photochromic DASA is an effective photoresponsive agent capable of generating robust photothermally-driven

mechanical output using low intensity visible light, which can drive a locomotive crawling motion.

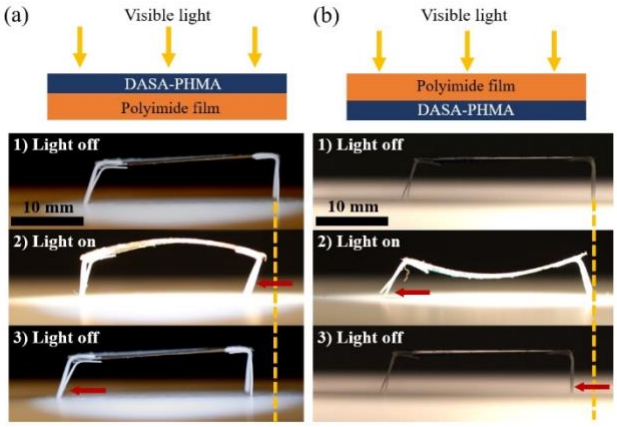

Figure 3.9 Demonstration of the application of a DASA–PHMA/PI bilayer film to form a remote-powered and controlled crawler. (a) A light-triggered convex bending motion is observed when DASA–PHMA and PI form the top and bottom layers, respectively. This leads to a robust, directional crawling motion, which can be described in three stages, 1) initial rest state before illumination, 2) backbone bending and rear foot dragging when the light is turned on, and 3) backbone relaxation, rear foot anchoring and stretching when the light is turned off. (b) The inverted geometry, where the PI film forms the top layer, also endows locomotion capability, following same 3 motion stages but with concave bending and forefoot anchoring in each cycle. Reprinted with permission from *ACS Appl. Mater. Interfaces* **2020**, *12*, 54075–54082. Copyright 2020 American Chemical Society.

3.6. Tunable photothermal actuator using negative photochromism

Finally, we sought to leverage DASA's negatively photochromic properties that shift the colored reactant to a colorless product to tune the magnitude of actuation. In contrast to tunable actuation using physical (i.e., structural patterning) or chemical (i.e., dynamic

networks and acid patterning) triggers, the use of photochromic molecules that shift the absorption of the chromophore to a range outside of the excitation light source provides a novel non-invasive photochemical control mechanism. In the case of DASAs, by simply modulating irradiation time, the extent of bleaching can be controlled, and thus the total amount of irradiant energy that can be converted to heat can be tuned. Because Figure 3.10a shows the corresponding color changes at different light exposure times from dark green (unswitched/open, 0 min) to yellow (fully switched/closed, 8 min), where the yellow color arises from intrinsic color of the PI film, as the closed DASA is transparent/colorless. A pristine dark green cantilever comprising of open DASA–PHMA records ~ 27.0 ± 0.2 mm peak deflection at 160 mW/cm2 irradiance with 5 mg added weight. The peak deflection decreases as the cantilever decolorizes, and an identical transparent cantilever comprising closed DASA–PHMA records only ~ 12.1 ± 0.2 mm peak deflection (Figure 3.10b). The enhanced actuation performance of the open-form DASA is expected, since the colored (open) DASA absorbs much more light energy, which is in turn dissipated as heat to the cantilever. Somewhat surprisingly, however, DASA–PHMA/PI bilayer still actuates, achieving 46% of the peak deflection value recorded for the open-form DASA–PHMA/PI bilayer. Thermal imaging of the closed-form transparent bilayer under 160 mW/cm^2 illumination reveals a temperature increase of ~ 16.4 °C which thus results in photothermal actuation (Figure 3.11). The ratio of temperature increases, 0.42, between the open-form (~ 39.2 °C) and closed-form DASA-based cantilevers approximates the ratio of end tip deflections, 0.45, for the same conditions, suggesting a direct correspondence between temperature difference and actuation performance. A control study of a single layer PI film

also showed a temperature increase, of ~ 13.5 °C, under illumination, which indicates that the absorbance of PI is one of the heat generation sources (Figure 3.11).

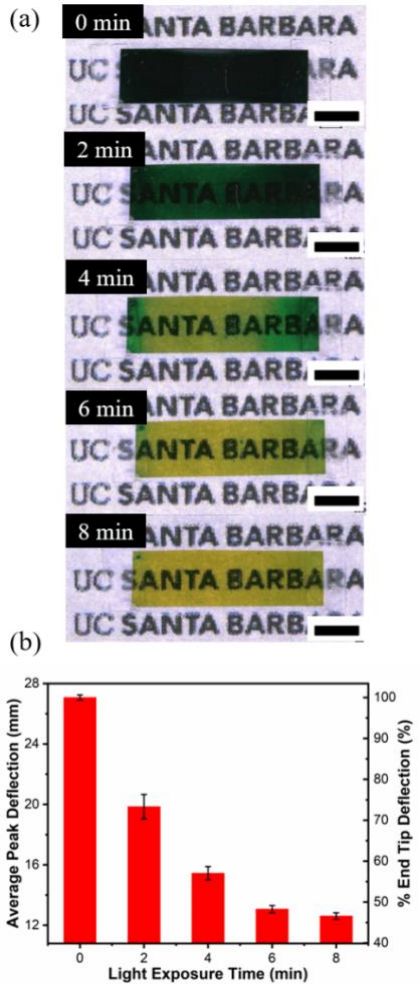

Figure 3.10 Photochemically-tunable photothermal actuation of a DASA–PHMA/PI bilayer cantilever. (a) A DASA–PHMA/PI cantilever changes color over light exposure time from dark green (open, top) to yellow (closed, bottom). In the closed form, the DASA–PHMA is clear and the yellow color is due to the PI film. (b) End tip deflection of DASA–PHMA/PI corresponding to the illumination time. Righthand axis gives relative deflection, as compared to the initial state (0 min). Reprinted with permission from *ACS Appl. Mater. Interfaces* **2020**, *12*, 54075–54082. Copyright 2020 American Chemical Society.

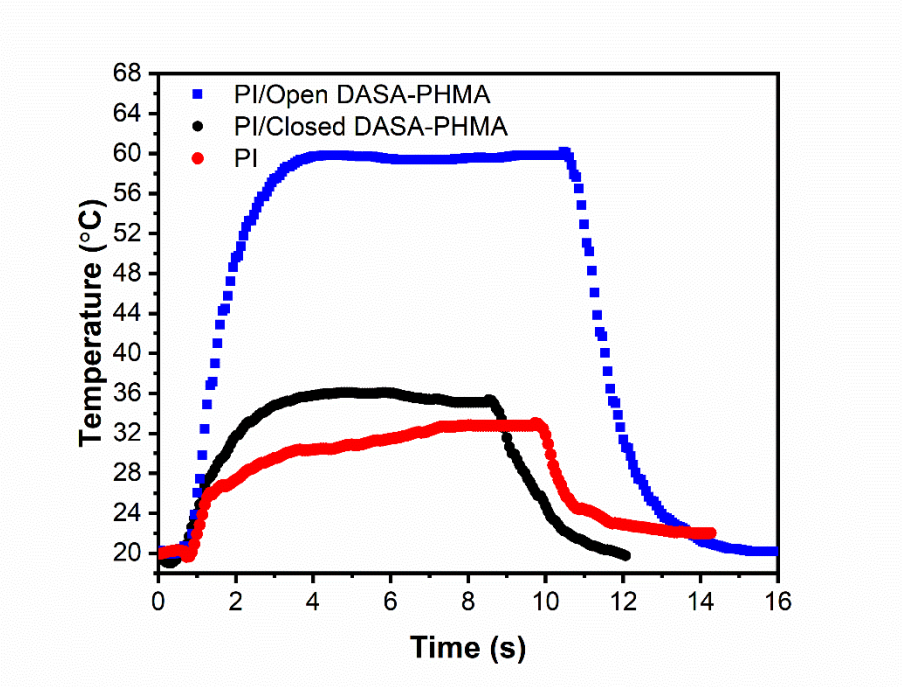

Figure 3.11 Temperatures of PI (self-standing), PI/open, and PI/closed DASA–PHMA under 160 mW/cm^2 illumination.

3.7. Thermal recovery

It is possible to restore the bleached sample to its original state by exposure of the closed-form (transparent) film to 75 °C for 1 min, which returns the sample to its open-form (colored) state. This reset sample can then be actuated again (Figure 3.12), however, the observed peak deflection amplitude is < 80% of the original deflection of the pristine sample, which we attribute to photodecomposition.[30,37] Ongoing work aims to improve the reconfigurability by modifying the photoswitching properties in order to improve thermal reversion for multiple cycles, as well as minimize the photothermal response of the bilayer system when DASA is in its closed transparent form. However, this proof-of-principle study demonstrates that the negatively photochromic properties of DASA can be used to program

the photothermal actuation in amorphous bilayer actuators. We speculate that stiffening of the polymer upon thermal recovery to the open form resulting in a new equilibrium and photodegradation might be leading to poor recover. We also cannot rule out that operating at temperatures higher than 10 °C above the Tg, is required to induce a sufficiently rubbery/viscous state for full recovery. As shown in Figure 3.13, 4 mol % DASA-PHMA (T_g = 23 °) has >90% recovery at 55 °C, compared to only ~70% at 35 °C. While this looks very promising, we have also observed that long irradiation times lead to decreased overall recovery which we believe is the result of decomposition. In addition, we observed after prolonged irradiation of 10 mol % DASA-PHMA at room temperature (>45 min) the sample is no longer completely soluble in chloroform.

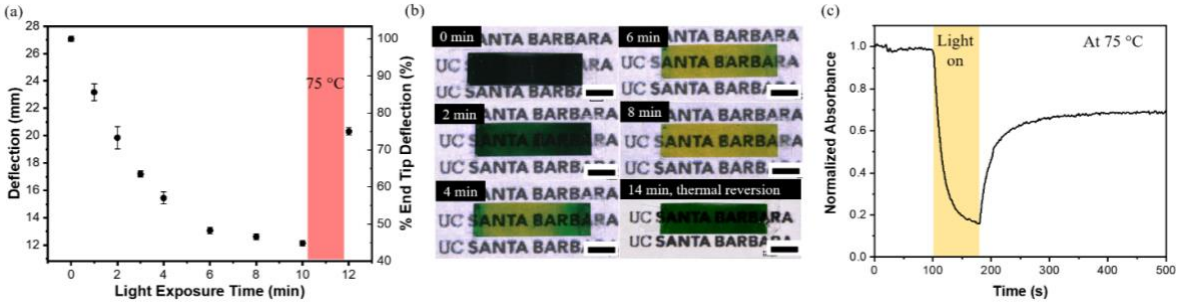

Figure 3.12 Actuation recovery of DASA–PHMA/PI bilayer cantilever. (a) End tip deflection for the cantilever as a function of light exposure time and a thermally recovered cantilever. (b) Optical images that show color change of the cantilever at each light exposure time. (c) Normalized absorbance change at λ_{max} for DASA–PHMA thin film before, during and after illumination light; here sample was maintained at 75 °C throughout the measurement.

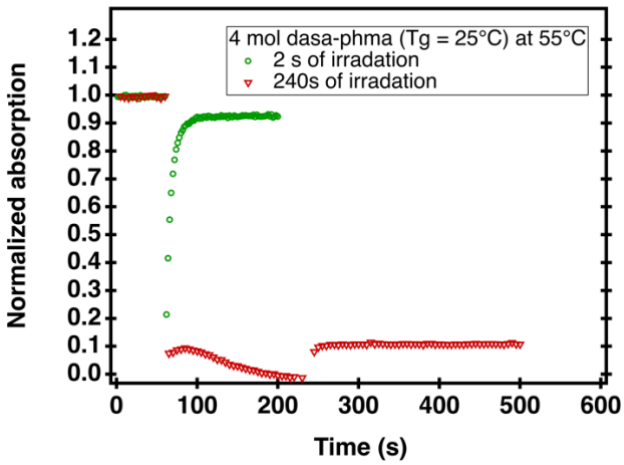

Figure 3.13 4 mol % DASA-PHMA (T_g = 23 °) has >90% recovery at 55 °C, compared to only ~70% at 35 °C.

3.8. Conclusion

A modular synthetic strategy using Diels–Alder click chemistry was exploited to enable chemical incorporation of DASA into a load-bearing PHMA matrix. Cantilevers generated from this material demonstrate photochemically-encoded tunable actuation as a result of the heat generated through their molecular absorbance. The photothermal actuation capabilities of DASA–PHMA were demonstrated by a cantilever lifting up to 13 times its weight under illumination, as well as a centimeter-scale remote-controlled crawler powered by robust light-activated bending. The negatively photochromic nature of DASA opens new possibilities for developing programmed actuators, “inching” the field toward smart soft robotics systems using broadband visible light.

3.9. References

(1) Lee, J.; Sroda, M. M.; Kwon, Y.; El-Arid, S.; Seshadri, S.; Gockowski, L. F.; Hawkes, E. W.; Valentine, M. T.; Read De Alaniz, J. Tunable Photothermal

Actuation Enabled by Photoswitching of Donor-Acceptor Stenhouse Adducts. *ACS Appl. Mater. Interfaces* **2020**, *12*, 54075–54082.

(2) Helmy, S.; Leibfarth, F. A.; Oh, S.; Poelma, J. E.; Hawker, C. J.; Read de Alaniz, J., Photoswitching Using Visible Light: A New Class of Organic Photochromic Molecules. *J. Am. Chem. Soc.* **2014,** *136*, 8169-8172.

(3) Helmy, S.; Oh, S.; Leibfarth, F. A.; Hawker, C. J.; Read de Alaniz, J., Design and Synthesis of Donor–Acceptor Stenhouse Adducts: A visible Light Photoswitch Derived from Furfural. *J. Org. Chem.* **2014,** *79*, 11316-11329.

(4) Lerch, M. M.; Szymański, W.; Feringa, B. L., The (Photo)Chemistry of Stenhouse Photoswitches: Guiding Principles and System Design. *Chem. Soc. Rev.* **2018,** *47*, 1910-1937.

(5) Han, B.; Zhang, Y.-L.; Chen, Q.-D.; Sun, H.-B., Carbon-Based Photothermal Actuators. *Adv. Funct. Mater.* **2018,** *28*, 1802235.

(6) Hemmer, J. R.; Poelma, S. O.; Treat, N.; Page, Z. A.; Dolinski, N. D.; Diaz, Y. J.; Tomlinson, W.; Clark, K. D.; Hooper, J. P.; Hawker, C.; Read de Alaniz, J., Tunable Visible and near Infrared Photoswitches. *J. Am. Chem. Soc.* **2016,** *138*, 13960-13966.

(7) Ulrich, S.; Hemmer, J. R.; Page, Z. A.; Dolinski, N. D.; Rifaie-Graham, O.; Bruns, N.; Hawker, C. J.; Boesel, L. F.; Read de Alaniz, J., Visible Light-Responsive Dasa-Polymer Conjugates. *ACS Macro Lett.* **2017,** *6*, 738-742.

(8) Hemmer, J. R.; Page, Z. A.; Clark, K. D.; Stricker, F.; Dolinski, N. D.; Hawker, C. J.; Read de Alaniz, J., Controlling Dark Equilibria and Enhancing Donor–Acceptor Stenhouse Adduct Photoswitching Properties through Carbon Acid Design. *J. Am. Chem. Soc.* **2018,** *140*, 10425-10429.

(9) Seshadri, S.; Gockowski, L. F.; Lee, J.; Sroda, M.; Helgeson, M. E.; Read de Alaniz, J.; Valentine, M. T., Self-Regulating Photochemical Rayleigh-Bénard Convection Using a Highly-Absorbing Organic Photoswitch. *Nat. Commun.* **2020,** *11*, 2599.

(10) Powell, A. W.; Stavrinadis, A.; Christodoulou, S.; Quidant, R.; Konstantatos, G., On-Demand Activation of Photochromic Nanoheaters for High Color Purity 3D Printing. Nano Lett. **2020,** *20*, 3485-3491.

(11) St. Amant, A. H.; Discekici, E. H.; Bailey, S. J.; Zayas, M. S.; Song, J.-A.; Shankel, S. L.; Nguyen, S. N.; Bates, M. W.; Anastasaki, A.; Hawker, C. J.; Read de Alaniz, J., Norbornadienes: Robust and Scalable Building Blocks for Cascade "Click" Coupling of High Molecular Weight Polymers. *J. Am. Chem. Soc.* **2019,** *141*, 13619-13624.

(12) Chen, Q.; Diaz, Y. J.; Hawker, M. C.; Martinez, M. R.; Page, Z. A.; Xiao-An Zhang, S.; Hawker, C. J.; Read de Alaniz, J., Stable Activated Furan and Donor–Acceptor Stenhouse Adduct Polymer Conjugates as Chemical and Thermal Sensors. *Macromolecules* **2019,** *52*, 4370-4375.

(13) Sinawang, G.; Wu, B.; Wang, J.; Li, S.; He, Y., Polystyrene Based Visible Light Responsive Polymer with Donor–Acceptor Stenhouse Adduct Pendants. *Macromol. Chem. Phys.* **2016,** *217*, 2409-2414.

(14) Yap, J. E.; Mallo, N.; Thomas, D. S.; Beves, J. E.; Stenzel, M. H., Comparing Photoswitching of Acrylate or Methacrylate Polymers Conjugated with Donor–Acceptor Stenhouse Adducts. *Polym. Chem.* **2019,** *10*, 6515-6522.

(15) Priimagi, A.; Cattaneo, S.; Ras, R. H. A.; Valkama, S.; Ikkala, O.; Kauranen, M., Polymer−Dye Complexes: A Facile Method for High Doping Level and Aggregation Control of Dye Molecules. *Chem. Mater.* **2005,** *17*, 5798-5802.

(16) Kaczmarek, H.; Kamińska, A.; van Herk, A., Photooxidative Degradation of Poly(Alkyl Methacrylate)S. *Eur. Polym. J.* **2000,** *36*, 767-777.

(17) Child, W. C.; Ferry, J. D., Dynamic Mechanical Properties of Poly-N-Hexyl Methacrylate. *J. Colloid Sci.* **1957,** *12*, 389-399.

(18) Lui, B. F.; Tierce, N. T.; Tong, F.; Sroda, M. M.; Lu, H.; Read de Alaniz, J.; Bardeen, C. J., Unusual Concentration Dependence of the Photoisomerization Reaction in Donor–Acceptor Stenhouse Adducts. *Photochem. Photobiol. Sci.* **2019,** *18*, 1587-1595.

(19) Yakacki, C. M.; Saed, M.; Nair, D. P.; Gong, T.; Reed, S. M.; Bowman, C. N., Tailorable and Programmable Liquid-Crystalline Elastomers Using a Two-Stage Thiol–Acrylate Reaction. *RSC Adv.* **2015,** *5*, 18997-19001.

(20) White, T. J., Photomechanical Effects in Liquid Crystalline Polymer Networks and Elastomers. *J. Polym. Sci., Part B: Polym. Phys.* **2018,** *56*, 695-705.

(21) Timoshenko, S., Analysis of Bi-Metal Thermostats. *J. Opt. Soc. Am.* **1925,** *11*, 233-255.

3.10. Experimental section

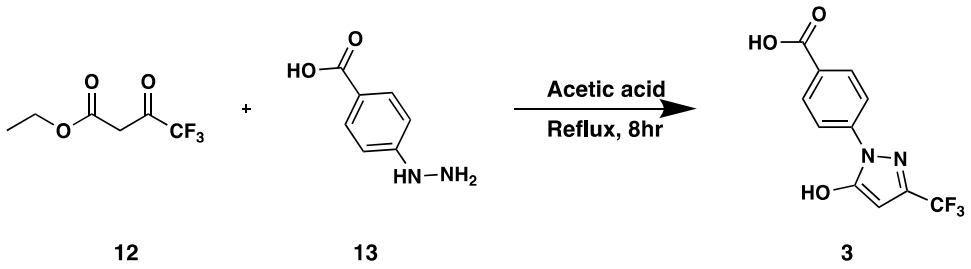

12 13 3

Scheme 3.2 4-(5-oxo-3-(trifluoromethyl)-4,5-dihydro-1*H*-pyrazol-1-yl)benzoic acid (**3**):

4-hydrazineylbenzoic acid **13** (15.20 g, 100.00 mmol, 1 equiv), acetic acid (100 mL), and ethyl 4,4,4-trifluoro-3-oxobutanoate **12** (18.40 g, 100.00 mmol, 1 equiv) were refluxed at 125 °C for 8 hrs. A crystalline material precipitated out and the reaction was cooled to room temperature, filtered, and washed with Et2O to **3** (17.92 g, 65.84 mmol, 66%) as an off-white crystalline solid. ^{1}H NMR indicated that the product favors the enol isomer. Spectral data matched that of reported literature.

3: ^{1}H NMR (500 MHz, DMSO-d_6) δ 12.93 (s, 2H), 8.12 – 8.03 (d, 1H), 7.91 (d, 2H), 5.97 (s, 1H). ^{13}C NMR (125 MHz, DMSO-d_6) δ 166.7, 154.5, 141.3, 130.5, 129.0, 121.3, 86.1. HRMS (ESI), calculated for $C_{11}H_6F_3N_2O_3^-$ (M-H)$^-$: 271.0336, observed 271.0331.

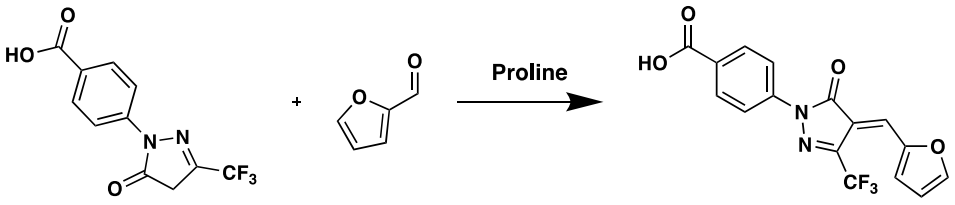

3 14 4

Scheme 3.3 (*E*)-4-(4-(furan-2-ylmethylene)-5-oxo-3-(trifluoromethyl)-4,5-dihydro-1*H*-pyrazol-1-yl)benzoic acid (**4**):

3 (6.00 g, 22.04 mmol, 1 equiv), distilled furfural **14** (12 mL, 10.34 g, 107.66 mmol, 4.88 equiv) and proline (600 mg, 5.21 mmol, 0.24 equiv) were combined in 12 mL of DCM. This was then left to stir 2-3 days and monitored by TLC (100% ethyl acetate) and checked by H^1 NMR for consumption of 3. Once the starting material was consumed, the reaction was filtered via vacuum filtration. The crude product was washed with DCM to afford 4 (5.65 g, 16.13 mmol, 73%) as a dark orange powder. This was used without further purification.

4: ^{1}H NMR (600 MHz, DMSO-d_6) δ 12.96 (s, 1H), 8.77 (d, J = 3.8 Hz, 1H), 8.45 (d, J = 1.6 Hz, 1H), 8.07 – 8.04 (m, 2H), 8.01 (dt, J = 6.6, 2.1 Hz, 2H), 7.76 (s, 1H), 7.06 (dd, J = 4.1, 1.6 Hz, 1H). IR (thin film) 3138, 2960, 2815, 2661, 2542, 1804, 1706, 1678, 1601, 1281, 1109, 975, 770 cm^{-1}. HRMS (ESI), calculated for $C_{16}H_8F_3N_2O_4^-$ (M-H)$^-$: 349.0442, observed 349.0436.

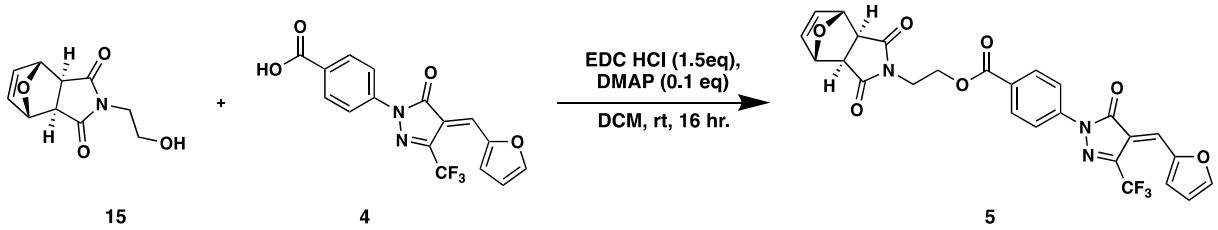

15 4 5

Scheme 3.4 2-((3a*R*,4*S*,7*R*,7a*S*)-1,3-dioxo-1,3,3a,4,7,7a-hexahydro-2*H*-4,7-epoxyisoindol-2-yl)ethyl 4-((*E*)-4-(furan-2-ylmethylene)-5-oxo-3-(trifluoromethyl)-4,5-dihydro-1*H*-pyrazol-1-yl)benzoate (**5**):

4 (1.28 g, 3.65 mmol, 1 equiv), **15** (1.85 g, 8.84 mmol, 2.42 equiv), EDC·HCl (859 mg, 4.48 mmol, 1.23 equiv), and dimethylaminopyridine (DMAP, 25 mg, 0.20 mmol, 0.05 equiv) were suspended in DCM (25 mL). The reaction was capped under an atmosphere of air and stirred at room temperature for 16 hrs or until **4** was consumed by TLC. The reaction was poured into an aqueous solution of HCl (1 M, 20 mL x3). This organic solution was then washed with

brine once. Organic layer was then dried over magnesium sulfate and solvent was removed under reduced pressure to obtain an orange solid. The product was further purified by column chromatography utilizing a mobile phase of Ethyl acetate: Hexanes (3:1) to yield a solid orange product **5** (1.04 g, 1.92 mmol, 53% yield).

5: ^{1}H NMR (500 MHz, Chloroform-*d*) δ 8.90 (d, *J* = 3.8 Hz, 1H), 8.16 – 7.98 (m, 4H), 7.89 (d, *J* = 1.2 Hz, 1H), 7.69 (s, 1H), 6.81 (d, *J* = 3.8 Hz, 1H), 6.49 (s, 2H), 5.24 (s, 2H), 4.45 (t, *J* = 5.3 Hz, 2H), 3.91 (t, *J* = 5.3 Hz, 2H), 2.87 (s, 2H). ^{13}C NMR (125 MHz, Chloroform-*d*) δ 176.1, 165.7, 161.6, 151.2, 150.8, 141.7, 136.7, 132.1, 130.9, 128.6, 126.8, 118.5, 115.9, 115.4, 81.1, 64.6, 61.4, 47.6, 37.9. IR (thin film) 3140, 3114, 2327, 2050, 1807, 1772, 1698, 1601, 1447, 1271, 1123, 1095, 976, 765.

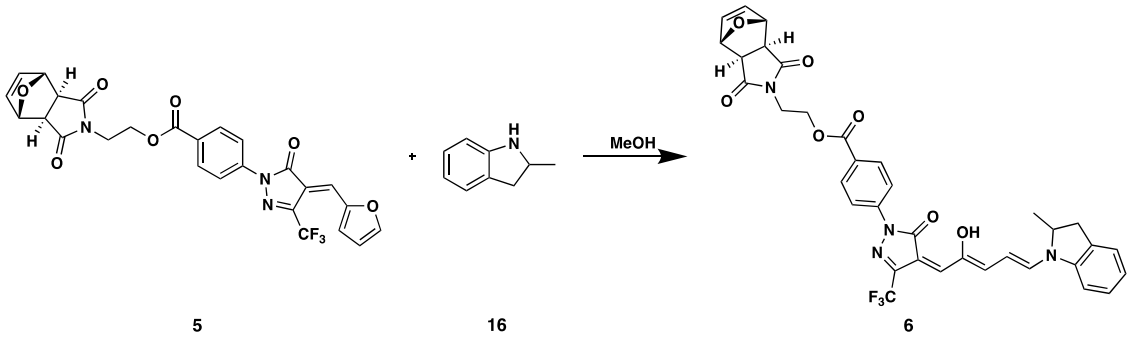

Scheme 3.5 2-((3a*R*,4*S*,7*R*,7a*S*)-1,3-dioxo-1,3,3a,4,7,7a-hexahydro-2*H*-4,7-epoxyisoindol-2-yl)ethyl 4-((*E*)-4-(furan-2-ylmethylene)-5-oxo-3-(trifluoromethyl)-4,5-dihydro-1*H*-pyrazol-1-yl)benzoate (**6**):

The furan adduct **5** (1.00 g, 1.85 mmol, 1 equiv) was stirred in minimal methanol (approximately 10mL) then 2-methylindoline **16** (492 mg, 3.69 mmol, 2 equiv) was added. The reaction was stirred for 4 h and monitored by TLC for consumption of **5**. The reaction

mixture was then filtered to yield the product as green crystals and washed with ether to afford the product **6** (655 mg, 0.97 mmol, 52%).

6: ^{1}H NMR (500 MHz, Chloroform-*d*) δ 12.92 (s, 1H), 8.25 – 7.89 (m, 4H), 7.69 (d, *J* = 12.6 Hz, 1H), 7.31 (d, *J* = 7.4 Hz, 2H), 7.18 (t, *J* = 7.4 Hz, 1H), 7.10 (d, *J* = 7.8 Hz, 1H), 6.76 (d, *J* = 12.3 Hz, 1H), 6.57 (s, 1H), 6.50 (s, 2H), 5.25 (s, 2H), 4.81 – 4.64 (m, 1H), 4.45 (t, *J* = 5.3 Hz, 2H), 3.91 (t, *J* = 5.3 Hz, 2H), 3.55 (dd, *J* = 16.1, 8.7 Hz, 1H), 2.87-2.84 (m, 3H), 1.47 (d, *J* = 6.5 Hz, 3H). ^{13}C NMR (125 MHz, Chloroform-*d*) δ 176.0, 165.9, 164.8, 150.7, 147.2, 143.6, 142.5, 140.7, 136.5, 133.1, 131.9, 130.6, 128.6, 126.6, 126.5, 126.2, 119.1, 106.9, 106.1, 80.9, 61.2, 57.8, 47.5, 37.8, 36.3, 19.8. IR (thin film) 2947, 1705, 1603, 1559, 1460, 1442, 1357, 1270, 1208, 1153, 1108, 986, 948, 717. HRMS (ESI), calculated for $C_{35}H_{29}F_3N_4NaO_7^+$: ($M+Na^+$) 697.1881, observed 697.1886.

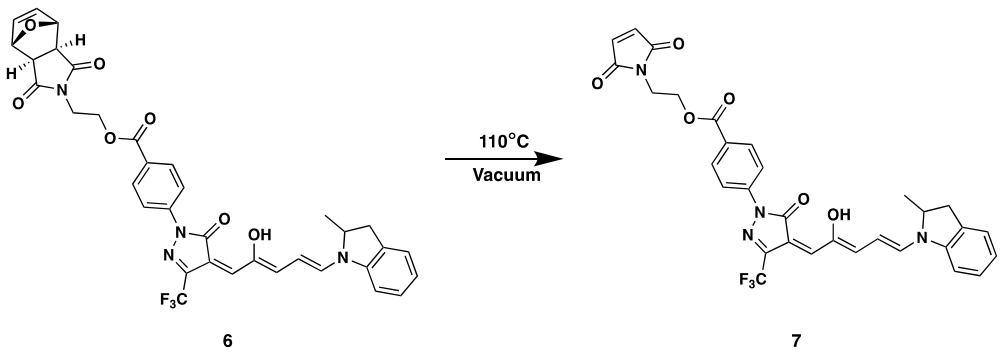

Scheme 3.6 2-(2,5-dioxo-2,5-dihydro-1*H*-pyrrol-1-yl)ethyl 4-((*Z*)-4-((2*Z*,4*E*)-2-hydroxy-5-(2-methylindolin-1-yl)penta-2,4-dien-1-ylidene)-5-oxo-3-(trifluoromethyl)-4,5-dihydro-1*H*-pyrazol-1-yl)benzoate (**7**):

6 (655 mg, 0.97 mmol) was collected in a vial and put under vacuum and heated to 110 °C for 36 hrs. The reaction was monitored by ^{1}H NMR for full deprotection of the maleimide **7** (582 mg, 0.96 mmol, 99%).

7: ^{1}H NMR (500 MHz, Chloroform-*d*) δ 12.88 (s, 1H), 8.02 (dd, *J* = 48.3, 8.8 Hz, 4H), 7.67 (d, *J* = 12.5 Hz, 1H), 7.26 (d, *J* = 14.5 Hz, 2H), 7.14 (t, *J* = 7.4 Hz, 1H), 7.04 (d, *J* = 7.8 Hz, 1H), 6.80 – 6.66 (m, 3H), 6.52 (s, 1H), 6.41 (t, *J* = 12.4 Hz, 1H), 4.81 – 4.63 (m, 1H), 4.44 (t, *J* = 5.3 Hz, 2H), 3.95 (t, *J* = 5.3 Hz, 2H), 3.53 (dd, *J* = 16.1, 8.7 Hz, 1H), 2.82 (d, *J* = 16.0 Hz, 1H), 1.44 (d, *J* = 6.5 Hz, 3H). ^{13}C NMR (125 MHz, Chloroform-*d*) δ 170.4, 165.9, 164.7, 150.5, 147.8, 144.1, 142.6, 140.8, 140.5, 134.3, 132.3, 132.0, 130.6, 128.6, 126.7, 126.6, 125.9, 121.9, 119.7, 119.0, 110.7, 106.4, 81.0, 62.0, 57.9, 47.5, 36.9, 36.2, 29.7, 19.8. IR (thin film) 3072, 3054, 2928, 1772, 1705, 1601, 1556, 1453, 1355, 1266, 1206, 1091, 984, 947, 824, 690, 562. HRMS (ESI), calculated for $C_{31}H_{25}F_3N_4NaO_6$+ ($M+Na^+$) 629.1618, observed 629.1624.

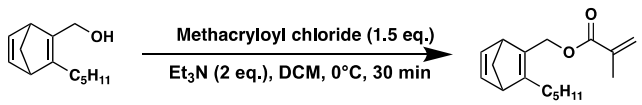

8 9

Scheme 3.7 (3-pentylbicyclo[2.2.1]hepta-2,5-dien-2-yl)methyl methacrylate (**9**):

A solution of **8** (3.94 g, 20.49 mmol, 1 equiv) and Et_3N (4.51 g, 40.98 mmol, 2 equiv) in DCM (100 mL) was cooled to 0 °C. Methacryloyl chloride (3.21 g, 30.74 mmol, 1.5 equiv) was added dropwise and the solution maintained at 0 °C until complete consumption of the starting material (TLC, 30-1 h min). The reaction was quenched with water (0.1 mL) and allowed to warm to rt. Silica gel (1 g) was added, the solvent removed, and the mixture was subjected to flash column chromatography (Hexane:EtOAc, 15:1). The fractions containing product were combined, several drops of an inhibitor solution (MEHQ, 1 mg/mL in DCM) were added, and the solvent removed to yield racemic **9** (2.77 g, 10.64 mmol, 52%) as a clear and colorless oil.

9: ^{1}H NMR (400 MHz, $CDCl_3$) δ 6.79 - 6.74 (m, 1H), 6.74 - 6.69 (m, 1H), 6.09 (s, 1 H), 5.55 (d, *J* = 1.2 Hz, 1H), 4.79 (d, *J* = 12.1 Hz, 1H), 4.66 (d, *J* = 12.5 Hz, 1H), 3.48 (br. s., 1H), 3.38 (br. s., 1H), 2.30 - 2.12 (m, 2H), 2.01 - 1.86 (m, 5H), 1.47 - 1.23 (m, 4 H), 1.23 - 1.12 (m, 2H). ^{13}C NMR (100 MHz, $CDCl_3$) δ 167.5, 155.2, 142.9, 141.9, 141.0, 136.5, 125.2, 71.3, 60.9, 53.8, 52.2, 31.3, 28.3, 26.8, 22.5, 18.4, 14.0. IR (thin film) 2961, 2930, 2864, 1716, 1638, 1453, 1293, 1157, 1010, 937, 814. HRMS (ESI), calculated for $C_{17}H_{24}NaO_2^+$ $(M+Na)^+$ 283.1669, observed 283.1671.

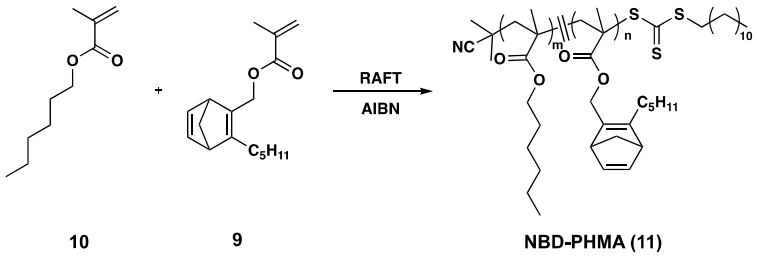

Scheme 3.8 NBD-PHMA (**11**)

NBD–PHMA (11): To a round bottom flask equipped with a magnetic stir bar and septum cap, compound **9** (2.00 g, 7.69 mmol, 35 equiv) and hexyl methacrylate **10** (12.2 g, 71.55 mmol, 270 equiv, HMA, **7**) were added and dissolved in THF (14.2 mL). At this time, AIBN (9 mg, 0.053 mmol, 0.2 equiv) and 2-cyano-2-propyl dodecyl trithiocarbonate (88.32 mg, 0.265 mmol, 1.0 equiv) were added to the reaction vial and the polymerization was degassed by nitrogen bubbling for 10 minutes. The polymerization was left to react at 60 °C and a crude ^{1}H NMR spectrum was taken in deuterated chloroform to estimate monomer conversion (70%). The THF was removed under reduced pressure and the crude mixture was redissolved in a minimal amount of DCM. The mixture was precipitated into cold methanol. The solid was redissolved in DCM and the precipitation process was repeated a total of 3-4 times. ^{1}H

NMR analysis indicates approximately 10% of the desired NBD functionality. Conversion 70%, $M_{n(theoretical)}$ = 38,000 g/mol, $M_{n(NMR)}$ = 28,000 g/mol, $M_{n(SEC)}$ = 16,000 g/mol, $Đ$ = 1.31.

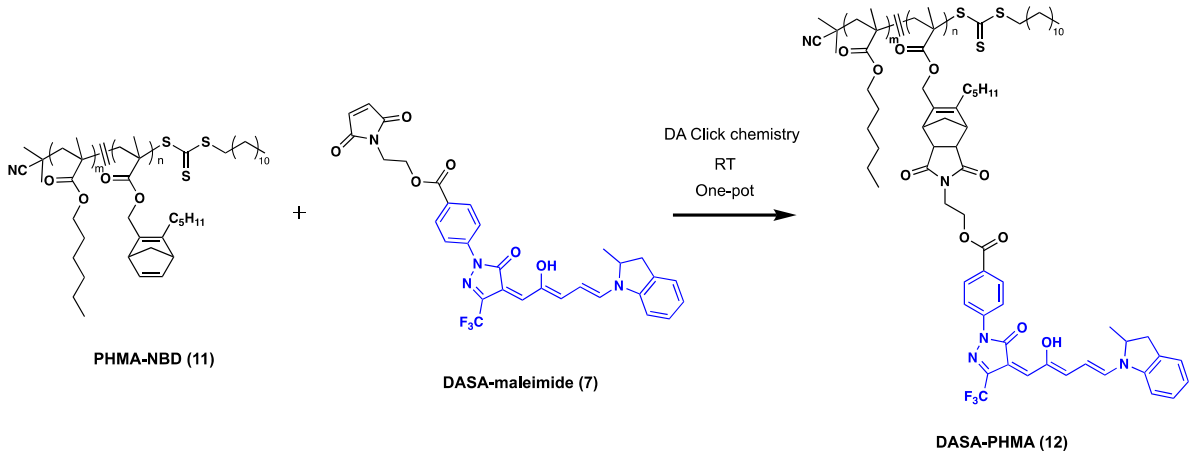

Scheme 3.9 DASA-PHMA (**12**)

DASA–PHMA (12): NBD–PHMA (11) (1.0 g, 0.0260 mmol, 1 equiv) and 3,6-di-2-pyridyl-1,2,4,5-tetrazine (153 mg, 0.649 mmol, 25 equiv, DpTz) were combined in $CDCl_3$ (100 mg/mL, 10 mL) under nitrogen atmosphere. The solution was stirred at rt for 5 h and complete conversion of NBD to cyclopentadiene was monitored by ^{1}H NMR. Upon completion, norbornylene (61 mg, 0.649 mmol, 25 equiv) was added to quench the excess DpTz. The solution goes from a pink to yellow color upon completion. To this, DASA–maleimide **7** (267 mg, 0.442 mmol, 17 equiv) was added. The reaction was left to stir for 15 h. The DCM was removed under reduced pressure and the crude mixture was redissolved in a minimal amount of DCM. The mixture was precipitated into cold methanol. The solid was redissolved in DCM and the precipitation process was repeated a total of 3-4 times. ^{1}H NMR analysis indicated successful incorporation of 10% of desired DASA functionality. ^{1}H NMR (600 MHz, $CDCl_3$) δ/ppm: 8.26-7.87 (4H, phenyl peaks), 4.05-3.85 (2H, polymer backbone). $M_{n(theoretical)}$ = 33,000 g/mol, $M_{n(NMR)}$ = 38,000 g/mol. T_g(DSC) = 45.3 °C.

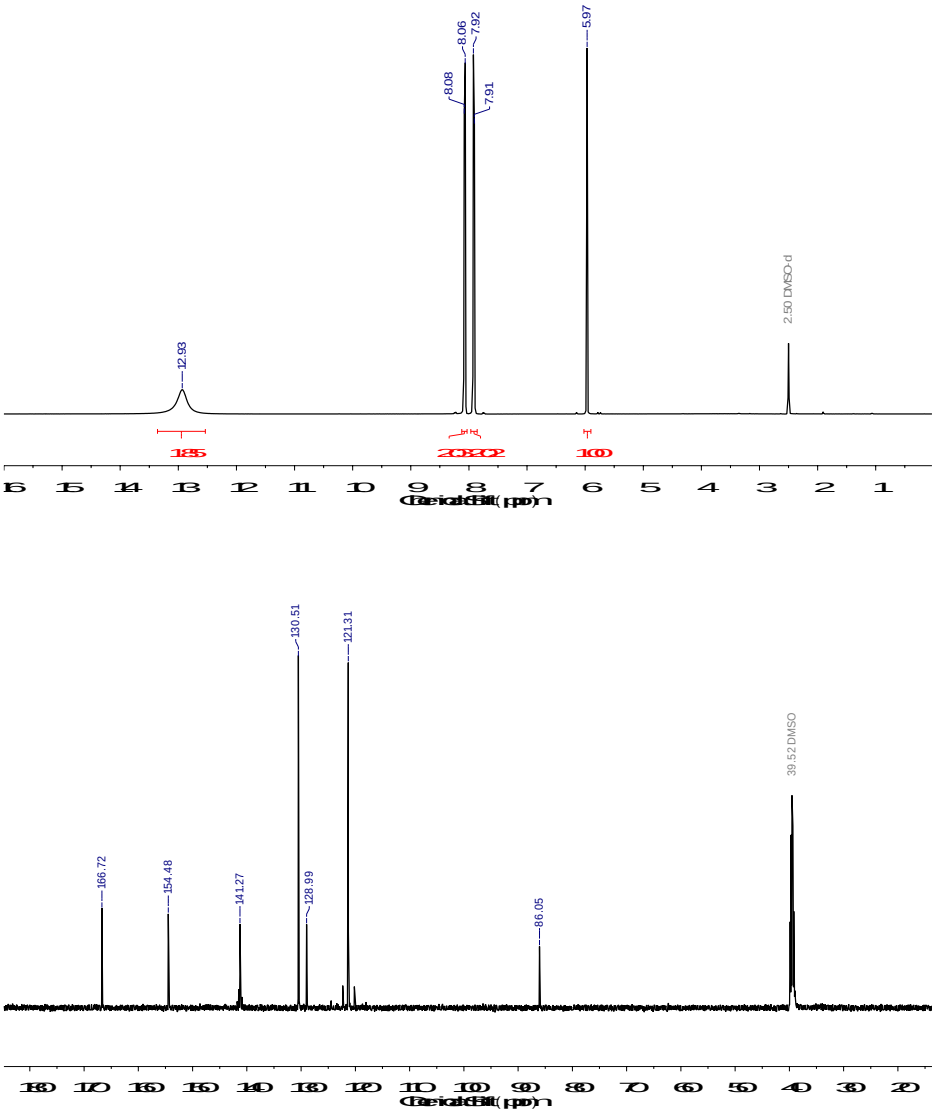

Scheme 3.10 ^{1}H NMR (top) and ^{13}C NMR (bottom) of **3** in DMSO-d.

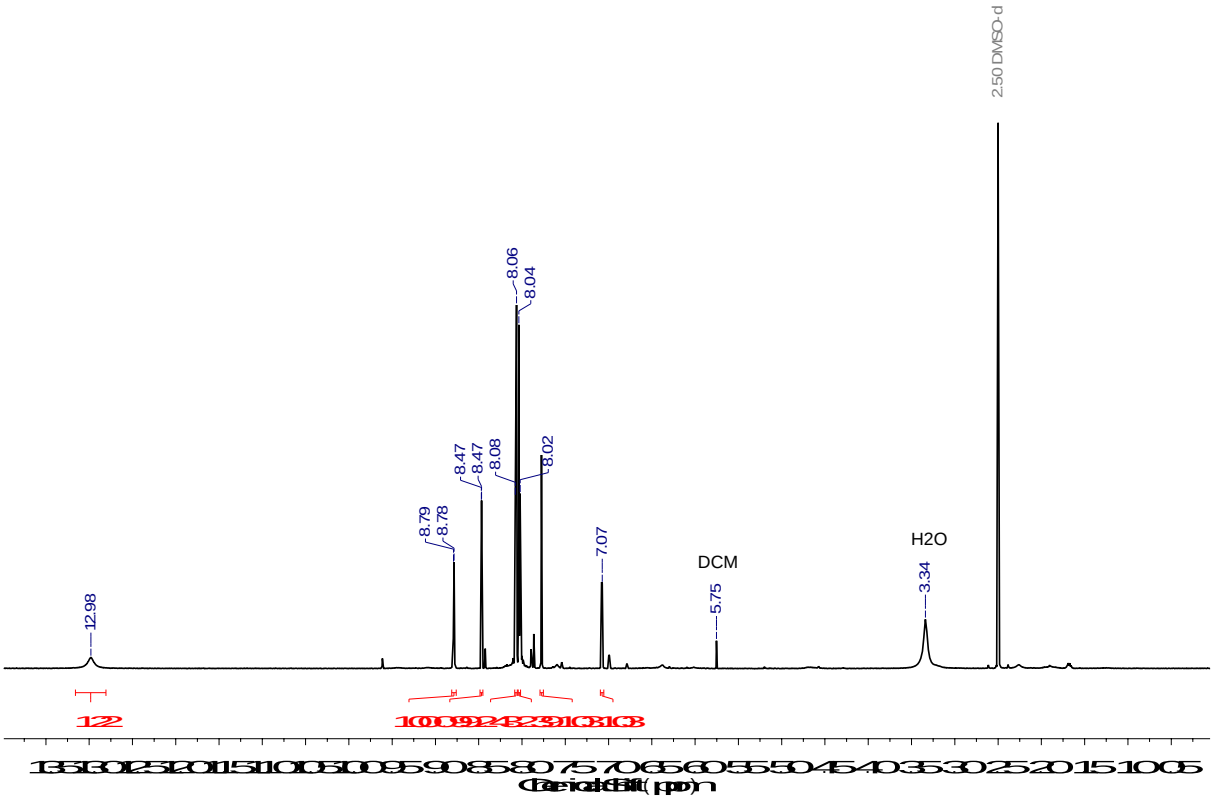

Scheme 3.11 ^{1}H NMR of **4** in DMSO-d.

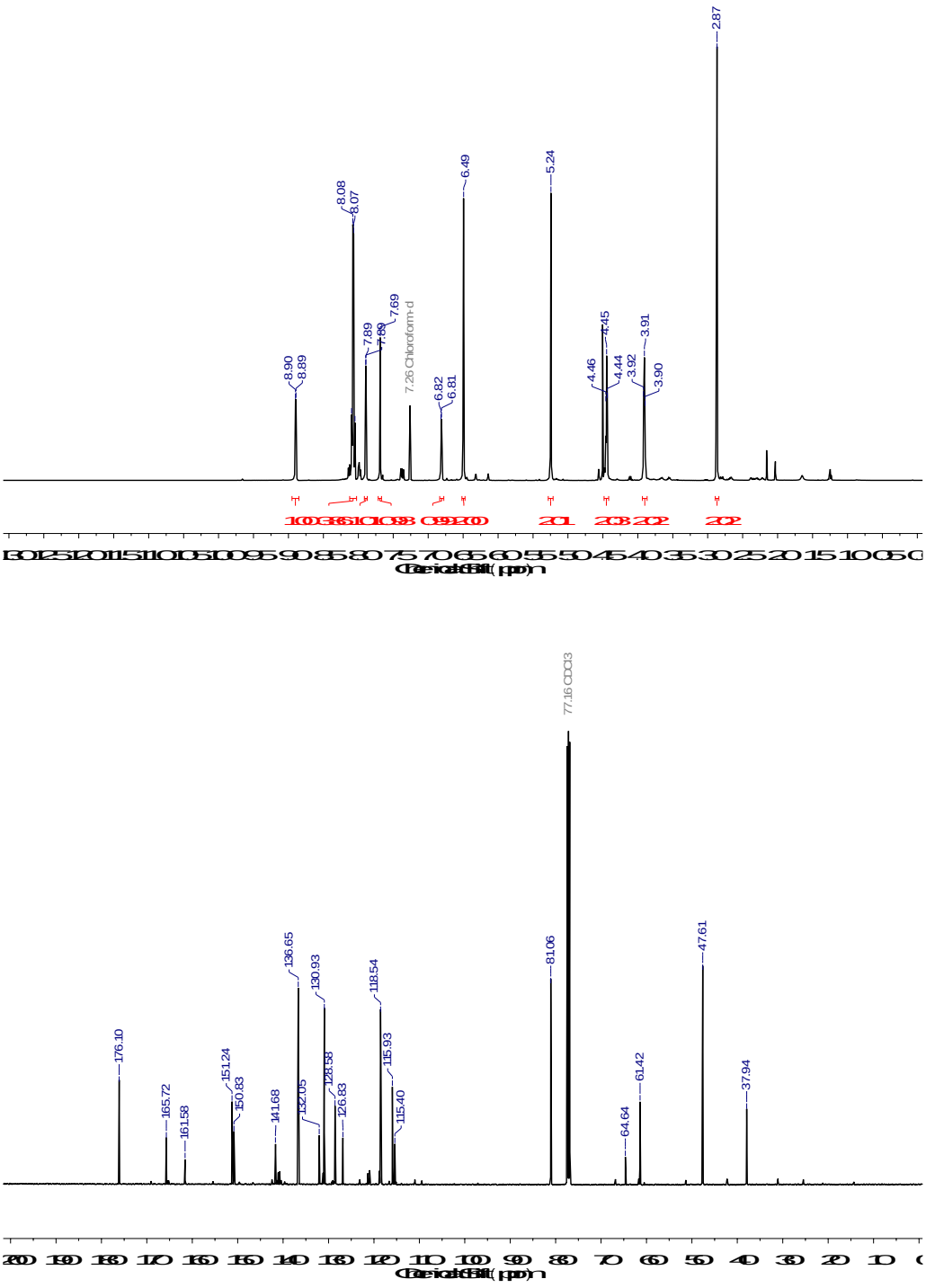

Scheme 3.12 ^{1}H NMR (top) and ^{13}C NMR (bottom) of **5** in Chloroform-d.

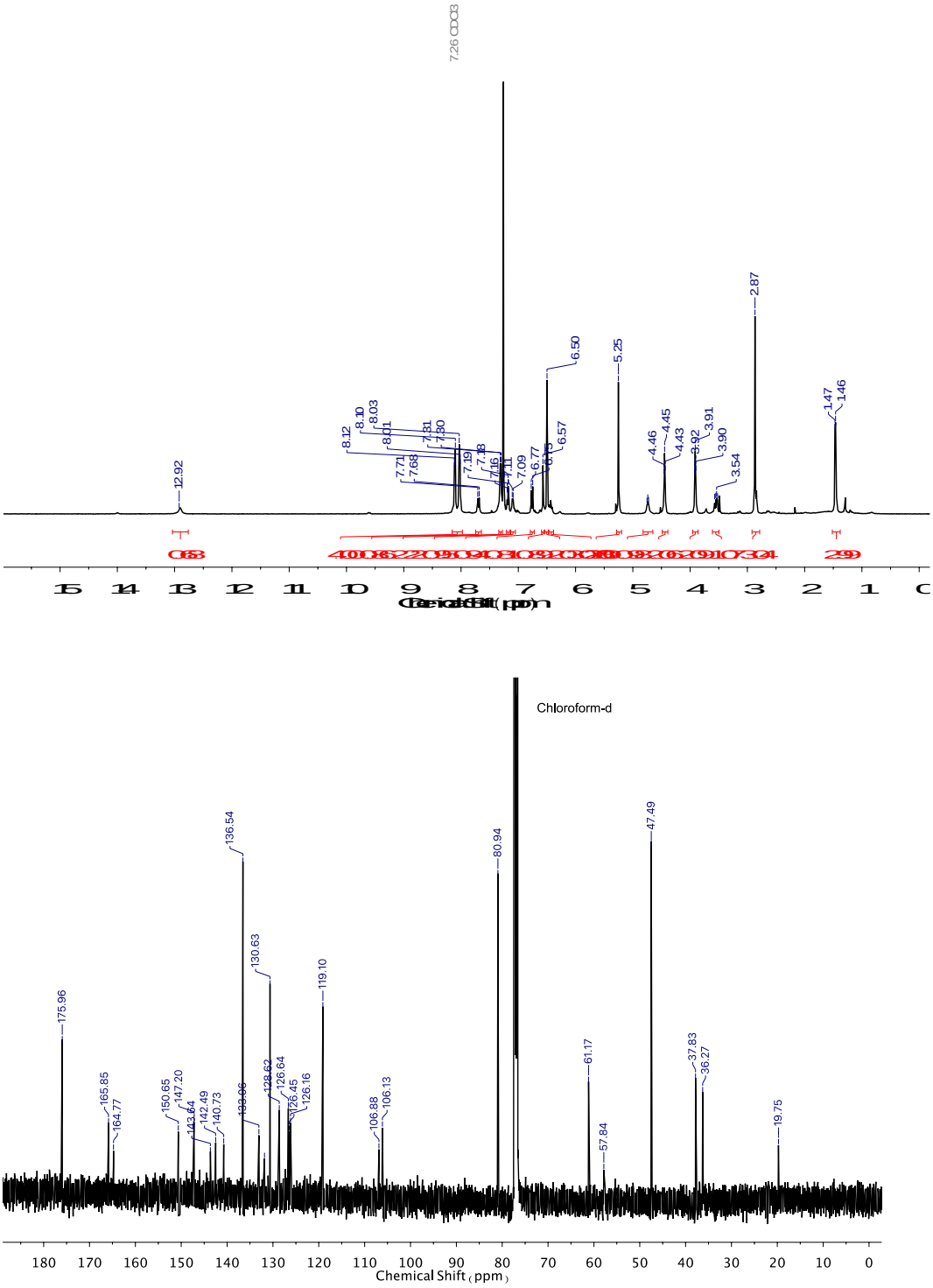

Scheme 3.13 ^{1}H NMR (top) and ^{13}C NMR (bottom) of **6** in Chloroform-d.

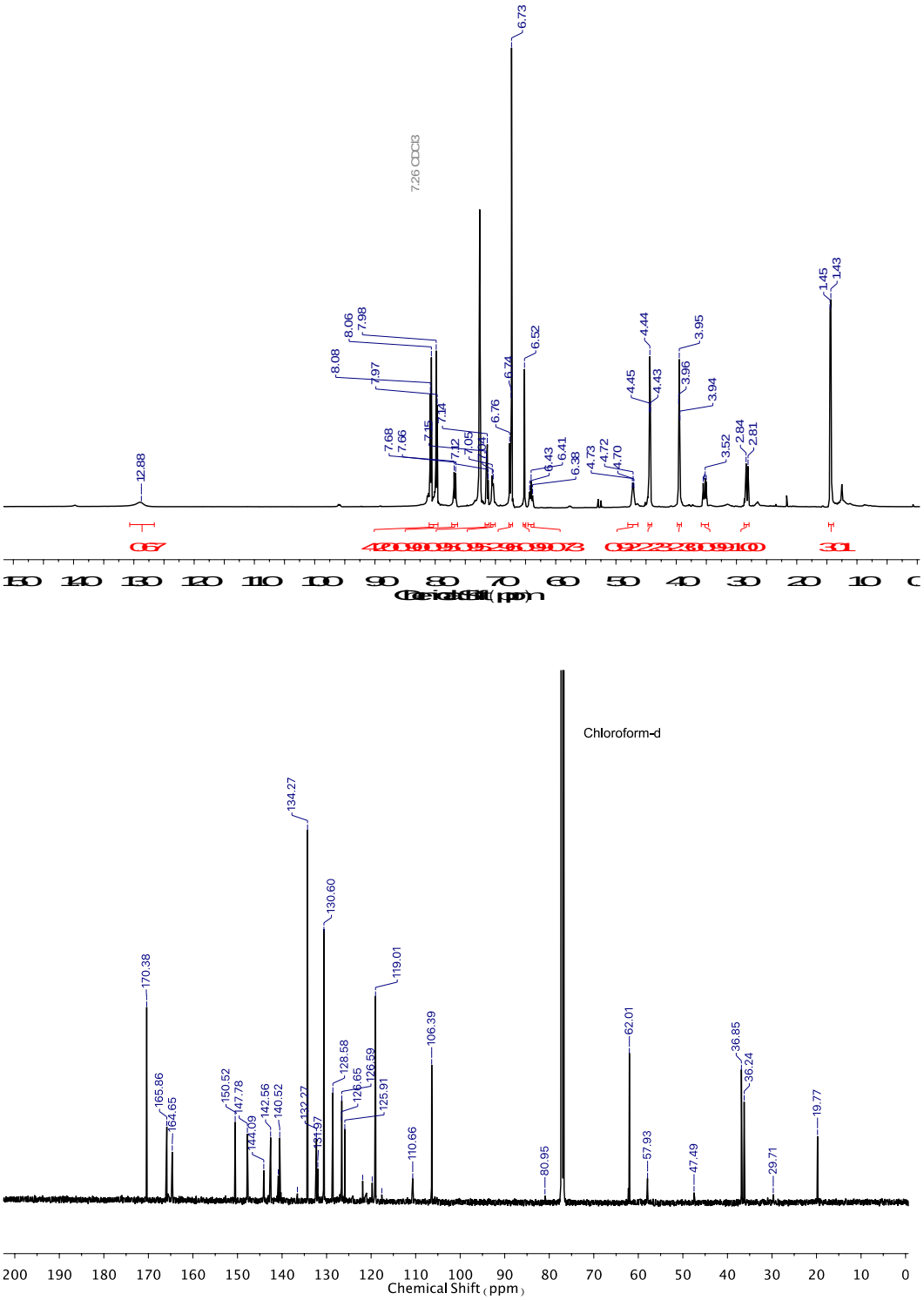

Scheme 3.14 ^{1}H NMR (top) ^{13}C NMR (bottom) of **7** in Chloroform-d.

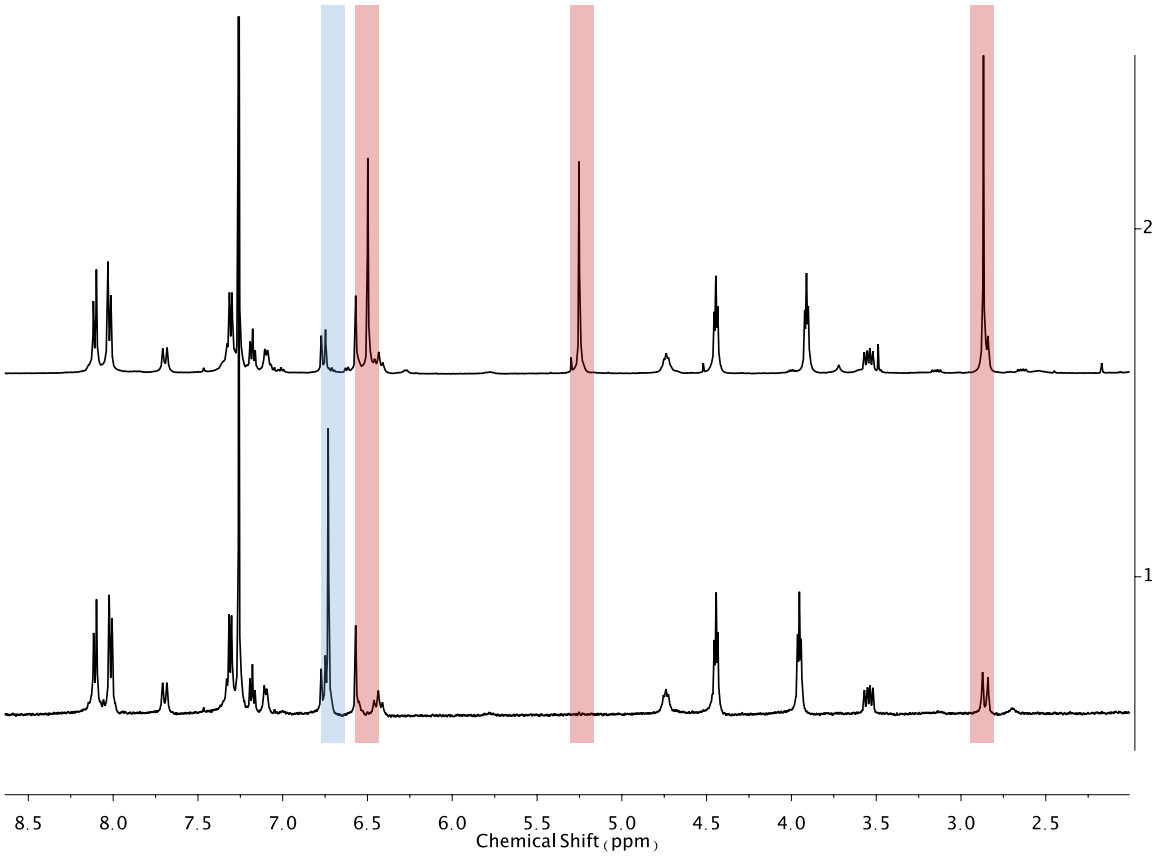

Scheme 3.15 ^{1}H NMR of deprotection of **6** (top) to **7** (bottom) in Chloroform-d.

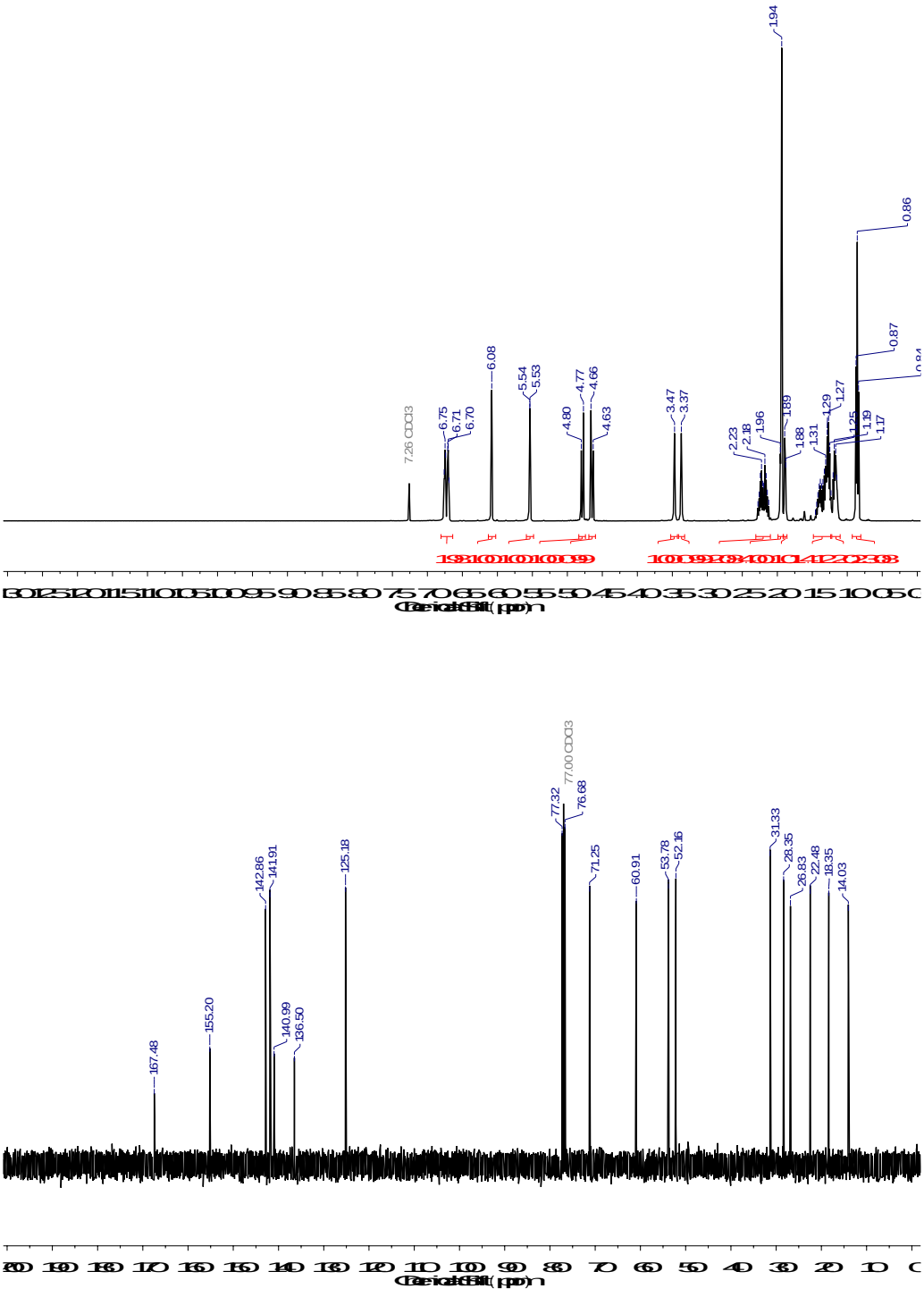

Scheme 3.16 ^{1}H NMR (top) and ^{13}C NMR (bottom) of **9** in Chloroform-d.

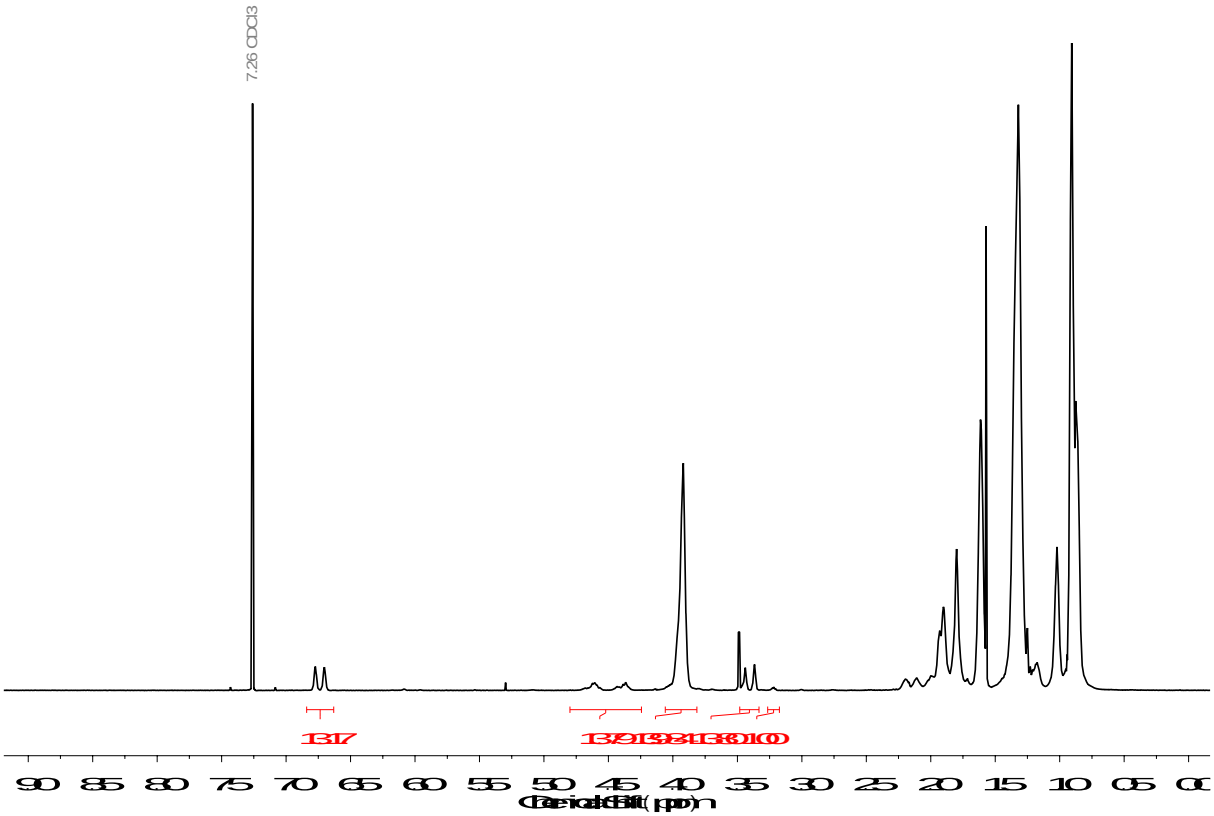

Scheme 3.17 ^{1}H NMR of spectrum of **11** in chloroform-d.

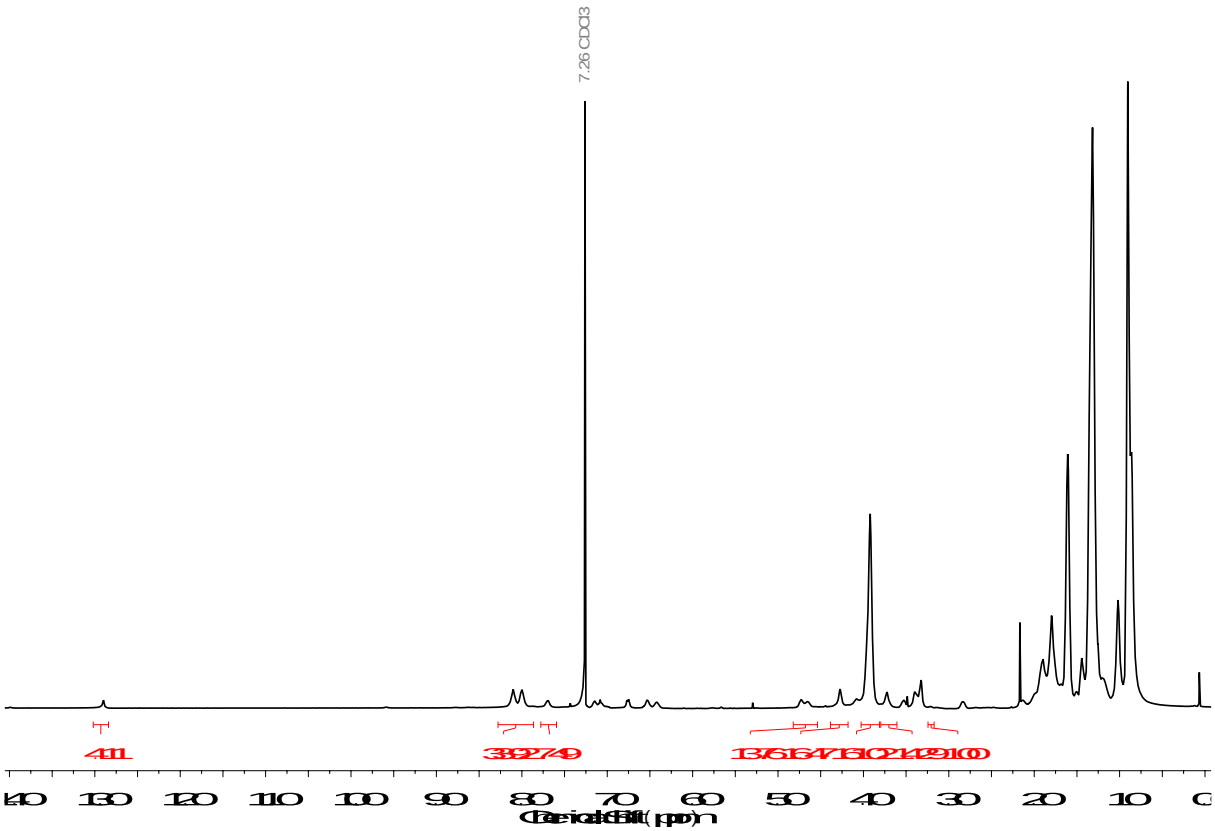

Scheme 3.18 ^{1}H NMR of spectrum of **12** in chloroform-d.

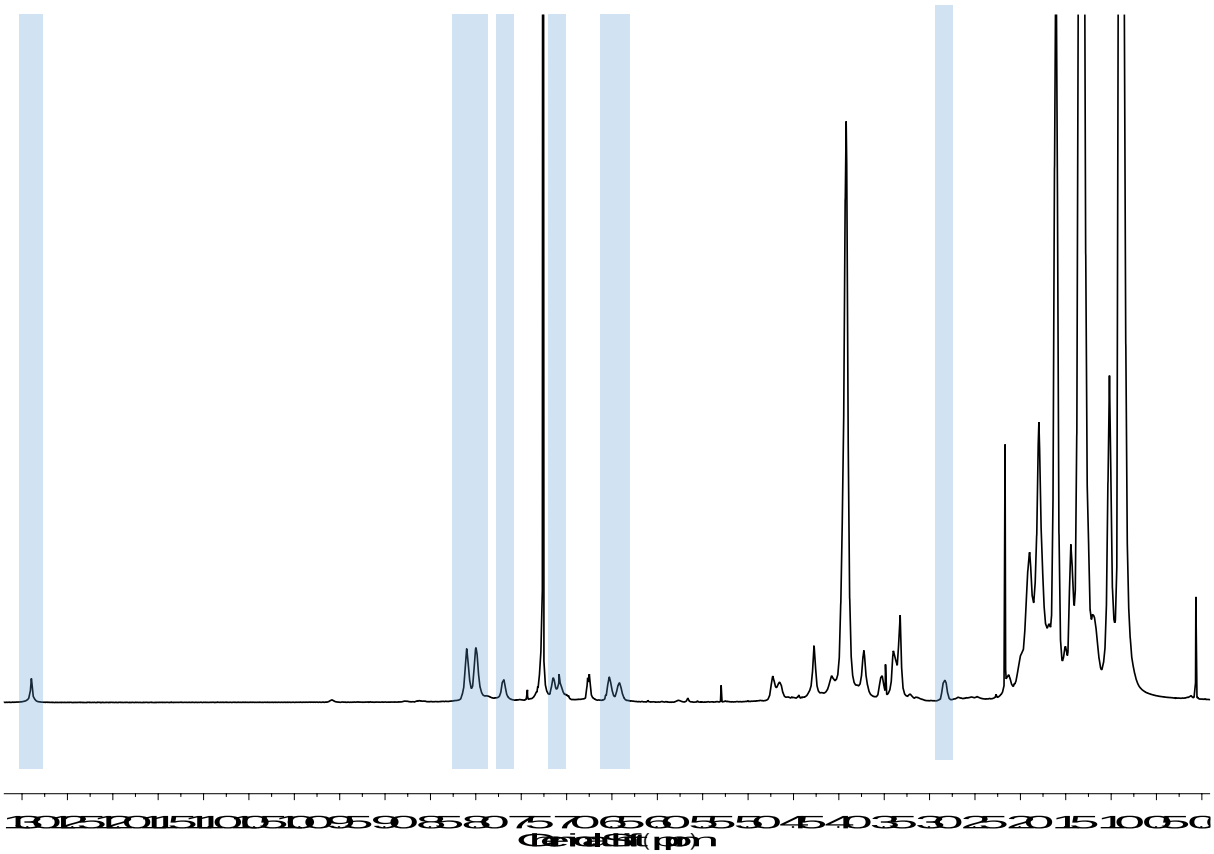

Scheme 3.19 ^{1}H NMR of functionalization of **NBD–PHMA 11 (top)** with **DASA–maleimide 7** (middle) to produce **DASA–PHMA 12 (bottom)** after purification in chloroform-d, highlighting distinct DASA functionality.

Chapter 4. The Role of Polymer Matrix and Photochrome Incorporation on the Photothermal Actuation of DASA-based Polymers

4.1. Abstract

We investigate the influence of the host matrix on the photothermally-driven actuation performance of negatively photochromic, donor–acceptor Stenhouse adduct (DASA)-based polymers. Using a modular Diels–Alder "click" platform, we designed polymeric materials with varying DASA incorporation and investigated the relationships between material composition and the resulting physical, mechanical, and photoswitching properties. We demonstrate that increasing the DASA concentration in polymer conjugates has a dramatic effect on the material's physical and mechanical properties, such as the glass transition temperature (T_g) and elastic modulus, as well as the photoswitching properties, which are found to be highly dependent on T_g. We establish using a simple photoresponsive bilayer that actuation performance is controlled by the bilayer stiffness rather than the photochrome incorporation of DASA. Finally, we report and compare the light-induced property changes in T_g and elastic modulus between the materials comprising the open or closed forms of DASAs. Our results demonstrate the importance of designing a material that is stiff enough to provide the mechanical strength required for actuation under load, but soft enough to reversibly switch at the operational temperature and provide key considerations for the development of application-geared photoswitchable materials. This Chapter was adapted with permission from *ACS Appl. Polym. Mater.* **2022**, *accepted*.[1] Copyright 2022 American Chemical Society. https://doi.org/10.1021/acsapm.1c01108

4.2. Introduction

Light-responsive materials have garnered significant attention for their abilities to form soft actuators, for example as locomotive robots,[2–6] artificial muscles,[7,8] grippers,[9,10] and oscillators.[11,12] Light offers numerous advantages: it is readily available by solar or artificial sources, does not require physical contact for delivery of power or signal, and has non-interacting internal degrees of freedom (wavelength, mode, polarization). In one straight-forward realization, light responsive bilayer actuators exploit the differential volumetric expansion between two material layers to generate motion and mechanical work under light stimulus via combined photothermal and photomechanical mechanisms.[10,12–14] Light-responsive bilayers are advantageous due to their fast response, high efficiency, and simple design. In a typical cantilevered configuration, a passive substrate, such as polyimide (PI), polyethylene terephthalate (PET), polyethylene (PE), polypropylene (PP), provides a low coefficient of thermal expansion (CTE) and physical support to the bilayer.[14] This passive layer is securely bonded to a photoactive layer and the bilayer is constrained at one end. Under illumination, the photoactive layer is rapidly heated and the material property mismatch between the two layers causes the development of mechanical stress at the interface, which leads to rapid and easily observed bending of the cantilever, with an amplitude that is highly sensitive to the bilayer stiffness. The stiffness in turn depends on the glass transition temperature T_g and elastic modulus.[15]

To boost the actuation potential of the active layer, additives including carbon-based materials,[16,17] gold nanoparticles,[18,19] and organic dyes[20] are often added to enhance the conversion of light energy into heat. Among additives, photoswitches offer particular benefits in energy conversion, tunability and high compatibility in soft materials.[21,22] A

visible-light-responsive bilayer actuator system driven by the photothermal properties of a unique molecular photoswitch: donor–acceptor Stenhouse adduct (DASA; Figure 4.1a) was recently developed by our group in collaboration with Valentine group (described in Chapter 3). This system demonstrates rapid and repeatable actuation capabilities, and the ability of the cantilever to lift more than ten times its own weight.[23] Moreover, by leveraging the negative photochromism of DASAs, in which the photoproduct absorption shifts to a shorter wavelength with respect to the reactant absorption (blue shift) and thus does not absorb the exciting light, we demonstrated tunable actuation performance of DASA–PHMA under constant light intensity.

Further use of DASA photoswitches in soft materials applications requires a deeper understanding of the effects of DASAs on the physical and mechanical properties of materials so that the material composition can be optimally designed. DASAs are known to be highly sensitive to their local environment,[24,25] and while the complicated and concentration dependent mechanisms of DASA switching in solution have gained considerable attention,[26–29] the effects of DASA incorporation on polymeric material properties including the glass transition temperature (T_g), coefficient of thermal expansion (CTE), and elastic modulus have not been thoroughly explored. Prior studies have shown that photoswitching of DASAs[30] and other photochromes[31–34] are highly influenced by the glass transition temperature as thermal reversion is inhibited in a glassy matrix that possesses high modulus. We anticipate that there will be an inherent trade-off between having a system that is stiff enough to actuate and perform work, but soft enough to enable photoswitching at the operational temperature.

In order to establish the relationships between material composition and actuation performance, we developed robust and scalable synthetic methods to access a range of DASA-based materials. Specifically, using a modular Diels–Alder "click" approach,[23,35] shown in Figure 4.1b, we elucidate the role of T_g and elastic modulus on photothermal actuation by tuning the polymer host matrix and DASA incorporation. By synthesizing materials with increasing DASA content and constant T_g, we can decouple the effects of DASA incorporation and T_g on material performance metrics. We show the effect of the performance of actuation is directly related to the material stiffness, which depends on the polymer host matrix, rather than photochrome incorporation of DASA alone. However, in a given polymer host matrix, increasing DASA incorporation increases the elasticity modulus and T_g of polymer conjugates, leading to improved actuation performance. The increase in glass transition temperature with increasing DASA incorporation also affects the forward and backward switching kinetics. The forward kinetics slow with increasing T_g, while thermal reversion is essentially shut down at temperatures below T_g. When materials are held at a temperature above T_g, regardless of incorporation or comonomer, there is increased recovery.

The molecular origins of these effects likely arise from changes in molecular volume, polarity, and molecular interactions between isomers and polymer chains as the photoswitches reversibly switch between two different isomers. Understanding how these molecular-level changes allow for photo-induced mechanical property changes between the photoreactant and photoproduct would provide an additional handle for actuator design.[36] Unlike P-type photoswitches, which use two different wavelengths of light to drive the reversible photochromic reaction, DASA is a T-type photoswitch with a switched state that

is colorless and non-absorbing, as shown in Figure 4.1a. To better understand the light-induced property changes in T_g and modulus we compare the properties of materials formed from open and closed forms of DASA. We observed a decrease in modulus and T_g upon photoswitching from the highly colored, extended, open form to the colorless, compact closed form, which can be further leveraged in photothermal actuator design.

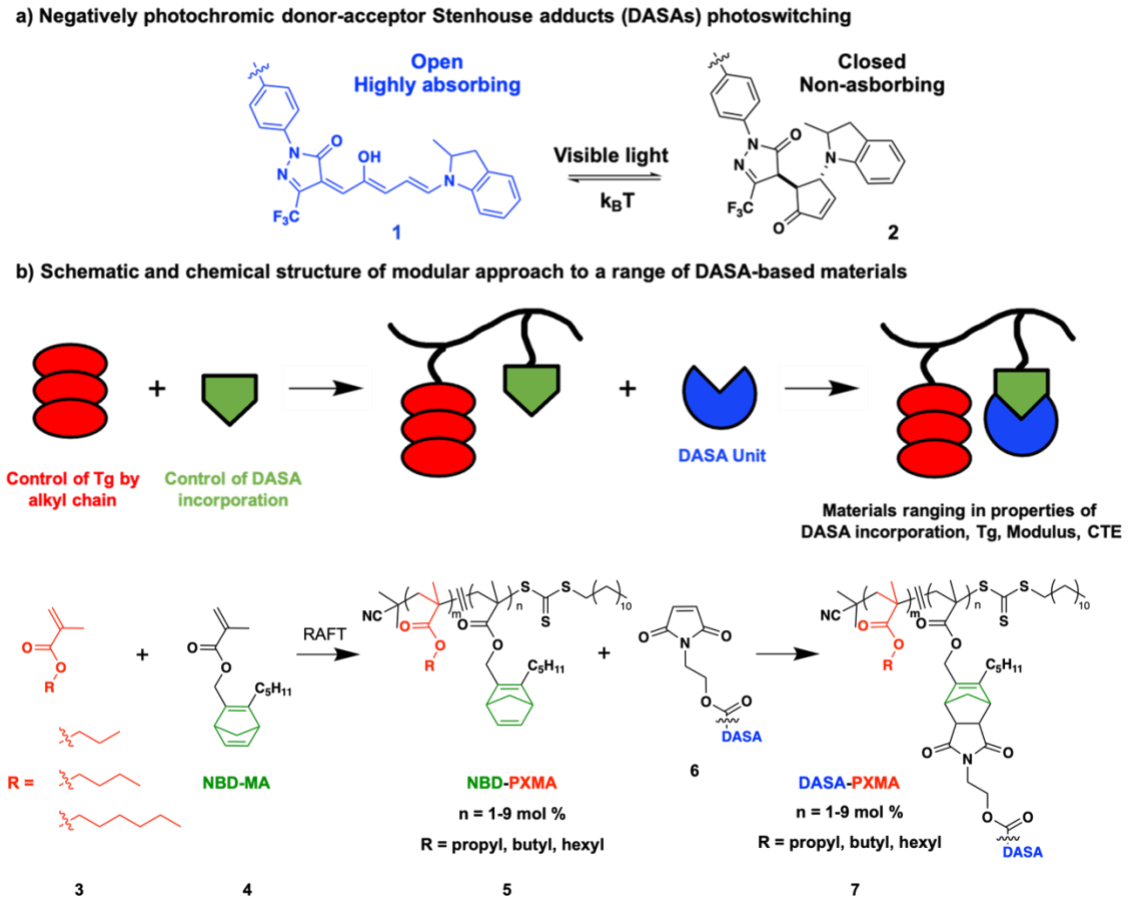

Figure 4.1 a) Upon irradiation with visible light, Donor-acceptor Stenhouse adducts (DASAs) undergo a conformational change from a highly colored, open-form to a colorless, closed-form. b) Schematic and chemical structure of modular cascading Diels–Alder "click" approach used to synthesize a range of DASA-based materials that vary in incorporation of the photoresponsive unit and glass transition temperature. Reprinted with permission from

ACS Appl. Polym. Mater. **2022**, *accepted*.[1] Copyright 2022 American Chemical Society. https://doi.org/10.1021/acsapm.1c01108

4.3. Synthesis of DASA-Based Materials

To understand how material composition, including host matrix properties and photochrome incorporation, influence the photoswitching, mechanics, and actuation performance, we need robust, modular, scalable methods that enable access to a range of DASA-based materials. Using a modular cascading Diels–Alder click approach, we can easily tune the polymer host matrix and incorporation of photoresponsive unit as shown in Figure 4.1b. We hypothesized that increasing the concentration of DASA, which acts as a photothermal agent, would increase the actuation performance due to higher heat generation. To test this experimentally, we synthesized copolymers containing poly (hexyl methacrylate) (PHMA) and the functional monomer norbornadiene methacrylate (NBD–MA) using reversible addition fragmentation chain-transfer (RAFT) polymerization. The incorporation of DASA was tuned by varying the equivalence of NBD-MA. Deprotection of the NBD group with tetrazine revealed the cyclopentadiene functional group that spontaneously reacts *in situ* with the maleimide functionalized DASA photoswitch. The mild and efficient nature of the cascading Diels–Alder chemistry enables facile incorporation of 1 mol %, 4 mol % and 9 mol % DASA (See Table 4.1 for incorporation of NDB and DASA based on ^{1}H NMR spectroscopy). To control the glass transition temperature, the host matrix was tuned by incorporating methacrylates with different alkyl chain length, such as hexyl, butyl, or propyl.

The incorporation of NBD after RAFT was confirmed using ^{1}H Nuclear Magnetic Resonance (NMR) spectroscopy included in Experimental section of this Chapter. NBD

incorporation is based on comparing the integration of distinct NBD peaks (~6.5-7.0 ppm, 2 H) compared to the alpha ester peaks on the polymer backbone (~3.75-4.2, 2 H).

Mol % NBD is calculated based on = $\frac{\text{NBD integration}}{\text{NBD intergation+ Backbone integration}}$* 100

After the DA click reaction, DASA incorporation is confirmed by ^{1}H NMR as well. DASA incorporation is based on comparing the integration of distinct DASA peaks (~7.8-8.25 ppm, 4 H) compared to the alpha ester peaks on the polymer backbone (3.75-4.2, 2 H).

Mol % DASA is calculated based on = $\frac{\frac{\text{DASA integration}}{4}}{\frac{\text{DASA integration}}{4}+\frac{\text{Backbone integration}}{2}}$* 100

Azobenzene incorporation is based on comparing the integration of distinct Azo peaks (~7.85-7.95 ppm, 2 H) compared to the alpha ester peaks on the polymer backbone (3.75-4.2, 2 H).

Mol % Azo is calculated based on = $\frac{Azo\ integration}{\text{Azo integration+ Backbone integration}}$* 100

Table 4.1 Summary of NBD and DASA incorporation by ^{1}H NMR

Material*	Target (NBD)	Observed (NBD)	Observed (Photochrome)
1 mol % NBD/DASA-PHMA	1.1	1.0	0.9
4 mol % NBD/DASA-PHMA	5.2	4.9	3.9
9 mol % NBD/DASA-PHMA	10.4	9.3	9.2
1 mol % NBD/DASA-PPMA	1.3	1.2	1.0
4 mol % NBD/DASA-PBMA	5.2	5.1	3.8
9 mol % NBD/Azo-PHMA	10.4	9.3	9.0

*Values reported in the manuscript and material name are based on observed photochrome incorporation rounded to the nearest whole number.

The molecular weight and polydispersity were characterized by advanced polymer chromatography (APC). Molecular weights of norbornadiene co-polymers above 33K were targeted to be above the molecular weight of entanglement of poly (hexyl methacrylate) (M_e = 33K).[37] The number average molecular weight determined by APC ranged from M_n = 40-70K, with dispersity of 1.3-1.7. Using materials designed with varying DASA incorporation

and matrix composition, we next investigated the role of the glass transition on photothermal actuation enabled by DASAs. Detailed synthetic procedures and characterization results are shown in Experimental Section of this Chapter.

4.4. Physical and Mechanical properties of DASA-based materials

For each material composition, Differential Scanning Calorimetry (DSC) and Dynamic Mechanical Analysis (DMA) experiments were performed to determine the glass transition temperature. Based on the DSC analysis, 1 mol %, 4 mol %, and 9 mol % DASA–PHMA conjugates indicated an increase in the T_g with increasing DASA content, to 2 °C, 23 °C, and 62 °C respectively, as shown in Figure 4.2 and summarized in Figure 4.6a, as compared to the T_g of the PHMA homopolymer, which is −6 °C. To compare the effect of DASA incorporation to that of a well-studied photoswitch, we also synthesized and characterized an azobenzene (Azo)-conjugated polymer, 9 mol % Azo-PHMA. The Azo-based material indicated T_g = 5 °C, only 11 °C above that of the PHMA homopolymer, in contrast to the equivalent DASA-based material which indicated T_g = 62 °C, an approximately 6-fold larger change (Figure 4.3). This result highlights the large effect DASA incorporation has on material properties. Presumably, the bulky conjugated groups on DASA increase the T_g of the polymer due to restricted segmental dynamics.[38,39]

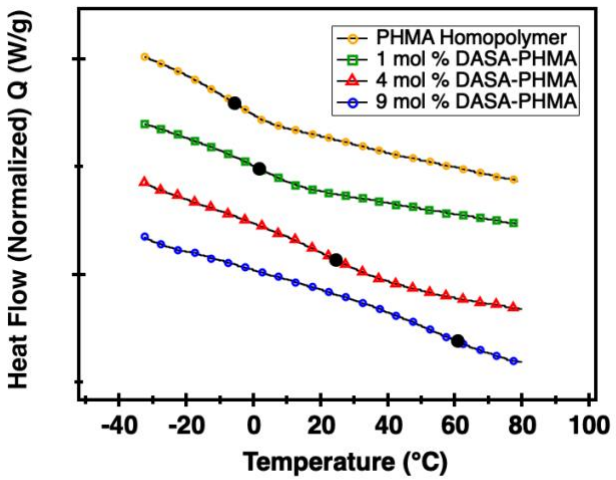

Figure 4.2 Differential scanning calorimetry (DSC) measurements of PHMA and 1, 4 and 9 mol % DASA–PHMA materials. The glass transition temperature increases from -6 °C to 2 °C, 23 °C, 62 °C, respectively, with increasing DASA incorporation. A black dot indicates the T_g of each material.

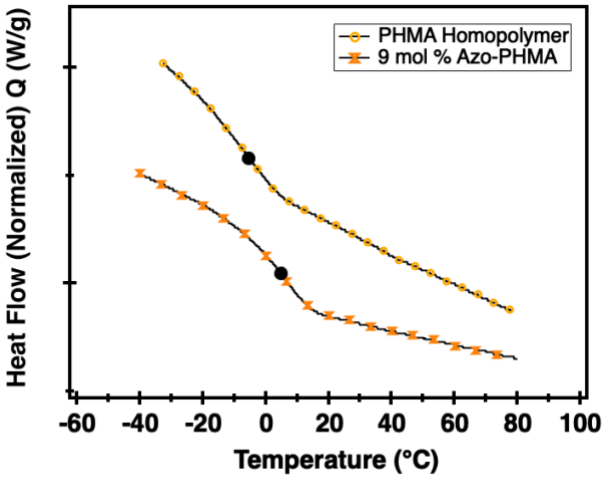

Figure 4.3 Differential scanning calorimetry (DSC) measurements of PHMA and 9 mol % Azo–PHMA. The glass transition temperature increases from -6 °C to 5 °C after 9 mol % Azo incorporation. A black dot indicates the T_g of each material.

With a better understanding of the effect of increasing DASA incorporation on T_g, we next selected specific co-monomers to produce materials with differing DASA content but similar T_g and compared their performance. This allowed us to decouple the effects of DASA incorporation and T_g on material properties. Materials with a T_g of approximately 60 °C were targeted, to facilitate comparisons with the PHMA-based material with the highest incorporation of DASA, 9 mol % DASA-PHMA. To achieve a 1 mol % DASA-based material with target T_g of ~ 60 °C, we selected copolymers containing propyl methacrylate, for which the homopolymer T_g = 57 °C (Figure 4.4). The resulting 1 mol % DASA-PPMA material has a T_g of 67 °C. To achieve a 4 mol % DASA-based material, butyl methacrylate was chosen, for which the homopolymer T_g = 32 °C (Figure 4.5). The resulting 4 mol % DASA-PBMA material has a T_g of 59 °C. While there is slight variation from the target value among the different compositions, the T_g values of all materials were within a narrow range from 59 °C – 67 °C, enabling quantitative comparisons of materials with an increasing incorporation of DASA and similar T_g, as shown in Figure 4.6b.

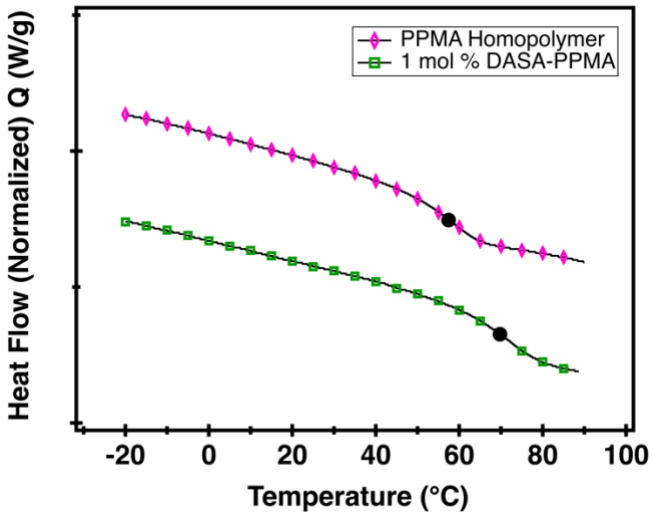

Figure 4.4 Differential scanning calorimetry (DSC) measurements of PPMA and 1 mol % DASA–PPMA. The glass transition temperature increases from 57 °C to 67 °C after 1 mol % DASA incorporation. A black dot indicates the T_g of each material.

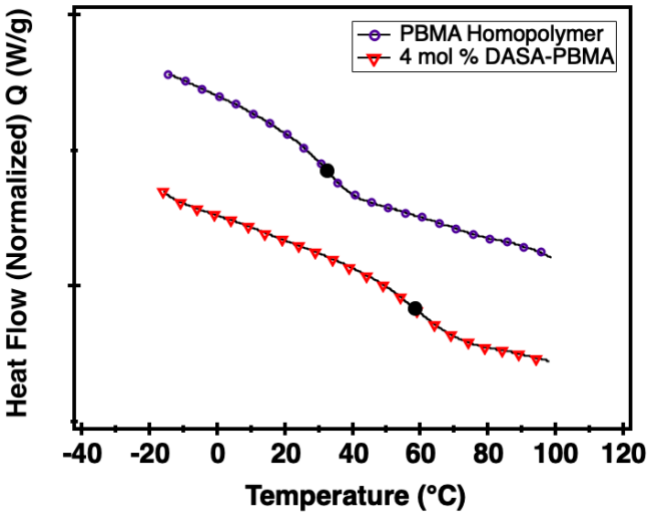

Figure 4.5 Differential scanning calorimetry (DSC) measurements of PBMA and 4 mol % DASA–PBMA. The glass transition temperature increases from 32 °C to 59 °C after 4 mol % DASA incorporation. A black dot indicates the T_g of each material.

With these materials in hand, we determined the mechanical properties of the various material compositions using DMA. Elastic moduli of DASA-PHMA exhibited an increase at all temperatures as shown in Figure 4.6c. The modulus in the glassy state increased with increasing DASA content. Each DASA-PHMA showed a decrease in modulus over its T_g and a modulus plateau was not observed due to the relatively low M_n. We found significantly different elastic moduli at 20 °C for DASA-PHMAs, where 1, 4, and 9 mol % DASA-PHMA showed 0.003 GPa, 0.495 GPa, and 1.608 GPa, respectively. When the materials with increasing incorporation of DASA and similar T_g were compared, we found them to have nearly identical moduli, as shown in Figure 4.6d, at 20 °C with an average value of 1.609 ± 0.004 GPa, as measured by 1 Hz oscillation in the small strain regime. We next measured the linear coefficient of thermal expansion (CTE) using DMA. We found that DASA-based materials in a glassy state (– 50 °C + T_g to – 10 + T_g have similar CTE values (130-160 × 10^{-6} /°C) regardless of DASA incorporation and matrix. These values are only based on the glassy region due to the significant creep behavior observed over T_g.

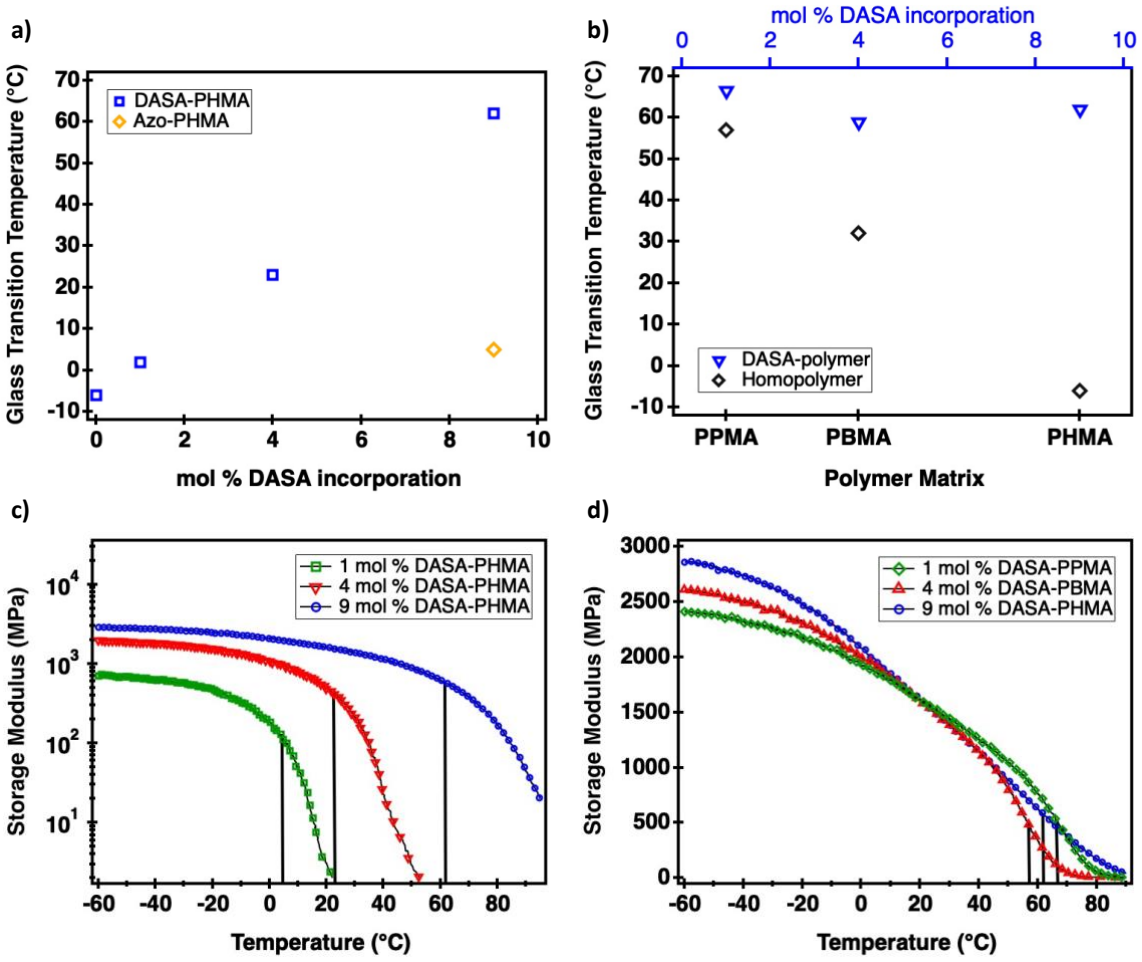

Figure 4.6 a) Differential scanning calorimetry (DSC) of DASA-PHMA materials shows that T_g increases with increasing DASA incorporation. At 9 mol% incorporation of photoswitch, there is a significantly larger increase in T_g after functionalization with DASA (blue) compared to azobenzene (Azo). b) T_g of increasing DASA incorporation with different methacrylate comonomers (blue, upper *x*-axis) and corresponding methacrylate homopolymers with no DASA to show the increase in T_g due to DASA incorporation (black). c) Dynamic mechanical analysis (DMA) shows an increase in the elastic modulus of DASA-PHMA with increasing DASA incorporation. d) By using different methacrylate comonomers, it is possible to obtain materials with varying DASA incorporation and similar modulus, with vertical lines indicating the similar T_g values of each material. Reprinted with

permission from *ACS Appl. Polym. Mater.* **2022**, *accepted*.[1] Copyright 2022 American Chemical Society. https://doi.org/10.1021/acsapm.1c01108

Taken together, our results demonstrate that increasing DASA incorporation has a significant effect on the T_g and modulus, but not the CTE, and that for a given matrix composition, adding DASA increases the material's stiffness. These structure-property relationships can have a profound effect on the ability of the material to bear loads. Through the use of strategic design, we were able to access DASA-materials with a range of mechanical properties. We expect these properties will be reflected in photoswitching and photoactuation performance as well.

4.5. Photoswitching properties of DASA-based materials

DASAs offer the unique advantage of negative photochromism, switching from a highly colored, absorbing open-form, to a colorless, non-absorbing closed-form upon irradiation with visible light (Figure 4.1a). Negative photochromism permits deep penetration of the incident light, allowing photoconversion of the entire sample, and also allows for tunable actuation based on absorbance where the highly absorbing, open form has increased photothermally-driven actuation, compared to the non-absorbing closed form.[23,40] To investigate the photoswitching kinetics of DASA-based polymer materials, and to establish the influence of the DASA content and material T_g, we used time-dependent pump-probe UV/Vis spectroscopy. The wavelength of maximum absorbance in all DASA materials was centered at ~ 648 nm as shown in Figure 4.7 and was used to monitor the rates of the forward photoswitching and the thermal back reaction. Using a two state model we can quantify the forward reaction rate under light ($k_{f,light}$) and effective quantum yield (φ_{eff}) during the transition from the open to closed form.[24] In order to quantify the recovery rate

constants k_b (s^{-1}), we utilized a first order exponential recovery model ($k_{b,exp}$, s^{-1}),[24] and a dynamic equilibrium model ($k_{b,dyn}$, s^{-1}).[41,42]

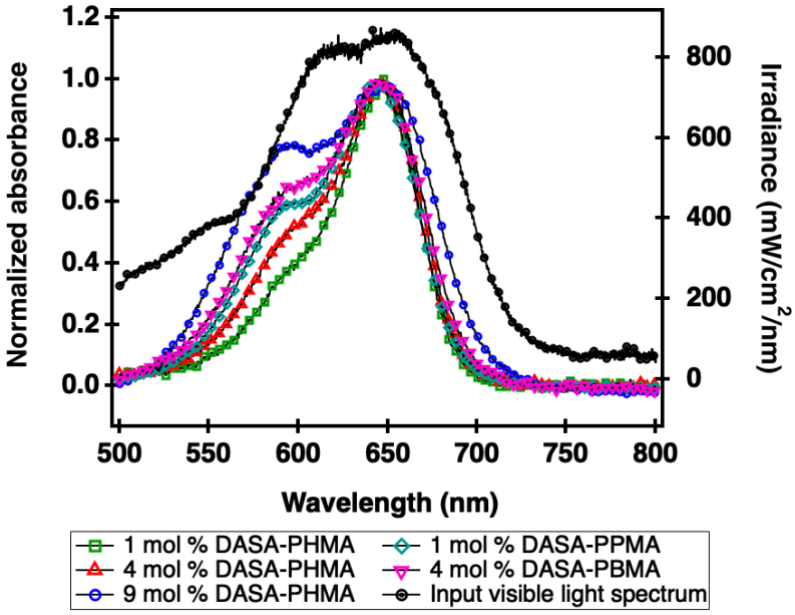

Figure 4.7 Absorption spectra of DASA-polymer thin films (left axis) compared to the irradiance of visible light (black curve, right axis). The absorption spectra of DASA-polymer thin films show broadening with increasing DASA incorporation and/or T_g; broadening was not observed in solution.

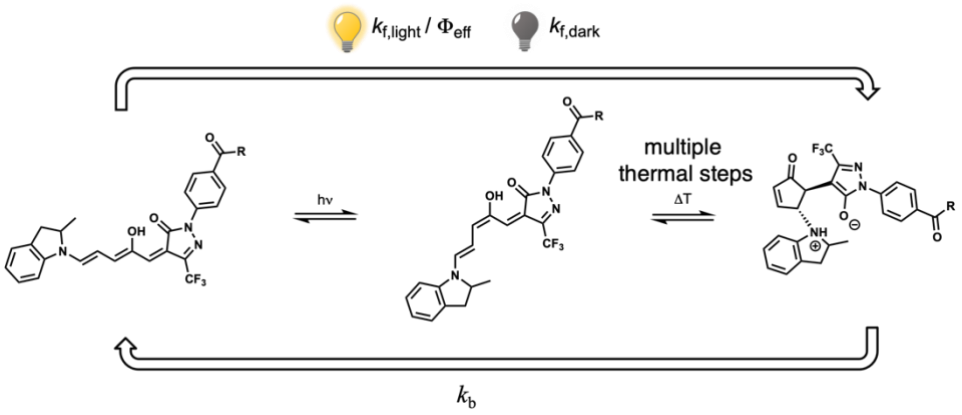

Scheme 4.1 Overall reaction and calculated rate equations.

To determine rate constants (Scheme 4.1) and quantum yields for the DASA-polymer conjugates several assumptions had to be made. The extinction coefficient of the DASA molecules in the polymers was assumed to be 100,000 M^{-1} cm^{-1} due to measurements in solutions reporting similar values.[40,43] Furthermore, due to high thermodynamic equilibrium in solution (>95 % open form in chloroform and toluene)[43] it was assumed that prior to irradiation all DASA molecules resided in the open form.

For recovery rate calculations,[24,42] data was obtained using time-dependent UV-Vis spectroscopy by recording the change in absorbance versus time after irradiation was stopped. This data was then fitted with two different functions representing two kinetic models. The first model is a dynamic equilibrium model that assumes first order rates of opening and closing, presuming two populations in equilibrium. Any change in absorbance is attributed to be DASA molecules adopting a new equilibrium between the open and closed forms due to the presence of the polymeric environment. This model implies that no molecules are lost to photodegradation and with this model, we obtain both a forward rate constant describing the rate of closing in the dark, $k_{f,dark,\ dyn,}$ and a back rate constant describing the rate of opening in the dark, $k_{b,dyn}$ where the subscript dyn indicates the dynamic equilibrium model.[42]

The model used was of the form:[42]

$$\frac{d[\mathrm{Open}]}{dt} = -k_{\mathrm{f,dark,dyn}}[\mathrm{Open}]_t + k_{\mathrm{b,dyn}}([\mathrm{Open}]_0 - [\mathrm{Open}]_t)$$

For recovery:

$$[\mathrm{Open}]_t = 1 - \frac{k_{\mathrm{f,dark,dyn}} + k_{\mathrm{b,dyn}} e^{-(k_{\mathrm{b,dyn}} + k_{\mathrm{f,dark,dyn}})t}}{k_{\mathrm{b,dyn}} + k_{\mathrm{f,dark,dyn}}}[\mathrm{Open}]_0$$

where $[\mathrm{Open}]_0$ represents the initial concentration of the open form and $[\mathrm{Open}]_t$ represents the concentration of the open form at time *t*. The measured absorbance is used as a proxy for the open form concentration. In this model the plotted absorbance values are given by the measured absorbance divided by the initial absorbance (the normalized absorbance, denoted 'norm. abs.') under that assumption that all DASA is in the open form prior to irradiation.

As second model, we use a first order exponential recovery function[24] that assumes that all loss of absorbance is due to photodegradation. The model was used in the form:[24]

$$\mathrm{Abs}_t = \mathrm{Abs}_{\mathrm{rec}} - (\mathrm{Abs}_{\mathrm{rec}} - \mathrm{Abs}_{\mathrm{PTSS}}) e^{-k_{\mathrm{b,1st}} * t}$$

where $k_{\mathrm{B,1st}}$ represents the rate of opening in the dark, $\mathrm{Abs}_{\mathrm{rec}}$ represents the absorption of open form at full recovery (the absorbance at t = 15,000 s after full recovery is used), $\mathrm{Abs}_{\mathrm{PTSS}}$ represents the absorption of open form at the photothermalstationary state (PTSS, the absorbance at t = 200 s as the last data point under irradiation was used) and Abs_t represents the absorption of the open form at time *t*. In this model we plot and fit the measured absorbance without normalization.

To determine the forward kinetics under irradiation we assume a simple two state model with absorbance being used as a substitute for the concentration of the open form. The model was used in the form:[24]

$$\text{Abs} \propto [\text{Open}]_t = \frac{[\text{Open}]_0 * k_\text{b}}{k_\text{f,light}} + [\text{Open}]_0 \left(1 - \frac{k_\text{b}}{k_\text{f,light}}\right) e^{-k_\text{f,light} * t}$$

k_b represents the rate of opening in the dark and is used as the previously calculated $k_\text{b,1st}$ or $k_\text{b,dyn}$[24]. $k_\text{f,light}$ represents the rate of closing under light irradiation, $[\text{Open}]_0$ represents the initial concentration of the open form and $[\text{Open}]_t$ represents the concentration of the open form at time *t*.

We find in all cases that $k_\text{f,light} >> k_\text{b}$ and as a result, the forward rate dominates and the small differences in determining k_B by the two presented above models do not lead to any significant differences in the calculation of $k_\text{f,light}$. The rate of closing under light ($k_\text{f,light}$) can be given as a function of the effective quantum yield (Φ_eff).[24]

$$k_\text{f,light} = \sigma \Phi_\text{eff} \text{I} - k_\text{b}$$

where σ represents the absorption cross section, I represents the light intensity, and k_b represents the rate of opening in the dark. σ can be calculated by multiplying the extinction coefficient with a conversion factor of 3.826×10^{-21}.[24] To determine the quantum yield, it was assumed due to spectral overlap between the illumination source and DASA absorption band (see Figure 4.7) that all light emitted by the white halogen lamp (WHL, halogen lamp, EKE 150 W with a fiber optic illuminator, 172 mW/cm^2) was absorbed by the samples and the area of the detector was used as the area of measurement (~0.1 cm^2). For the calculation $k_\text{b,1st}$ was used; since $k_\text{f,light} >> k_\text{b}$ there is no significant change between the two kinetic models considered. Note, this is an effective quantum yield from open to closed and that the change

observed as the T_g or the polymer matrix is varied most likely cannot be attributed to a change in the actinic step, but rather in a change in one or more of the subsequent thermal steps of the DASA switching mechanism.[28] Furthermore, due to the number of assumptions made in this modeling, the values should only be used in relative comparison between conditions tested here, and the relevance for external comparison with absolute values may be limited. This will be further explored in future work.

For the kinetic studies, thin films were prepared by drop casting and irradiated with a light source (halogen lamp, EKE 150 W with a fiber optic illuminator, 172 mW/cm^2) for 140 s at room temperature. In order to achieve an absorbance ~1, 1 mol %, 4 mol % and 9 mol % DASA-based materials thin films were prepared with different thicknesses of 10 µm, 2.5 µm and 1 µm, respectively, with the assumption that DASA has a molar extinction coefficient in the solid-state similar to what has been experimentally determined in solution, ~100,000 M^{-1} cm^{-1}.[40,44] With increasing DASA content and increasing T_g, we observed a slowing of the forward and backward reaction rates as shown in Figure 4.8a. The 1 mol% DASA–PHMA material with the lowest T_g has significantly more recovery at room temperature, at 71% of the initial absorbance, as compared to the 9 mol% DASA–PHMA material with the highest T_g, which recovers only 20% after 15,000 s (> 4 hours). Analysis of the forward rate constants of 1 mol %, 4 mol %, and 9 mol % DASA–PHMA conjugates under illumination indicated a decrease in rate constants ($k_{f,\,light}$, s^{-1}) with increasing DASA content, 0.1350 s^{-1}, 0.0660 s^{-1}, and 0.0271 s^{-1} respectively. While there is slight variation between the two kinetic models for recovery, they are both in agreement that the rate constants decrease with increasing DASA incorporation and increasing T_g. Overall, the light driven forward reaction rate dominates the kinetics, while the thermal back reaction rate occurs on a much slower

time scale, which does not affect the macroscopic properties. The photoswitching kinetics are summarized in Table 4.2. We repeated the switching study with all DASA–PHMA materials at temperatures above their T_g using a heating bath that can reach a maximum sample temperature of 70 °C. When each material is held over T_g, all materials recover to >70% as shown in Figure 4.9.

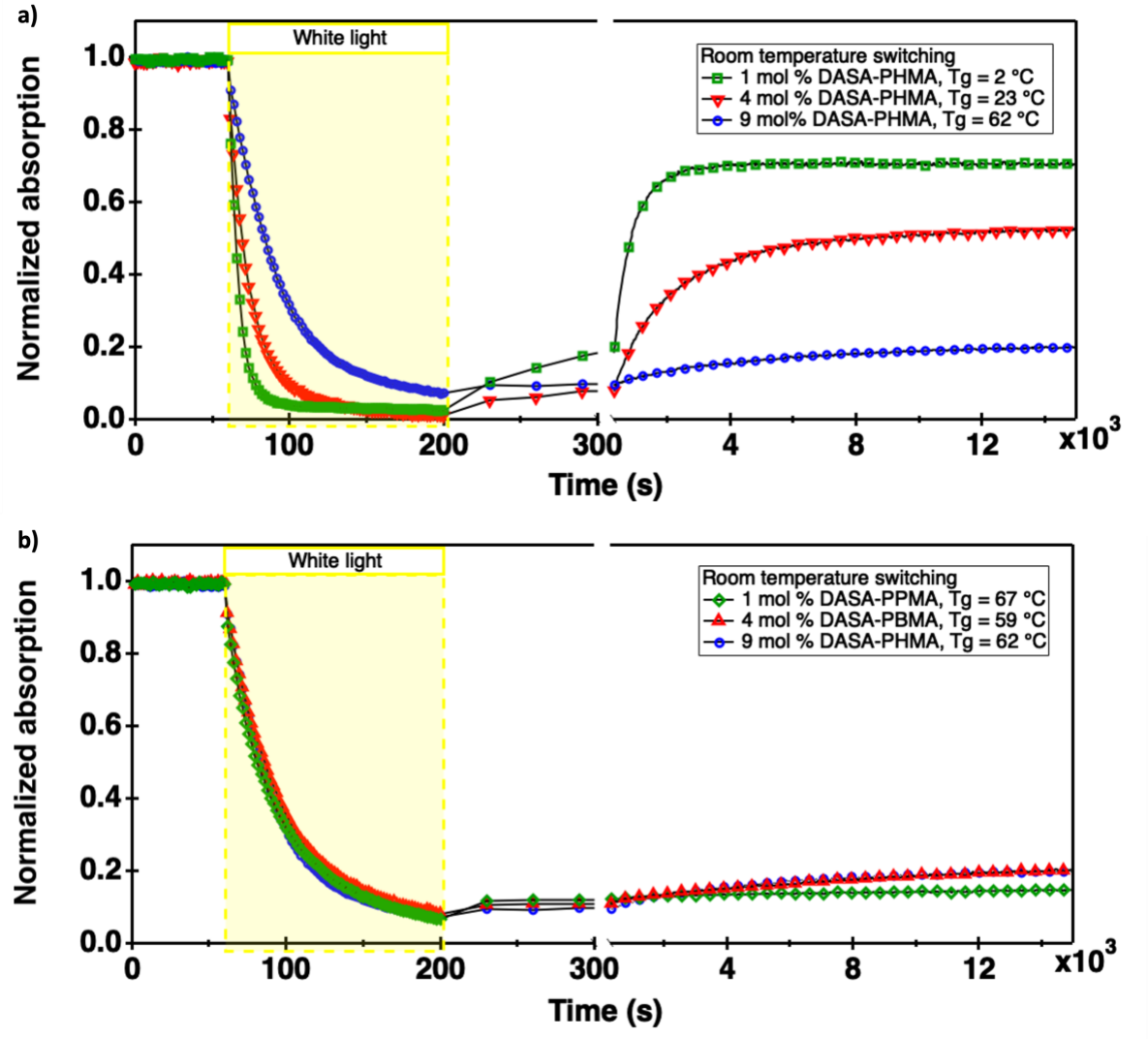

Figure 4.8 The influence of increasing DASA incorporation and T_g on the switching kinetics was determined using time-dependent pump-probe UV/Vis spectroscopy. Thin

films were irradiated (halogen lamp, EKE 150 W with a fiber optic illuminator, 172 mW/cm^2) starting at time t = 60 s and ending at t = 200 s (indicated by the shaded box in the time traces); the subsequent thermal recovery in the dark was measured. a) Time-dependent UV/Vis analysis of DASA-PHMA materials with T_g ranging from 2-62 °C due to increasing DASA incorporation. In a polymer matrix of fixed monomer composition, increasing DASA results in a decrease in the forward and backward reaction rates, as well as lower recovery. b) Time-dependent UV/Vis analysis of materials with increasing DASA incorporation and different methacrylate comonomers resulting in materials with T_g ranging from 59-67 °C. In materials with a high T_g >> room temperature, and with similar initial absorbance, increasing DASA results in similar forward and backward reaction rates, and similarly low recovery. Reprinted with permission from *ACS Appl. Polym. Mater.* **2022**, *accepted*.[1] https://doi.org/10.1021/acsapm.1c01108

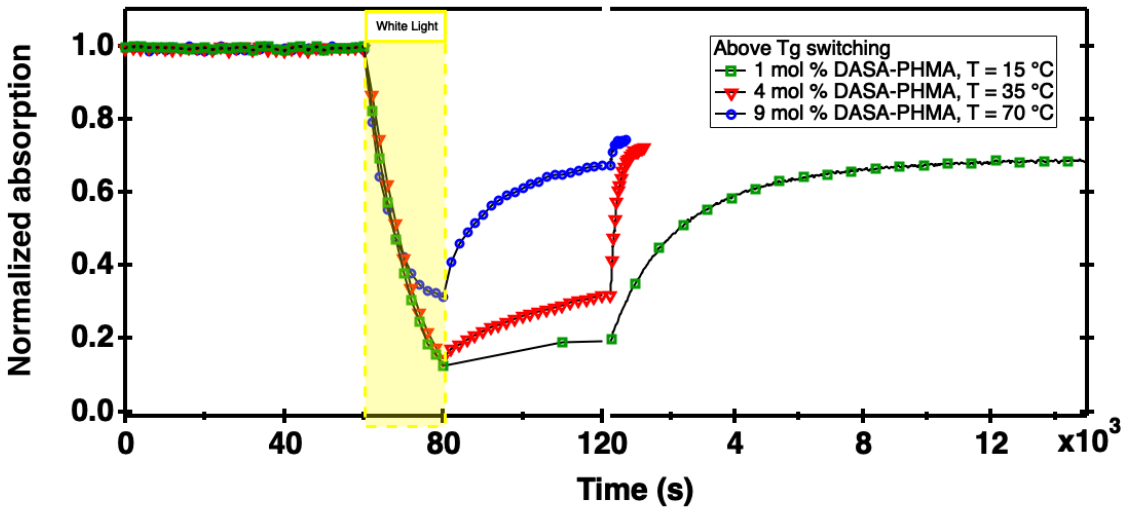

Figure 4.9 Influence of increasing DASA incorporation in PHMA on their switching kinetics, determined by using time-dependent pump-probe UV/Vis spectroscopy above T_g. Thin films were irradiated with a light source (Thin films were irradiated with a light source

(halogen lamp, EKE 150 W with a fiber optic illuminator, 172 mW/cm^2).). The irradiation started at t = 60 s and ceased at t = 80 s (indicated by the shaded box in the time traces); the subsequent thermal recovery in the dark and at temperatures above T_g were measured. The DASA-PHMA materials have T_g ranging from 2-62°C and the sample temperatures are included in the legend. This figure is reprinted from an article currently under review. Copyright permissions will be requested upon acceptance.

We then repeated these experiments for 1 mol% DASA-PPMA and 4 mol% DASA-PBMA materials that have T_g values of ~60 °C. Based on the results obtained using the 9 mol% DASA-PHMA with similar T_g, we did not expect to see significant recovery at room temperature. Indeed, as shown in Figure 4.8b, the three materials with similar T_g and initial absorbance all showed similar forward rate constants ($k_{f,\ light}$, s^{-1}), with increasing DASA content, 0.0271 s^{-1}, 0.0244 s^{-1}, and 0.0271 s^{-1} respectively. In addition, both kinetic models indicated similar rate constants for the thermal recovery of the materials bearing similar T_g, regardless of DASA incorporation, as summarized in Table 4.2. The slight variation in recovery is likely due to the slight differences in T_g, where 1 mol% DASA-PPMA matrix material with the highest T_g of 67 °C is the poorest recovering material. At 70 °C, above the T_g of all three materials, there is a significant increase in thermal recovery, as shown in Figure 4.10. Consistent with the results obtain using the PHMA-based materials, recovery is roughly 70–80% regardless of matrix composition and level of DASA incorporation when the operating temperature is held above T_g. Additional studies are underway to better understand the 20–30% loss upon switching which we believe may arise either because the material is reaching a new thermodynamic equilibrium or due to decomposition. Based on these results, it is clear that DASA incorporation dramatically influences the T_g of the

material which in turn dramatically influences the photoswitching properties. As such, both matrix selection and extent of incorporation have a large effect on the photoswitching behavior.

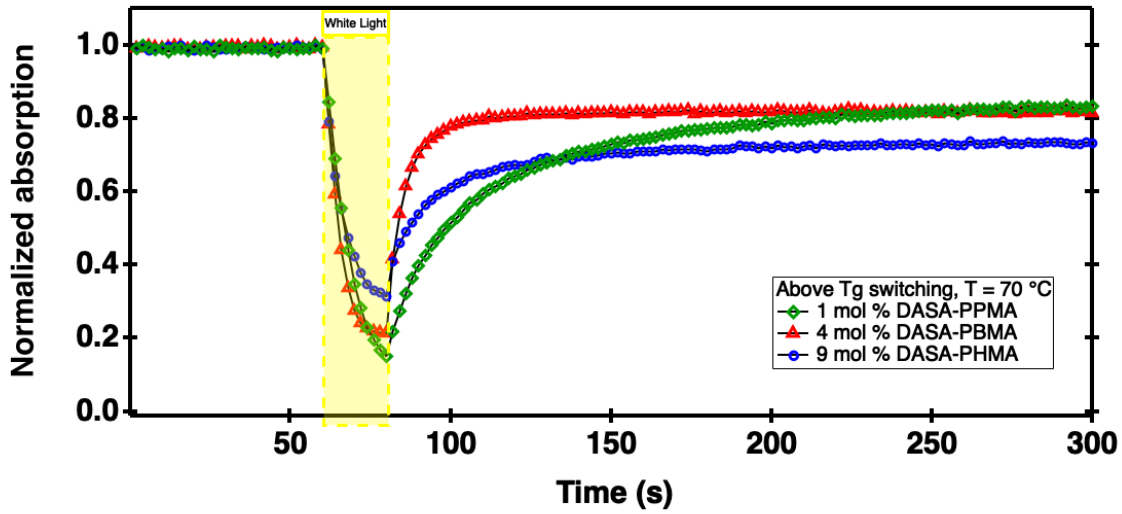

Figure 4.10 Influence of increasing DASA incorporation with different methacrylate comonomers on their switching kinetics, determined by using time-dependent pump-probe UV-Vis spectroscopy above T_g. Thin films were irradiated with a light source (halogen lamp, EKE 150 W with a fiber optic illuminator, 172 mW/cm^2). The irradiation started at t = 60 s and ceased at t = 80 s (indicated by the shaded box in the time traces); the subsequent thermal recovery in the dark and at temperatures above T_g were measured. The DASA-based materials have T_g ranging from 59-67°C and the materials were all measured at 70 °C.

Table 4.2 Summary of photoswitching kinetics of DASA-based materials.

Material	Half-life (s)	$k_{f,dark,dyn}$ (s^{-1}) x 10^6	$k_{b,dyn}$ (s^{-1}) x 10^7	$k_{b,1st}$ (s^{-1}) x 10^6	$k_{f,light}$ (s^{-1}) x 10^4	Φ_{eff}[a] x 10^5	% recovery at t = 15000 s with respect to the initial absorbance
1 mol % DASA-PHMA	570	484 ± 2	11520 ± 10	1651 ± 8	1350 ± 20	650 ± 10	71
4 mol % DASA-PHMA	1170	224 ± 2	2390 ± 20	424 ± 3	660 ± 10	323 ± 5	53
9 mol % DASA-PHMA	2010	163 ± 2	416 ± 4	243 ± 2	271 ± 3	132 ± 2	20
1 mol % DASA-PPMA[b]	N.D.	111± 4	195 ± 7	146 ± 1	271 ± 3	132 ± 2	15
4 mol % DASA-PBMA	2250	76 ± 1	225 ± 3	166 ± 1	244 ± 3	119 ± 2	20

Approximate sample temperature equals 22 °C [a]Effective quantum yield from open to closed and not of the actinic step. See Scheme 4.1. [b] recovery is barely observable. N.D. = not determined.

4.6. Photothermal actuation performance

To demonstrate the effect of material design on light-driven actuation performance, we prepared bilayer actuators by drop casting DASA-based materials onto a commercially-obtained polyimide (PI) film (purchased from McMaster, Kapton polyimide film, CTE ~ $22.8 \pm 0.1 \times 10^{-6}$ /°C and elastic modulus ~ 3.4 GPa at 1 Hz). The resulting material has a responsive DASA-based layer thickness of ~10 μm and passive layer thickness of ~25 μm (Figure 4.11), and the planar sheet is cut into thin strips of 1.5 mm by 15 mm. Because stiffness increases by the cube of the thickness, all cantilevers are prepared with the same thickness of ~10 μm, regardless of mol % DASA incorporation. To evaluate the actuation performance of the different materials, a light source (halogen lamp, EKE 150 W with a

fiber optic illuminator) located above the cantilever directly illuminated the DASA–PHMA layer. For each experiment, the displacement of the cantilever tip was continuously recorded before, during, and after irradiation, as shown in Figure 4.12a. An infrared camera (FLIR E60) was used to record the temperature of the bilayer cantilever under illumination. The actuation performance was measured under conditions of short- or long-term irradiation. Short-term irradiation is defined herein as ~ 4 s of irradiation time, resulting in negligible photoswitching in high T_g materials, as compared to long-term irradiation defined herein as > 2 min of irradiation time, resulting in non-negligible photoswitching in all materials.

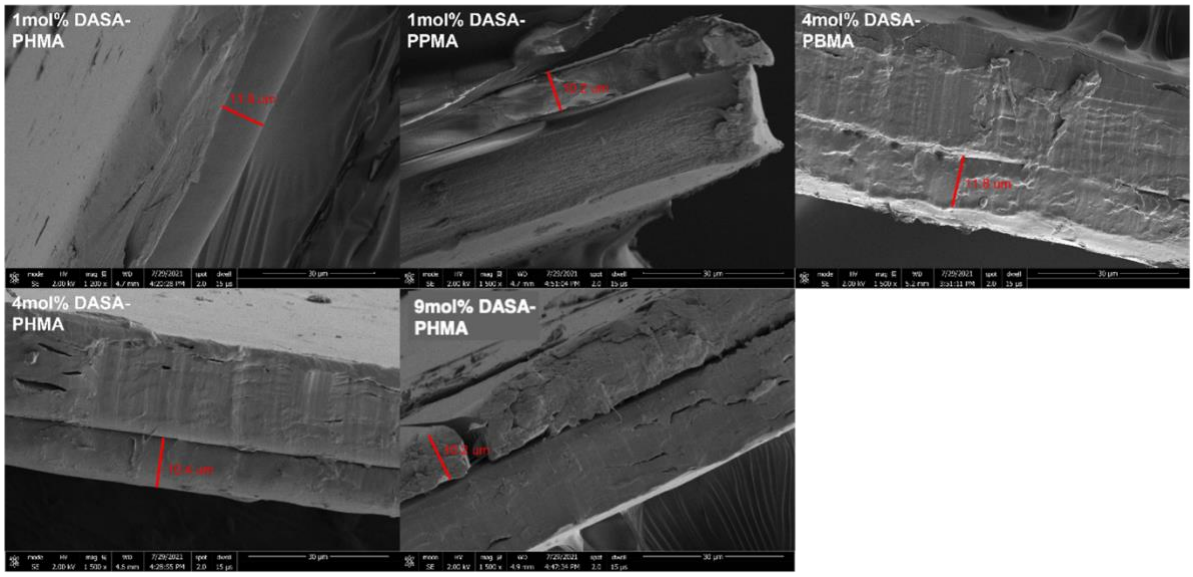

Figure 4.11 Cross-sectional images of the bilayer of DASA-based materials taken by an SEM indicated that the thicknesses of the DASA-based materials vary from 10.2 μm to 11.9 μm.

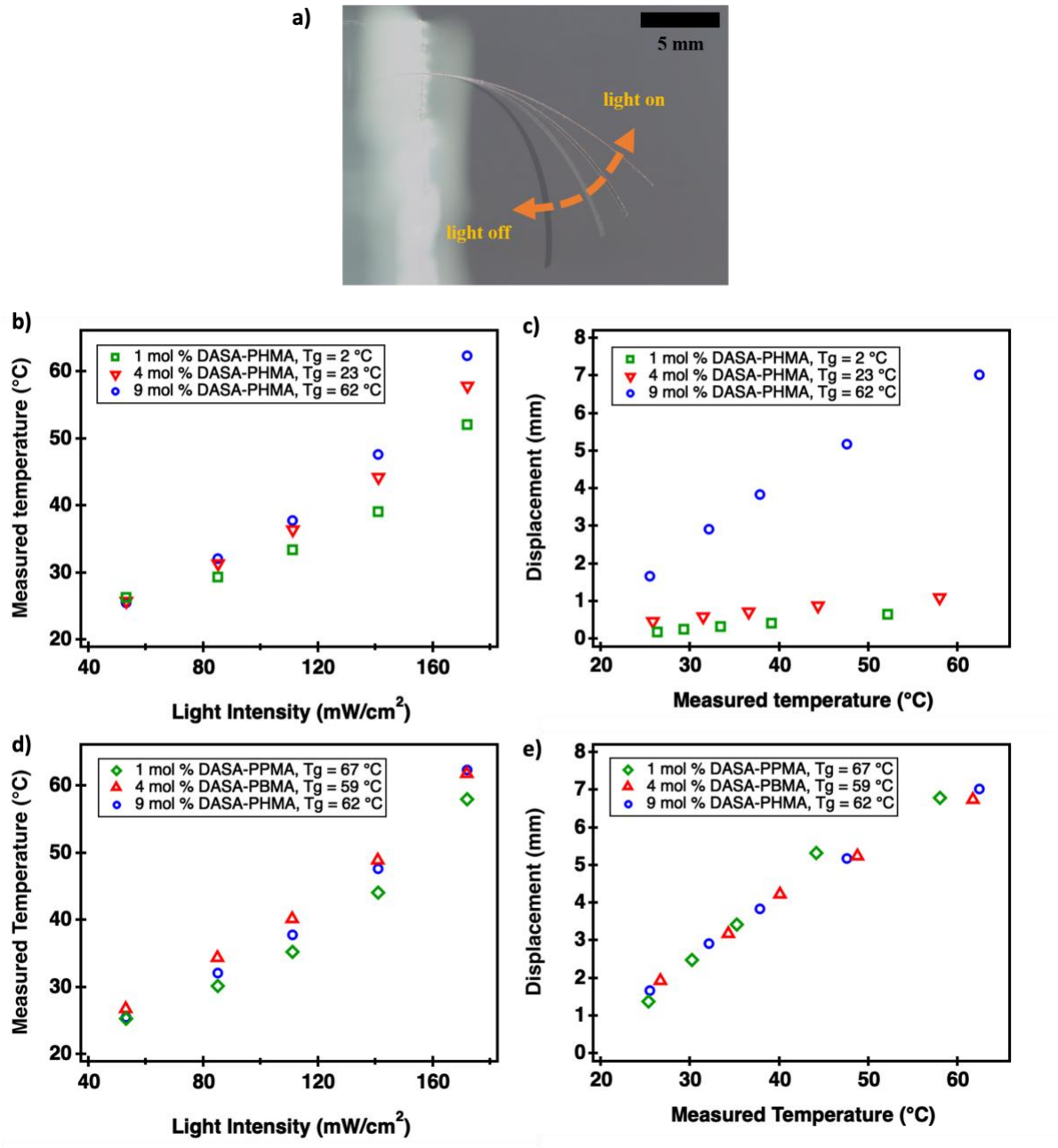

Figure 4.12 Photothermally-driven actuation of DASA-based materials. a) Using a cantilevered actuator geometry, we demonstrate the ability of DASA-polymer to photothermally actuate upon irradiation with visible light. b) Averaged peak temperature vs light intensity of DASA-PHMA materials with increasing DASA incorporation, resulting in a slight increase in temperature with increasing DASA incorporation. c) Averaged peak

displacement vs averaged measured temperature at different light intensities are plotted for DASA-PHMA materials, with significantly higher actuation for 9 mol % DASA-PHMA compared to lower incorporations. d) Averaged peak temperature vs light intensity of DASA materials with increasing DASA incorporation and different methacrylate comonomers (PXMA). e) Averaged peak displacement vs averaged measured temperature at different light intensities are plotted for DASA-PXMA materials, with similar actuation and temperature for all three materials. Averaged peak displacement is averaged over 5 total peak displacements and averaged peak temperature is averaged over 3 total measurements. Reprinted with permission from *ACS Appl. Polym. Mater.* **2022**, *accepted*.[1] Copyright 2022 American Chemical Society. https://doi.org/10.1021/acsapm.1c01108

To evaluate the short-term photothermal actuation of responsive bilayer materials, we initially measured cantilever tip displacement and temperature at different light intensities using the DASA–PHMA coated materials with 1 mol %, 4 mol %, and 9 mol % incorporation of DASA (Figure 4.12b, Figure 4.13, and Table 4.3). At a given light intensity, we observed a slight temperature increase as the concentration of DASA increased. At the maximum light intensity of 172 mW/cm^2, for 1 mol %, 4 mol %, and 9 mol % DASA–PHMA conjugates, we measured 52.1 °C, 57.9 °C, and 62.4 °C respectively. We attribute the slight variation in maximum measured temperature to (*i*) increasing DASA incorporation and (*ii*) the increased forward switching kinetics in lower T_g materials as shown in Figure 4.8a. The latter effectively lowers the percentage of photothermal agent within the low T_g materials. The displacement versus measured temperature at different light intensities is summarized in Figure 4.12c. Here, we observed a significant increase in displacement as the concentration of DASA increases at a given light intensity. At the maximum light

intensity of 172 mW/cm^2, a cantilever containing a 9 mol % DASA–PHMA active layer reached a maximum deflection of 7.0 ± 0.1 mm and temperature of 62.4 °C. Identical cantilevers containing 1 mol % and 4 mol % DASA–PHMA reached slightly lower temperatures of 52.1 °C and 57.9 °C but demonstrated an approximately order-of-magnitude smaller displacement, of 0.65 ± 0.06 mm and 1.11 ± 0.06 mm, respectively. We attribute the large difference in actuation performance to the differences in the stiffness of the materials, reflected in the T_g and modulus values. The 1 mol % and 4 mol % DASA–PHMA materials have T_g at or below room temperature, and elastic moduli of 0.495 GPa and 0.003 GPa at 20 °C, respectively. As a result, they do not provide enough bending stiffness to actuate the system. By contrast, the stiffer 9 mol % DASA–PHMA with a T_g = 62 °C significantly above room temperature, and elastic modulus = 1.608 GPa, outperforms the lower incorporation materials. While the role of the increasing concentration of photothermal agent cannot be decoupled from the resulting change in mechanical properties among these three materials, it is clear that for a given passive bilayer, increasing the active layer stiffness improves actuation performance.

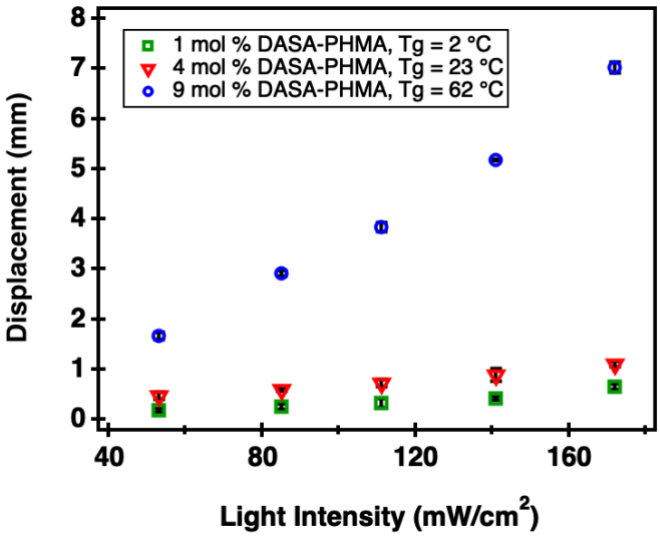

Figure 4.13 Photothermally-driven actuation of DASA-based materials. Averaged peak displacement vs light intensity DASA-PHMA materials, with significantly higher actuation for 9 mol % DASA-PHMA compared to lower incorporations at all light intensities measured.

In order to decouple the changes in thermal and mechanical properties of DASA-based materials that result from increasing DASA incorporation, we next tested the materials with differing comonomer composition, thereby allowing us to increase the DASA incorporation without changing the T_g or modulus values and evaluated their actuation performance in our cantilever device. Now, despite the significant differences in DASA incorporation, we measured very similar temperatures for all three materials, as shown in Figure 4.12d. Moreover, we observed similar displacements and temperatures at the same light intensities as the concentration of DASA increases (Figure 4.12e, Figure 4.14 and Table 4.3). Initially, we were surprised by this result because one would anticipate that higher concentration of the photothermal DASA agent would provide better performance. However, this result is consistent with the Beer-Lambert law where sample heating reaches an

asymptotic limit when chromophore absorbance values are greater than ~1.[40,45] Due to the high molar extinction coefficient of DASA (~100,000 M^{-1} cm^{-1}), even at the lowest incorporation of 1 mol % DASA, the absorbance of the active layer has already reached this limit. Given that these materials have higher T_g values (~60 °C), they will have reduced forward photoswitching rates compared to the lower T_g materials, thus negligible short-term switching unlike the 1 mol % DASA-PHMA with a T_g = 2 °C. Together, these results establish that short-term actuation performance is not dependent on DASA incorporation in the range of 1-9 mol %, and that the actuation amplitude is primarily governed by the stiffness of the material as reported by the T_g and modulus.

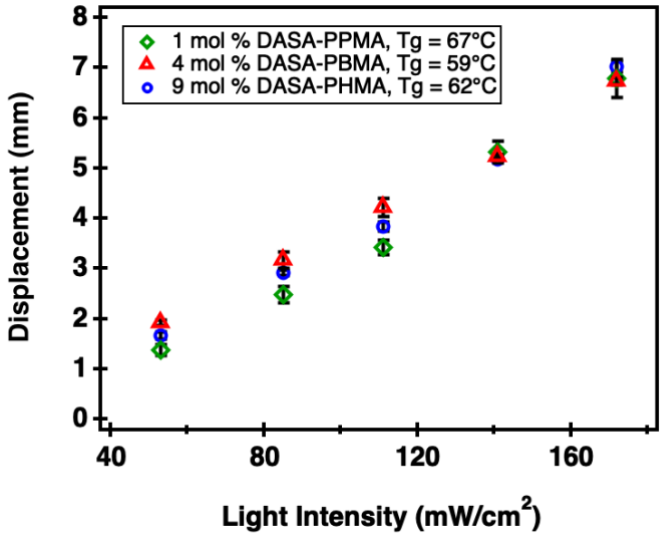

Figure 4.14 Photothermally-driven actuation of DASA-based materials. Averaged peak displacement vs light intensity for DASA materials with increasing DASA incorporation and different methacrylate comonomers (PXMA), with similar displacement at all light intensities measured.

Table 4.3 Summary of material properties of DASA-based materials.

Material	T_g	Modulus[a]	CTE[b] ($\times 10^{-6}$ /°C)	Temp.[c]	Displacement[c]
1 mol % DASA-PHMA	2 °C	0.003 GPa	142.8 ± 1.4	52.1 °C ± 3.6	0.65 ± 0.06 mm
4 mol % DASA-PHMA	23 °C	0.495 GPa	153.6 ± 0.9	57.9 °C ± 1.7	1.11 ± 0.06 mm
9 mol % DASA-PHMA	62 °C	1.608 GPa	148.4 ± 0.6	62.4 °C ± 0.9	7.0 ± 0.1 mm
1 mol % DASA-PPMA	67 °C	1.613 GPa	134.7 ± 1.1	58.0 °C ± 0.8	6.8 ± 0.4 mm
4 mol % DASA-PBMA	59 °C	1.604 GPa	140.2 ± 0.7	61.7 °C ± 1.4	6.73 ± 0.08 mm

[a]Measured at 20 °C by 1 Hz oscillation in the small strain regime. [b]Measured in the glassy state from -50 + T_g to -10 + T_g. [c] Measured at 172 mW/cm^2.

4.7. Photo-induced material property changes

Unlike traditional photothermal agents or photoswitches, which absorb light in both states, DASAs are colorless and non-absorbing in the switched state. This negative photochromism significantly impacts our photothermal material and provides a unique opportunity to leverage the properties of DASA in actuator design. To determine the relationship between actuation and photoswitching, we measured the long-term actuation performance. For these studies we compared the 1 mol % DASA-PPMA, 4 mol % DASA-PBMA and 9 mol % DASA-PHMA, all with high T_g values of ~ 60 °C and DASA-layer with a thickness of 10 μm. Based on studies of bleaching front propagation in solution,[40] we anticipate that the bleaching front propagates faster in the case of lower DASA incorporation, lowering the absorbance below the asymptotic limit more quickly than for the case of higher DASA incorporation. Experimentally, this was confirmed: as shown in Figure 4.15, the 1 mol % DASA–PPMA decreases in absorbance and maximum displacement more quickly than the 9 mol % DASA–PHMA. However, the 4 mol % DASA-PBMA and 9 mol

% DASA-PHMA had surprisingly similar long-term performance. Thus, while DASA incorporation does not govern the initial displacement obtained under short-term irradiation, it plays a role in how long the actuator has chemical energy (in the form of the light-absorbing species) to sustain the maximum (peak) performance.

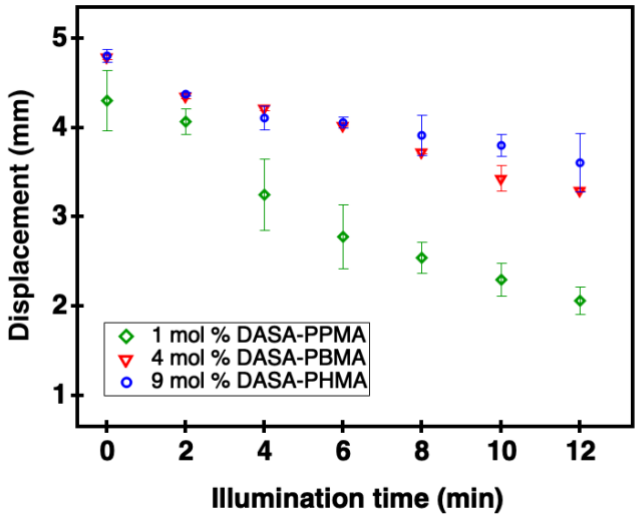

Figure 4.15 Long-term actuation performance of 1 mol % DASA-PPMA, 4 mol % DASA-PBMA and 9 mol % DASA-PHMA. 1 mol % DASA–PPMA decreases in absorbance and maximum displacement more quickly than the 9 mol % DASA–PHMA, but 4 mol % DASA-PBMA and 9 mol % DASA-PHMA have surprisingly similar displacement. We hypothesize this is due to 1) change in absorbance 2) change in material properties.

The difference in performance under long irradiation times led us to also investigate the light-induced changes in mechanical properties between the photoreactant (open-form) and photoproduct (closed-form), which we anticipate may arise from the large change in molecular volume,[44] polarity[25,44] and molecular interactions between the isomers. Using DSC, we determined the T_g of the closed-form 9 mol % DASA-PHMA using the first

cooling cycle. This contrasts our analysis of the open-form material, where three cooling cycles were analyzed, as subsequent heating cycles will thermally recover DASA to the open form as previously shown. These results show there is a marked decrease in T_g of ~20 °C between the open (62 °C) and closed (42 °C) DASA forms, as shown in Figure 4.16a. The glass transition step is followed by a relaxation enthalpy due to the non-equilibrium state. We suspect the decrease in T_g is due to the change in volume between the extended, open-form and compact, closed-form. The photo-induced reduction in T_g is also supported by DMA as shown in Figure 4.16b. In addition, we observed a drop in elastic modulus at 20 °C between the open- and closed-form by DMA from 1.608 GPa to 1.130 GPa, as measured by 1 Hz oscillation in the small strain regime as shown in Figure 4.16a. This suggests that the long-term actuation behavior is much more complex than a simple change in absorbance/temperature change, and that there is a simultaneous and coupled change in material properties (modulus and T_g). To fully unlock the design potential of DASA-based materials, it is imperative to consider how these property changes may play a role in short- and long-term actuation performance, as well as the photoswitching reaction rates which are highly dependent on these properties. To the best of our knowledge this is the first example of photo-induced mechanical property changes of DASA-based materials. Such property changes have been observed in azobenzene-modified materials, although at near 100% photochrome incorporation.[36] The ability to access significant property changes at relatively low (<10%) DASA incorporation shines light on the promise of DASAs to achieve for more complex photo-induced property changes, in addition to their promise for applications in photoactuation.

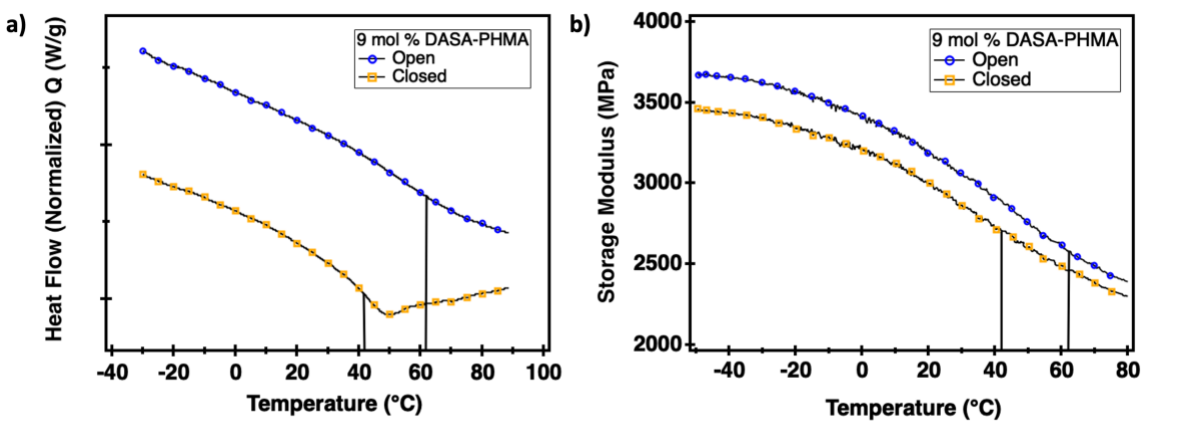

Figure 4.16 Photo-induced changes in mechanical properties between the open and closed-form of DASA. a) 9 mol % DASA–PHMA shows a 20 °C drop in T_g upon switching by DSC. b) A decrease in elastic modulus between open and closed-form at all temperatures is also observed using DMA. The vertical lines indicate the T_g. Reprinted with permission from *ACS Appl. Polym. Mater.* **2022**, *accepted*.[1] Copyright 2022 American Chemical Society. https://doi.org/10.1021/acsapm.1c01108

4.8. Conclusion

Utilizing a modular Diels–Alder synthetic approach, we designed five materials which systematically vary in DASA incorporation and glass transition temperature, as well as properties governing actuation performance such as elastic modulus. The results demonstrate important considerations for the design of application-geared DASA-materials, which address the trade-off of having a material that is stiff enough to actuate, but soft enough to reversibly switch at the operating temperature. Additionally, our results reveal light-induced property changes in T_g and modulus between the open and closed forms of DASA-based materials. This work establishes the foundational relationships between

mechanical and photoswitching properties and is critical to advancing the use of DASA-based materials.

4.9. References

(1) Sroda, M. M.; Lee, J.; Kwon, Y.; Stricker, F.; Park, M.; Valentine, M. T.; Read de Alaniz, J. The Role of The Glass Transition Temperature on Photothermal Actuation of DASA-Based Polymers. *ACS Appl. Polym. Mater.* **2022**, *accepted*.

(2) Kohlmeyer, R. R.; Chen, J. Wavelength-Selective, IR Light-Driven Hinges Based on Liquid Crystalline Elastomer Composites. *Angew. Chem. Int. Ed.* **2013**, *52* (35), 9234–9237.

(3) Jiang, Z. C.; Xiao, Y. Y.; Yin, L.; Han, L.; Zhao, Y. "Self-Lockable" Liquid Crystalline Diels–Alder Dynamic Network Actuators with Room Temperature Programmability and Solution Reprocessability. *Angew. Chem. Int. Ed.* **2020**, *59* (12), 4925–4931.

(4) Zuo, B.; Wang, M.; Lin, B. P.; Yang, H. Visible and Infrared Three-Wavelength Modulated Multi-Directional Actuators. *Nat. Commun.* **2019**, *10(1)* (4539), 1–11.

(5) Verpaalen, R. C. P.; Pilz da Cunha, M.; Engels, T. A. P.; Debije, M. G.; Schenning, A. P. H. J. Liquid Crystal Networks on Thermoplastics: Reprogrammable Photo-Responsive Actuators. *Angew. Chem. Int. Ed.* **2020**, *59* (11), 4532–4536.

(6) Pilz da Cunha, M.; Ambergen, S.; Debije, M. G.; Homburg, E. F. G. A.; den Toonder, J. M. J.; Schenning, A. P. H. J. A Soft Transporter Robot Fueled by Light. *Adv. Sci.* **2020**, *7* (5), 1–7.

(7) Islam, M. R.; Li, X.; Smyth, K.; Serpe, M. J. Polymer-Based Muscle Expansion and Contraction. *Angew. Chem. Int. Ed.* **2013**, *52* (39), 10330–10333.

(8) Mirvakili, S. M.; Hunter, I. W. Artificial Muscles: Mechanisms, Applications, and Challenges. *Adv. Mater.* **2018**, *30* (6), 1–28.

(9) Qian, X.; Chen, Q.; Yang, Y.; Xu, Y.; Li, Z.; Wang, Z.; Wu, Y.; Wei, Y.; Ji, Y. Untethered Recyclable Tubular Actuators with Versatile Locomotion for Soft Continuum Robots. *Adv. Mater.* **2018**, *30* (29), 1–6.

(10) Lahikainen, M.; Zeng, H.; Priimagi, A. Reconfigurable Photoactuator through Synergistic Use of Photochemical and Photothermal Effects. *Nat. Commun.* **2018**, *9* (1), 1–8.

(11) White, T. J.; Tabiryan, N. V.; Serak, S. V.; Hrozhyk, U. A.; Tondiglia, V. P.; Koerner, H.; Vaia, R. A.; Bunning, T. J. A High Frequency Photodriven Polymer Oscillator. *Soft Matter* **2008**, *4* (9), 1796–1798.

(12) Gelebart, A. H.; Vantomme, G.; Meijer, E. W.; Broer, D. J. Mastering the Photothermal Effect in Liquid Crystal Networks: A General Approach for Self-Sustained Mechanical Oscillators. *Adv. Mater.* **2017**, *29 (18)* (1606712).

(13) Tang, Z.; Gao, Z.; Jia, S.; Wang, F.; Wang, Y. Graphene-Based Polymer Bilayers with Superior Light-Driven Properties for Remote Construction of 3D Structures. *Adv. Sci.* **2017**, *4 (5)* (1600437), 1–10.

(14) Verpaalen, R. C. P.; Engels, T.; Schenning, A. P. H. J.; Debije, M. G. Stimuli-Responsive Shape Changing Commodity Polymer Composites and Bilayers. *ACS Appl. Mater. Interfaces* **2020**, *12* (35), 38829–38844.

(15) Balani, K.; Verma, V.; Agarwal, A.; Narayan, R. *Physical, Thermal, and Mechanical Properties of Polymers*, 1st ed.; John Wiley & Sons, Inc., 2014.

(16) Jiang, W.; Niu, D.; Liu, H.; Wang, C.; Zhao, T.; Yin, L.; Shi, Y.; Chen, B.; Ding, Y.;

Lu, B. Photoresponsive Soft-Robotic Platform: Biomimetic Fabrication and Remote Actuation. *Adv. Funct. Mater.* **2014**, *24* (48), 7598–7604.

(17) Ma, H.; Hou, J.; Wang, X.; Zhang, J.; Yuan, Z.; Xiao, L.; Wei, Y.; Fan, S.; Jiang, K.; Liu, K. Flexible, All-Inorganic Actuators Based on Vanadium Dioxide and Carbon Nanotube Bimorphs. *Nano Lett.* **2017**, *17* (1), 421–428.

(18) Lu, X.; Zhang, H.; Fei, G.; Yu, B.; Tong, X.; Xia, H.; Zhao, Y. Liquid-Crystalline Dynamic Networks Doped with Gold Nanorods Showing Enhanced Photocontrol of Actuation. *Adv. Mater.* **2018**, *30* (14), 1–8.

(19) Kuenstler, A. S.; Kim, H.; Hayward, R. C. Liquid Crystal Elastomer Waveguide Actuators. *Adv. Mater.* **2019**, *31* (24), 25.

(20) Livshits, M. Y.; Razgoniaev, A. O.; Arbulu, R. C.; Shin, J.; McCullough, B. J.; Qin, Y.; Ostrowski, A. D.; Rack, J. J. Generating Photonastic Work from Irradiated Dyes in Electrospun Nanofibrous Polymer Mats. *ACS Appl. Mater. Interfaces* **2018**, *10* (43), 37470–37477.

(21) Ryabchun, A.; Li, Q.; Lancia, F.; Aprahamian, I.; Katsonis, N. Shape-Persistent Actuators from Hydrazone Photoswitches. *J. Am. Chem. Soc.* **2019**, *141* (3), 1196–1200.

(22) Lancia, F.; Ryabchun, A.; Katsonis, N. Molecular Machines. **2019**, *3* (September).

(23) Lee, J.; Sroda, M. M.; Kwon, Y.; El-Arid, S.; Seshadri, S.; Gockowski, L. F.; Hawkes, E. W.; Valentine, M. T.; Read De Alaniz, J. Tunable Photothermal Actuation Enabled by Photoswitching of Donor-Acceptor Stenhouse Adducts. *ACS Appl. Mater. Interfaces* **2020**, *12*, 54075–54082.

(24) Lui, B. F.; Tierce, N. T.; Tong, F.; Sroda, M. M.; Lu, H.; Read de Alaniz, J.; Bardeen,

C. J. Unusual Concentration Dependence of the Photoisomerization Reaction in Donor-Acceptor Stenhouse Adducts. *Photochem. Photobiol. Sci.* **2019**, *18* (6), 1587–1595.

(25) Sroda, M. M.; Stricker, F.; Peterson, J. A.; Bernal, A.; Read de Alaniz, J. Donor–Acceptor Stenhouse Adducts: Exploring the Effects of Ionic Character. *Chem. A Eur. J.* **2021**, *27* (12), 4183–4190.

(26) Lerch, M. M.; Wezenberg, S. J.; Szymanski, W.; Feringa, B. L. Unraveling the Photoswitching Mechanism in Donor-Acceptor Stenhouse Adducts. *J. Am. Chem. Soc.* **2016**, *138* (20), 6344–6347.

(27) Lerch, M. M.; Di Donato, M.; Laurent, A. D.; Medved', M.; Iagatti, A.; Bussotti, L.; Lapini, A.; Buma, W. J.; Foggi, P.; Szymański, W.; Feringa, B. L. Solvent Effects on the Actinic Step of Donor–Acceptor Stenhouse Adduct Photoswitching. *Angew. Chemie Int. Ed.* **2018**, *57* (27), 8063–8068.

(28) Zulfikri, H.; Koenis, M. A. J. J.; Lerch, M. M.; Di Donato, M.; Szymański, W.; Filippi, C.; Feringa, B. L.; Buma, W. J.; Di, M.; Szyma, W.; Filippi, C.; Feringa, B. L.; Buma, W. J. Taming the Complexity of Donor-Acceptor Stenhouse Adducts: Infrared Motion Pictures of the Complete Switching Pathway. *J. Am. Chem. Soc.* **2019**, *141* (18), 7376–7384.

(29) Sanchez, D. M.; Raucci, U.; Ferreras, K. N.; Martínez, T. J. Putting Photomechanical Switches to Work: An Ab Initio Multiple Spawning Study of Donor-Acceptor Stenhouse Adducts. *J. Phys. Chem. Lett.* **2020**, *11* (18), 7901–7907.

(30) Ulrich, S.; Hemmer, J. R.; Page, Z. A.; Dolinski, N. D.; Rifaie-graham, O.; Bruns, N.; Hawker, C. J.; Boesel, L. F.; Read de Alaniz, J. Visible Light-Responsive DASA-

Polymer Conjugates. *ACS Macro Lett.* **2017**, *6*, 738–742.

(31) Eisenbach, C. Effect of Polymer Matrix on the Cis-trans Isomerization of Azobenzene Residues in Bulk Polymers. *Die Makromol. Chemie* **1978**, *179* (10), 2489–2506.

(32) Eisenbach, C. D. Cis-Trans Isomerization of Aromatic Azo Compounds Built in the Polyester Segment of Poly (Ester Urethanes). *Polym. Bull.* **1979**, *1*, 517–522.

(33) Eisenbach, C. D. Investigation of Structure and Segmental Mobility of Poly(Ester Urethane)S By Using Photochromic Azobenzene Probes. *J. Am. Chem. Soc.* **1980**, *21* (2), 309–310.

(34) Eisenbach, C. D. Isomerization of Aromatic Azo Chromophores in Poly(Ethyl Acrylate) Networks and Photomechanical Effect. *Polymer (Guildf).* **1980**, *21* (10), 1175–1179.

(35) St. Amant, A. H.; H. Discekici, E.; J. Bailey, S.; S. Zayas, M.; Song, J.-A.; L. Shankel, S.; N. Nguyen, S.; W. Bates, M.; Anastasaki, A.; J. Hawker, C.; Read de Alaniz, J. Norbornadienes: Robust and Scalable Building Blocks for Cascade "Click" Coupling of High Molecular Weight Polymers. *J. Am. Chem. Soc.* **2019**, *141* (34), 13619–13624.

(36) Shin, J.; Sung, J.; Kang, M.; Xie, X.; Lee, B.; Lee, K. M.; White, T. J.; Leal, C.; Sottos, N. R.; Braun, P. V.; Cahill, D. G. Light-Triggered Thermal Conductivity Switching in Azobenzene Polymers. *Proc. Natl. Acad. Sci.* **2019**, *116* (13), 5973–5978.

(37) Polymer Database: Poly(hexyl methacrylate) https://polymerdatabase.com/polymers/polyhexylmethacrylate.html (accessed Nov 2, 2021).

(38) Hiemenz, P. C.; Lodge, T. P. *Polymer Chemistry*, 3rd ed.; CRC Press, 2020.

(39) Strobl, G. R. *The Physics of Polymers: Concepts for Understanding Their Structures and Behavior*, 3rd ed.; Springer-Verlag Berlin Heidelberg, 2007.

(40) Seshadri, S.; Gockowski, L. F.; Lee, J.; Sroda, M.; Helgeson, M. E.; Read de Alaniz, J.; Valentine, M. T. Self-Regulating Photochemical Rayleigh-Bénard Convection Using a Highly-Absorbing Organic Photoswitch. *Nat. Commun.* **2020**, *11* (1), 1–8.

(41) Hemmer, J. R.; Poelma, S. O.; Treat, N.; Page, Z. A.; Dolinski, N. D.; Diaz, Y. J.; Tomlinson, W.; Clark, K. D.; Hooper, J. P.; Hawker, C.; Read de Alaniz, J. Tunable Visible and Near Infrared Photoswitches. *J. Am. Chem. Soc.* **2016**, *138* (42), 13960–13966.

(42) Dolinski, N. D.; Page, Z. A.; Eisenreich, F.; Niu, J.; Hecht, S.; Read de Alaniz, J.; Hawker, C. J. A Versatile Approach for In Situ Monitoring of Photoswitches and Photopolymerizations. *ChemPhotoChem* **2017**, *1* (4), 125–131.

(43) Hemmer, J. R.; Page, Z. A.; Clark, K. D.; Stricker, F.; Dolinski, N. D.; Hawker, C. J.; Read de Alaniz, J. Controlling Dark Equilibria and Enhancing Donor-Acceptor Stenhouse Adduct Photoswitching Properties through Carbon Acid Design. *J. Am. Chem. Soc.* **2018**, *140* (33), 10425–10429.

(44) Helmy, S.; Leibfarth, F. A.; Oh, S.; Poelma, J. E.; Hawker, C. J.; Read de Alaniz, J. Photoswitching Using Visible Light: A New Class of Organic Photochromic Molecules. *J. Am. Chem. Soc.* **2014**, *136* (23), 8169–8172.

(45) Spence, G. T.; Hartland, G. V.; Smith, B. D. Activated Photothermal Heating Using Croconaine Dyes. *Chem. Sci.* **2013**, *4* (11), 4240–4244.

4.10. Experimental section

Compounds **NBD-MA (4)**[23] **and Azo-maleimide (24)**[35] were prepared according to the literature and matched published spectral analysis.

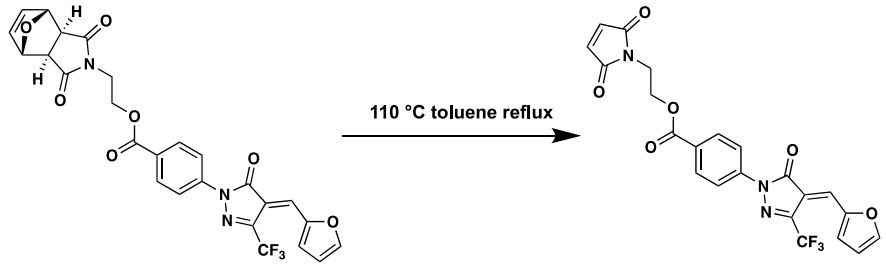

8 9

Scheme 4.2 2-(2,5-dioxo-2,5-dihydro-1H-pyrrol-1-yl)ethyl (E)-4-(4-(furan-2-ylmethylene)-5-oxo-3-(trifluoromethyl)-4,5-dihydro-1H-pyrazol-1-yl)benzoate **(9)**:

9: FA-protected **8** (2.8 g, crude material) was dissolved in 200 mL of toluene and the reaction was stirred for 4 hours under reflux. The solvent was removed under reduced pressure. The product was dissolved in DCM and further purified by running through a silica plug utilizing a mobile phase of Ethyl acetate. The solvent was removed under reduced pressure to yield a solid orange product **9** (1.15 g, 2.43 mmol, 67% yield from crude).
9: ^{1}H NMR (600 MHz, Chloroform-d) δ 8.92 (d, *J* = 3.8 Hz, 1H), 8.13 – 8.04 (m, 4H), 7.91 (dd, *J* = 1.6, 0.6 Hz, 1H), 7.71 (s, 1H), 6.83 (dd, *J* = 3.9, 1.6, 0.8 Hz, 1H), 6.74 (s, 2H), 4.46 (dd, *J* = 5.7, 4.8 Hz, 2H), 3.96 (t, *J* = 5.3 Hz, 2H). ^{13}C NMR (125 MHz, Chloroform-d) δ 170.5, 165.8, 161.6, 151.3, 150.9, 141.7, 134.4, 132.1, 131.0, 128.6, 126.7, 118.6, 116.0, 115.4, 62.3, 37.0. IR (thin film) 3127, 2954, 2175, 2151, 1602, 1537, 1511, 1453, 1432, 1407, 1361, 1328, 1268, 1216, 1181, 1157, 1117, 1093, 1046, 1026, 972, 937, 884, 852,

832, 806, 762, 720, 692, 606, 593, 552, 528, 501, 473 cm^{-1}. HRMS (ESI), calculated for $C_{22}H_{14}F_3N_3NaO_6^+$ ($M+Na^+$) 496.0732, observed 496.0735.

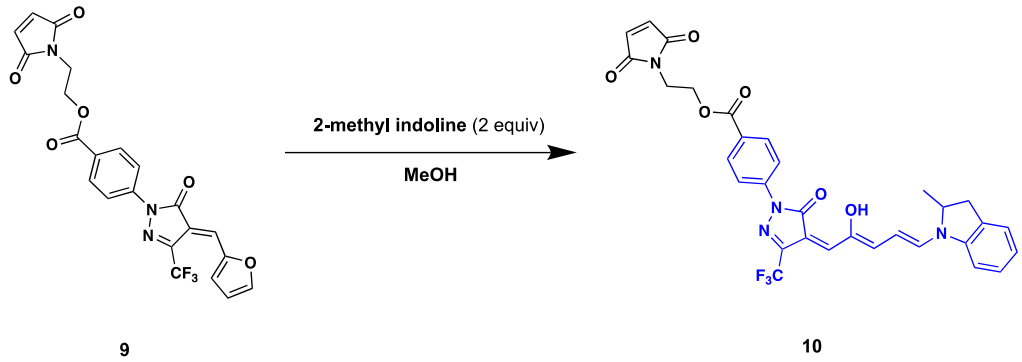

9 10

Scheme 4.3 2-(2,5-dioxo-2,5-dihydro-1H-pyrrol-1-yl)ethyl 4-((Z)-4-((2Z,4E)-2-hydroxy-5-(2-methylindolin-1-yl)penta-2,4-dien-1-ylidene)-5-oxo-3-(trifluoromethyl)-4,5-dihydro-1H-pyrazol-1-yl)benzoate (**10**):

10: The furan adduct **9** (385 mg, 0.813 mmol, 1 equiv) was stirred in minimal methanol (approximately 3 mL) then 2-methylindoline (217 mg, 1.63 mmol, 2 equiv) was added. The reaction was stirred for 2 h and monitored by TLC for consumption of **9**. The reaction mixture was then filtered to yield the product as dark blue crystals and washed with diethyl ether to afford the product **10** (380 mg, 0.627 mmol, 77%).

10: ^{1}H NMR (600 MHz, Chloroform-d) δ 12.90 (s, 1H), 8.12 – 7.98 (m, 4H), 7.70 (d, *J* = 12.6 Hz, 1H), 7.31 (d, *J* = 7.4 Hz, 2H), 7.18 (t, *J* = 7.4 Hz, 1H), 7.10 (d, *J* = 8.0 Hz, 1H), 6.76 (d, *J* = 12.3 Hz, 1H), 6.73 (s, 2H), 6.57 (s, 1H), 6.44 (t, *J* = 12.4 Hz, 1H), 4.74 (t, *J* = 7.4 Hz, 1H), 4.44 (t, *J* = 5.3 Hz, 2H), 3.95 (t, *J* = 5.3 Hz, 2H), 3.54 (dd, *J* = 16.1, 8.7 Hz, 2H), 2.86 (d, *J* = 15.9 Hz, 2H), 1.47 (d, *J* = 6.5 Hz, 3H). Characterization matched published spectral analysis.[23]

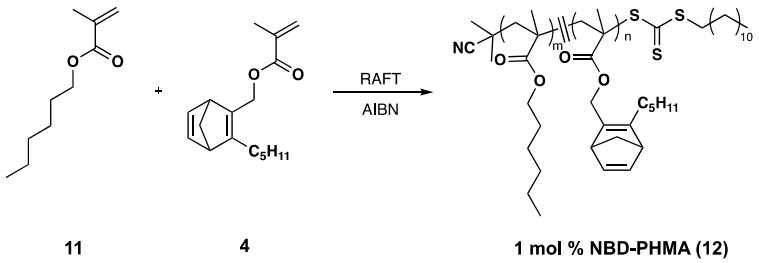

Scheme 4.4 1 mol % NBD–PHMA (**12**):

To access the **1 mol % NBD–PHMA (12)**, : To a round bottom flask equipped with a magnetic stir bar and septum cap, compound **NBD-MA (4)** (68 mg, 0.26 mmol, 6.5 equiv) and hexyl methacrylate **11** (4.58 mL, 23.2 mmol, 580 equiv, HMA) were added and dissolved in tetrahydrofuran (THF, 4.64 mL). To this solution, azobisisobutyronitrile (AIBN, 1.3 mg, 0.008 mmol, 0.2 equiv) and 2-cyano-2-propyl dodecyl trithiocarbonate (13.8 mg, 0.040 mmol, 1.0 equiv) were added to the reaction vial and the polymerization was degassed by nitrogen bubbling for 10 minutes. The polymerization was left to react at 60 °C and a crude ^{1}H NMR spectrum was taken in deuterated chloroform to estimate monomer conversion (75%). The THF was removed under reduced pressure and the crude mixture was redissolved in a minimal amount of DCM. The mixture was precipitated into cold methanol. The solid was redissolved in DCM and the precipitation process was repeated a total of 3-4 times. ^{1}H NMR analysis indicates approximately 1% of NBD functionality. $M_{n(theoretical)}$ = 75,000 g/mol, $M_{n(NMR)}$ = 83,000 g/mol, $M_{n(SEC)}$ = 59,000 g/mol, $Đ$ = 1.34

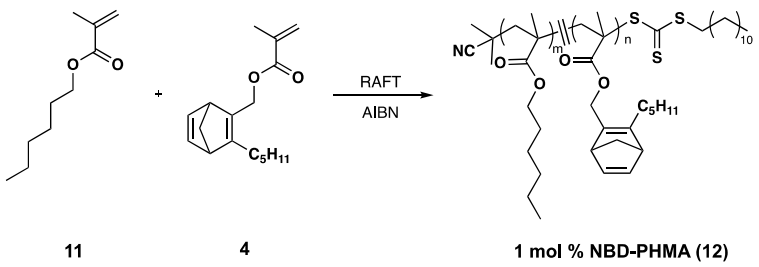

Scheme 4.5 4 mol % NBD–PHMA (**12**):

4 mol % NBD–PHMA (12): To a round bottom flask equipped with a magnetic stir bar and septum cap, compound **NBD-MA (4)** (234 mg, 0.90 mmol, 30 equiv) and hexyl methacrylate **11** (3.23 mL, 16.35 mmol, 545 equiv, HMA) were added and dissolved in THF (3.46 mL). To this solution, AIBN (1.0 mg, 0.006 mmol, 0.2 equiv) and 2-cyano-2-propyl dodecyl trithiocarbonate (10.4 mg, 0.030 mmol, 1.0 equiv) were added to the reaction vial and the polymerization was degassed by nitrogen bubbling for 10 minutes. The polymerization was left to react at 60 °C and a crude ^{1}H NMR spectrum was taken in deuterated chloroform to estimate monomer conversion (70%). The THF was removed under reduced pressure and the crude mixture was redissolved in a minimal amount of DCM. The mixture was precipitated into cold methanol. The solid was redissolved in DCM and the precipitation process was repeated a total of 3-4 times. ^{1}H NMR analysis indicates approximately 5% of NBD functionality. Conversion 70%, $M_{n(theoretical)}$ = 70,000 g/mol, $M_{n(NMR)}$ = 81,000 g/mol, $M_{n(SEC)}$ = 59,000 g/mol, $Đ$ = 1.70.

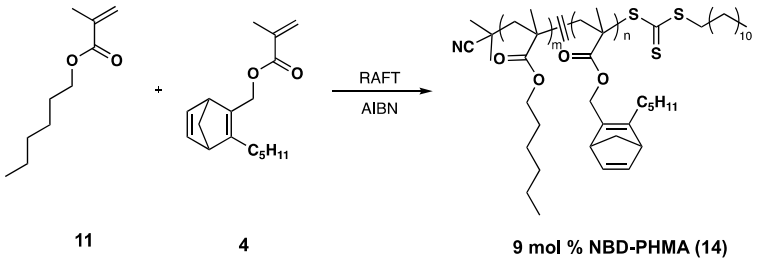

11 4 9 mol % NBD-PHMA (14)

Scheme 4.6 9 mol % NBD–PHMA (14):

9 mol % NBD–PHMA (14): To a round bottom flask equipped with a magnetic stir bar and septum cap, compound **NBD-MA (4)** (916 mg, 3.52 mmol, 58 equiv) and hexyl methacrylate **11** (6.0 mL, 30.4 mmol, 502 equiv, HMA) were added and dissolved in THF (6.0 mL). To this solution, AIBN (2.0 mg, 0.012 mmol, 0.2 equiv) and 2-cyano-2-propyl dodecyl trithiocarbonate (21.0 mg, 0.061 mmol, 1.0 equiv) were added to the reaction vial and the polymerization was degassed by nitrogen bubbling for 10 minutes. The polymerization was left to react at 60 °C and a crude ^{1}H NMR spectrum was taken in deuterated chloroform to estimate monomer conversion (55%). The THF was removed under reduced pressure and the crude mixture was redissolved in a minimal amount of DCM. The mixture was precipitated into cold methanol. The solid was redissolved in DCM and the precipitation process was repeated a total of 3-4 times. ^{1}H NMR analysis indicates approximately 9% of NBD functionality. Conversion 55%, $M_{n(theoretical)}$ = 55,000 g/mol, $M_{n(NMR)}$ = 45,000 g/mol, $M_{n(SEC)}$ = 39,000 g/mol, $Đ$ = 1.46.

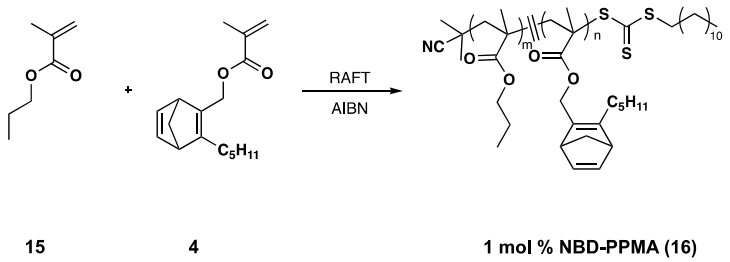

15 4 1 mol % NBD-PPMA (16)

Scheme 4.7 1 mol % NBD–PPMA (**16**):

1 mol % NBD–PPMA (16): To a round bottom flask equipped with a magnetic stir bar and septum cap, compound **NBD-MA (4)** (104 mg, 0.4 mmol, 10 equiv) and propyl methacrylate **15** (4.34 mL, 30.4 mmol, 760 equiv, PMA) were added and dissolved in THF (4.44 mL). To this solution, AIBN (1.3 mg, 0.008 mmol, 0.2 equiv) and 2-cyano-2-propyl dodecyl trithiocarbonate (13.8 mg, 0.040 mmol, 1.0 equiv) were added to the reaction vial and the polymerization was degassed by nitrogen bubbling for 10 minutes. The polymerization was left to react at 60 °C and a crude ^{1}H NMR spectrum was taken in deuterated chloroform to estimate monomer conversion (70%). The THF was removed under reduced pressure and the crude mixture was redissolved in a minimal amount of DCM. The mixture was precipitated into cold methanol. The solid was redissolved in DCM and the precipitation process was repeated a total of 3-4 times. ^{1}H NMR analysis indicates approximately 1% of NBD functionality. Conversion 70%, $M_{n(theoretical)}$ = 70,000 g/mol, $M_{n(NMR)}$ = 60,000 g/mol, $M_{n(SEC)}$ = 59,000 g/mol, $Đ$ = 1.40.

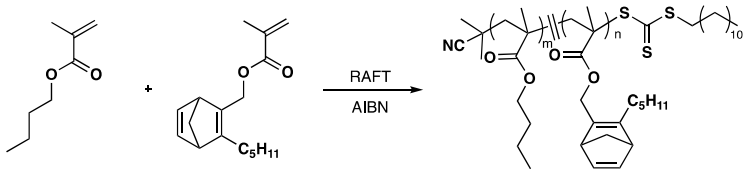

17 4 4 mol % NBD-PBMA (18)

Scheme 4.8 4 mol % NBD–PBMA (**16**):

4 mol % NBD–PBMA (18): To a round bottom flask equipped with a magnetic stir bar and septum cap, compound **NBD-MA (4)** (258 mg, 0.99 mmol, 33 equiv) and butyl methacrylate **17** (2.86 mL, 18.0 mmol, 600 equiv, BMA) were added and dissolved in THF (3.12 mL). To this solution, AIBN (1.0 mg, 0.006 mmol, 0.2 equiv) and 2-cyano-2-propyl dodecyl trithiocarbonate (10.4 mg, 0.030 mmol, 1.0 equiv) were added to the reaction vial and the polymerization was degassed by nitrogen bubbling for 10 minutes. The polymerization was left to react at 60 °C and a crude ^{1}H NMR spectrum was taken in deuterated chloroform to estimate monomer conversion (80%). The THF was removed under reduced pressure and the crude mixture was redissolved in a minimal amount of DCM. The mixture was precipitated into cold methanol. The solid was redissolved in DCM and the precipitation process was repeated a total of 3-4 times. ^{1}H NMR analysis indicates approximately 5% of NBD functionality. Conversion 80%, $M_{n(theoretical)}$ = 80,000 g/mol, $M_{n(NMR)}$ = 83,000 g/mol, $M_{n(SEC)}$ = 68,000 g/mol, $Đ$ = 1.85.

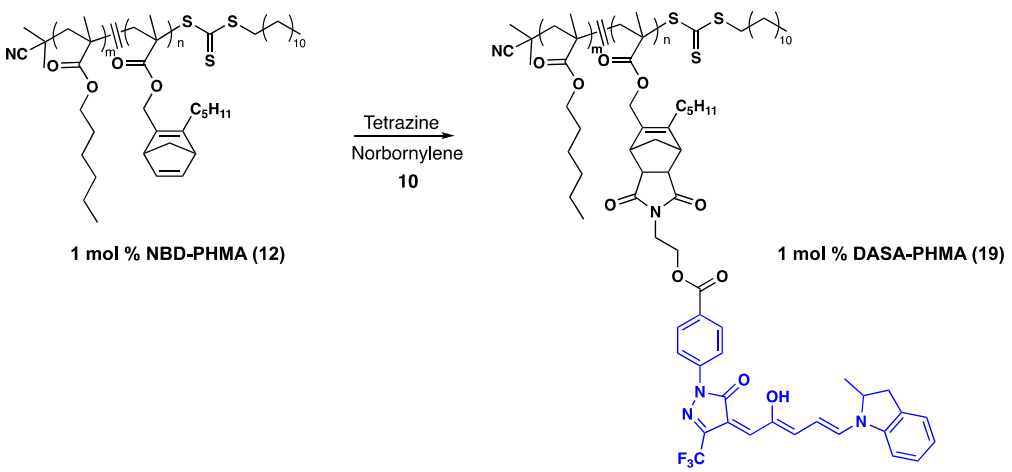

Scheme 4.9 1 mol % DASA–PHMA (**19**):

1 mol % DASA–PHMA (19): 1 mol % NBD–PHMA (12) (842 mg, 0.010 mmol, 1 equiv) and 3,6-di-2-pyridyl-1,2,4,5-tetrazine (21 mg, 0.090 mmol, 9 equiv, DpTz) were combined in $CDCl_3$ (100 mg/mL, 8.42 mL) under nitrogen atmosphere. The solution was stirred for 8 h and complete conversion of NBD to cyclopentadiene was monitored by ^{1}H NMR. Upon completion, norbornylene (8.5 mg, 0.090 mmol, 9 equiv) was added to quench the excess DpTz. The solution transitions from a pink to yellow color upon completion. To this, DASA–maleimide **10** (36 mg, 0.060 mmol, 6 equiv) was added. The reaction was left to stir for 15 h. The DCM was removed under reduced pressure and the crude mixture was redissolved in a minimal amount of DCM. The mixture was precipitated into cold methanol. The solid was redissolved in DCM and the precipitation process was repeated a total of 3-4 times. ^{1}H NMR analysis indicated incorporation of 1% of DASA functionality. ^{1}H NMR (600 MHz, $CDCl_3$) δ/ppm: 8.22-7.95 (4H, phenyl peaks), 4.05-3.85 (2H, polymer backbone). $M_{n(SEC)}$ = 72,000 g/mol, $Đ$ = 2.31. T_g (DSC) = 2°C. T_g (DMA) = 7°C.

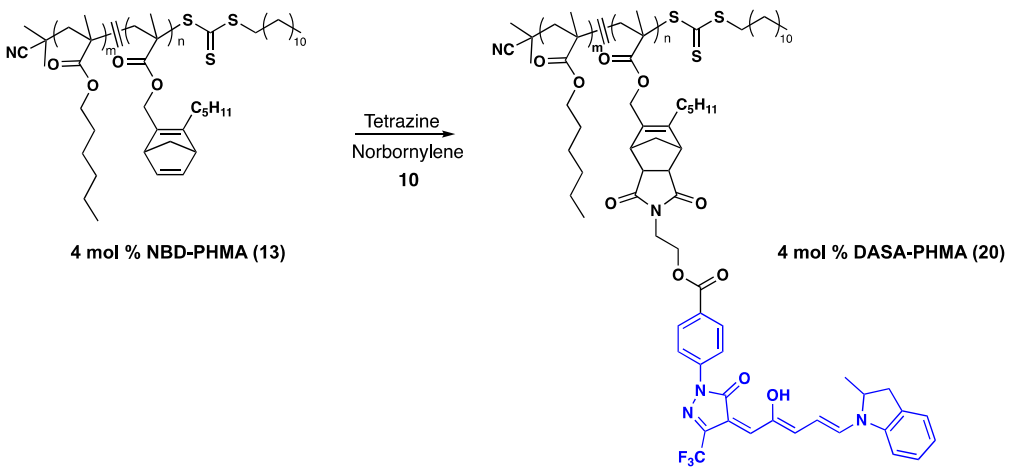

Scheme 4.10 4 mol % DASA–PHMA (**20**):

4 mol % DASA–PHMA (20): 4 mol % NBD–PHMA (13) (1.0 g, 0.012 mmol, 1 equiv) and 3,6-di-2-pyridyl-1,2,4,5-tetrazine (77 mg, 0.33 mmol, 27.5 equiv, DpTz) were combined in $CDCl_3$ (100 mg/mL, 10 mL) under nitrogen atmosphere. The solution was stirred for 8 h and complete conversion of NBD to cyclopentadiene was monitored by ^{1}H NMR. Upon completion, norbornylene (31 mg, 0.33 mmol, 27.5 equiv) was added to quench the excess DpTz. The solution transitions from a pink to yellow color upon completion. The reaction was diluted to 20 mg/mL and DASA–maleimide **10** (127 mg, 0.21 mmol, 17.5 equiv) was added. The reaction was left to stir for 15 h. The DCM was removed under reduced pressure and the crude mixture was redissolved in a minimal amount of DCM. The mixture was precipitated into cold methanol. The solid was redissolved in DCM and the precipitation process was repeated a total of 3-4 times. ^{1}H NMR analysis indicated incorporation of 4% of DASA functionality. ^{1}H NMR (600 MHz, $CDCl_3$) δ/ppm: 8.21-7.90 (4H, phenyl peaks), 4.02-3.84 (2H, polymer backbone). $M_{n(SEC)}$ = 65,000 g/mol, $Đ$ = 2.49. T_g (DSC) = 23°C. T_g (DMA) = 25°C.

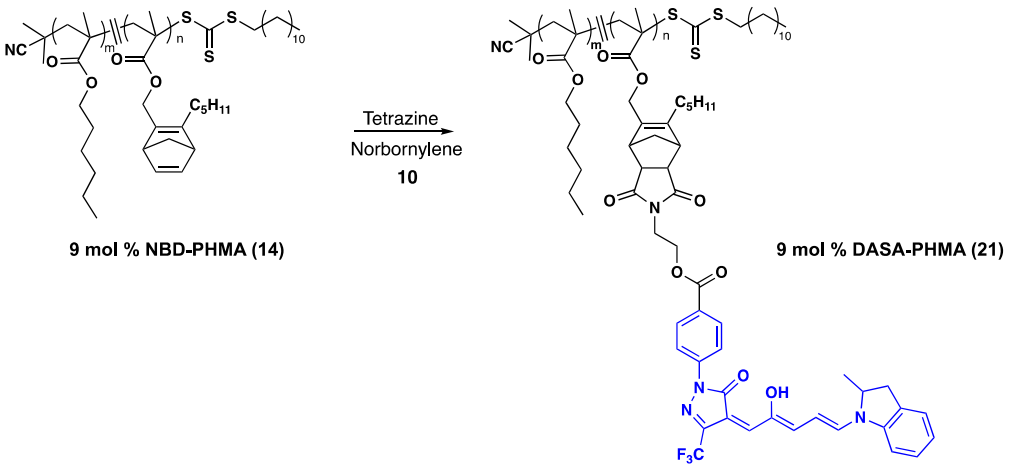

Scheme 4.11 9 mol % DASA–PHMA (**21**):

9 mol % DASA–PHMA (21): 9 mol % NBD–PHMA (14) (1.5 g, 0.033 mmol, 1 equiv) and 3,6-di-2-pyridyl-1,2,4,5-tetrazine (239 mg, 1.01 mmol, 30 equiv, DpTz) were combined in $CDCl_3$ (100 mg/mL, 10 mL) under nitrogen atmosphere. The solution was stirred for 8 h and complete conversion of NBD to cyclopentadiene was monitored by ^{1}H NMR. Upon completion, norbornylene (95 mg, 1.01 mmol, 30 equiv) was added to quench the excess DpTz. The solution transitions from a pink to yellow color upon completion. The reaction was diluted to 10 mg/mL and DASA–maleimide **10** (456 mg, 0.75 mmol, 23 equiv) was added. The reaction was left to stir for 15 h. The DCM was removed under reduced pressure and the crude mixture was redissolved in a minimal amount of DCM. The mixture was precipitated into cold methanol. The solid was redissolved in DCM and the precipitation process was repeated a total of 3-4 times. ^{1}H NMR analysis indicated incorporation of 9% of DASA functionality. ^{1}H NMR (600 MHz, $CDCl_3$) δ/ppm: 8.21-7.90 (4H, phenyl peaks), 4.04-3.82 (2H, polymer backbone). $M_{n(theoretical)}$ = 53,000 g/mol. T_g (DSC) = 62 °C. T_g (DMA) = 68 °C.

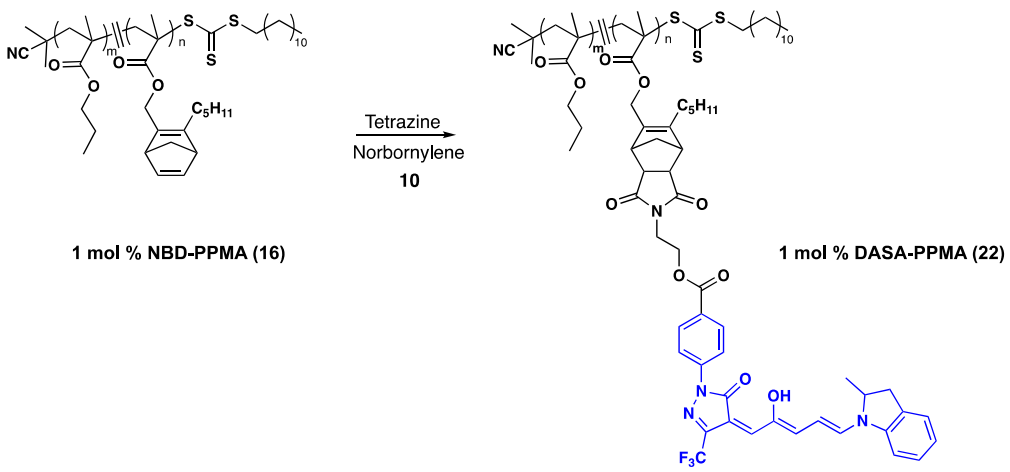

Scheme 4.12 1 mol % DASA–PPMA (**22**):

1 mol % DASA–PPMA (22): 1 mol % NBD–PPMA (16) (1.75 g, 0.0292 mmol, 1 equiv) and 3,6-di-2-pyridyl-1,2,4,5-tetrazine (65 mg, 0.275 mmol, 9 equiv, DpTz) were combined in $CDCl_3$ (100 mg/mL, 17.5 mL) under nitrogen atmosphere. The solution was stirred for 8 h and complete conversion of NBD to cyclopentadiene was monitored by ^{1}H NMR. Upon completion, norbornylene (26 mg, 0.275 mmol, 9 equiv) was added to quench the excess DpTz. The solution transitions from a pink to yellow color upon completion. The reaction was diluted to 50 mg/mL, DASA–maleimide **10** (104 mg, 0.172 mmol, 6 equiv) was added. The reaction was left to stir for 15 h. The DCM was removed under reduced pressure and the crude mixture was redissolved in a minimal amount of DCM. The mixture was precipitated into cold methanol. The solid was redissolved in DCM and the precipitation process was repeated a total of 3-4 times. ^{1}H NMR analysis indicated incorporation of 1% of DASA functionality. ^{1}H NMR (600 MHz, $CDCl_3$) δ/ppm: 8.22-7.96 (4H, phenyl peaks), 4.07-3.77 (2H, polymer backbone). $M_{n(SEC)}$ = 74,000 g/mol, $Đ$ = 2.21. Tg (DSC) = 66 °C. T_g (DMA) = 67 °C.

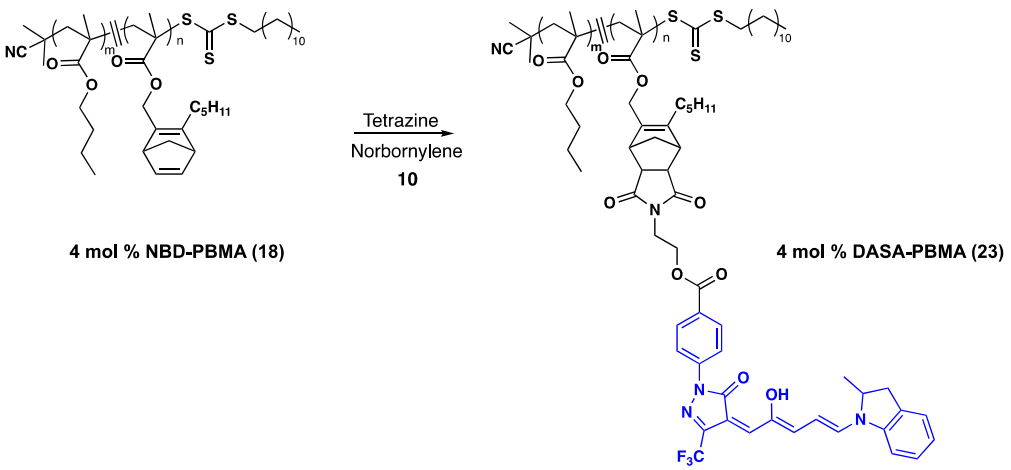

Scheme 4.13 4 mol % DASA–PBMA (**23**):

4 mol % DASA–PBMA (23): 4 mol % NBD–PBMA (18) (1.0 g, 0.012 mmol, 1 equiv) and 3,6-di-2-pyridyl-1,2,4,5-tetrazine (90 mg, 0.381 mmol, 32 equiv, DpTz) were combined in $CDCl_3$ (100 mg/mL, 10 mL) under nitrogen atmosphere. The solution was stirred for 8 h and complete conversion of NBD to cyclopentadiene was monitored by ^{1}H NMR. Upon completion, norbornylene (36 mg, 0.381 mmol, 32 equiv) was added to quench the excess DpTz. The solution transitions from a pink to yellow color upon completion. The reaction was diluted to 20 mg/mL and DASA–maleimide **10** (151 mg, 0.249 mmol, 23 equiv) was added. The reaction was left to stir for 15 h. The DCM was removed under reduced pressure and the crude mixture was redissolved in a minimal amount of DCM. The mixture was precipitated into cold methanol. The solid was redissolved in DCM and the precipitation process was repeated a total of 3-4 times. ^{1}H NMR analysis indicated incorporation of 4% of DASA functionality. ^{1}H NMR (600 MHz, $CDCl_3$) δ/ppm: 8.21-7.90 (4H, phenyl peaks), 4.05-3.83 (2H, polymer backbone). $M_{n(SEC)}$ = 63,000 g/mol, $Đ$ = 2.37. T_g (DSC) = 59 °C. T_g (DMA) = 57 °C.

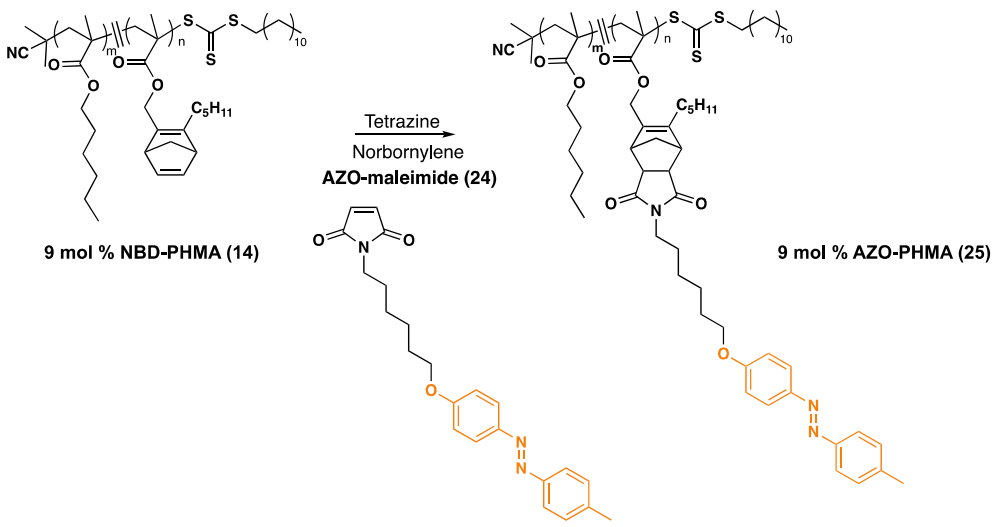

Scheme 4.14 9 mol % Azo-PHMA (**25**):

9 mol % Azo-PHMA (25): **9 mol % NBD–PHMA (14)** (1.2 g, 0.0312 mmol, 1 equiv) and 3,6-di-2-pyridyl-1,2,4,5-tetrazine (260 mg, 1.09 mmol, 35 equiv, DpTz) were combined in $CDCl_3$ (100 mg/mL, X mL) under nitrogen atmosphere. The solution was stirred for 8 h and complete conversion of NBD to cyclopentadiene was monitored by ^{1}H NMR. Upon completion, norbornylene (102 mg, 1.09 mmol, 35 equiv) was added to quench the excess DpTz. The solution transitions from a pink to yellow color upon completion. The reaction was diluted to 10 mg/mL and **Azo–maleimide (24)**[35] (205 mg, 0.524 mmol, 17 equiv) was added. The reaction was left to stir for 15 h. The DCM was removed under reduced pressure and the crude mixture was redissolved in a minimal amount of DCM. The mixture was precipitated into cold methanol. The solid was redissolved in DCM and the precipitation process was repeated a total of 3-4 times. ^{1}H NMR analysis indicated incorporation of 9% of DASA functionality. ^{1}H NMR (600 MHz, $CDCl_3$) δ/ppm: 7.93-7.84 (2H, phenyl peaks), 3.98-3.82 (2H, polymer backbone). $M_{n(SEC)}$ = 44,000 g/mol, $Đ$ = 1.61. T_g (DSC) = 5 °C.

10 was previously synthesized as shown in Scheme 4.15.[23] While this method yielded **10**, it was wasteful and did not scale well (< 500 mg). The major limitations of the current method included: 1) this route required column chromatography of FA-protected (**8**), which had a tendency to stick to the silica column and required large amount of ethyl acetate, which had to then be removed, 2) the solid-state deprotection of **26** at 110 °C had long reaction times varying from 36-72 hours depending on scale (< 1g), 3) the solid-state deprotection of **26** could not be scaled over a gram and resulted in increasing reaction times >72 hours that resulted in decomposition prior to full deprotection, thus destroying precious material. Accessing a gram of material took roughly a week and a lot of ethyl acetate. To overcome these challenges, we sought an alternative to the solid-state deprotection of DASA-maleimide. In solution DASA decomposed prior to deprotection under reflux in toluene. However, we found that the FA-protected (**8**) could be deprotected to the FA-maleimide (**9**) under reflux in toluene, and that this reaction could be performed on larger scales (2.8 g) with shorter reaction times (< 4 hr). In addition, the FA-protected (**8**) could be used crude and taken directly from the EDC work-up and deprotected. Moreover, the FA-maleimide (**9**) was much more soluble than the protected-FA, allowing us to run a quick plug, which saved time and reduced waste. The plugged material could be reacted with 2-methyl indoline to yield DASA-maleimide **10**, as shown in Scheme 4.16. However, this route was not initially taken as the 2-methyl indoline could potentially add in through a Michael-addition with the functional maleimide handle. We found even with 2 equivalents of amine the maleimide remained intact by ^{1}H NMR. Overall, this approach offered several advantages: the solution-state FA-protected (**8**) could be scaled with moderate reaction times, due to changes in solubility the FA-maleimide (**9**) could be purified via a plug, and

the DASA forming step yield was increased from 52% to 77%. Most importantly, using the optimized route, FA-protected (**8**) could be brought forward to the DASA-maleimide (**10**) in one 8-hour shift saving time and resources.

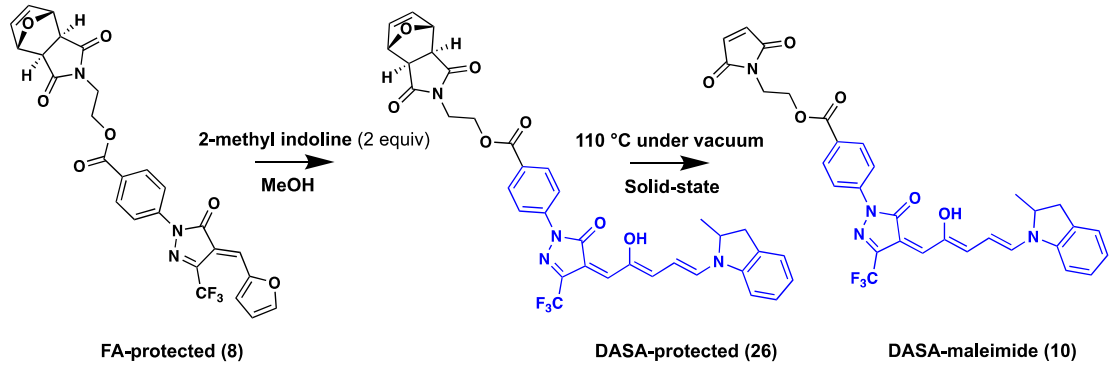

Scheme 4.15 Previous synthetic route to **10**.

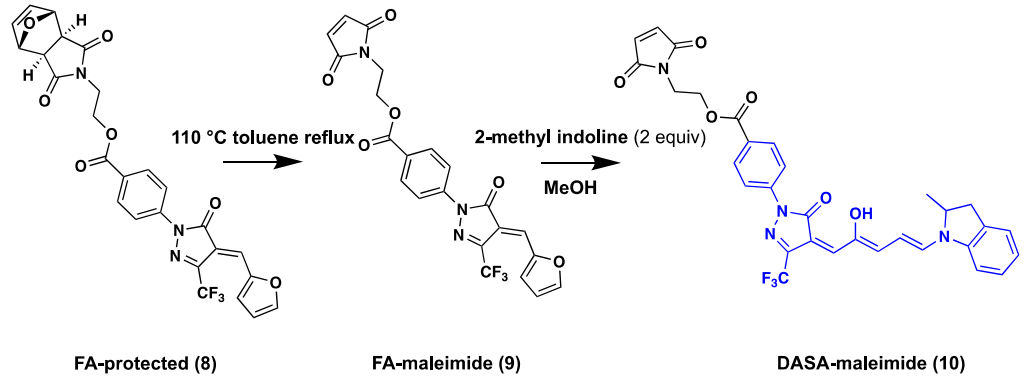

Scheme 4.16 Optimized synthetic route to **10**.

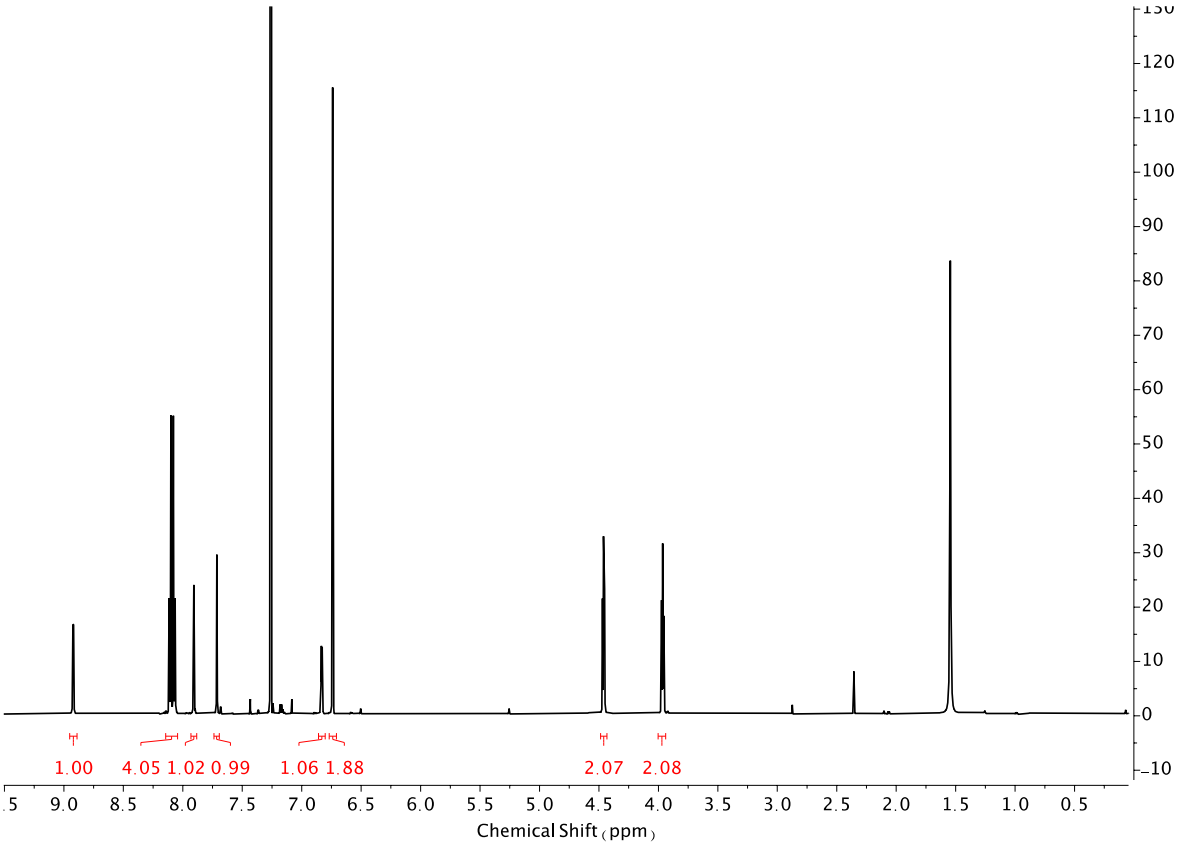

Scheme 4.17 ^{1}H NMR of **FA-maleimide (9)** in Chloroform-d.

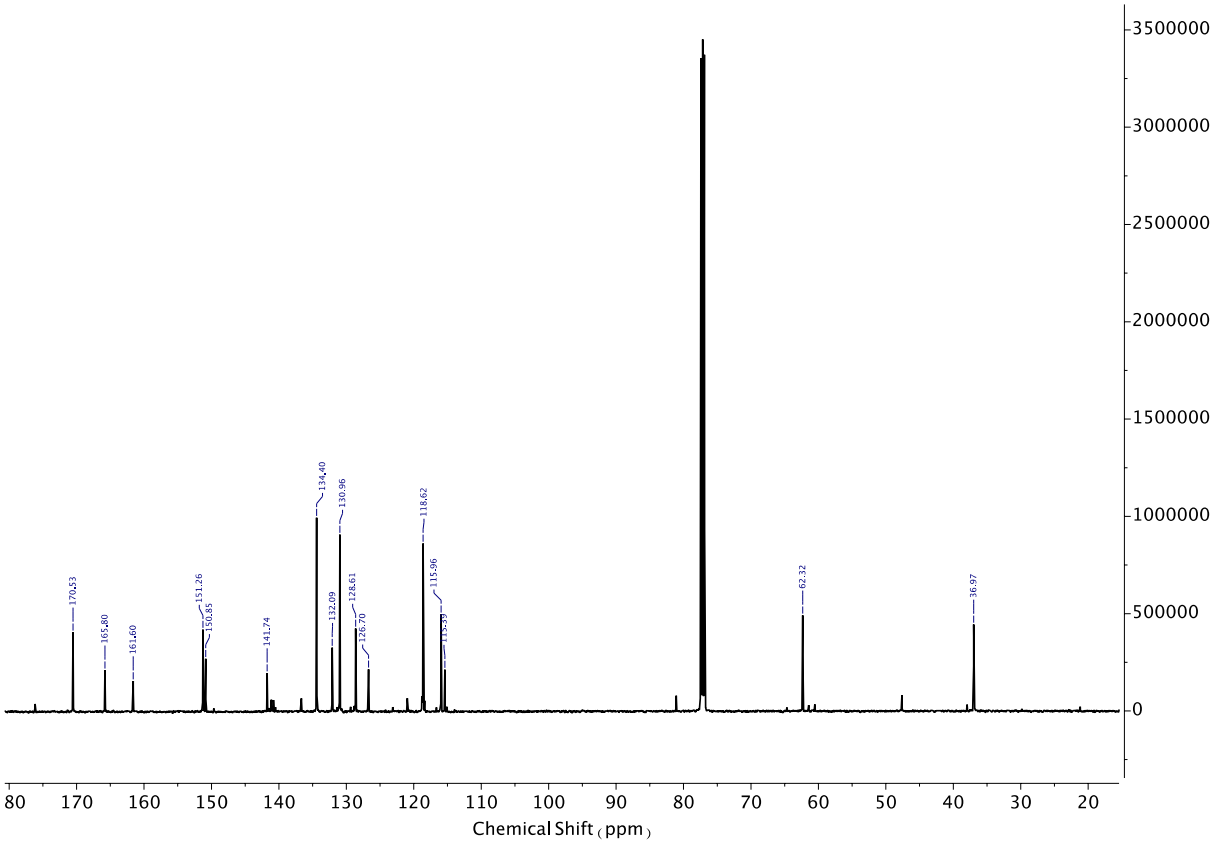

Scheme 4.18 ^{13}C NMR of **FA-maleimide (9)** in Chloroform-d.

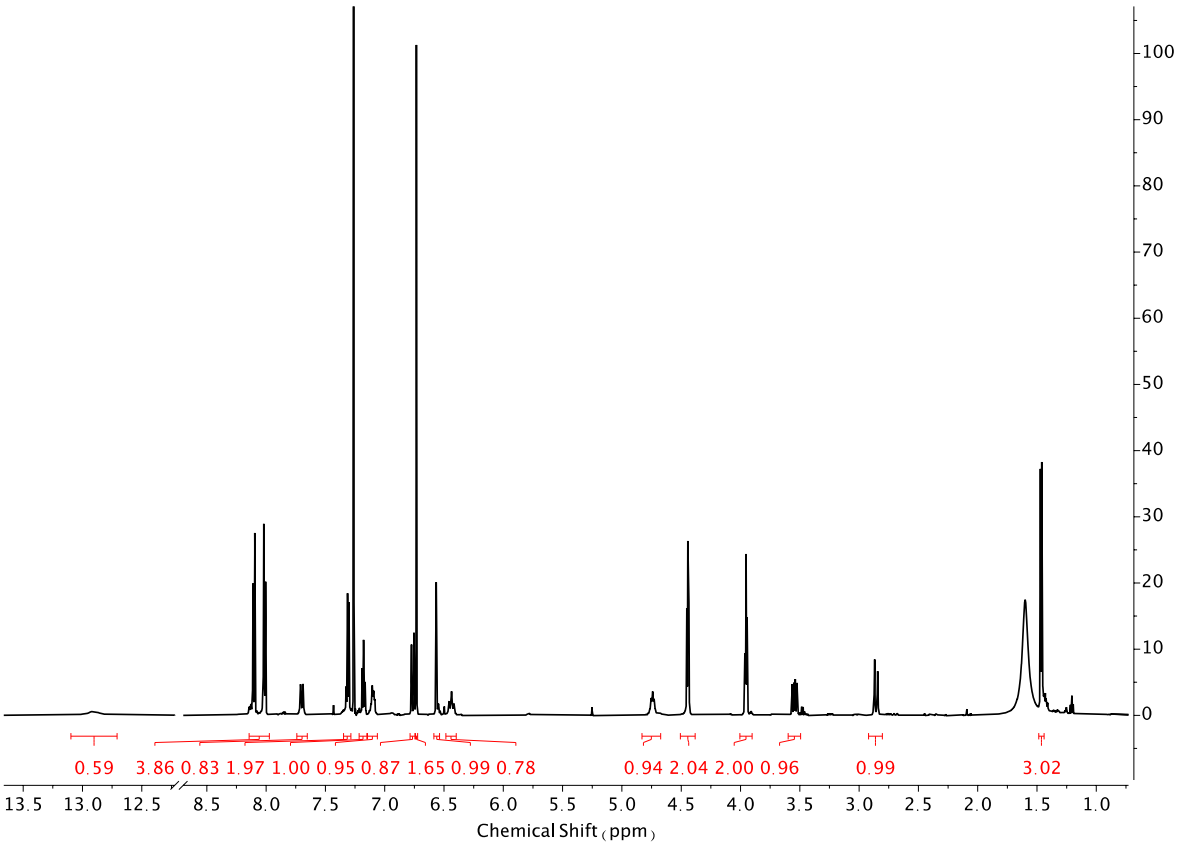

Scheme 4.19 ^{1}H NMR of **DASA-maleimide (10)** in Chloroform-d.

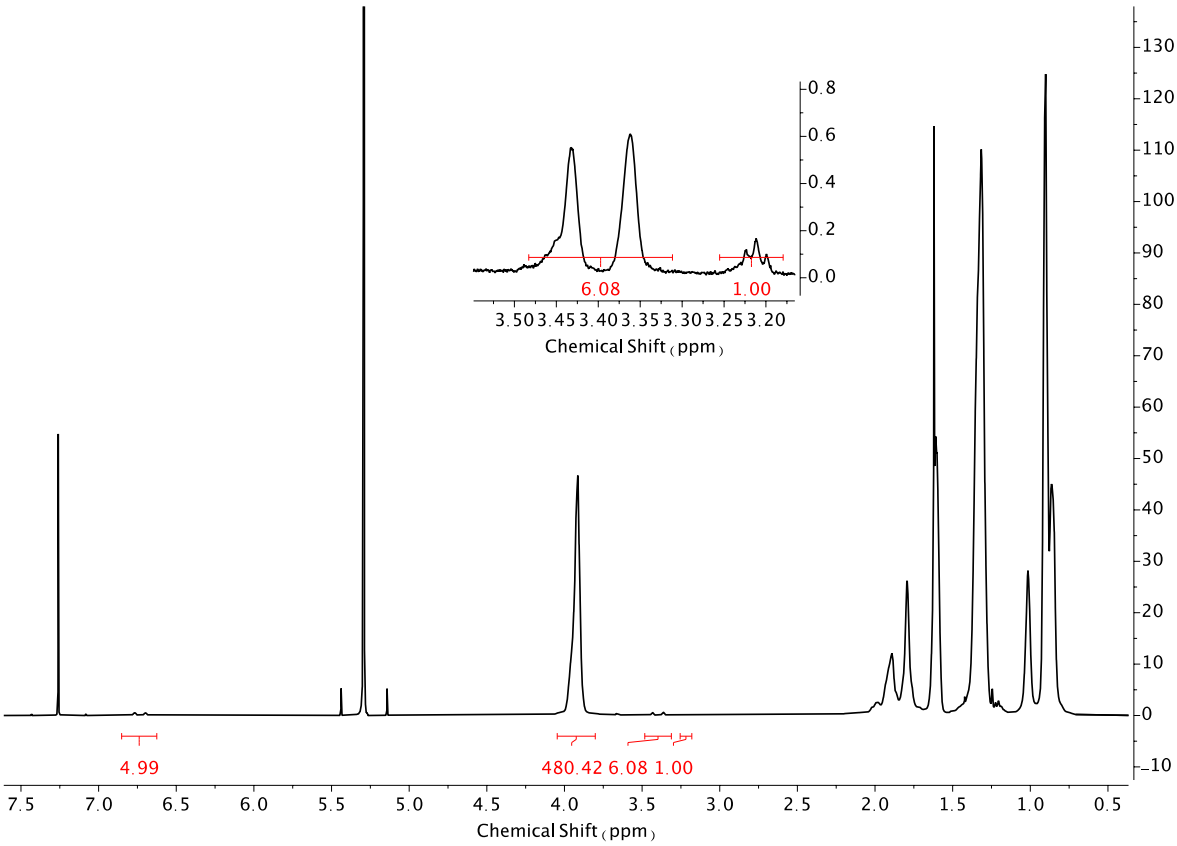

Scheme 4.20 ^{1}H NMR of **1 mol % NBD-PHMA (12)** in Chloroform-d.

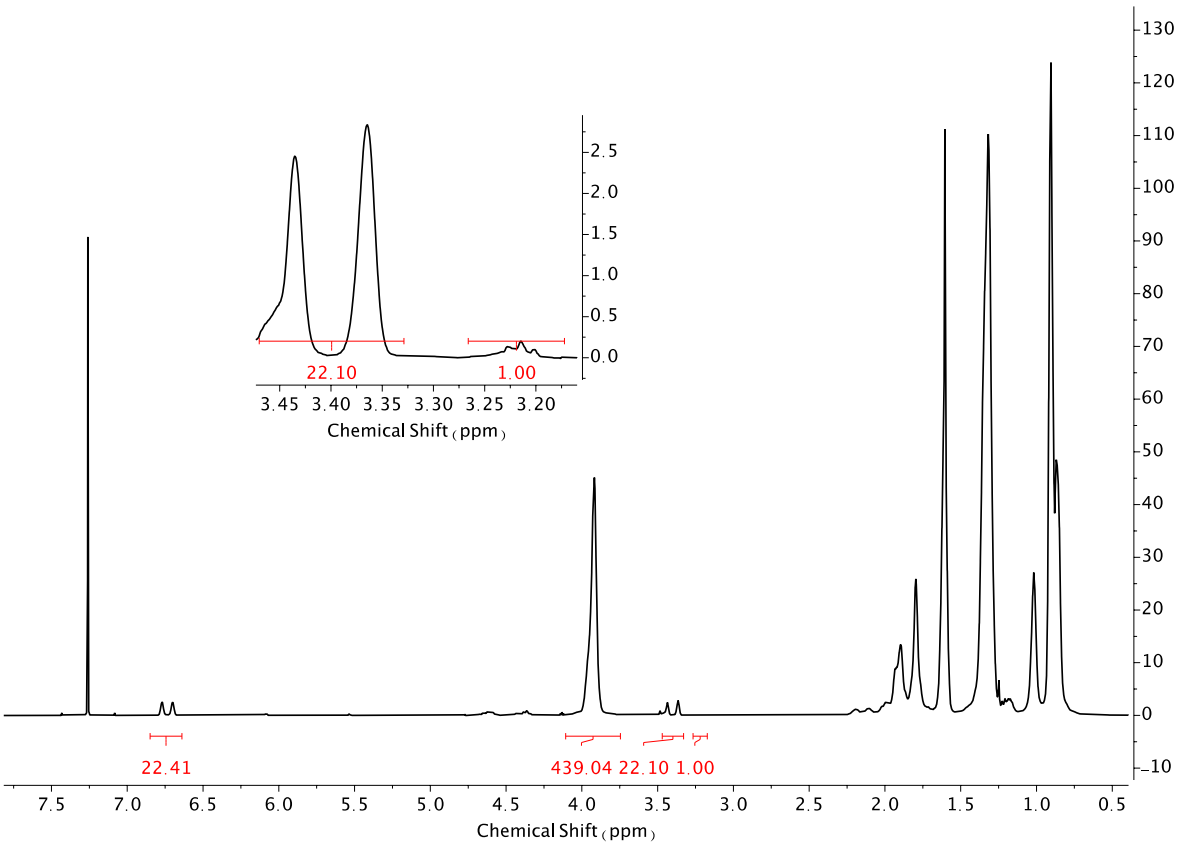

Scheme 4.21 ^{1}H NMR of **4 mol % NBD-PHMA (13)** in Chloroform-d.

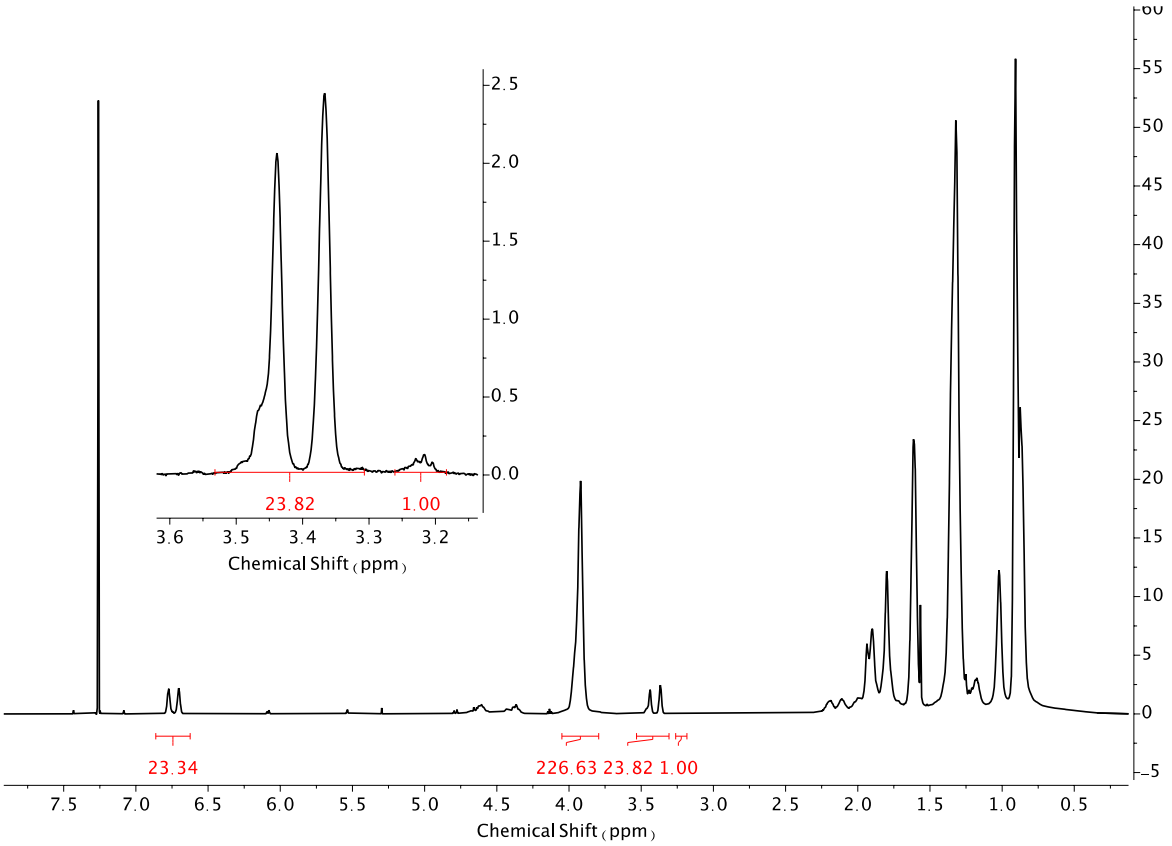

Scheme 4.22 ^{1}H NMR of **9 mol % NBD-PHMA (14)** in Chloroform-d.

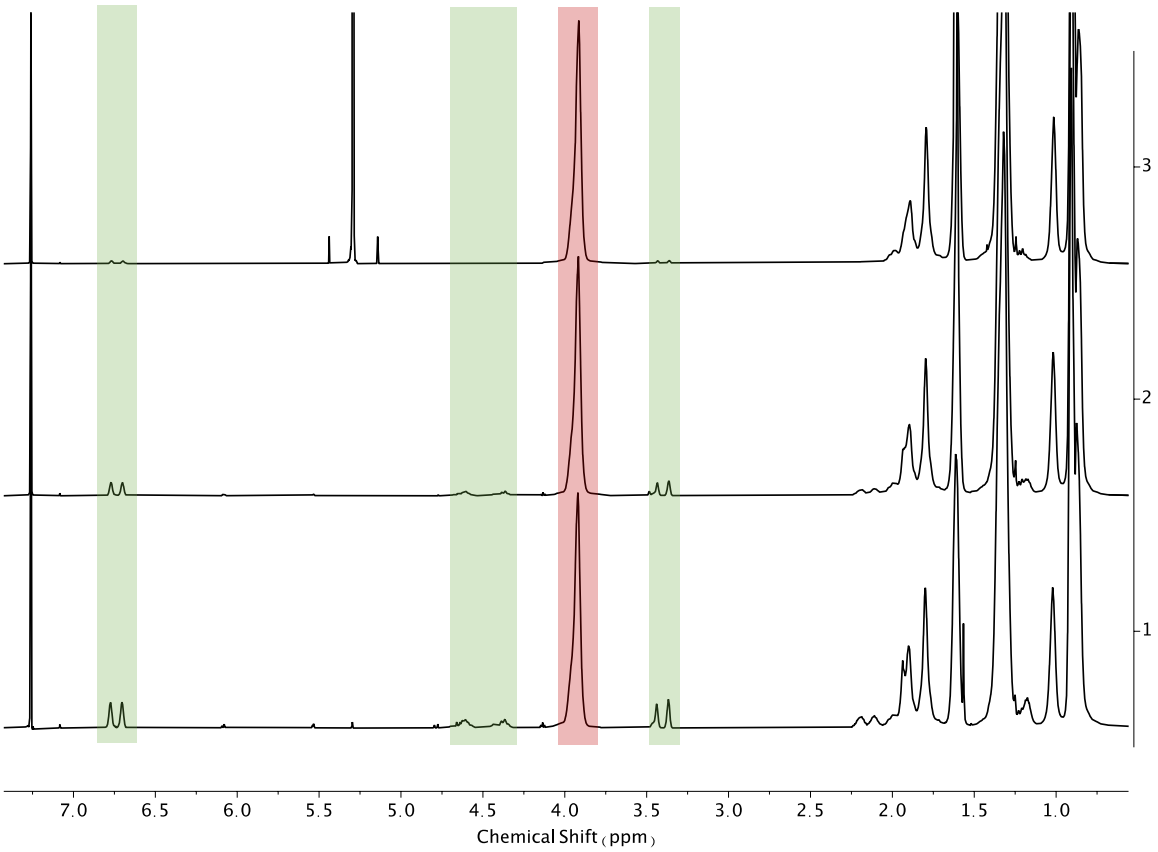

Scheme 4.23 ^{1}H NMR of **NBD-PHMA** materials with increasing incorporation of NBD in Chloroform-d. Highlighting distinct NBD functionality in green and the polymer backbone in red. Top: **1 mol % NBD–PHMA**, middle: **4 mol % NBD-PHMA**, bottom: **9 mol % NBD-PHMA**.

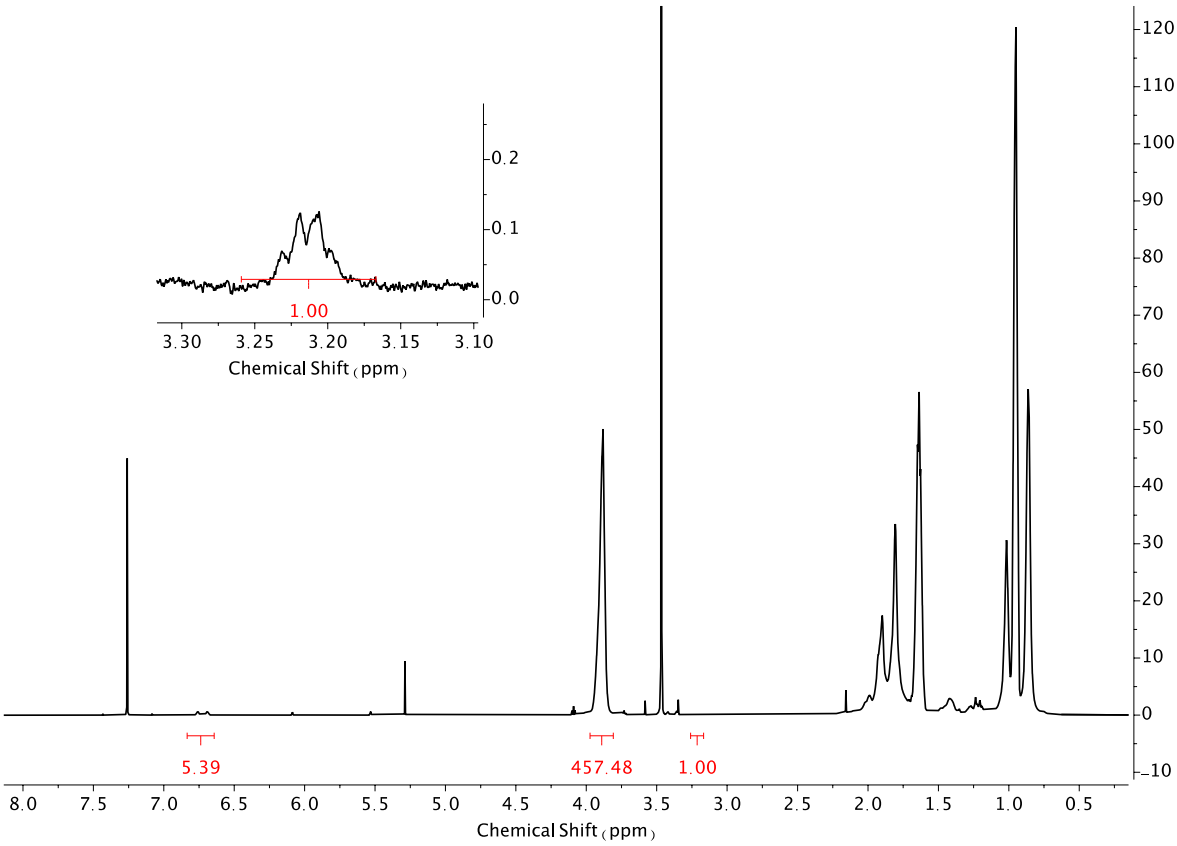

Scheme 4.24 ^{1}H NMR of **1 mol % NBD-PPMA (16)** in Chloroform-d.

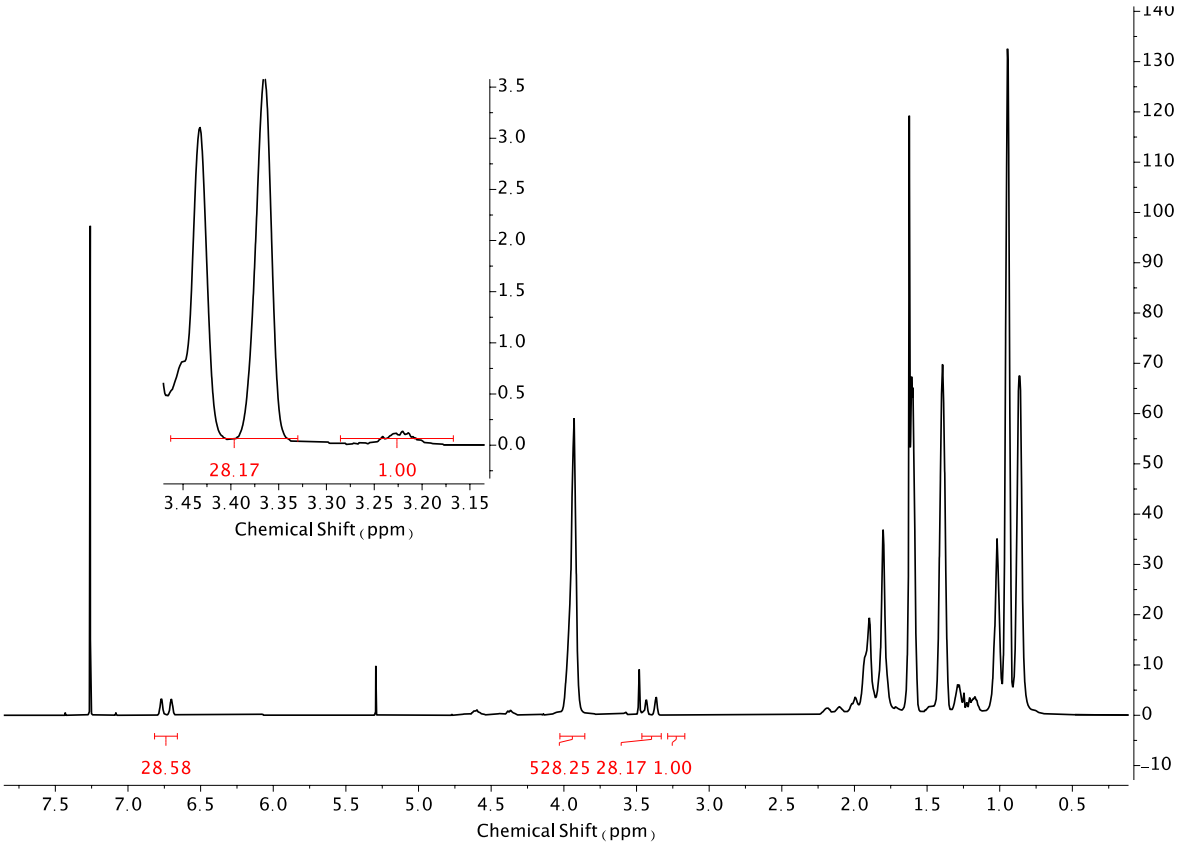

Scheme 4.25 ^{1}H NMR of **4 mol % NBD-PBMA (18)** in Chloroform-d.

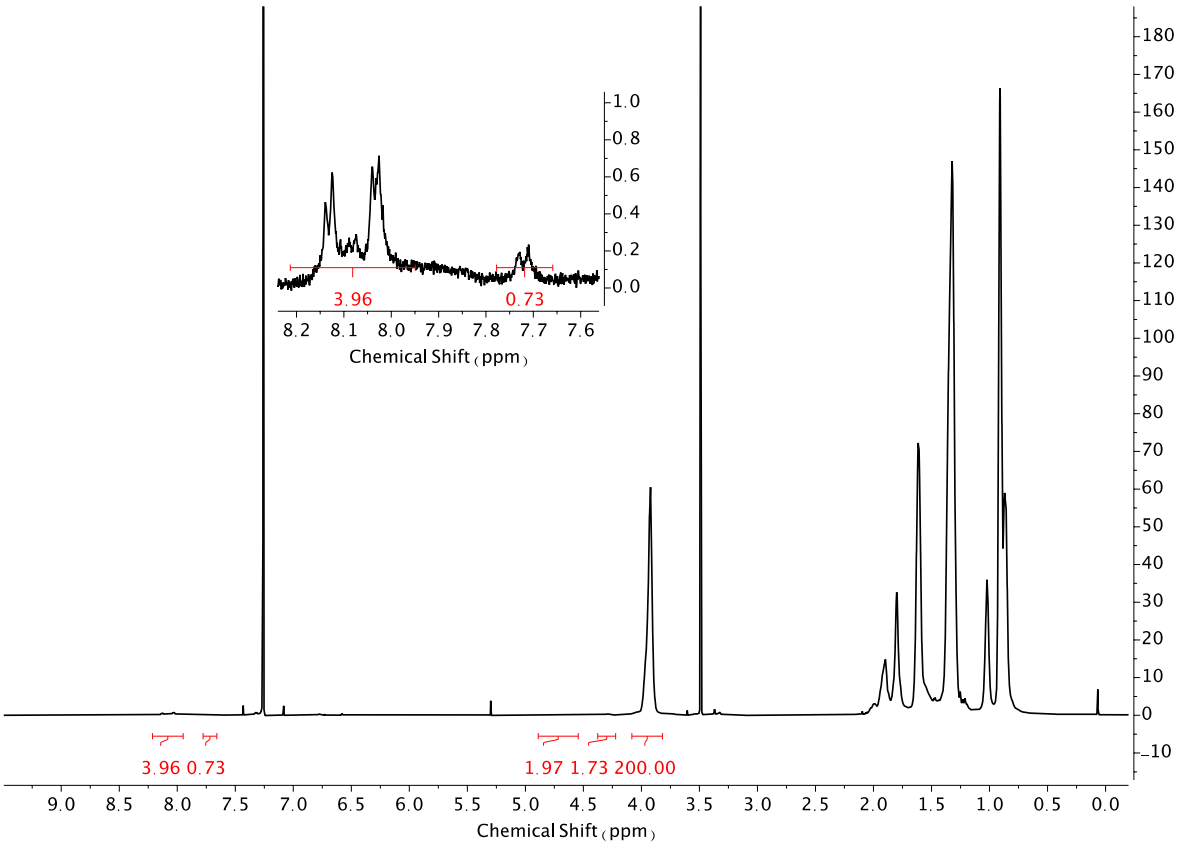

Scheme 4.26 ^{1}H NMR of **1 mol % DASA-PHMA (19)** in Chloroform-d.

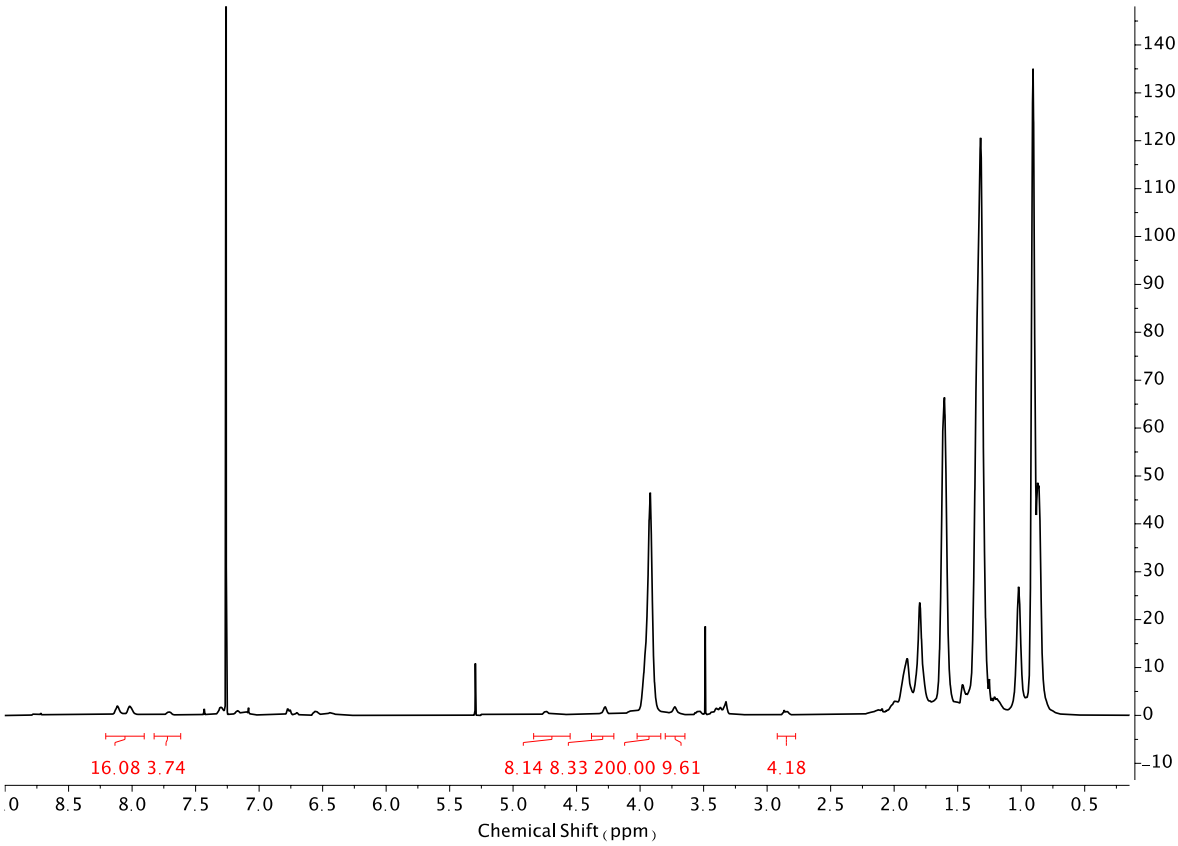

Scheme 4.27 ^{1}H NMR of **4 mol % DASA-PHMA (20)** in Chloroform-d.

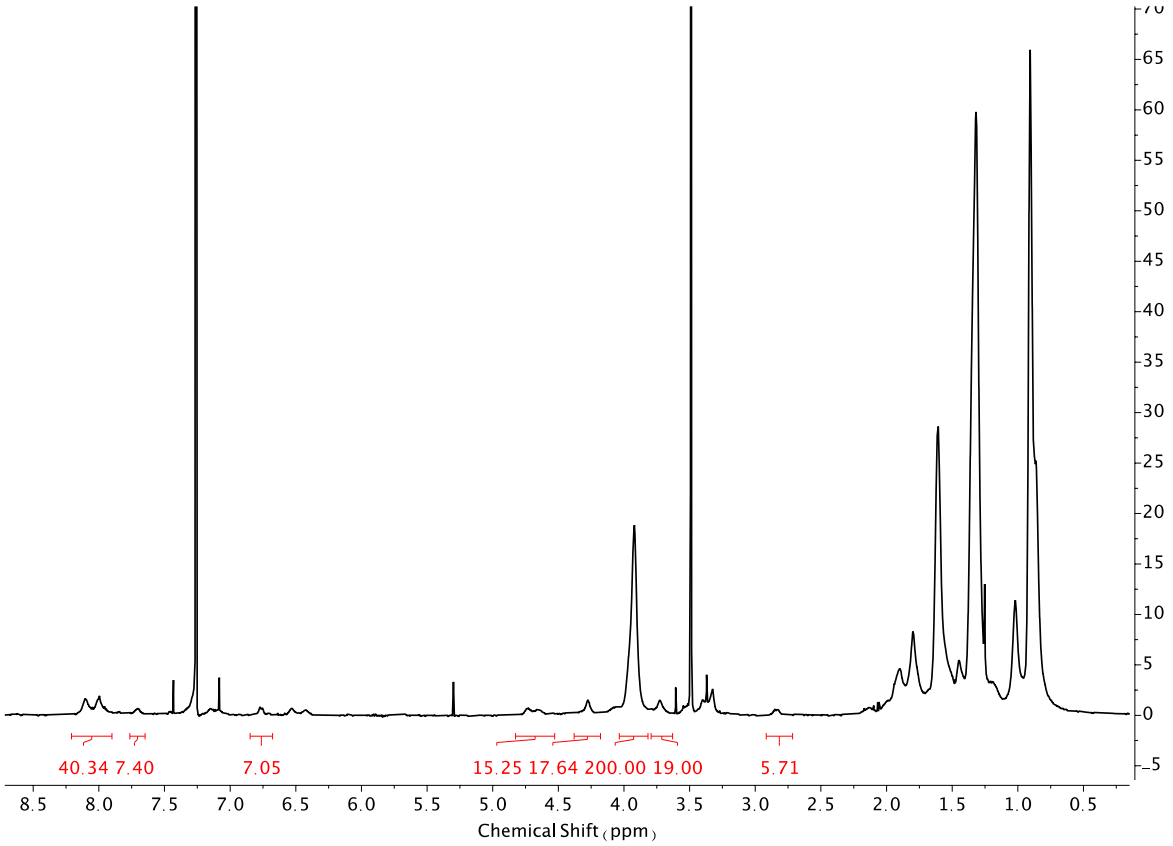

Scheme 4.28 ^{1}H NMR of **9 mol % DASA-PHMA (21)** in Chloroform-d.

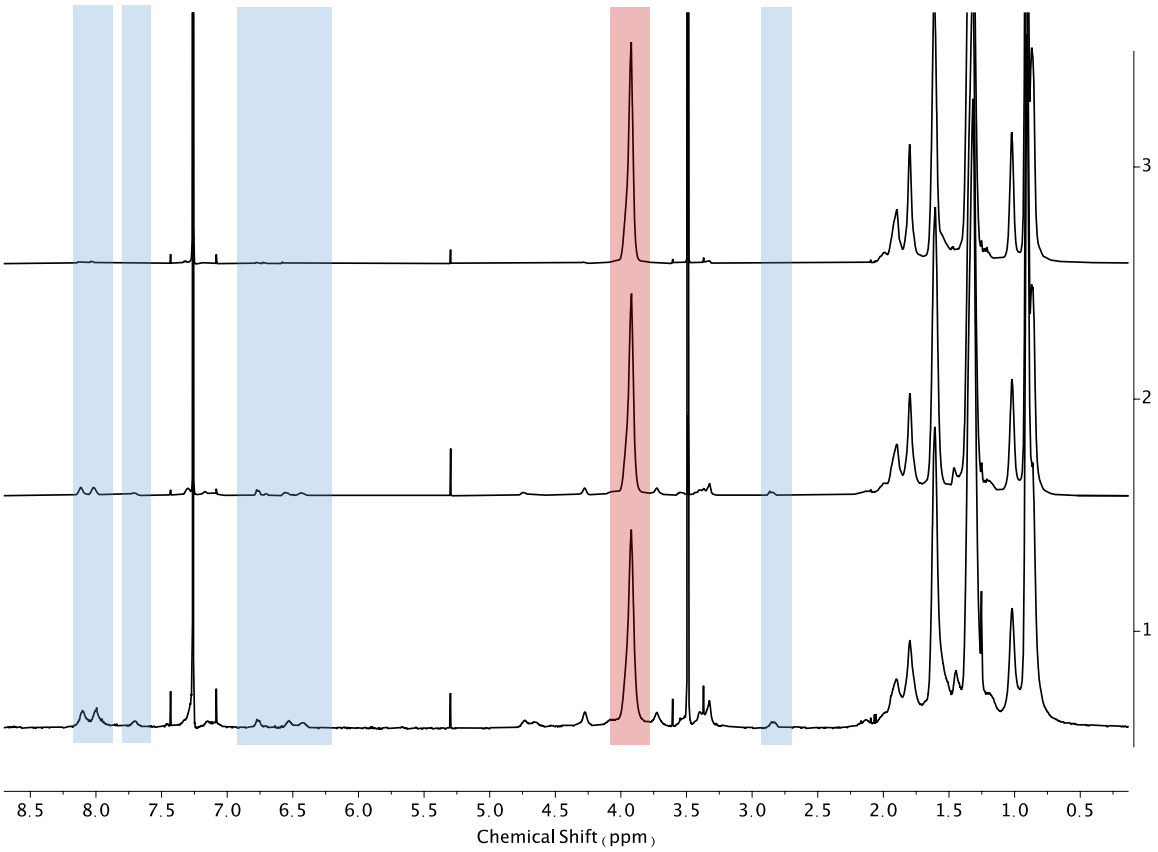

Scheme 4.29 ^{1}H NMR of **DASA-PHMA** materials with increasing incorporation of DASA in Chloroform-d. Highlighting distinct DASA functionality in blue and the polymer backbone in red. Top: **1 mol % DASA–PHMA**, middle: **4 mol % DASA-PHMA**, bottom: **9 mol % DASA-PHMA**.

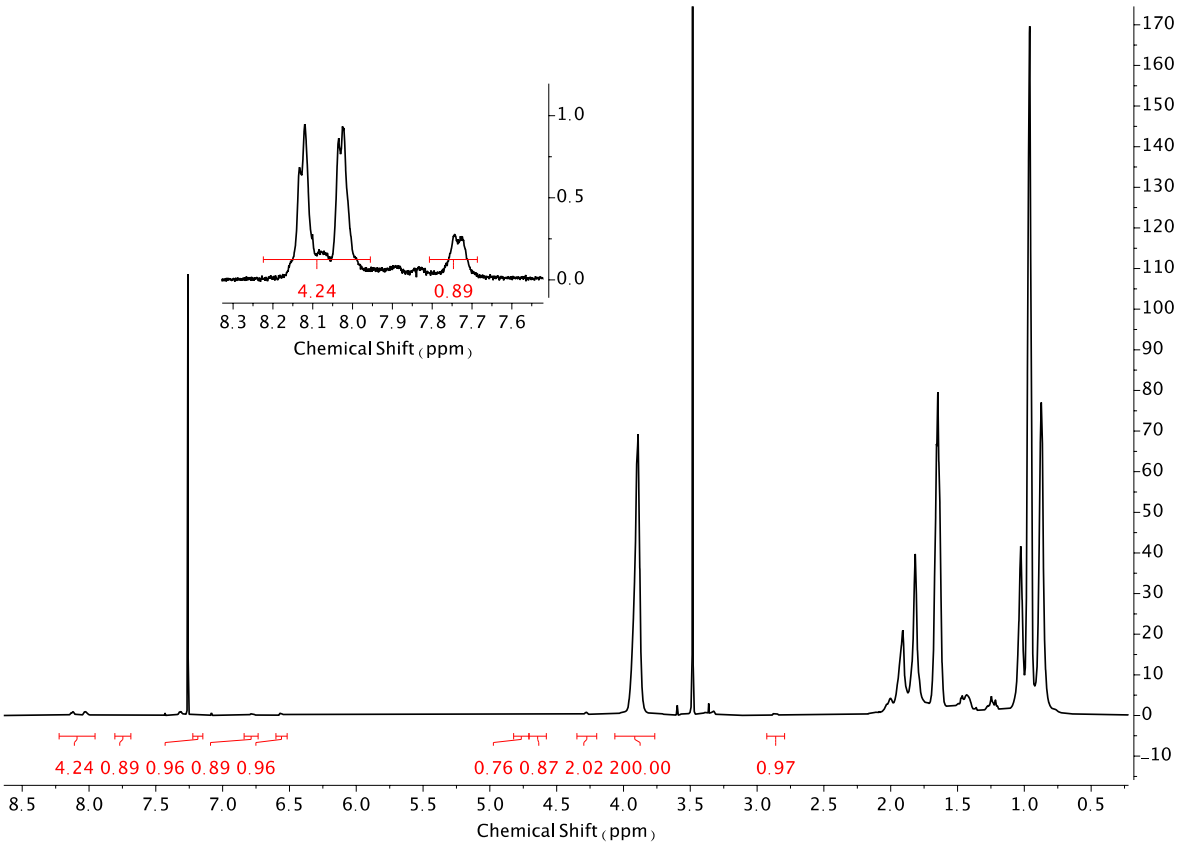

Scheme 4.30 ^{1}H NMR of **1 mol % DASA-PPMA (22)** in Chloroform-d.

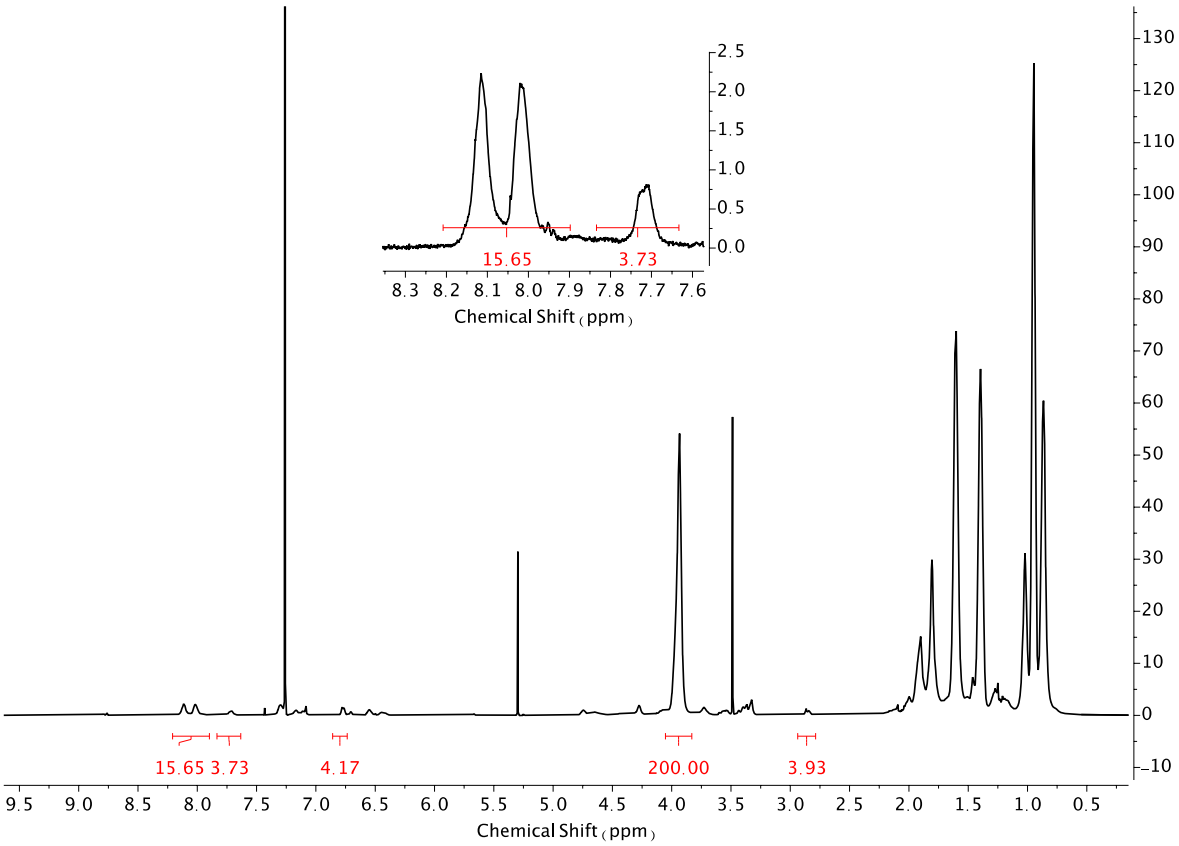

Scheme 4.31 ^{1}H NMR of **4 mol % DASA-PBMA (23)** in Chloroform-d.

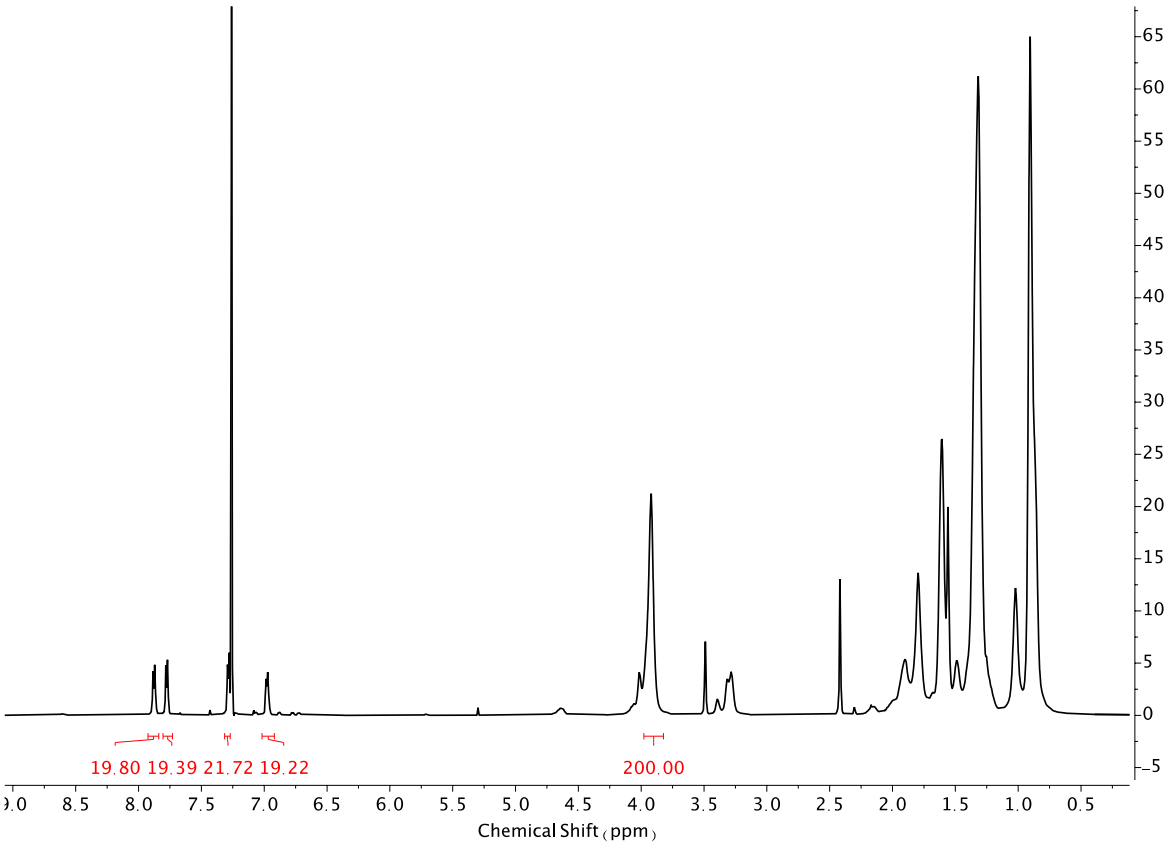

Scheme 4.32 ^{1}H NMR of **9 mol % AZO-PHMA (25)** in Chloroform-d.

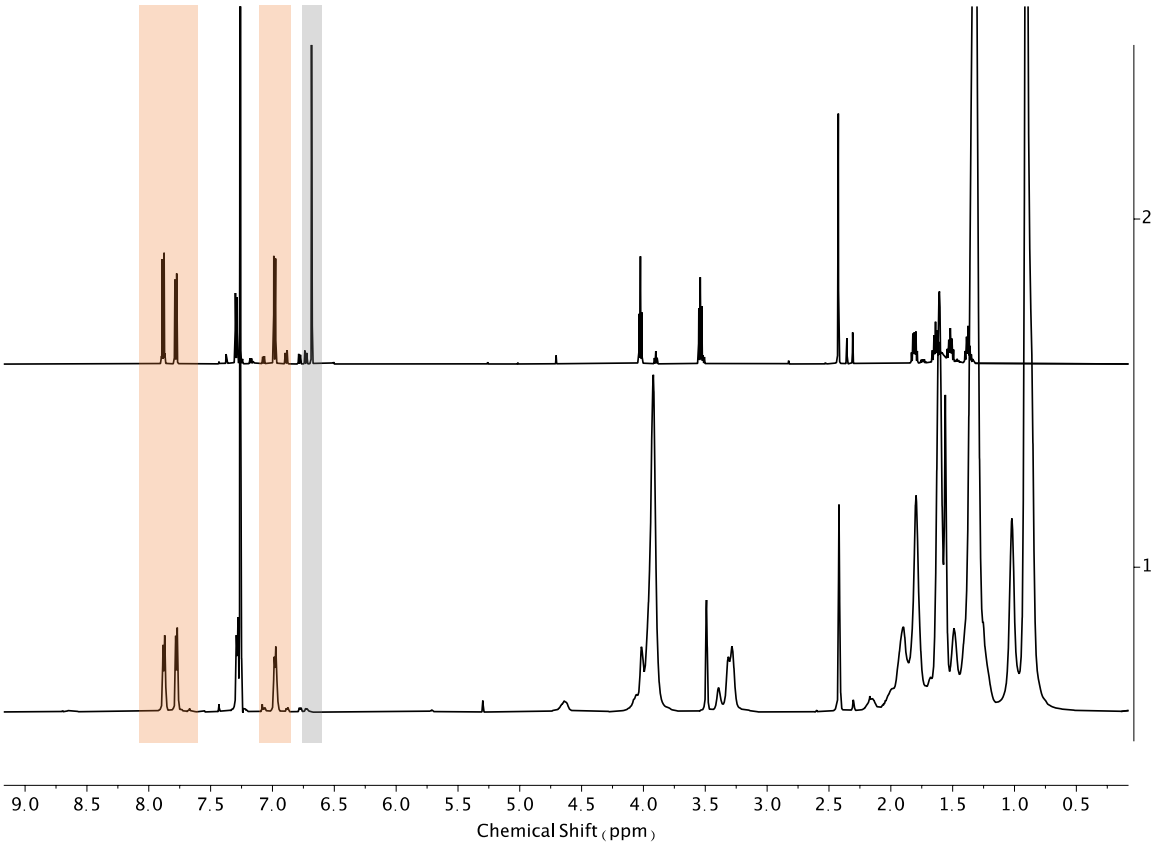

Scheme 4.33 ^{1}H NMR of **AZO–maleimide (24)** (top) functionalize to produce **9 mol % AZO–PHMA (25)** (bottom) after purification in chloroform-d, highlighting distinct Azobenzene functionality in orange and disappearance of distinct maleimide functionality in grey.

Chapter 5. Directions for future work and conclusion

5.1. Electrospinning DASA fibers

Electrospinning is one of the most common nanofiber fabrications techniques. This method produces nanofibers from a viscoelastic liquid using an external electric field. The charged threads of polymer form fibers in the range of micrometers to nanometers.[1] Current applications of electrospun fibers using photochromes include optical sensors, processing media, optical data storage devices, and functional components for smart surfaces,[2] but very little work has been done to explore the benefit of using electrospun fibers for actuation. Rack et al. have shown one of the only examples using electrospun fibers for actuation.[3] By blending a non-isomerizing Rhodamine dye into polylactic acid (PLA), which is electrospun into nanofibrous polymer mats, they create a heat gradient and produce photothermally driven actuation upon irradiation. This work highlights the ease of fabrication of light-driven electrospun materials, makes use of only commercially available starting materials and simple polymer blends. We are interested in using electrospinning as a practical technique to incorporate photochromes into highly aligned nanofibers to produce mechanical work. Electrospun fibers have a number of advantageous properties making them especially promising for photomechanical materials. These include, (i) fibers can be easily aligned to build in strain using methods such as a mechanical alignment or by manipulating the electric field,[4] eliminating the need for specific chemistries such as thiol-Michael additions and radical polymerizations, which are not compatible with all photoswitches, (ii) they have a high surface area to volume ratio, which is beneficial to maximize the performance of photochromes with limited depth penetration, as well as improve heat dissipation compared to thin films, and (iii) there are a variety of different architectures to explore including

nonwoven mats, aligned fibers, single fibers, and core- shell. As mentioned, electrospun materials can be easily aligned.[4–6] The earliest, most straightforward method of fiber alignment is using a rotating drum.[6] This can be a mandrel, wire drum, wheel, or cone. During electrospinning, high voltage electrifying your polymer solution exits a spinneret as a charged jet resulting in a whipping instability, these fibers are then collected on a grounded rotating drum. The high velocities and mechanical stretching forces on the rotating cylinder surface result in fiber alignment.[6] Spraybase the instrument located in California NanoSystems Institute has a rotating drum with controlled rotating velocity and a translational emitter to produce aligned fibers that is commercially available. Another alignment technique is post-drawing.[5–7] Nonwoven mats can be reprocessed by applying uniaxial stretching forces, which effectively induce reorientation of the randomly aligned nonwoven fibers in the direction of the stretching force. Zong and coworkers explored electrospun PLA-based fibers under traditional spinning conditions, and then post-drawn to an extension ratio of 200% at 60 °C once.[7] The resulting fibers show improved alignment with a fiber diameter of 1 μm. The reprocessing temperature is a minimum of the T_g of the material. One of the major advantages of this approach is the ease of implantation. Thus, we could start aligning DASA/PMMA fibers by utilizing a tension stage that can be put in an oven to control temperature. Other methods include near-field electrospinning and parallel plates (available for purchase from Spraybase).[1,6]

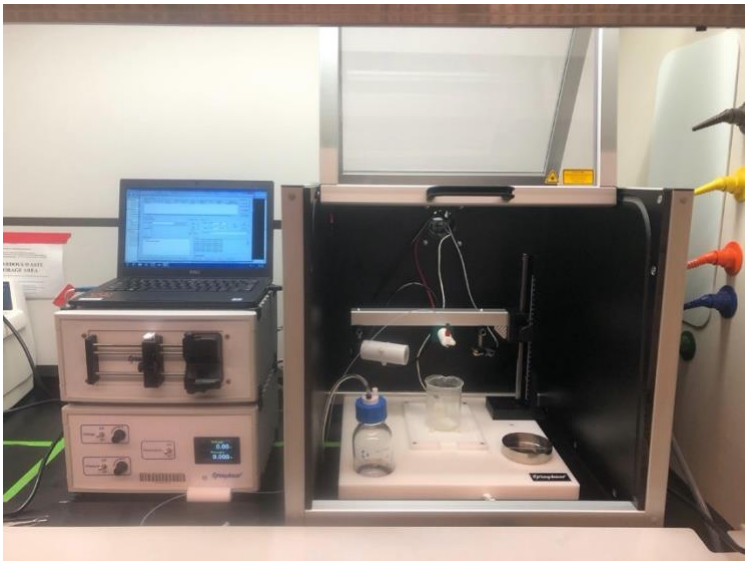

Figure 5.1 Photographic image of the Spraybase® 20 kV Coaxial Electrospraying Kit I-0200-0006-01. The Spraybase is located in Elings 2410.

In order to explore DASA-based nanofibers, we used a Spraybase® 20 kV Coaxial Electrospraying Kit I-0200-0006-01, as shown in Figure 5.1. We are specifically interested in electrospinning DASA-based nanofibers due to their negative photochromism, resulting in a photogenerated compact, colorless isomer, allowing deep penetration of light during photoconversion.[8,9] In addition we have recently demonstrated the photothermal properties of DASA can be leveraged to drive tunable photothermal actuation utilizing a bilayer design.[10] Using DASA/PMMA blends, we electrospun uniform nonwoven mats, resulting in brightly blue colored micrometer fibers (8-9 micrometers). We visualized the fibers using a Keyence (Figure 5.2) and optical microscope. A solution of 2 wt % DASA 3-IP (structure shown in Figure 5.2) in PMMA was sonicated in DCM (20 wt %). The electrospinning conditions used include a flow rate of 1.2 mL/hour, the distance between plate and needle of 10 cm, and voltage of 15 kV.[11] Note that when the Spraybase® was placed inside the fume hood during these experiments, the solvent evaporated quickly resulting in significant

buildup of material at the needle tip, therefore we removed it. We also utilized the electrospray dish collector (it is best to use the electrospinning flat plate for fibers). Upon irradiation of the electrospun fibers with visible light, the negatively photochromic DASA switches from highly colored to colorless, resulting in white fibers due to the PMMA, as shown in Figure 5.3. In order to demonstrate actuation, we fabricated a bilayer by collecting fibers from the aluminum dish with scotch tape. The DASA-PMMA fiber/scotch tape bilayer was irradiated with a light source (halogen lamp, EKE 150 W with a fiber optic illuminator) and resulted in actuation, as shown in Figure 5.4. We hypothesize the mechanism of actuation is photothermally driven based on our previous DASA-PHMA/PI bilayer system.

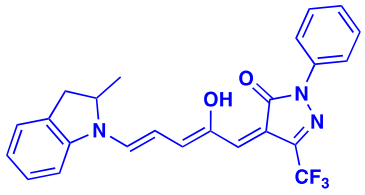

1

DASA 3-IP

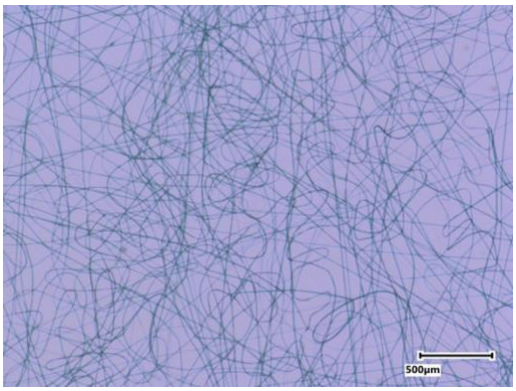

Figure 5.2 DASA 3-IP structure shown on right. Keyence microscope images of uniform electrospun fibers on right. Scale bar is 500 µm.

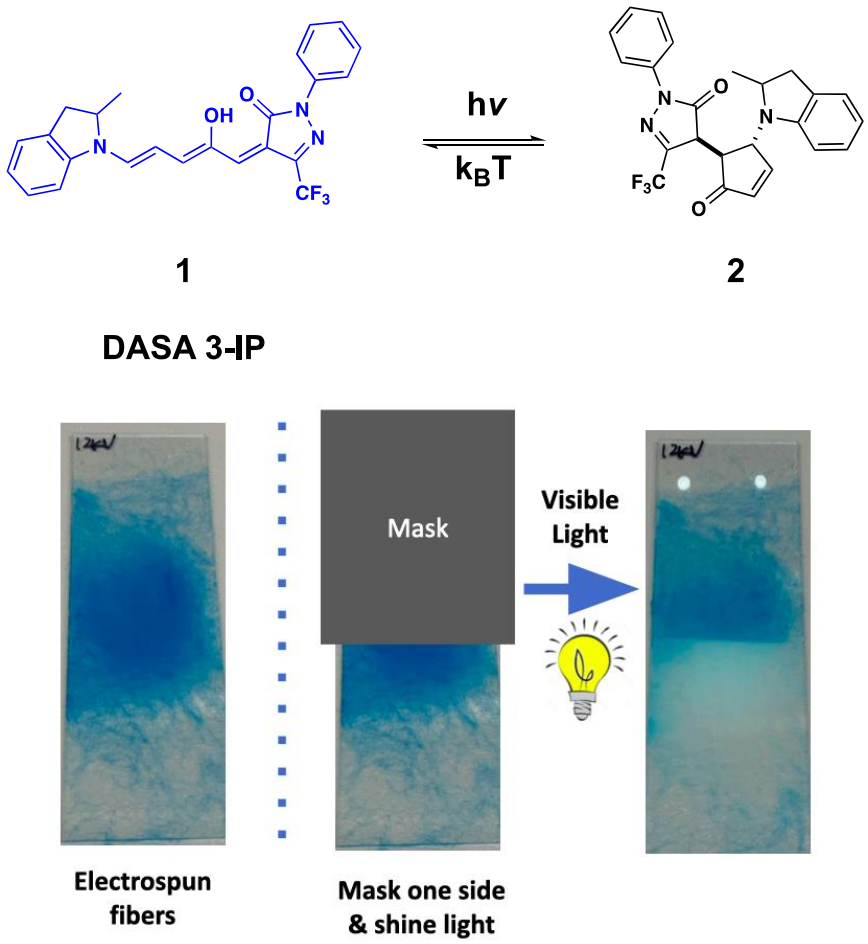

Figure 5.3 Upon irradiation with visible light the highly colored blue fibers become colorless. Fibers spun onto one-inch by three-inch glass slides.

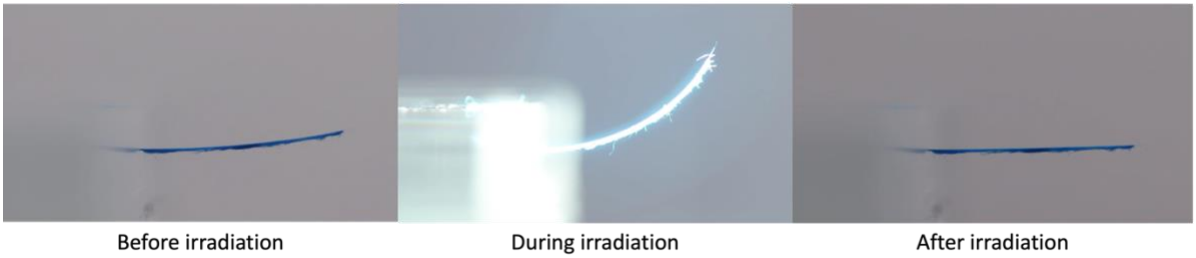

Figure 5.4 The DASA-PMMA fiber/scotch tape bilayer was irradiated with a light source (halogen lamp, EKE 150 W with a fiber optic illuminator) and resulted in actuation. Upon removal of the light source the bilayer returns to the initial position.

In addition to electrospinning uniform fibers, we demonstrated "dancing" yarn fibers. A solution of 2 wt % DASA 3-IP in PMMA was sonicated in DMF (250 mg DASA+PMMA in 1.25 mL DMF). The electrospinning conditions used include a flow rate of 2.4 mL/hour, the distance between plate and needle of 10 cm, and voltage of 15 kV. The resulting fibers were lightly colored, presumably due to equilibration to the closed form isomer in DMF as shown in Figure 5.5. It is worth noting there was residual solvent in the sheets. When we slightly changed the conditions to a flow rate of 1.2 mL/hour, we observed self-buckling in yarn fibers as shown in Figure 5.6. The lightly colored yarn fibers could be thermally reverted to the open form upon drying under vacuum (house vacuum for 5 days), resulting in highly colored, brittle, PMMA-like yarn fibers (Figure 5.7). Yarn formation/self-buckling has been previously observed in the literature.[12–14] Electrospun yarn fibers have been demonstrated using: stable jet electrospinning,[12] self-bundling using a grounded needle,[13] and AC voltage.[14] A possible mechanism for the self-bundling is that the high conductivity of the polymer solution results in the change of the shape of the electrostatic field, resulting in self-bundling.[13] Based on this mechanism, we believe that the zwitterionic nature of the closed form may increase the conductivity of the solution resulting in self-bundling. An interesting follow-up study would be to electrospin a second-generation DASA that has a neutral closed form, such as DASA 2-IM, and observe for the formation of yarn bundles. Overall, these results demonstrate a simple method to fabricate fiber bundles of DASA/PMMA blends. It would be interesting to investigate if there are heat gradients within the fiber bundles that could be leveraged for photothermal actuation. This could allow us to leverage the increase in strength and alignment of the fibers using this technique. In addition, Figure 5.7 shows a bundle with different thicknesses throughout the thread,

which may be an interesting parameter to explore. While this work only focused on using blends, one could also explore using the conjugated materials described in Chapter 4.

Figure 5.5 Lightly colored DASA 3-IP-PMMA blended sheets electrospun from DMF.

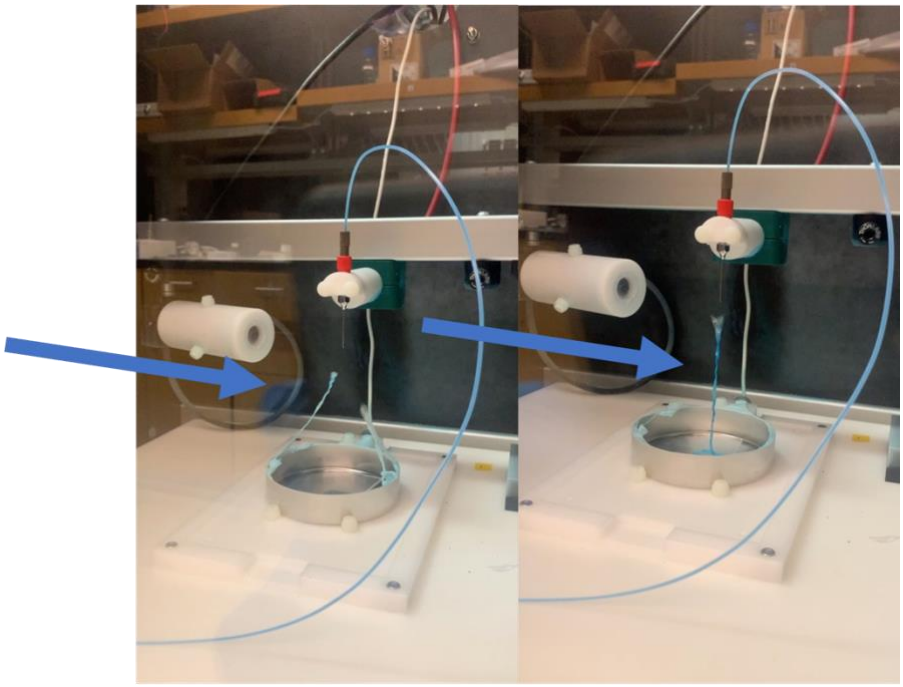

Figure 5.6 Photographic images of "dancing" yarn fibers of DASA 3-IP/PMMA blends in DMF.

Figure 5.7 Upon removal of residual DMSO, the previously lightly colored fibers are dark blue upon thermal reversion to the highly colored, open form DASA 3-IP.

Another potential project could be utilizing our Diels–Alder chemistry to synthesize high molecular weight liquid crystalline materials. This would further improve the order in the fibers and maximize the efficiency of converting light directly to mechanical work. While a few groups have explored electrospinning liquid crystalline materials,[15–19] this remains a challenge. The existing linear azobenzene liquid crystal polymers with low molecular weight are difficult to be constructed into fibers through the unstable jetting process.[15] Lagerwall and coworkers tried to overcome this issue by using coaxial electrospinning via phase separation to make a liquid crystal core with a support polymer shell and found only irreversible contraction. They hypothesize that if the shell polymer could be removed while keeping the liquid crystal elastomer core intact that electrospun fibers could be used for actuation.[19] Thus, utilizing our Diels–Alder chemistry may provide a route to electrospinning higher molecular weight liquid crystalline materials.

In conclusion, electrospinning would be an extremely interesting architecture to explore for photo-actuation. Preliminary results show the formation of DASA-based fibers

and photoactuation of a fiber/scotch tape bilayer. One could explore fabricating yarn fibers, aligning nanofibers, and overcoming challenges with liquid crystal materials in electrospinning.

5.2. Wavelength selective DASA-based actuator

One of the major advantages of donor–acceptor Stenhouse adducts is the synthetic tunability of the absorption profile. For example, DASA 1-EM and DASA 3-IP have > 100 nm shift in the lambda max (λ_{max}), as shown in Figure 5.8. To highlight the modular nature of our Diels–Alder click chemistry and leverage wavelength selective photoactuation, future work aims to use our click chemistry approach to access first- and third-generation DASA materials. This method overcomes limitations of the previous functionalization strategies that rely on chemically conjugating the donor or acceptor to the polymer backbone, limiting overall modularity.[20,21] In addition, DASA formation in the final step on the polymer backbone results in long reaction times, incomplete functionalization, and multiple post-polymerization steps. In chapter 3 and 4 we synthesized third-generation DASA-PHMA and azobenzene-PHMA, this work expands the maleimide toolbox by synthesizing a first-generation DASA maleimide and first-generation DASA-PHMA polymer.

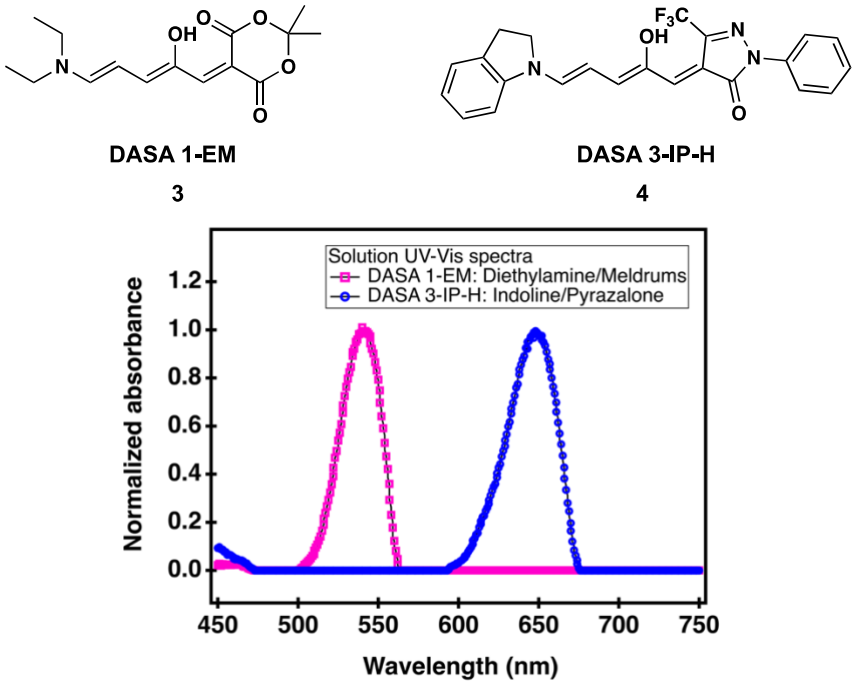

Figure 5.8 UV/Vis spectra of first- and third-generation DASAs, demonstrating the tunable absorption spectra.

In order to synthesize a first-generation maleimide, we utilized the synthetic route shown in Scheme 5.1. Previous work in our group developed a synthetic route to a Meldrum's acid activated furan with *exo* furan-protected maleimide functionality.[20] Expanding on this work, we reacted the furan adduct with diethylamine in order to synthesize a first-generation *exo* furan-protected maleimide DASA. To deprotect the maleimide, we started with using the same solid-state deprotection conditions as the third-generation maleimide (110 °C under vacuum). Instead of deprotection, this approach resulted in decomposition. Next, we attempted a solution-state deprotection in toluene at 110 °C. Interestingly this did not produce the desired DASA maleimide. Instead, the major product was a Meldrum's acid activated furan maleimide as highlighted in green in Scheme 5.2. The reformation of the furan adduct is further studied in section 5.2.2.

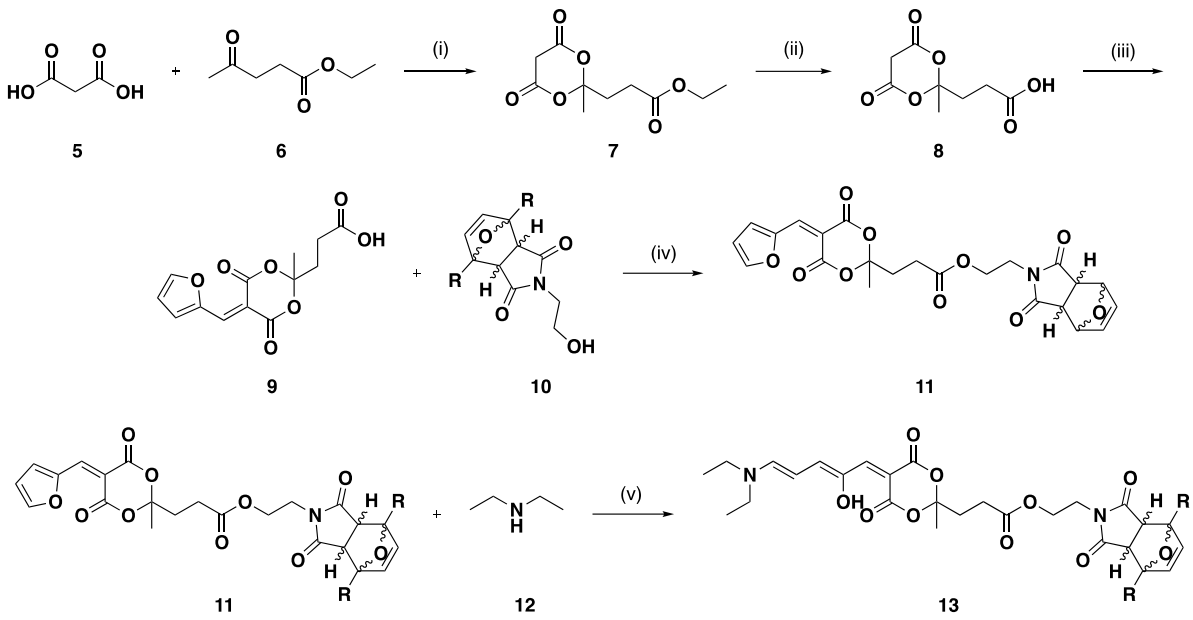

Scheme 5.1 Synthetic route to first-generation DASA maleimide utilizing different furan-protected maleimides (*exo*, *endo*, R = H, or R = Me). Reaction conditions: (i) H_2SO_4, Ac_2O, rt, overnight (ii) 1) NaOH, 2) HCl (iii) furfural, H_2O, rt, 15 hr (iv) EDC, DMAP, DCM, rt, 15 hr (v) 1 equiv. diethylamine, EtOAc, 10 min.

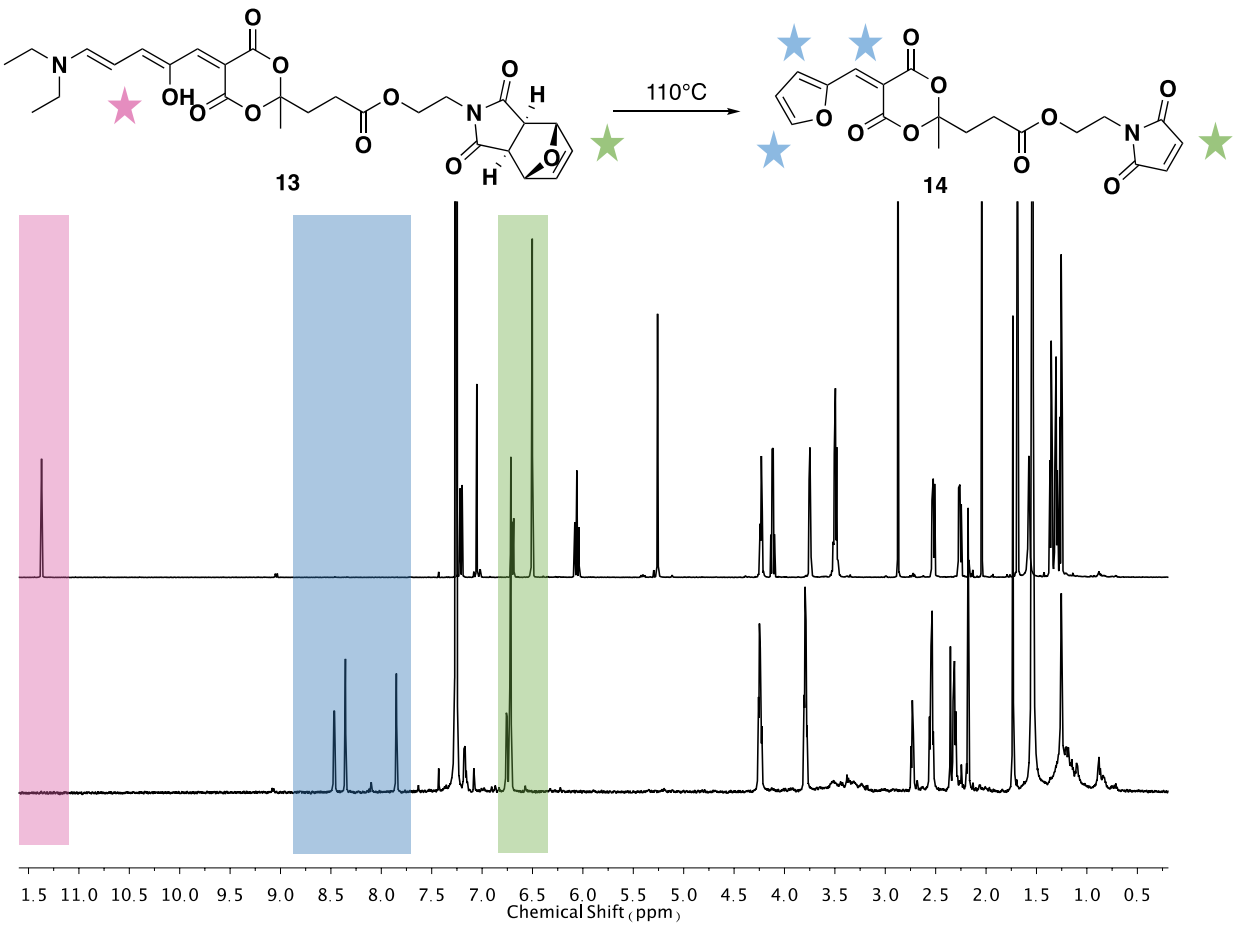

Scheme 5.2 ^{1}H NMR spectra of a solution-state deprotection of a first-generation *exo* furan-protected maleimide (top) resulting in Meldrum's furan adduct maleimide (bottom). Pink highlights DASA functionality, which is no longer present after deprotection. Green highlights conversion of the *exo* furan-protected maleimide to maleimide. Blue highlights the presence of furan adduct functionality, which was not previously present in the starting material.

Based on these results, the *exo* furan-protected maleimide deprotection conditions are not compatible with this DASA derivative. From here, we utilized different protected-maleimides which undergo deprotection at lower temperatures. An *exo* dimethylfuran-protected maleimide which undergoes deprotection as 80 °C resulted in both the desired

product, first-generation DASA maleimide, and the undesired product, Meldrum's acid furan adduct maleimide. Finally, we utilized an *endo* furan-protected maleimide which undergoes deprotection at 60 °C.[22] As shown in Scheme 5.3, using solution-state deprotection, the major product is the desired first-generation DASA maleimide. To access the *endo* furan-protected maleimide on large scale we relied on method recently developed by Zhu.[23] With first-generation maleimide in hand, using our Diels–Alder click chemistry we synthesized first-generation DASA-PHMA, as shown in Scheme 5.4, which has a λ_{max} at 540 nm.

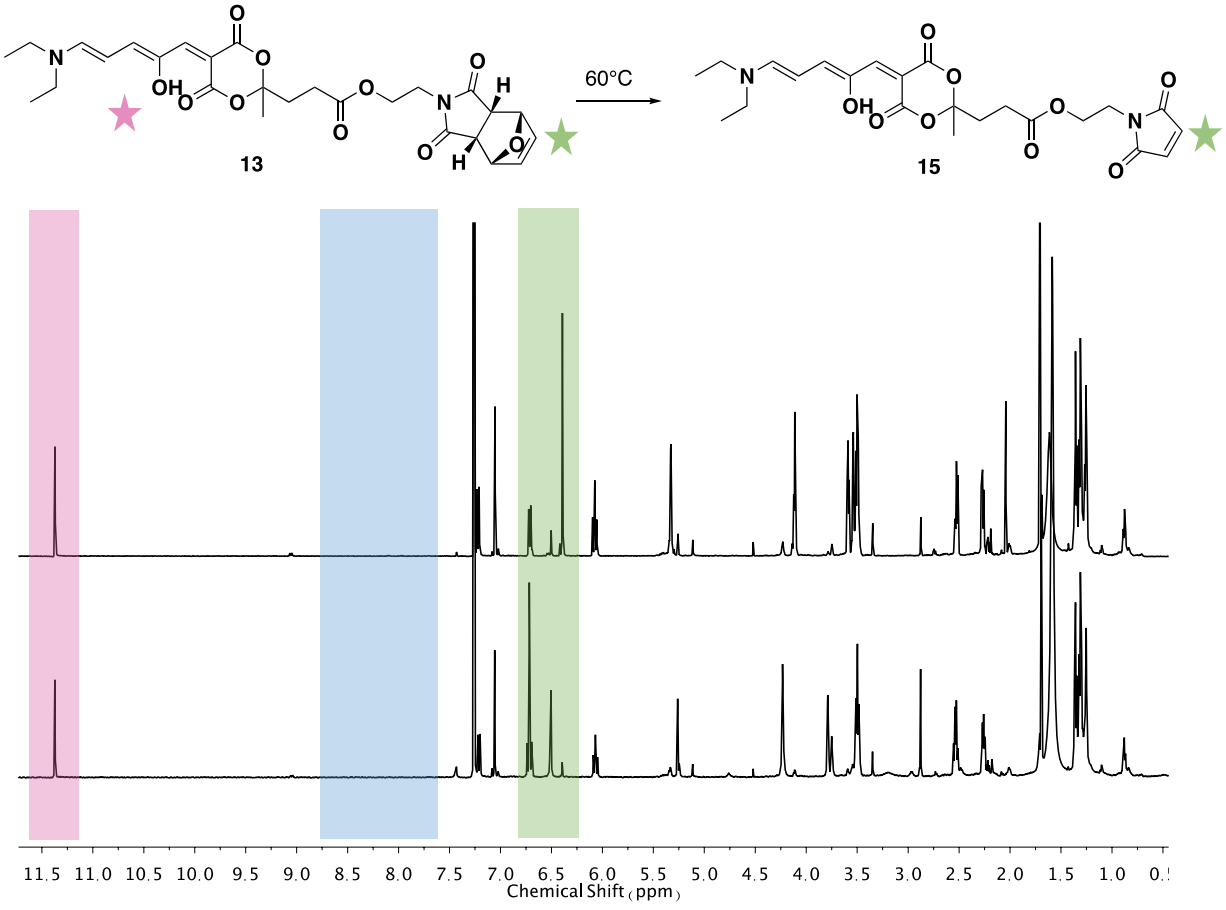

Scheme 5.3 ^{1}H NMR spectra of a solution-state deprotection of a first-generation *endo* furan-protected maleimide (top) resulting in the major product of a first-generation DASA

maleimide (bottom). Pink highlights DASA functionality. Green highlights conversion of the *endo* furan-protected maleimide to maleimide. Blue highlights the absence of furan adduct functionality in both the starting material and product.

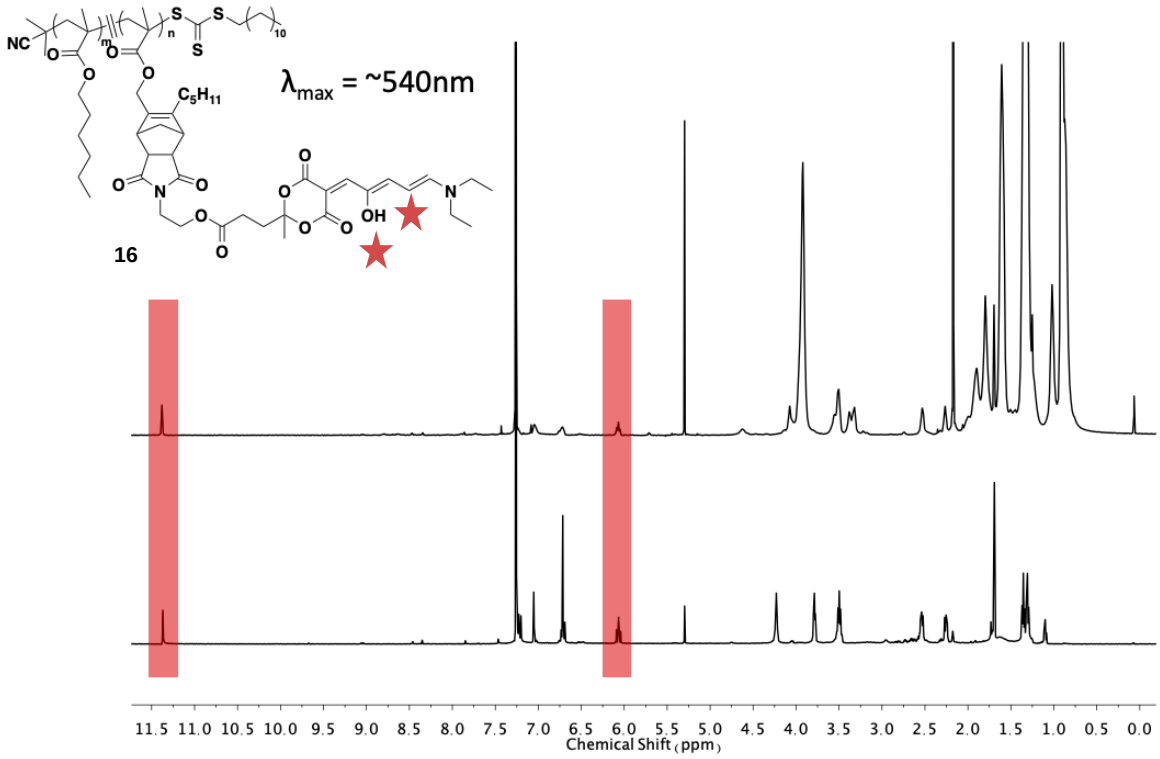

Scheme 5.4 ^{1}H NMR of first-generation DASA-PHMA. Red highlights the DASA functionality from the maleimide to the polymer.

5.2.1. Tri-layer actuator design

With first-generation DASA materials in hand, we next need to do proof-of-concept experiments with DASA blends. The proposed tri-layer actuator design is shown in Figure 5.9. The tri-layer design is based on previous work by Yang and coworkers, they demonstrate a multidirectional actuator using liquid crystal elastomers and organic dyes which were selected as three independent photothermal conversion fillers, which had sharp

and almost non-interfered absorptions.[24] The tri-layer will have a polyimide passive layer with a first- and third-generation DASA material adhered to both sides. We hypothesize upon irradiation with a 650 nm LED the actuator will result in downward actuation. This will be the result of photothermal actuation based on the third-generation DASA, which is highly absorbing at 650 nm, whereas the first generation does not absorb over 610 nm. In contrast, upon irradiation with a 530 nm LED the actuator will result in upward actuation. This will be the result of photothermal actuation based on the first-generation DASA, which is highly absorbing at 530 nm, whereas the third-generation is not highly absorbing at 530 nm. The first approach to fabricate a tri-layer is shown in Figure 5.10. Overall, using this approach we propose leveraging the tunable absorption profile of DASA to develop a wavelength selective actuator. Upon successful proof-of-concept studies, future actuator designs will leverage the conjugated first-generation DASA-based materials, in order to minimize potential aggregation, while also leveraging wavelength selectivity as well as the photoinduced property changes described in Chapter 4.

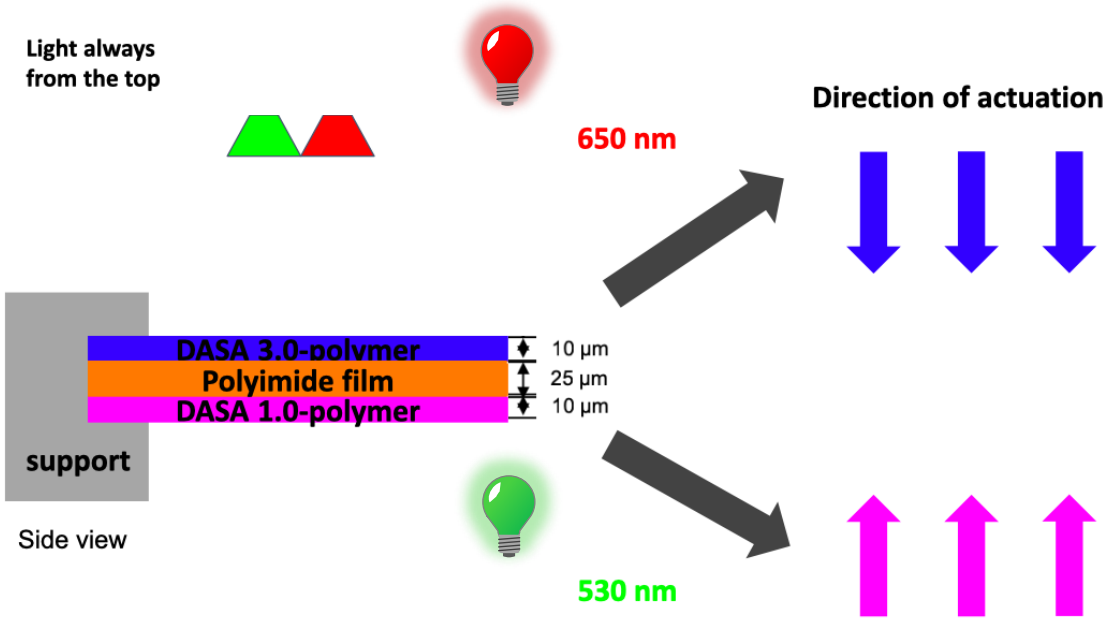

Figure 5.9 DASA-based wavelength selective actuator design.

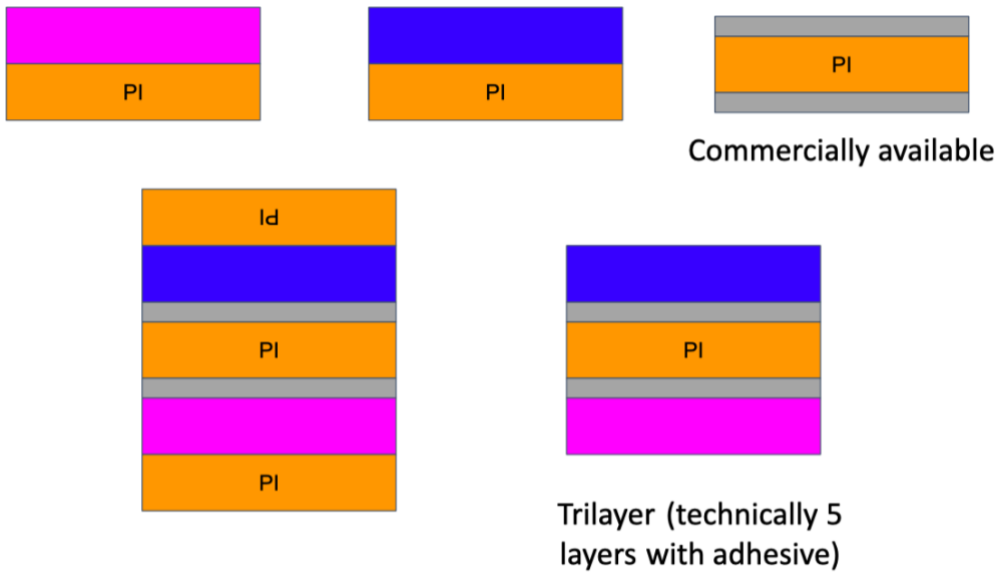

Figure 5.10 Proposed trilayer fabrication using a film transfer technique.

5.2.2. Reformation of the furan adduct: One decomposition pathway for DASA derivatives.

While significant efforts have been undergone to study the photoswitching mechanism of DASAs,[25–31] to the best of our knowledge, no decomposition pathways has been presented to date. Herein, we report the first thermal decomposition pathway of DASAs, resulting in reformation of the furan adduct. We explore the effect of temperature, concentration, and substituents on the decomposition kinetics. We further show that after reformation of the furan adduct, the furan adduct can be purified and reused. This expands on previous work in our group as amine "catching" sensors,[32] introducing a mechanism for thermal "release". In addition, thermal limits of materials are crucial to understand for applications requiring high temperatures, such as photothermal actuation.

To better understand the decomposition pathway of DASAs shown in Scheme 5.2, we used a first-generation DASA as a model compound, DASA 1-EM (Scheme 5.5). We employed time-dependent ^{1}H NMR experiments to study the decomposition kinetics of DASA under different conditions including temperature and concentration. At 115 °C in toluene, DASA 1-EM showed near quantitative conversion to the furan adduct in three hours (Scheme 5.6). We investigated the effect of temperature and found faster decomposition kinetics at higher temperatures as shown in Figure 5.11. In addition, we looked at decomposition as a function of concentration and found slightly increased decomposition with increasing concentration as shown in Figure 5.12. Computational work within our group found that methyl substitution on the C5 position of the triene destabilized the closed form (Scheme 5.7). Interestingly, we experimentally observed DASA 1-MM-C5 undergoes decomposition to the furan adduct at room temperature and does not require elevated

temperatures like DASA 1-EM. Upon synthesis, DASA 1-MM-C5 forms a highly colored and crashes out of solution, similar to DASA 1-EM, upon precipitation and washing the material turns orange/yellow and only furan adduct can be isolated. While the experiments for DASA 1-EM were in toluene, due to the high boiling point, DASA 1-MM-C5 decomposed in chloroform at room temperature. Scheme 5.8 shows our proposed mechanism of the reformation of the furan adduct. And finally, we found we can recover pure starting material as shown in Figure 5.13. It is important to note that the solution is still colored after the ^{1}H NMR reveals conversion to the furan adduct, owing to the high molar absorptivity of DASA which can be misleading. Upon running the crude recycled material through a silica plug, pure furan adduct can be isolated.

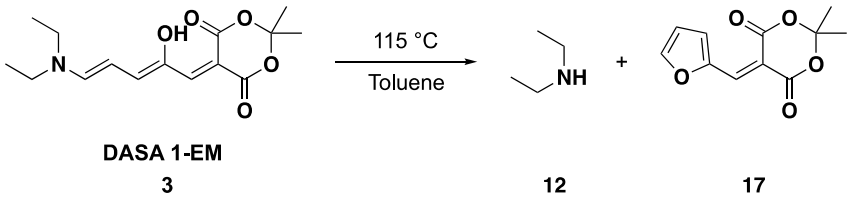

Scheme 5.5 First-generation DASA, DASA 1-EM, studied for decomposition to the furan adduct.

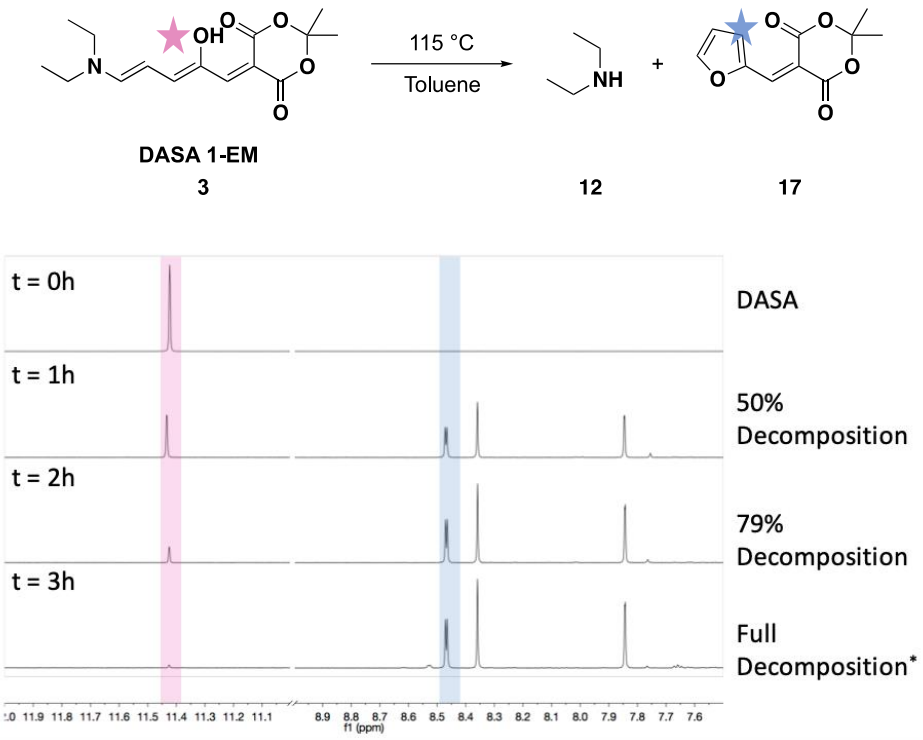

Scheme 5.6 Time-dependent ^{1}H NMR study of the decomposition of DASA 1-EM to the furan adduct at 115 °C in toluene.

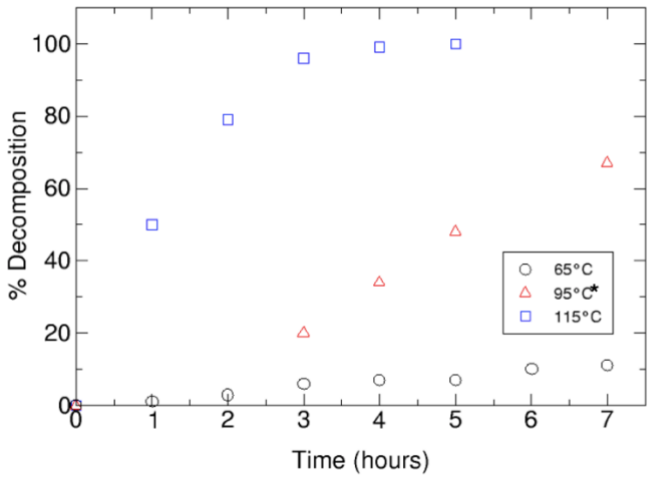

Figure 5.11 Time-dependent ^{1}H NMR study of the decomposition of DASA 1-EM to the furan adduct in toluene at different temperatures at 1mg/mL. *Taken at 0.5 mg/mL concentration.

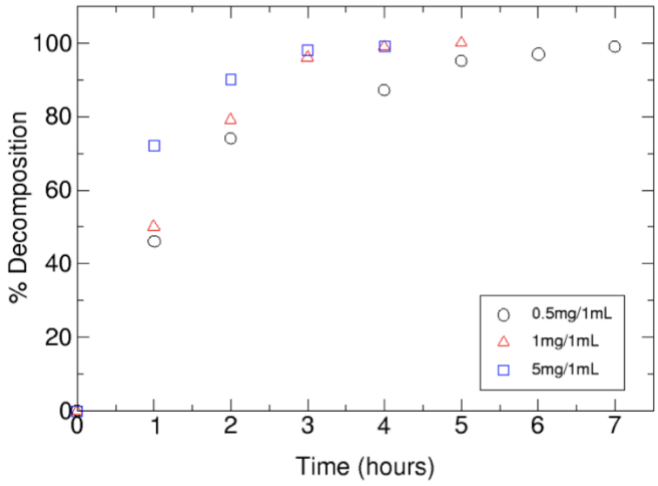

Figure 5.12 Time-dependent ^{1}H NMR study of the decomposition of DASA 1-EM to the furan adduct in toluene at different concentrations at 115 °C.

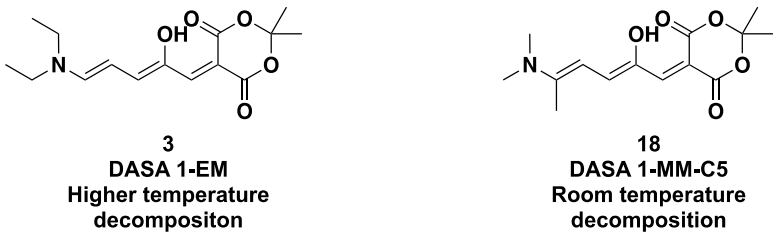

Scheme 5.7 C5 substitution of DASA 1-MM-C5 lowers energy barrier for decomposition, resulting in observable decomposition at room temperature.

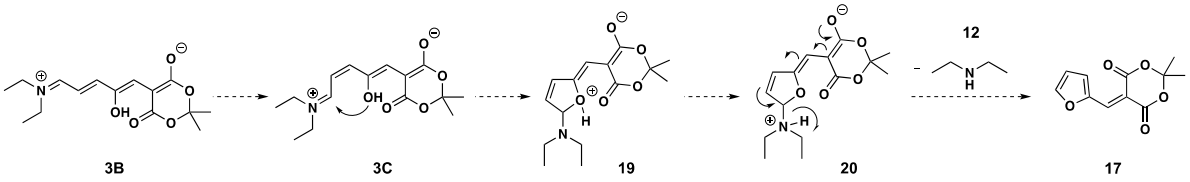

Scheme 5.8 Proposed mechanism of reformation of the furan adduct.

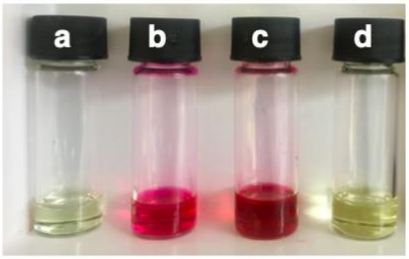

a) **Control** Furan Adduct
b) **Control** DASA 1.0
c) **Crude** Recycled Furan Adduct
d) **Purified** Recycled Furan Adduct

Figure 5.13 Isolation of purified recycled furan adduct.

This work presents the first decomposition pathway of DASAs. We explored the effect of temperature, concentration, and substituents on the decomposition kinetics. This provides key insights into thermal limitations for DASA applications in solution. More work needs to be done to explore decomposition in the solid-state. Previous work has shown decoloration of materials at high temperatures, which we believe could be due to release of the volatile amine.[20] In addition, it may be possible to leverage substituents to tune the decomposition temperature for applications to be able to "catch" and "release" amines at moderate temperatures. This could be interesting for developing networks where light is able to "lock" a material in the closed form, whereas in the dark the material decomposes to its starting materials, releasing amine.

5.3. Conversion of DASA to the closed form in the absence of light

In Chapter 3 we introduced a difference in deflection amplitude between the open and closed DASA-based actuator. In addition, we discovered the photo-induced property changes of DASA-based materials from the open to closed form, with a reduction in the elastic modulus and glass transition temperature in Chapter 4. Another important parameter

of photothermally induced actuation is having a difference in coefficient of thermal expansion (CTE) between the active and passive layers. For instance, using the 10 mol % DASA-PHMA/PI bilayer, 10 mol % DASA-PHMA (open form) has a 9x larger CTE than polyimide. While we were able to measure the CTE of the open form film, we were unable to measure the CTE of the closed form because the measurement requires a 100 μm self-standing film which requires long irradiation times and does not fully bleach. In addition, the long irradiation time may result in photodegradation. It would therefore be beneficial for us to be able to access materials with the closed form of DASA in the absence of light. In this aim, we looked for different strategies throughout the literature for closing DASAs. One strategy is using π-bridge substitution, Sampedro and coworkers showed they could drive DASAs to the closed form based on the location of the substitution on the π-bridge.[33] While we were able to synthesize a third-generation substituted DASA using the synthetic route shown in Scheme 5.9, the resulting DASA could not be purified resulting in an orange solution. We were able to confirm the closed form by ^{1}H NMR (Scheme 5.10) in the absence of light. Unfortunately, we found the compound was stable in methanol and not chloroform, which was not compatible with our click chemistry reaction.

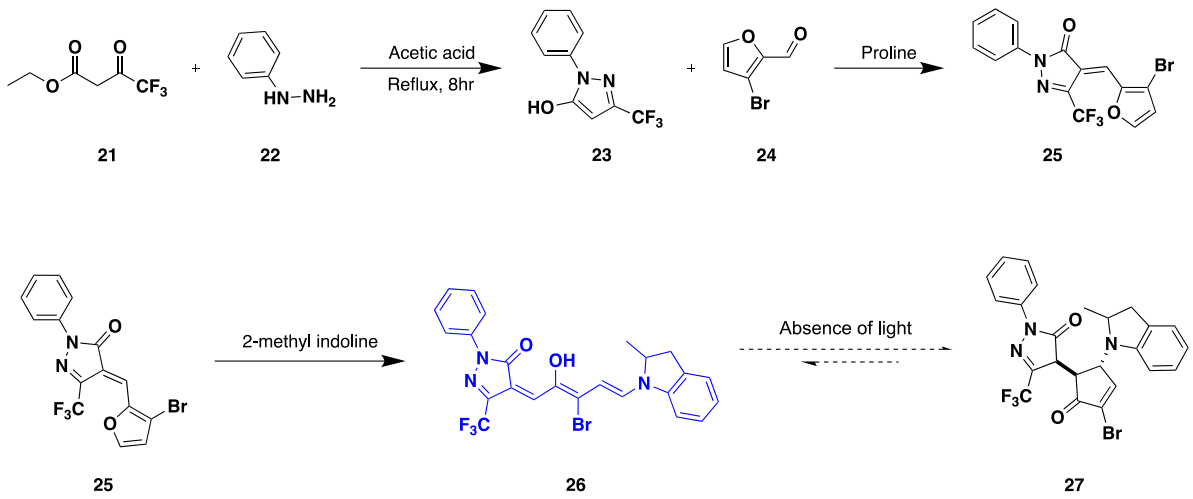

Scheme 5.9 Synthetic route to a third-generation π-bridge substituted DASA.

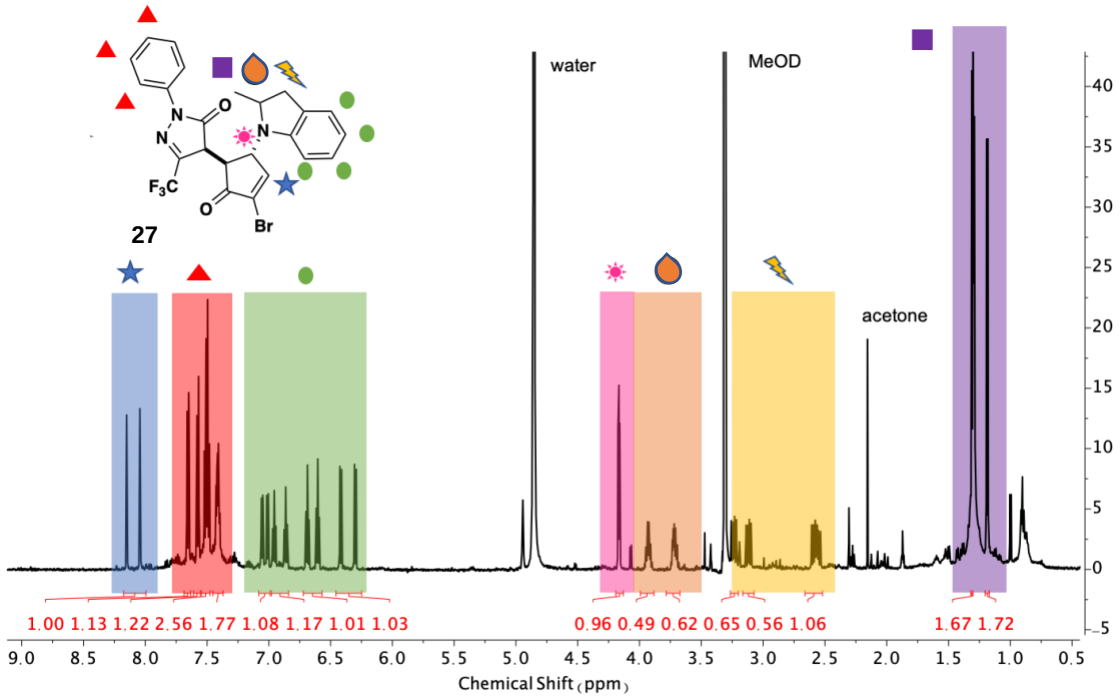

Scheme 5.10 ^{1}H NMR of a third-generation π-bridge substituted DASA in methanol-d.

The next approach we utilized to access the closed form of DASA in the absence of light was based on work by Sameh Helmy in our group.[34] He investigated using different additives to drive the open form DASA to the closed form using DMAP, DABCO, and

PPh_3. These results demonstrated that using one equivalence of either DMAP, DABCO or PPh_3 in acetonitrile at 75 °C for 3 hours resulted in the closed form. Based on these results we wanted to investigate if we could use these conditions to isolate closed form polymer material. Based on the optimization in Table 5.1, we found upon 2 equiv. of DMAP in toluene at room temperature resulted in closed form 1 mol % DASA-PHMA. Some advantages of DMAP compared to PPh_3 include DMAP is soluble in methanol which is ideal for precipitation purification of DASA-based materials and the isomerization takes place at room temperature. Furthermore, based on optimization Table 5.2 on the small molecule DASA 3-IP, we found that the reaction between DMAP and DASA was not catalytic. We hypothesize the basic DMAP is shifting the equilibrium to the closed form. The closed form is confirmed by ^{1}H NMR as shown in Scheme 5.11. The next step was to switch DASA-based material to the closed form and isolate it prior to thermal recovery to the open form. To do this the DMAP had to be fully removed in one single precipitation as redissolving the material in DCM would stabilize the open form. We first tried using DMAP-functionalized beads, but this resulted in displacement of the indoline donors of DASA. We next tried adding a few drops of concentrated HCl into the stirring methanol. Upon precipitation the material was initially pale, but quickly equilibrated back to the open form while stirring upon removal of DMAP as shown in Figure 5.14. We found if we only allowed the solution to stir for 2 minutes, partially closed DASA material could be isolate while additional stirring results in the open form material as shown in Figure 5.15. In conclusion, using DMAP we were able to isolate partially closed DASA-based materials.

Table 5.1 Optimization of chemically driving 1 mol % DASA-PHMA to the closed form.

Trial	Catalyst	Solvent	Temp	Time	Crude results
1 (Sameh's conditions)	PPh_3 (2 eq)	MeCN	75 °C	3 hr 24 hr	Bad solvent, dark blue polymer ppt
2	PPh_3 (2 eq)	Toluene	75 °C	3 hr 24 hr	Blue Brownish-yellow material
3	DMAP (2 eq)	Toluene	75 °C	15 min	Brownish-yellow material
4	**DMAP (2 eq)**	**Toluene**	**RT**	**1 hr**	**Brownish-yellow material**

Table 5.2 Investigating the effect of different equivalence of DMAP on the equilibrium of DASA.

Trial	Catalyst	Equiv.	Solvent	Temp	Time	Crude results
1	DMAP	1	$CDCl_3$	RT	1.5 hr	80% closed
2	DMAP	0.25	$CDCl_3$	RT	1.5 hr	30% closed
3	DMAP	0.05	$CDCl_3$	RT	1.5 hr	Very little change
4	DMAP	1.25	$CDCl_3$	RT	1.5 hr	98% closed
5	**DMAP**	**1.5**	**$CDCl_3$**	**RT**	**1.5 hr**	**99% closed**

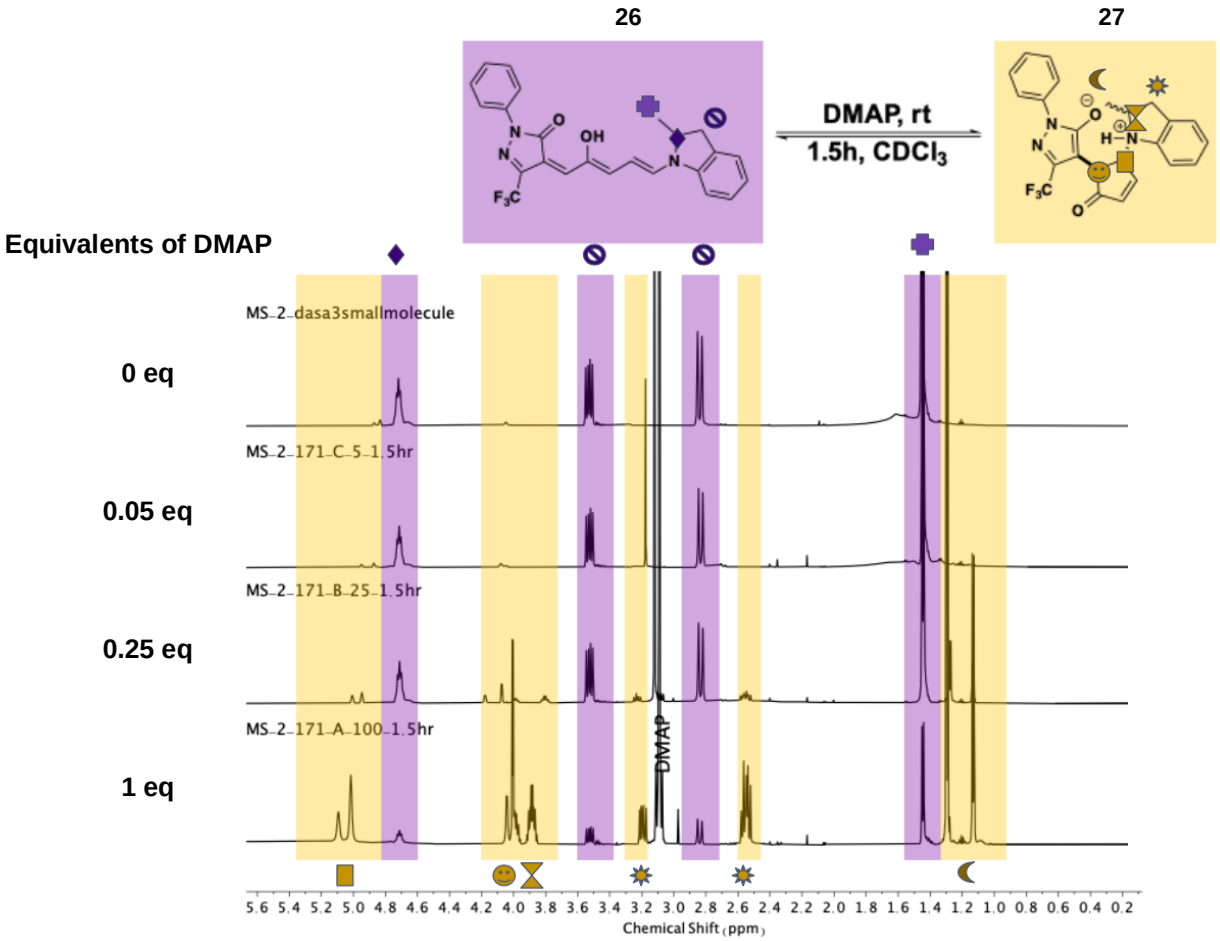

Scheme 5.11 ^{1}H NMR confirmation of the closed form with increasing DMAP in chloroform-d.

Figure 5.14 Upon precipitation into acidic methanol in an ice bath, the closed-form (top) quickly began equilibrating to the open form while stirring and could be isolated at room temperature (bottom).

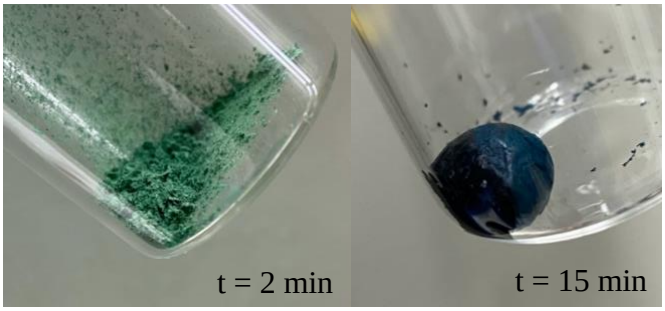

Figure 5.15 Upon precipitation at 0 °C into acidic methanol with two minutes of stirring, partially closed material can be isolated (left). Upon additional stirring (~ 15 minutes) the material equilibrates to the open form (right).

5.4. Conclusion

This section concludes and summarizes this dissertation titled “The Synthesis and Development of Photo-Actuating Materials using Organic Photochromes.” The question that motivated this work is how to convert light directly into actuation using organic photoswitches. To accomplish this goal, we moved beyond traditional chromophores to find photoswitches whose optoelectronic properties are optimized for a given scenario. Among these, donor–acceptor Stenhouse adducts (DASAs), which were introduced in Chapter 1, are especially promising due to their negative photochromism, tunable absorption profile, and large volume change. To incorporate DASAs into photo-actuating materials a better understanding of the photophysical properties is crucial, as well as understanding the concentration dependence. In this effort, we explored the concentration dependence and effect of ionic character on DASAs in Chapter 2. Second, developing a high efficiency photoswitch is not sufficient to make a viable photo-actuating material. Once such a molecule is incorporated into a solid matrix, numerous factors can affect its ability to react, including polymer matrix and photochrome density. We need robust, scalable, and efficient methods to access a range of DASA-based materials and actuator designs to evaluate actuation performance. In Chapter 3, we demonstrated a synthetic platform to chemically conjugate DASA to a load-bearing poly(hexyl methacrylate) (PHMA) matrix via Diels−Alder click chemistry that enables access to DASA-based materials on scale. By leveraging the ease of fabrication of a bilayer design, we developed a tunable, visible light-responsive bilayer actuator driven by the photothermal properties of DASAs. Further, we investigate the influence of the host matrix on the photothermally-driven actuation performance of DASA-based polymers in Chapter 4. We designed polymeric materials with

varying photochrome incorporation and investigated the relationships between material composition and the resulting physical, mechanical, and photoswitching properties. This study led us to the light-induced property changes in T_g and elastic modulus between the materials comprising the open or closed forms of DASAs. Directions for future studies in Chapter 5 include exploring DASA-based nanofibers using electrospinning, leveraging the tunable absorption profile of DASA by wavelength-selective actuation and developing control closed form materials.

5.5. References

(1) Xue, J.; Wu, T.; Dai, Y.; Xia, Y. Electrospinning and Electrospun Nanofibers: Methods, Materials, and Applications. 2019, pp 5298–5415.

(2) Canyon Hydro; Summary, E.; Of, F.; Potential, T. H. E.; Ferreres, X. R.; Font, A. R.; Ibrahim, A.; Maximilien, N.; Lumbroso, D.; Hurford, A.; Winpenny, J.; Wade, S.; Sataloff, R. T.; Johns, M. M.; Kost, K. M.; State-of-the-art, T.; Motivation, T.; Norsuzila Ya'acob1, Mardina Abdullah1, 2 and Mahamod Ismail1, 2; Medina, M.; Talarico, T. L.; Casas, I. A.; Chung, T. C.; Dobrogosz, W. J.; Axelsson, L.; Lindgren, S. E.; Dobrogosz, W. J.; Kerkeni, L.; Ruano, P.; Delgado, L. L.; Picco, S.; Villegas, L.; Tonelli, F.; Merlo, M.; Rigau, J.; Diaz, D.; Masuelli, M. Photochromic Nanofibers. *Intech* **2013**, *32* (July), 137–144.

(3) Livshits, M. Y.; Razgoniaev, A. O.; Arbulu, R. C.; Shin, J.; McCullough, B. J.; Qin, Y.; Ostrowski, A. D.; Rack, J. J. Generating Photonastic Work from Irradiated Dyes in Electrospun Nanofibrous Polymer Mats. *ACS Appl. Mater. Interfaces* **2018**, *10* (43), 37470–37477.

(4) Richard-Lacroix, M.; Pellerin, C. Molecular Orientation in Electrospun Fibers: From

Mats to Single Fibers. *Macromolecules* **2013**, *46* (24), 9473–9493.

(5) Afifi, A. M.; Nakajima, H.; Yamane, H.; Kimura, Y.; Nakano, S. Fabrication of Aligned Poly(L-Lactide) Fibers by Electrospinning and Drawing. *Macromol. Mater. Eng.* **2009**, *294* (10), 658–665.

(6) Yuan, H.; Zhou, Q.; Zhang, Y. 6 - Improving Fiber Alignment during Electrospinning. In *Woodhead Publishing Series in Textiles*; Afshari, M. B. T.-E. N., Ed.; Woodhead Publishing, 2017; pp 125–147.

(7) Zong, X.; Bien, H.; Chung, C. Y.; Yin, L.; Fang, D.; Hsiao, B. S.; Chu, B.; Entcheva, E. Electrospun Fine-Textured Scaffolds for Heart Tissue Constructs. *Biomaterials* **2005**, *26* (26), 5330–5338.

(8) Helmy, S.; Leibfarth, F. A.; Oh, S.; Poelma, J. E.; Hawker, C. J.; Read de Alaniz, J. Photoswitching Using Visible Light: A New Class of Organic Photochromic Molecules. *J. Am. Chem. Soc.* **2014**, *136* (23), 8169–8172.

(9) Helmy, S.; Oh, S.; Leibfarth, F. A.; Hawker, C. J.; Read de Alaniz, J. Design and Synthesis of Donor-Acceptor Stenhouse Adducts: A Visible Light Photoswitch Derived from Furfural. *J. Org. Chem.* **2014**, *79* (23), 11316–11329.

(10) Lee, J.; Sroda, M. M.; Kwon, Y.; El-Arid, S.; Seshadri, S.; Gockowski, L. F.; Hawkes, E. W.; Valentine, M. T.; Read De Alaniz, J. Tunable Photothermal Actuation Enabled by Photoswitching of Donor-Acceptor Stenhouse Adducts. *ACS Appl. Mater. Interfaces* **2020**, *12*, 54075–54082.

(11) Li, L.; Jiang, Z.; Li, M.; Li, R.; Fang, T. Hierarchically Structured PMMA Fibers Fabricated by Electrospinning. *RSC Adv.* **2014**, *4* (95), 52973–52985.

(12) Yuan, H.; Zhao, S.; Tu, H.; Li, B.; Li, Q.; Feng, B.; Peng, H.; Zhang, Y. Stable Jet

Electrospinning for Easy Fabrication of Aligned Ultrafine Fibers. *J. Mater. Chem.* **2012**, *22* (37), 19634–19638.

(13) Wang, X.; Zhang, K.; Zhu, M.; Yu, H.; Zhou, Z.; Chen, Y.; Hsiao, B. S. Continuous Polymer Nanofiber Yarns Prepared by Self-Bundling Electrospinning Method. *Polymer (Guildf).* **2008**, *49* (11), 2755–2761.

(14) Maheshwari, S.; Chang, H. C. Assembly of Multi-Stranded Nanofiber Threads through AC Electrospinning. *Adv. Mater.* **2009**, *21* (3), 349–354.

(15) Liu, Y.; Zhu, C.; Zhao, Y.; Qing, X.; Wang, F.; Deng, D.; Wei, J.; Yu, Y. Directed Pinning of Moving Water Droplets on Photoresponsive Liquid Crystal Mats. *Adv. Mater. Interfaces* **2019**, *6*, 1901158.

(16) Lagerwall, J. P. F.; McCann, J. T.; Formo, E.; Scalia, G.; Xia, Y. Coaxial Electrospinning of Microfibres with Liquid Crystal in the Core. *Chem. Commun.* **2008**, No. 42, 5420–5422.

(17) Bertocchi, M. J.; Simbana, R. A.; Wynne, J. H.; Lundin, J. G. Electrospinning of Tough and Elastic Liquid Crystalline Polymer-Polyurethane Composite Fibers: Mechanical Properties and Fiber Alignment. *Macromol. Mater. Eng.* **2019**, *304*, 1900186.

(18) Kye, Y.; Kim, C.; Lagerwall, J. Multifunctional Responsive Fibers Produced by Dual Liquid Crystal Core Electrospinning. *J. Mater. Chem. C* **2015**, *3* (34), 8979–8985.

(19) Sharma, A.; Lagerwall, J. P. F. Electrospun Composite Liquid Crystal Elastomer Fibers. *Materials (Basel).* **2018**, *11* (3).

(20) Chen, Q.; Diaz, Y. J.; Hawker, M. C.; Martinez, M. R.; Page, Z. A.; Zhang, S. X.; Hawker, C. J.; Read de Alaniz, J. Stable Activated Furan and Donor–Acceptor

Stenhouse Adduct Polymer Conjugates as Chemical and Thermal Sensors. *Macromolecules* **2019**, *52*, 4370–4375.

(21) Ulrich, S.; Hemmer, J. R.; Page, Z. A.; Dolinski, N. D.; Rifaie-graham, O.; Bruns, N.; Hawker, C. J.; Boesel, L. F.; Read de Alaniz, J. Visible Light-Responsive DASA-Polymer Conjugates. *ACS Macro Lett.* **2017**, *6*, 738–742.

(22) Discekici, E. H.; St. Amant, A. H.; Nguyen, S. N.; Lee, I. H.; Hawker, C. J.; Read De Alaniz, J. Endo and Exo Diels-Alder Adducts: Temperature-Tunable Building Blocks for Selective Chemical Functionalization. *J. Am. Chem. Soc.* **2018**, *140* (15), 5009–5013.

(23) Han, F.; Shi, Q.; Zhang, L.; Liu, B.; Zhang, Y.; Gao, Y.; Jia, R.; Zhang, Z.; Zhu, X. Stereoisomeric Furan/Maleimide Adducts as Latent Monomers for One-Shot Sequence-Controlled Polymerization. *Polym. Chem.* **2020**, *11* (9), 1614–1620.

(24) Zuo, B.; Wang, M.; Lin, B. P.; Yang, H. Visible and Infrared Three-Wavelength Modulated Multi-Directional Actuators. *Nat. Commun.* **2019**, *10(1)* (4539), 1–11.

(25) Lerch, M. M.; Wezenberg, S. J.; Szymanski, W.; Feringa, B. L. Unraveling the Photoswitching Mechanism in Donor-Acceptor Stenhouse Adducts. *J. Am. Chem. Soc.* **2016**, *138* (20), 6344–6347.

(26) Lerch, M. M.; Szymański, W.; Feringa, B. L. The (Photo)Chemistry of Stenhouse Photoswitches: Guiding Principles and System Design. *Chem. Soc. Rev.* **2018**, *47* (6), 1910–1937.

(27) Lerch, M. M.; Di Donato, M.; Laurent, A. D.; Medved', M.; Iagatti, A.; Bussotti, L.; Lapini, A.; Buma, W. J.; Foggi, P.; Szymański, W.; Feringa, B. L. Solvent Effects on the Actinic Step of Donor–Acceptor Stenhouse Adduct Photoswitching. *Angew.*

Chemie Int. Ed. **2018**, *57* (27), 8063–8068.

(28) Sanchez, D. M.; Raucci, U.; Ferreras, K. N.; Martínez, T. J. Putting Photomechanical Switches to Work: An Ab Initio Multiple Spawning Study of Donor-Acceptor Stenhouse Adducts. *J. Phys. Chem. Lett.* **2020**, *11* (18), 7901–7907.

(29) Mallo, N.; Brown, P. T.; Iranmanesh, H.; MacDonald, T. S. C.; Teusner, M. J.; Harper, J. B.; Ball, G. E.; Beves, J. E. Photochromic Switching Behaviour of Donor-Acceptor Stenhouse Adducts in Organic Solvents. *Chem. Commun.* **2016**, *52* (93), 13576–13579.

(30) García-Iriepa, C.; Marazzi, M.; Sampedro, D. From Light Absorption to Cyclization: Structure and Solvent Effects in Donor-Acceptor Stenhouse Adducts. *ChemPhotoChem* **2019**, *3* (9), 866–873.

(31) Article, E.; Mallo, N.; Luis, E. T.; Foley, E. D.; Iranmanesh, H.; Kennedy, A. D. W.; Harper, J. B.; Beves, J. E. Chemical Science Acceptor Stenhouse Adduct Photochromic Switches †. **2018**, 8242–8252.

(32) Diaz, Y. J.; Page, Z. A.; Knight, A. S.; Treat, N. J.; Hemmer, J. R.; Hawker, C. J.; Read de Alaniz, J. A Versatile and Highly Selective Colorimetric Sensor for the Detection of Amines. *Chem. - A Eur. J.* **2017**, *23* (15), 3562–3566.

(33) Martínez-Lopez, D.; Santamaría-Aranda, E.; Marazzi, M.; García-Iriepa, C.; Sampedro, D. π-Bridge Substitution in DASAs: The Subtle Equilibrium between Photochemical Improvements and Thermal Control. *Chem. - A Eur. J.* **2021**, *27* (13), 4420–4429.

(34) Helmy, S. Design and Development of Donor-Acceptor Stenhouse Adducts: A New Visible Light Activated Photochromic Compound, 2015